MICROSTRUCTURAL CHARACTERISATION OF SILICON NITRIDE – SILICON CARBIDE PARTICULATE COMPOSITES

SERVET TURAN

Churchill College

Cambridge

A Dissertation Submitted to the University of Cambridge

For the Degree of Doctor of Philosophy

PREFACE

This dissertation is submitted for the degree of Doctor of Philosophy in the University of Cambridge. The research described in this work was carried out by myself in the period October 1990 to March 1995 under the supervision of Dr. K.M. Knowles in the Department of Materials Science and Metallurgy at the University of Cambridge.

To the best of my knowledge the work described in this dissertation is original, except where due reference has been made to the work of others, and nothing is included which is the outcome of work done in collaboration. No part of this dissertation, or any similar to it, has been, or is currently being, submitted for any degree, or other qualification, at any other university. It is less than 60,000 words in length.

Some part of the work described here have been published or accepted for publication (for details see Turan and Knowles in Reference Section at the end of the dissertation).

Servet Turan

March 1995

Abstract

Microstructural characterisation of hot isostatically pressed SiC matrix composites with either 10 or 20 wt% Si_3N_4 particulate reinforcement has been undertaken in this study. The composites were hot isostatically pressed in tantalum cans at 2100°C for one hour under a pressure of 200 MPa. The aim of the research was to obtain an understanding of how the composite microstructure evolved during processing. One batch of material was processed from as-received powders and the other was processed from powder compacts which had been deoxidised to eliminate surface silica on the powder particles. The principal experimental techniques used in the study were X-ray diffraction (XRD) and transmission electron microscopy (TEM).

XRD and TEM showed that the α-SiC starting powder had almost completely transformed to 3C SiC in the composites made from as-received powders, while α-SiC remained untransformed in the composites made from deoxidised green compacts.

Conventional and high resolution transmission electron microscopy (HREM) showed the existence of submicron-size hexagonal BN inclusions at interfaces, and inside SiC and Si_3N_4 grains. There are a number of ways in which these inclusions might arise, but it was concluded that the most likely way is as a product of a chemical reaction between Si_3N_4 and/or SiC with B_2O_3 (which exists on the surface of BN powder used as a protective layer) in the presence of a nitrogen atmosphere (from the decomposition of Si_3N_4). Small Si_3N_4 precipitates inside 3C SiC grains were also observed in the composites made from as-received powders, but not in the composites made from deoxidised materials.

HREM, diffuse dark field and Fresnel defocus imaging techniques have all been used to characterise the nature of the grain boundary and interphase boundary structure in these materials. Most interfaces in the composites prepared from as-received powders were found to be wetted by ≈ 10 Å wide amorphous intergranular films, with the exception of twin boundaries, and what could be inferred from their crystallography to be special low energy interfaces. By contrast, most interfaces in the deoxidised material were free of such intergranular films.

The various theories on the equilibrium amorphous film thickness at interfaces have been reviewed and used to explain the experimental results obtained throughout this study and reported by others in the literature. Whenever the theories failed or were insufficient to explain the results, the theories have been extended. For example, when BN grains were on one side of the interfaces, the film thickness was found experimentally to depend on the interface orientation with respect to the basal plane of the adjacent hexagonal BN grain.

The existence of intergranular phases in composites prepared from as-received powders and the relative absence of such films in composites prepared from deoxidised powder compacts, coupled with the much lower densification rates for composites prepared from deoxidised powders, suggest strongly that densification took place efficiently in the composites made from as-received powders because of liquid phase sintering. Liquid phase sintering and the nitrogen atmosphere present in the composites during the hot isostatic pressing are concluded to catalyse the 'reverse' α → β SiC phase transformation found in the composites made from as-received powders.

Contents

Preface i
Acknowledgements ii
Abstract iv
Contents v

Chapter 1
Introduction

1.1 Thesis background 1
1.2 Thesis organisation 3

Chapter 2
Introduction to Interfaces

2.1 Introduction 4
2.2 Description, classification and terminology of interfaces 4
2.2.1 Homophase boundaries (grain boundaries) 5
2.2.2 Heterophase boundaries (interphase boundaries) 7
2.2.3 Classification in terms of the structure of interfaces 8
2.3 Why is it important to study interface properties? 9
2.4 Are the structure of interfaces in ceramics similar to those in metals? 10
2.5 Characterisation of interfaces 11
2.5.1 Characterisation of interfaces containing intergranular films 12
2.5.1.1 Defocus Fresnel fringe imaging 12
What are the necessary conditions for the observation of useful Fresnel fringes? 13
How can useful information be deduced from Fresnel fringes? 15
2.5.1.2 Diffuse dark field imaging 16
2.5.1.3 High resolution electron microscope imaging (HREM) 16
2.5.1.4 Drawbacks of the techniques 17
2.5.1.5 Which is the best technique to measure intergranular film thickness? 20
2.5.2 Characterisation of structured interfaces 22
2.6 Summary 24

Chapter 3
General Microstructure of the Composites

3.1 Introduction 25

3.2 Justification of the choice of materials and processing route 25

3.2.1 Why ceramics? 25

3.2.2 Why not ceramics? 26

3.2.3 Why composites? 26

3.2.4 Why particulate reinforced composites? 26

3.2.5 Why silicon nitride-silicon carbide composites? 26

3.2.6 Why hot isostatic pressing? 27

3.2.7 Why deoxidation? 28

3.3 Introduction to silicon carbide and silicon nitride 29

3.3.1 Structure of silicon carbide and polytypism 29

3.3.2 Structure of silicon nitride 31

3.3.3 Densification mechanism of silicon carbide 32

3.3.4 Densification mechanism of silicon nitride 37

3.4 Materials 38

3.5 Experimental procedure 40

3.5.1 Density measurements 40

3.5.2 X-ray diffraction 40

3.5.3 Transmission electron microscope analysis 40

3.6 Experimental results 42

3.6.1 Density measurements 42

3.6.2 X-ray diffraction results 42

3.6.3 Microstructure of composites made from as-received powders 44

3.6.4 Microstructure of composites made from deoxidised compacts 45

3.7 Discussion 46

3.7.1 Relative densities of the composites 46

3.7.1.1 The effect of deoxidation on the densification behaviour 46

3.7.1.2 The effect of silicon nitride content on the densification behaviour 49

3.7.2 Comparison of general microstructure 50

3.8 Conclusions 51

Chapter 4
TEM Observations of Graphite-like Inclusions

4.1 Introduction 53
4.2 Experimental results and discussions 54
4.2.1 Observation of inclusions 54
4.2.2 PEELS analysis of boron nitride inclusions 56
4.2.3 Carbon layers in h-BN inclusions 62
4.2.4 Morphology and size of the inclusions 63
4.2.5 Stacking faults and dislocations in h-BN inclusions 64
4.2.6 Delamination cracks 65
4.2.7 Introduction to misorientation bands 67
4.2.7.1 Deformation bands 67
4.2.7.2 Twinning 68
4.2.7.3 Kink bands 68
4.2.7.4 Observations of misorientation bands 71
4.2.8 Possible formation mechanisms of h-BN inclusions 76
4.3 Conclusions 81
Appendix 4.1 Formal description of twinning crystallography 83

Chapter 5
Equilibrium Film Thicknesses at Interfaces in Engineering Ceramics and Ceramic Matrix Composites

5.1 Introduction 84
5.2 Wetting behaviour of interfaces 84
5.3 Equilibrium film thickness 88
5.4 The theory of the equilibrium film thickness by Clarke's model 89
5.4.1 Force balancing approach 89
5.4.2 Attractive forces 90
5.4.2.1 External pressure 90
5.4.2.2 Van der Waals forces 91
5.4.3 Repulsive forces 92
5.4.3.1 Structural or steric forces 92
5.4.3.2 Electrical double-layer forces 92

5.5 Estimate of the equilibrium film thickness by Clarke's model 94
5.6 Is Clarke's theory sufficient to explain the experimental observations? 95
5.7 The calculation of Hamaker constants of interphase boundaries 98
5.8 Results and discussion 100
5.8.1 Equilibrium film thickness at interphase boundaries 100
5.8.2 Case study: Effect of misorientation on the film thickness 105
5.8.3 Other parameters effecting the equilibrium film thickness 107
5.8.3.1 The effect of film composition 107
How do these theoretical considerations relate to experimental observations? ... 110
5.8.3.2 Combined effect of repulsive forces ($\Pi_{ST} + \Pi_{EDL}$) 113
5.8.3.3 The effect of liquid volume on the film thickness 116
5.9 Conclusions 117

Chapter 6
Characterisation of Interfaces in Si_3N_4 - SiC Composites

6.1 Introduction 119
6.2 Assessment of accuracy of TEM techniques on the detection and measurement of film thickness 120
6.3 Interface structures in the composites made from as-received powders 123
6.3.1 Interfaces between SiC grains 123
6.3.2 Grain boundaries between Si_3N_4 grains 125
6.3.3 Interphase boundaries between SiC and Si_3N_4 128
Interphase boundaries between SiC grains and Si_3N_4 precipitates 128
Interphase boundaries between SiC and Si_3N_4 grains 131
6.3.4 Interphase boundaries between h-BN inclusions and SiC grains 134
6.3.5 Interphase boundaries between h-BN inclusions and Si_3N_4 grains 139
6.3.6 Grain boundaries between h-BN inclusions 141
6.5 Microstructural characterisation of composites made from deoxidised powder compacts 144
6.6 The composition of intergranular films 146
6.7 Discussion and conclusions 149

Chapter 7
$\alpha \rightarrow \beta$ Reverse Transformations of SiC

7.1 Introduction 153

7.2 Background to polytype stability and SiC phase transformations..... 153

7.2.1 Polytype stability..... 153

7.2.2 The $\beta \rightarrow \alpha$ SiC transformation..... 154

7.2.3 The $\alpha \rightarrow \beta$ SiC 'reverse' transformation..... 155

7.2.4 Transformation mechanisms..... 157

7.2.5 Transformation kinetics..... 157

7.3 Materials..... 158

7.4 Results..... 159

7.4.1 XRD results..... 159

7.4.2 Diffraction pattern analysis in TEM..... 160

7.4.3 Transmission electron microscopy observations..... 162

7.4.3.1 Hexoloy SA material..... 162

7.4.3.2 Hexoloy ST material..... 162

7.4.3.3 Layered SiC composite with graphite interlayer..... 162

7.4.3.4 As-received Si_3N_4-SiC composites..... 163

7.5 Discussion..... 163

7.5.1 XRD and diffraction pattern analysis..... 163

7.5.2 The effect of existence and content of Si_3N_4 (or nitrogen atmosphere) on the reverse transformation..... 164

7.5.4 The effect of a liquid medium on the reverse transformations..... 164

7.5.5 Does the existence of BN effect the rate of reverse transformation?..... 166

7.5.5 What is the mechanism of the reverse transformation?..... 171

7.6 Conclusions..... 175

Chapter 8
Conclusions and Suggestions for Further Work

8.1 Summary and conclusions..... 177

8.2 Suggestions for further work..... 183

References..... 185

Chapter 1

Introduction to the Thesis

1.1 Scope of this study

Ceramic matrix composites are a family of materials which have been developed to try and overcome the intrinsic brittle nature of monolithic ceramics by incorporating fibres, whiskers and particulates as discrete second phases. Fibre- and whisker-reinforced composites have good toughness and superior mechanical properties in comparison to monolithic ceramics, but there are a number of problems associated with their use. For example, the toxicity of the whiskers limits their appeal and the use of fibre reinforced composites are limited to low temperatures, in addition to the increased difficulty in their fabrication and in any reasonably complex near-net shaping. Therefore, particulate reinforced composites, and especially 'nanocomposites' continue to be of research interest.

The structure and properties of grain boundaries and interphase boundaries influence almost all mechanical, physical, chemical and electronic properties of the materials. Although there has been research on grain boundaries over a number of years, there is a continuing need for a more detailed knowledge about the properties of individual grain boundaries and their dependence on parameters such as their grain boundary crystallography and their chemical doping.

In this study, Si_3N_4 particulate reinforced SiC composite was chosen with the eventual aim of being able to characterise thoroughly the microstructure and in particular the structure of grain boundaries and interphase boundaries and to relate these observations to the current understanding of interfaces in composite materials.

However, as the studies progressed some additional aims for the study emerged. The composites were fabricated using hot isostatic pressing to overcome the need to add sintering aids which generate a liquid phase at fabrication temperatures and ease the densification, but remain as amorphous intergranular films at interfaces and triple junctions at room temperature. They are able to creep at high temperatures, therefore limiting the temperature capability of the ceramic material. In view of this, there are some attempts reported in the literature to densify SiC and Si_3N_4 monolithic ceramics without using any sintering additives by hot isostatic pressing, but intergranular films were still detected at interfaces in Si_3N_4 ceramics where the films arise from thin surface films of silica in the starting powder. Therefore, hot isostatic pressing was conducted on both as-received powders and deoxidised powder compacts where the surface silica had been reduced prior to full composite consolidation. Because of this, the aims of the work were widened to give an assessment of the effect of pretreatment on the composite densification behaviour through a detailed examination of the composite microstructure by transmission electron microscopy.

During transmission electron microscope investigations, submicron size graphite-like inclusions were detected. This enlarged the study further, making it necessary to identify the crystal structure of these inclusions and to find out how they were formed and also to characterise the interphase boundaries formed between the inclusions and the adjacent SiC and Si_3N_4 grains

1.2 Structure of the thesis

This dissertation consists of eight chapters and a section at the end where the references used throughout the dissertation are displayed in alphabetical order.

This introductory Chapter is followed by Chapter 2 where the interfaces are introduced in general, starting with a description, classification and the terminology used. Also questions are asked and answered about why it is important to study interfaces, how the interfaces in ceramics differ from the interfaces in metals and how the interfaces are characterised by using transmission electron microscopes.

In Chapter 3, justification of the choice of materials and the fabrication route is discussed. This Chapter also includes sections of introductory briefings about the structure and densification mechanisms of SiC and Si_3N_4 materials. Then, the fabrication and characterisation techniques of materials used in this study are described. Finally, the very general microstructure of the composites are presented and some questions are raised to form a basis for the following chapters.

At the beginning of Chapter 4, a short introduction is given about inclusions in SiC-based materials observed in the literature and how these inclusions effect the properties of ceramic materials. Secondly, experimental results are discussed in the light of reported results in the literature. The Chapter concludes by proposing possible formation mechanisms for the inclusions.

Chapter 5 contains an introduction to the existing theories about the equilibrium film thicknesses in ceramics. These theories are then tested to explain some of my own experimental results as well as some information from the literature to provide a background to Chapter 6 where the experimental results obtained throughout this study on the characterisation of individual interfaces are presented. Whenever the theories failed or were insufficient to explain the results, the theories have been extended. Furthermore, some of the incorrectly interpreted experimental results in the literature are reviewed.

In Chapter 7, microstructural observations on the $\alpha \rightarrow \beta$ SiC reverse transformations are reported and towards the end of this chapter a mechanism believed to be responsible for the occurrence of this unusual reverse transformation is proposed. The effect of inclusions on the transformations are also examined.

Finally in Chapter 8, the main conclusions are drawn from this work and suggestions have been made for future work.

Chapter 2

Introduction to Interfaces

2.1 Introduction

The structure and properties of interfaces influence almost all mechanical, physical, chemical and electronic properties of materials. Before explaining how they effect these properties and before describing details about the structure of interfaces it is necessary to discuss the terminology used to describe these interfaces and how they are classified.

2.2 Description, classification and terminology of interfaces

First of all, *what is an interface?* It is a meeting surface between two dissimilarly oriented perfect crystals or between two chemically different crystals. In other words, an interface is a crystallographic or chemical discontinuity. Hence, classification of interfaces can be achieved by considering two different criteria (Fig. 2.1):

i) In terms of crystal structure and chemistry of adjacent crystals, interfaces can be classified into homophase and heterophase boundaries (Cahn and Kalonji, 1982 & Finnis and Rühle, 1993). *Homophase boundaries* form between grains of identical crystal structure and composition, *e.g.*, grain boundaries, twin boundaries, domain boundaries and stacking faults. On the other hand, *heterophase boundaries* form between regions of different crystal structure and/or chemical composition, *e.g.*, interfaces between coexisting polytypes, between metal-ceramic joints and most interfaces between the matrix and the reinforcing agents in composite materials. Therefore, in this dissertation, the term "*interfaces*" is used as a general term and the terms "*grain boundary*" and "*interphase boundary*" are used to distinguish between the two types of interface.

ii) In terms of the structure, interfaces in ceramics can be divided into those interfaces which contain intergranular phases and those which are structured.

2.2.1 Homophase boundaries (grain boundaries)

Grain boundaries can be grouped into low angle and high angle boundaries in terms of the misorientation across the interface. Interfaces with a misorientation less than $\approx 15^\circ$ are known as *low angle* grain boundaries where the interface structure can be described as an array of lattice dislocations (Read and Shockley, 1950). A characteristic of a low angle boundary structure is that the spacing of the dislocations decreases as the misorientation angle increases. When the misorientation angle is higher than 15°, the spacing of the dislocations becomes comparable with the interatomic spacing. Grain boundaries with angular misorientation larger than 15° are called *high angle* grain boundaries.

In order to express the structure of high angle grain boundaries, the coincident site lattice (CSL) model has been developed (Kronberg and Wilson, 1949). In the purely geometric formalism of this model, when two crystal lattices are rotated with respect to one another through certain angles, a fraction of lattice sites in one crystal may coincide with a fraction of lattice sites in the other crystal. This lattice of coincident sites is called a CSL and the inverse of the fraction of the coincident lattice sites is defined to be Σ. The simplest form of CSL in f.c.c. materials is the $\Sigma = 3$ twin boundary, formed by a rotation of 180° about [111]. $\Sigma = 3$ signifies that one-third of the lattice sites on either side of the interface are common to both grains. An example of a CSL is given in Fig. 2.2(a). which is a [001] projection showing the two interpenetrating f.c.c. lattices 1 and 2, misoriented by a rotation of 36.87° around a common axis [001].

The misorientation in an exact low-energy CSL orientation is considered to be accommodated by arrays of closely spaced 'primary' grain boundary dislocations and small departures from CSL orientation are accommodated by arrays of more coarsely spaced 'secondary' grain boundary dislocations which can maintain the low energy structure at the interface (Forwood and Clarebrough, 1991). The spacing of secondary grain boundary dislocations decreases with increasing angular separation from the exact CSL orientation in the same way as the spacings of dislocations in low angle boundaries decreases with the increasing misorientation. It is also proposed that in order for secondary grain boundary dislocations to maintain the CSL structure, they must have Burgers vectors which are lattice vectors or sums or differences of lattice vectors. This class of vectors was first introduced by

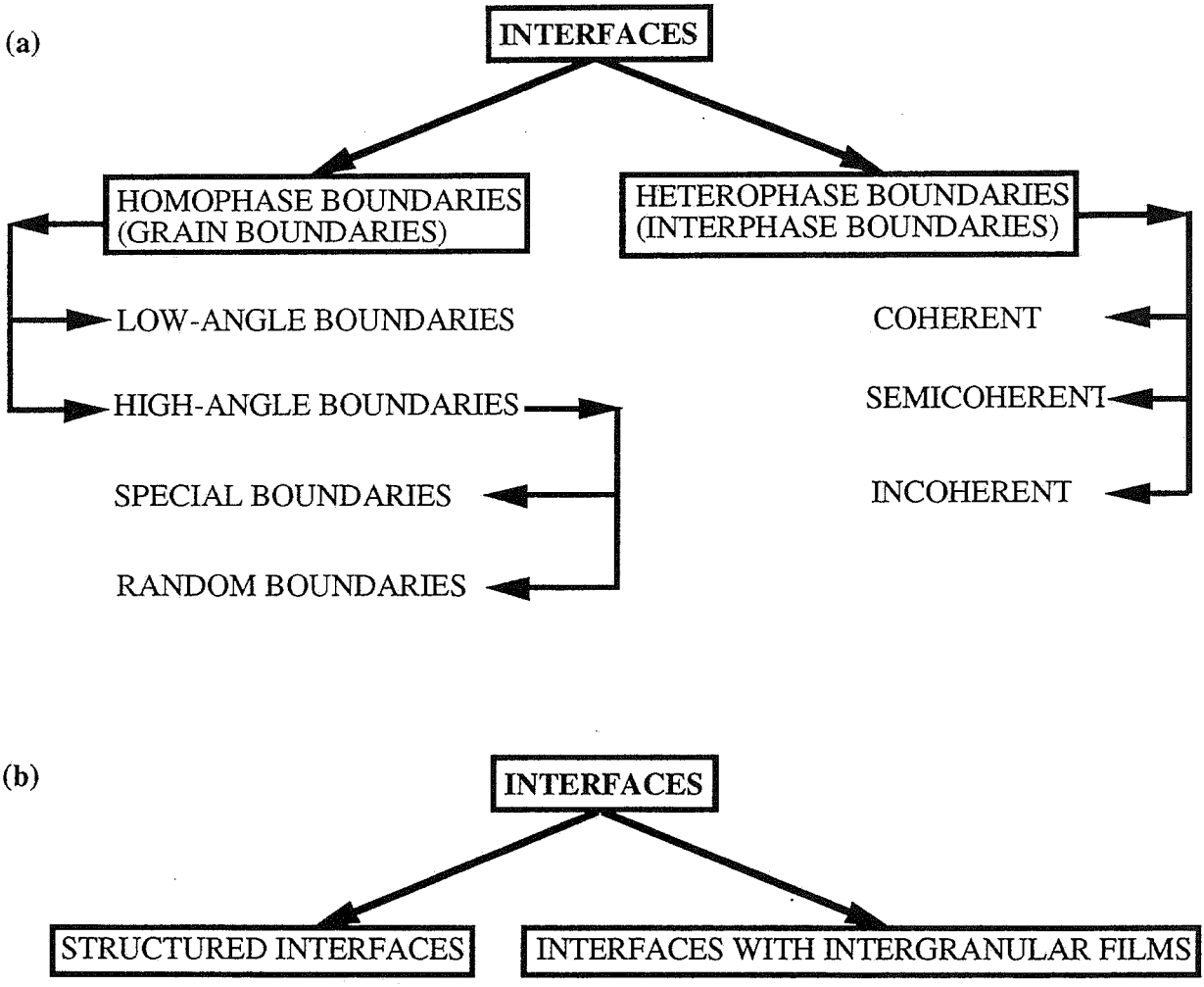

Fig. 2.1 The classification of internal interfaces in terms of two different criteria: (a) in terms of crystal structure and chemistry of adjacent phases and (b) in terms of chemistry and defect structure of the boundary.

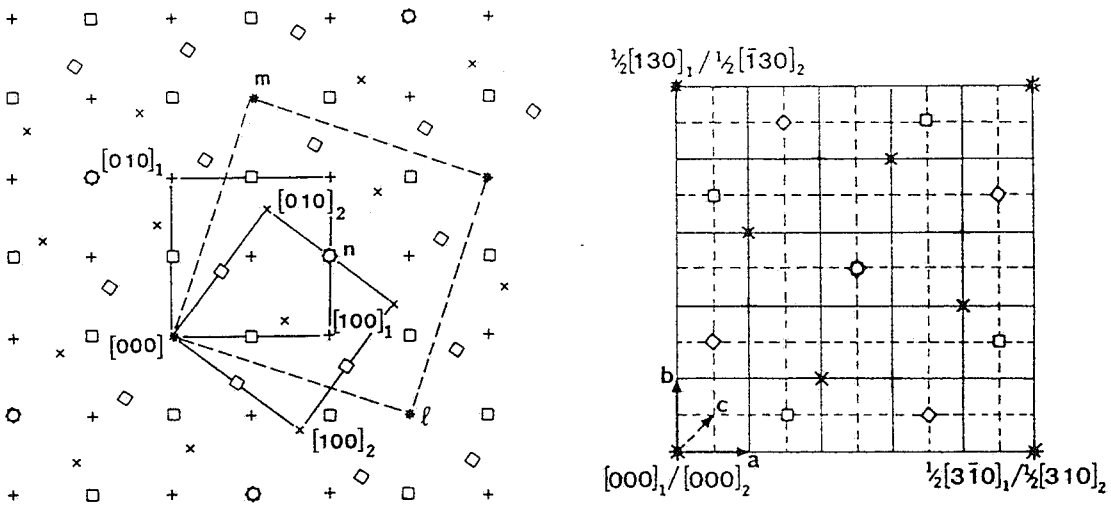

(a) **(b)**

Fig. 2.2. (a) [001] projection of two interpenetrating f.c.c. lattices at the $\Sigma = 5$ CSL orientation. Lattice 1 is represented by the symbols + and □, where + is in the plane of the page and □ is (1/2) [001] below the plane of the page. Similarly, lattice 2 is represented by the symbols x in the plane of the page and ◊ is (1/2) [001] below the plane of the page. (b) The CSL and DSC lattices for two f.c.c. lattices misoriented at the $\Sigma = 5$ CSL orientation (after Forwood and Clarebrough, 1991).

Bollmann (1967 and 1967a) and belongs to a lattice known as the DSC (displacement shift complete) which is the coarsest lattice that contains all the lattice points of both interpenetrating lattices when they are at the exact CSL orientation. An important point is that when the degree of coinciding lattice sites decrease, the CSL lattice tends to become larger and the DSC lattice becomes smaller. An example of DSC lattice is also shown in Fig. 2.2(b).

For non-cubic crystals exact CSLs can only be found for rotations about a very restricted number of crystal axes. For example, in the hexagonal close-packed materials exact CSLs only occur for rotations about [0001] and for other axes only when the axial ratio c/a is such that $(c/a)^2$ is a rational number (Bruggeman *et al.*, 1972). Bonnet *et al.* (1981) extended the CSL model to non-cubic materials taking secondary grain boundary dislocations accommodating not only a small departure but also the strain required to bring near coincident lattice sites in the interpenetrating lattices into a constrained coincidence, *i.e.*, to form near CSL (n-CSL) or a constrained CSL. The n-CSL value can be obtained by stretching or compressing the real structure until $(c/a)^2$ is a rational number.

O-lattice theory (Bollmann, 1970) is developed as a more general concept in comparison with the CSL, in that it proposes a registry between the two lattices rather than only the lattice points. Although the O-lattice is the most complete model and despite the existence of other models (structural unit model and coincident axial direction model) for describing grain boundary geometry, the CSL model is found to be appropriate and satisfactory for the characterisation of large datasets in polycrystals and, therefore, it is the most largely used model (Randle, 1993).

However, not all the grain boundaries are close to CSL orientations. Therefore, high angle grain boundaries can be further divided into two sub-divisions, *i.e.*, special grain boundaries which are strictly at or near CSL orientations and random grain boundaries which are at non-CSL orientations. The CSL model does not predict absolute properties of the grain boundaries since the properties only partially depend on the grain boundary geometry and also depend on the local defect structure (relaxations at the interface), chemistry and electronic bonding (Sutton and Balluffi, 1987).

Grain boundaries can also be described according to the relative position of the rotation axis with respect to the interface plane. When the interface plane is parallel to the rotation axis it is called a *tilt* boundary, whereas if the interface plane is the plane perpendicular to the rotation axis and the indices of the plane is the same in both grains, it is called a *twist* boundary. For tilt boundaries, if the indices of the plane are different in both grains the grain boundary is known as *asymmetric tilt* boundary, but if the indices are the same then it is known as *symmetrical tilt* boundary. Mixed grain boundaries have both tilt and twist components. The *rotation axis* (also called *misorientation axis*) is a rotation through an angle θ about an axis UVW which has the same indices in both neighbouring grains. The *interface plane* is the surface between two grains which defines the interface referred to by the crystallographic coordinates of its normal in both grains.

2.2.2 Heterophase boundaries (interphase boundaries)

Interphase boundaries can form between two chemically different phases whose crystal structures are the same (*e.g.*, γ/γ' phases in Ni-Al alloys (f.c.c.)). Such condition give rise to the simplest type of interphase boundaries being two cubic crystals in the so-called cube-on-cube orientation. More complicated interphase boundaries form when the interface involves either both the grains have different chemistry and crystal structure (*e.g.*, SiC (f.c.c.) and mullite (orthorhombic)) or same non-cubic crystal structure but different chemistry (*e.g.*, Si_3N_4 (h.c.p.) and SiC (h.c.p.)).

Interphase boundaries can be classified in terms of a misfit at the interface. If the atom planes between two crystals at the interface match perfectly, then it is called a *coherent*[@] *interface*. Conversely, if there is no continuity of planes across the interface, *i.e.*, a one-on-one atomic matching does not exist even locally, then the interface is referred to as a *incoherent interface* (Christian, 1975). Schematic views of coherent, incoherent and semi-coherent interfaces are shown in Fig. 2.3. The energy of the interface formed between the two crystals is dependent on the misfit between the lattices. Calculations of the dependence of interfacial energy with atomic fit have been dominated by the work of Frank and van der Merwe and their work has

---

[@] *The term epitaxial is sometimes used instead of coherent. To avoid confusion the term epitaxy will be used when referring to the growth process, while the atomic structure at the interface will be characterised in terms of the concepts of coherency (Wolf, 1992).*

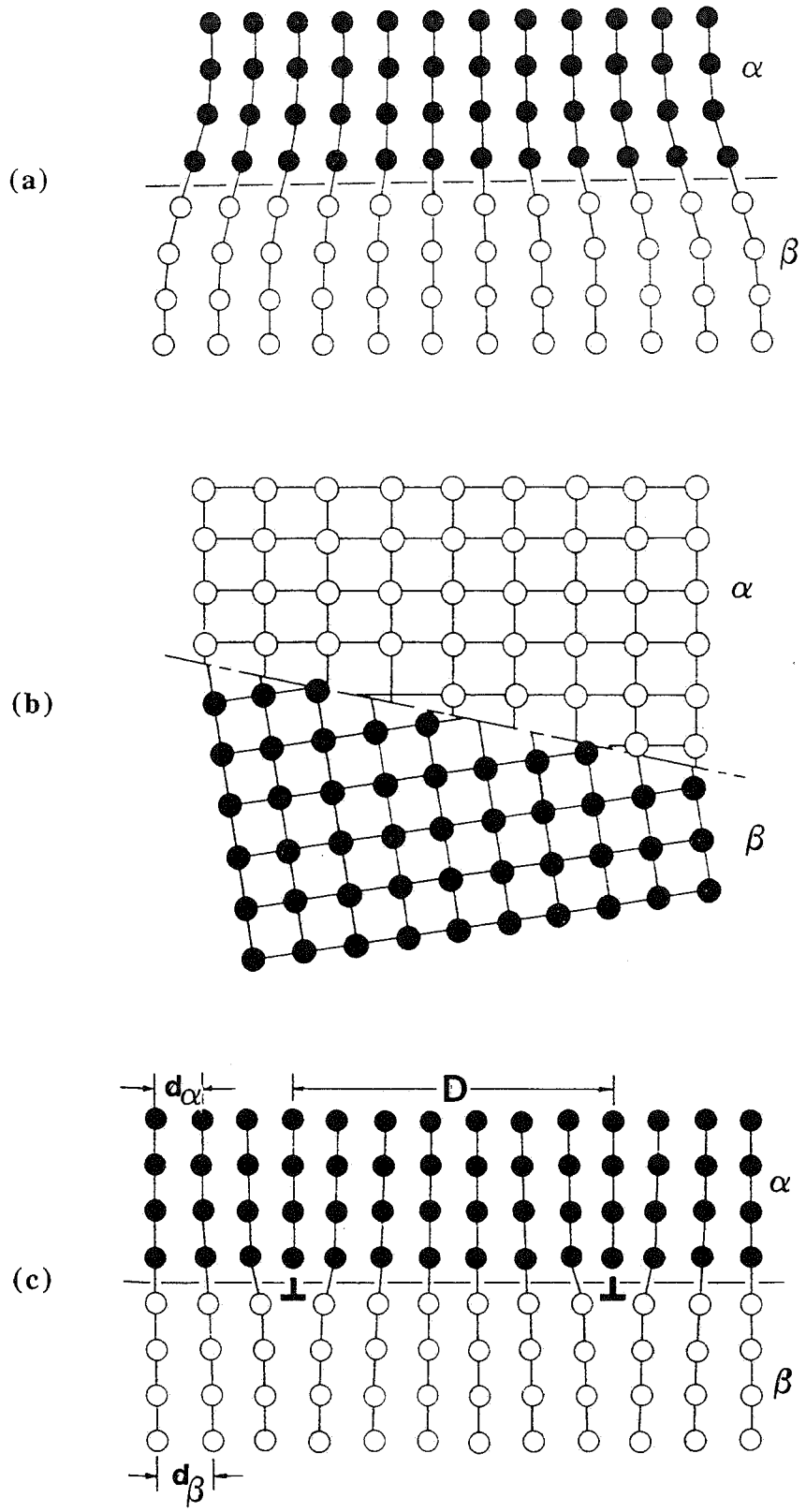

Fig. 2.3 Schematic views of (a) coherent, (b) incoherent and (c) semi-coherent interfaces (after Porter and Easterling, 1992).

been extensively reviewed by Matthews (1975). Because of the elastic energy involved, a coherent interface can be formed only for a relatively small lattice parameter mismatch *(f)*,

$$f = \frac{d_\alpha - d_\beta}{d_\beta}$$

where d_α and d_β refer to the unstrained lattice parameters of the substrate and thin film overlayer, respectively.

The strains associated with a coherent interface raise the total energy of the system, and for sufficiently large atomic misfit, or interfacial area, it becomes energetically more favourable to replace the coherent interface with a semicoherent interface in which the disregistry is periodically taken up by misfit dislocations as shown in Fig. 2.3(c). The energies of coherent, semicoherent and incoherent interfaces increases monotonically and are generally in the range up to $\approx$ 200, 200-500 and 500-1000 mJm^{-2}, respectively (Porter and Easterling, 1992).

The geometry of interphase boundaries may be described in the same way as grain boundaries by using CSL model. The problems associated with the construction of CSL for non-cubic crystals apply to interphase boundaries as well. In a way, the extension of CSL to n-CSL can also be adopted to construct CSL orientations at interphase boundaries. The adoption procedure of CSL model to interphase boundaries have been discussed in Forwood and Clarebrough (1991).

2.2.3 Classification in terms of the structure of interfaces

Irrespective of whether the interfaces are homophase boundaries or heterophase boundaries they are either structured or they contain intergranular phases. In general, the nature of the interfaces are determined by their energies, as will be discussed in Chapter 6. It is believed that interfaces are structured if they are low-angle and low index special high-angle boundaries, whereas interfaces containing intergranular phases can be either a high-angle random boundary or a high index special high-angle boundary.

The intergranular phases could be crystalline (rarely) or amorphous (mostly). From now on, the term "intergranular films" will be used to describe the phases at the interfaces. If the film is amorphous, then a distinction has to be made between segregation and a genuine intergranular film. Rühle *et al.* (1984) have suggested that an intergranular film forms when the density of any segregated impurities is larger than one atomic layer, otherwise it is called segregation. Note that it is also dangerous to use a term like "glassy films" to describe intergranular films since there is some evidence that these films are more ordered than the glass at triple junctions (Marion *et al.*, 1987).

2.3 Why is it important to study interface properties?

The structure and properties of interfaces control most of the properties of the polycrystalline materials. For example, interface energy is determined by interface structure and plays a central role in various interface properties such as impurity segregation, interface mobility and fracture, diffusion and cavitation.

Wolf (1982) computed the structures and energies of <001> twist boundaries (assumed to be clean, *i.e.*, neither intrinsic defects nor impurities are present) and obtained a rather high interface energy which increases with increasing twist angle. The energies of the twist boundaries are almost double the energy of a free surface, implying that twist boundaries are unstable in oxide ceramics. The effect of interface energy on the wetting behaviour of interfaces in ceramics and composites will be examined in Chapter 5.

Further phenomena are also influenced by the properties of interfaces as highlighted by Clarke (1979) and Randle (1993). For example, interfaces are known to be preferred fracture paths if the interface bonding is weak and also control a range of creep behaviour (Blumenthal and Evans, 1984). In addition, they are paths for rapid solute diffusion and other segregation phenomena (Kingery, 1974). Barium titanate positive temperature coefficient devices, zinc oxide and titanium oxide varistors derive their unique properties from the property changes that occur at their grain boundaries, and do not show the same properties in their single crystal form (Clarke, 1990). The current-carrying capability of a high-T_C superconductor is dependent on the nature and form of any interface impurities it contains.

Most of the interfaces in ceramics contain intergranular films which can be detrimental to the high temperature properties (such as creep, oxidation behaviour) as well as low temperature properties (such as fracture toughness) of the materials by altering the fracture mode from transgranular to intergranular fracture. It is also found (Clarke, 1991) that the strength varies with the dihedral angle of triple junction phases which is controlled by the impurities. The rupture strength of magnesite refractories is known to increase with increasing dihedral angle. The dihedral angle can be increased by the addition of Cr_2O_3 or can be decreased by the addition of Fe_2O_3. However, intergranular films are not always harmful to the properties of materials and in some cases they are beneficial. For example, 20 wt% SiC-Si_3N_4 nanocomposites derive their superplastic properties from the intergranular films that they contain (Wakai *et al.*, 1990). A second example is that in Mn-Zn ferrites an insulating intergranular film is necessary to increase the resistivity of the material without affecting the overall magnetic properties.

Rühle (1984) suggested that the existence of amorphous intergranular film lowers the energies of the random interfaces, and thereby increasing the strength and toughness of the material. He reached this conclusion in the light of the experimental evidence that all strong and tough ceramics like ZrO_2 and ZrO_2-Al_2O_3 composites contain thin intergranular films.

2.4 Are the structure of interfaces in ceramics similar to those in metals?

Kingery (1974) suggested that, from a purely phenomenological viewpoint, interfaces in ceramics should have many similarities to those in metals. However, there exist important differences. In general, interfaces in ceramic materials can show a wide range of 'structures' depending on factors such as the nature of bonding, the presence of impurities and/or second phases, and the crystallography of the interface (its axis/angle pair, interface plane and any rigid body displacements of the grains on either side of the interface) (Norton and Carter, 1990).

Most of the findings until 1973 about the grain boundaries in ceramics are reviewed by Kingery (1974). Recent findings about the interfaces in structural ceramics have been reviewed by Clarke (1990) & Norton and Carter (1990). Norton and Carter (1990) concluded that:

1. Structured interfaces (both low- and high-angle) can exist in ionic ceramics (Sun and Balluffi, 1982 & Morrisey and Carter, 1984).

2. Amorphous intergranular films occur at interfaces in both covalently bonded and ionicly bonded ceramics (Stenton and Harmer, 1983). Most amorphous films in ceramic interfaces are siliceous and their widths vary generally in the range of 5–100 Å.

3. The structure of interfaces in ceramics tends to be relatively more open (and therefore less dense) than interfaces in metals because of either the ionic or the covalent nature of the bonding (Carter *et al.*, 1986 & Duffy and Tasker, 1986).

2.5 Characterisation of interfaces

As has been pointed out above, there are basically two types of interfaces to consider in ceramic materials, those without intergranular films and those with intergranular films. Because of the size scales required when examining interfaces, characterisation of interfaces requires high magnifications and high instrumental resolutions. It is therefore almost limited to transmission electron microscope (TEM) techniques. Currently available TEM techniques for the characterisation of interfaces are bright field imaging, dark field imaging, diffuse dark field imaging, weak beam dark field imaging, diffraction pattern analysis, Fresnel defocus imaging and high resolution transmission electron microscope (HREM) imaging. Some of the above techniques are particularly useful for characterising interfaces containing intergranular films, but in addition, analytical electron microscopy techniques such as energy dispersive X-ray (EDX) and parallel electron energy loss spectroscopy (PEELS) have to be used to obtain chemical information about the intergranular film.

There is no single technique capable of fully characterising an interface structure. Therefore, it is desirable to use complementary techniques in order to maximise the available information as well as the reliability of the results. In the remaining part of this Chapter, some of the above mentioned techniques are discussed in detail.

2.5.1 Characterisation of interfaces containing intergranular films

Intergranular films arise due to several different processes. The first and most important one is as a result of the remnants of densification aids since many ceramic materials (especially covalently bonded) require the use of minor trace elements known as additives to obtain full densification. Secondly, they form from the impurities present in the starting powders. Thirdly, they exist because the materials are prepared from incomplete crystallisation processes. Whatever the reason is, they all remain at interfaces and triple junctions and effect the properties of the materials. Therefore, the identification and measurement of their thicknesses becomes very important. There are three principal techniques for the identification of intergranular films (Clarke, 1979). These are defocus Fresnel fringe imaging, diffuse dark field imaging and HREM imaging.

2.5.1.1 Defocus Fresnel fringe imaging

This is a technique well suited to the detection of amorphous intergranular films and for measuring their thickness. The technique is based on the interpretation of contrast produced at the interfaces where there is an abrupt discontinuity in the mean inner potential when the interface is imaged in an out-of focus condition under coherent illumination. The simplest way to visualise the occurrence of Fresnel fringes is by holding two very stable fingers (with a small gap between them) against a light source and defocusing your eyes by moving towards your fingers until a set of dark and bright fringes can be seen. The fringes form due to a phase shift $\Delta\Phi$ as expressed by Clarke (1979) in terms of the difference in mean inner potential (ΔV) is as follows:

$$\Delta\Phi = \pi it\Delta Vek_o / E \tag{2.1}$$

where t is the specimen thickness, e is the electron charge, k_o is the magnitude of the incident wave vector and E is the acceleration voltage. The mean inner potential (V_o) of a crystal can be calculated by using the equation (Doyle and Turner, 1968):

$$V_0 = \frac{h^2}{2\pi me\Omega} \sum_{unit\ cell} f_j(0) \tag{2.2}$$

where h is Planck's constant, m is electron mass and Ω is unit cell volume and the summation is over f_j, the electron scattering factor of the atoms in the unit cell.

The technique has been used in different fields, but Clarke (1979) was the first who applied the technique in the field of ceramic materials to show the presence of thin intergranular films that occur in MgO-doped Si_3N_4. He confirmed this by diffuse dark-field imaging. The technique then found new applications due to the various causes of variations in the mean inner potential at an interface and has been developed further in a number of laboratories (Stobbs and co-workers in Cambridge, Rühle and co-workers in Germany and Carter and co-workers in U.S.A.). A general description and the recent developments of the technique is highlighted by Stobbs and Ross (1989).

The mean inner potential can vary (Rühle *et al.*, 1984) as a result of changes in density, *e.g.*, due to dislocations, changes in composition or stoichiometry, impurity segregation, thickness variations and a space charge at the interface. Rühle and Sass (1984) have attempted to use changes in the spacings of the Fresnel fringes to deduce a value for the scattering potential at the dislocation cores in low-angle end-on NiO grain boundaries. Ness *et al.* (1986) showed that the mean scattering potential of intergranular films in ceramics could be determined and associated the values obtained with the film composition. Their work has established an important new use of the technique, *i.e.*, as a complementary technique to EDX and PEELS in compositional analysis.

What are the necessary conditions for the observation of useful Fresnel fringes?

1. The interface must be aligned edge-on, *i.e.*, with the interface plane parallel to the electron beam. This can be assessed by observing the symmetry of the Fresnel fringes at either side of the film (Fig. 2.4(a)). If the interface is not edge-on, the fringes will be asymmetrical as shown in Fig. 2.4(b) and will effect the information that can be obtained from Fresnel fringes. Tilted interfaces can cause an uncertainty in the interface diffuseness, a general reduction in Fresnel contrast and overestimation of film thickness, but these effects are only serious at detectable tilts (Ross, 1989).
2. Both the grains should be diffracting weakly to increase the contrast. Even if faint lattice fringes are present, it is very difficult to find the precise location of Fresnel fringe maxima.

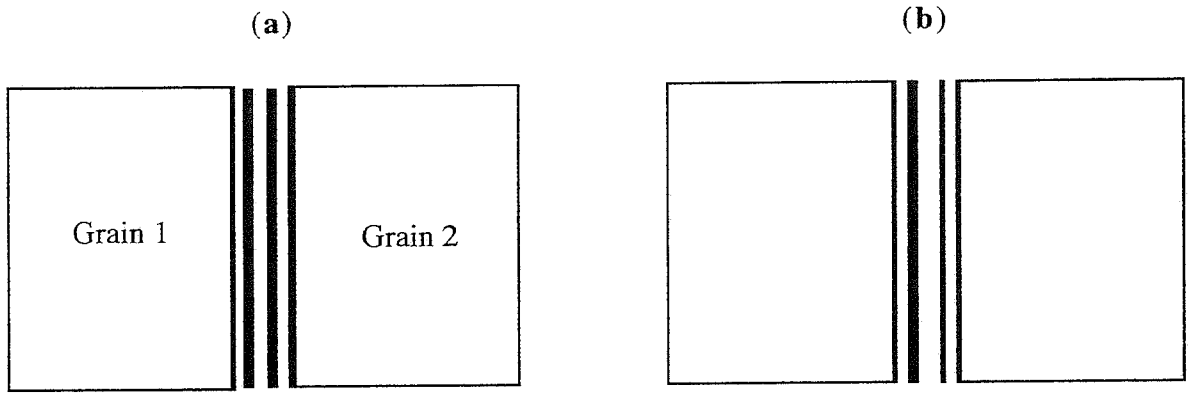

Fig. 2.4 Fresnel contrast from (a) an edge-on and (b) a tilted interface.

3. The objective aperture should be small enough to exclude the first diffracted beam, again to avoid lattice fringes especially if the resolution limit of the microscope is below the d-spacing of the planes.
4. The objective astigmatism should be carefully corrected since it can effect the details of the Fresnel contrast and reduce the signal-to-noise ratio in experimental Fresnel contrast profiles.
5. It is important to take through focal series from underfocus to overfocus and to use small defocus steps in the very low defocus range to obtain an image reasonably close to the Gaussian focus.
6. Using a high beam current temporarily while taking the micrographs avoids using long exposure times which cause a blur due to specimen drift. It also avoids high beam convergence which causes low visibility of the Fresnel fringes.
7. The specimen edge, useful for understanding the defocus status of each image, should be included in the micrographs wherever possible.
8. Coherent illumination is necessary for good visibility, which necessitates the use of a LaB_6 filament.
9. Careful calibration of microscope operating parameters is required for accurate simulations to be carried out.
10. Most importantly for the simulations, the specimen thickness variation along the interface should be known.

How can useful information be deduced from Fresnel fringes?

In addition to its capability of revealing intergranular films at the interfaces, the technique is also useful for determining its thickness (h). According to Reimer (1989), fringe spacing (W) varies with defocus (ΔF) approximately as given in the equation:

$$h = W - (3\lambda|\Delta F|)^{1/2} \tag{2.3}$$

where λ is the electron wavelength and ΔF is the defocus distance. A schematic diagram of the variation of fringe spacing with defocus is shown in Fig. 2.5. The fringe spacing at around Gaussian focus ($\Delta F = 0$) corresponds to the intergranular film thickness.

Most of the intergranular films in ceramics have a lower mean inner potential than that of the grains either side of the interface. Therefore, if the interface is imaged using an underfocussed lens, the intergranular film would appear as a bright line with dark fringes between the film and the adjacent grains. The contrast reverses if an overfocussed lens is used. However, if the mean inner potential of the film is higher, then the film appear dark at underfocus imaging conditions. The general behaviour of Fresnel fringes from a thin film at the interface is shown in Fig. 2.6. The above analysis can be used to determine the composition changes from one interface to the other.

The magnitude of fringe contrast is approximately proportional to the scattering potential difference, ΔV, between the matrix and the intergranular film at a given specimen thickness and defocus.

The advantages of the technique are its ease of use (since no requirement for high resolution microscope), it is sensitive to defocus to give interface width and it can provide both qualitative and quantitative information on the change in mean inner potential at interfaces, and it is able to detect and measure compositional changes across an interface with a resolution of a few atomic layers. The most attractive feature of the technique is that its resolution is not probe size limited.

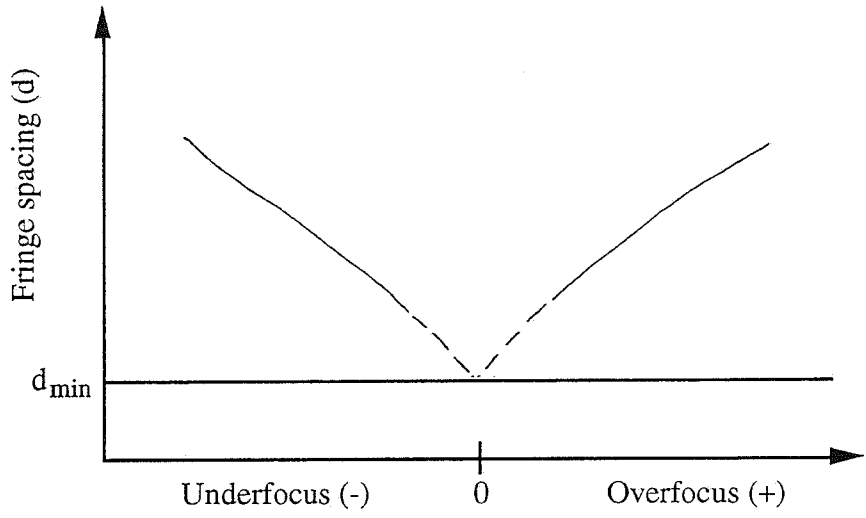

Fig. 2.5 Schematic diagram of the variation of fringe spacing with defocus.

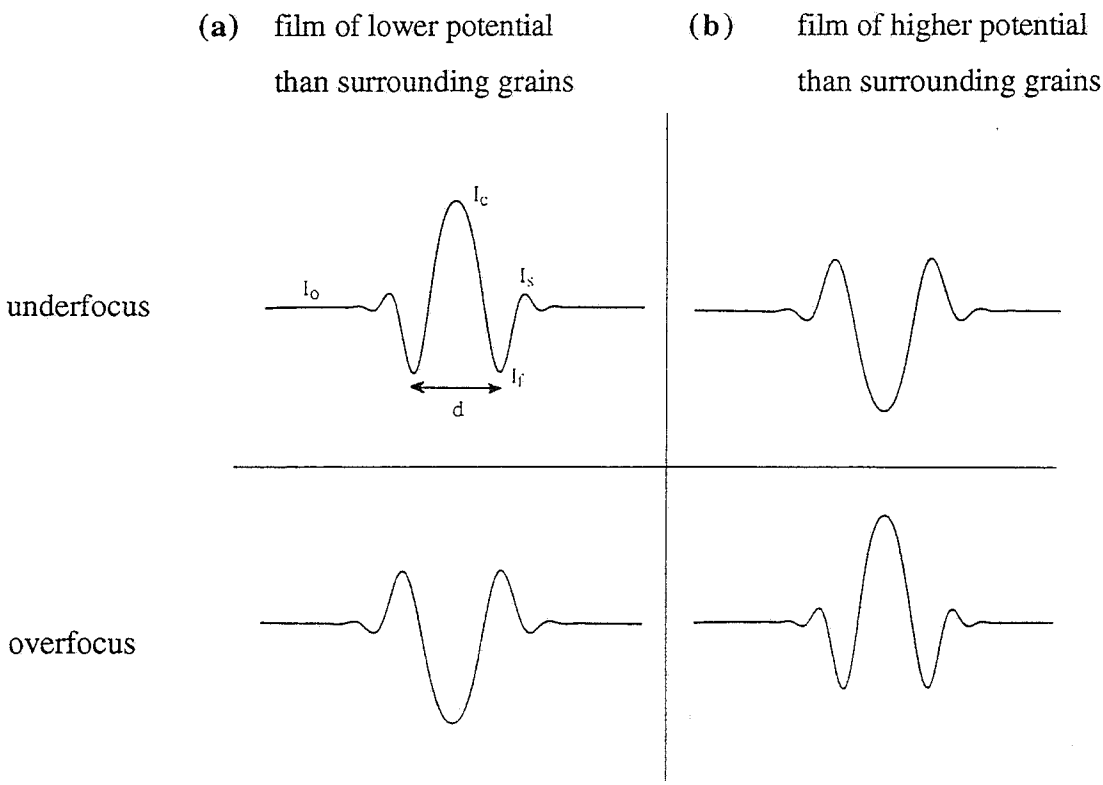

Fig. 2.6 General behaviour of fringes from an interface containing thin intergranular films. Where I_o is the background intensity, I_c central fringe intensity, I_f first fringe intensity and I_s second fringe intensity.

2.5.1.2 Diffuse dark field imaging

This is the most successful technique to image noncrystalline intergranular films. The basis for the technique is to collect (and image) a portion of the scattered electrons diffracted by the intergranular film and exclude those electrons diffracted by the adjacent grains. The method for doing this is shown schematically in Fig. 2.7. By placing a small objective aperture in the position indicated as (2) in the diagram, only electrons scattered by the intergranular film are passed to the imaging lenses of the microscope. In the resulting image the intergranular phase will appear bright and the adjacent grains dark. However, for most of the interfaces, the diffuse scattering ring is too weak to be distinguished in the electron diffraction pattern. In this case, an image would be obtained by moving the objective aperture in the direction from 1 to 3 and taking the picture when the interface is brightest. This would happen when the objective aperture is placed on (2) where the diffuse ring would normally appear. However extreme care should be taken to avoid sampling other diffraction effects from the interface and from the adjacent grains. In order to do this, the aperture should be placed 45° relative to the interface trace and away from any strong reflections.

The advantages of the technique are that it is relatively simple to apply, can be performed at low magnification and the contrast is independent of the orientation of the interface with respect to the viewing direction. The disadvantages are the limitation of examining only the thinnest regions of a sample since the extent of inelastic scattering increases with the foil thickness, which in turn decreases the image contrast, unobtainable crystallographic information about the interface and the generation of contrast by carbon coating due to preferential interface etching or thinning (Clarke, 1982).

2.5.1.3 High resolution electron microscope imaging (HREM)

The use of HREM technique on the detection of intergranular films have been pioneered by Clarke and Thomas (1977) & (1978). This technique is basically an extension of the bright field imaging using bigger objective apertures to include many diffracted beams. The required diffraction pattern/objective aperture geometry for lattice fringe and structure imaging of an interface is represented schematically in Fig. 2.8. There are a few imaging modes, axial illumination bright field, tilted illumination bright field and tilted illumination

dark field. The axial illumination bright field is the predominant choice of most microscopists and this is the only mode adopted throughout this study. The early application of the technique was usually known as lattice fringe imaging since the resolution of the microscopes only allowed the detection of one dimensional fringes. In the lattice-fringe imaging mode one set of lattice planes in both of the adjacent grains are imaged and any discontinuity other than a line is identified as an intergranular film.

The information obtained by the application of the method are presence of any intergranular phase and its morphology, if it is amorphous film then its width. The necessary conditions are that the interface is viewed edge-on, both the grains must be oriented in strongly diffracting conditions and the specimen thickness should be small enough (Clarke, 1979). Note that interface should be edge-on the same is required for Fresnel imaging, but the adjacent grains must be diffracting strongly opposite to Fresnel imaging technique.

The advantages are simple in principle and can show interface morphology (such as faceting) to a resolution of one fringe spacing (*i.e.*, crystallography).

A complete review of HREM imaging and its applications to interfaces is well beyond the concept of this thesis and therefore for details reader should refer to the following review articles and/or books (Clarke, 1979 and 1979a, Spence, 1988, Smith, 1989 & Buseck *et al.*, 1992).

2.5.1.4 Drawbacks of the techniques

Fresnel fringes will appear along any interface where there is a discontinuity in the projected scattering potential in the specimen. For example, small displacements at twin boundaries produce Fresnel fringes (Wood *et al.*, 1984) and any chemical segregation at interfaces will also change the mean inner potential there and produce Fresnel effects without the need for a discrete second phase. In this context, Das Chowdhury *et al.* (1992) investigated the structure of a fabricated $\Sigma = 13$ supposedly clean tilt boundary in silicon by employing Fresnel and HREM techniques. Although HREM showed the absence of any film at the interface, strong Fresnel fringes were observed by defocus imaging. Such Fresnel fringe contrast will also be found when there is a thin gap between the grains or when the interface

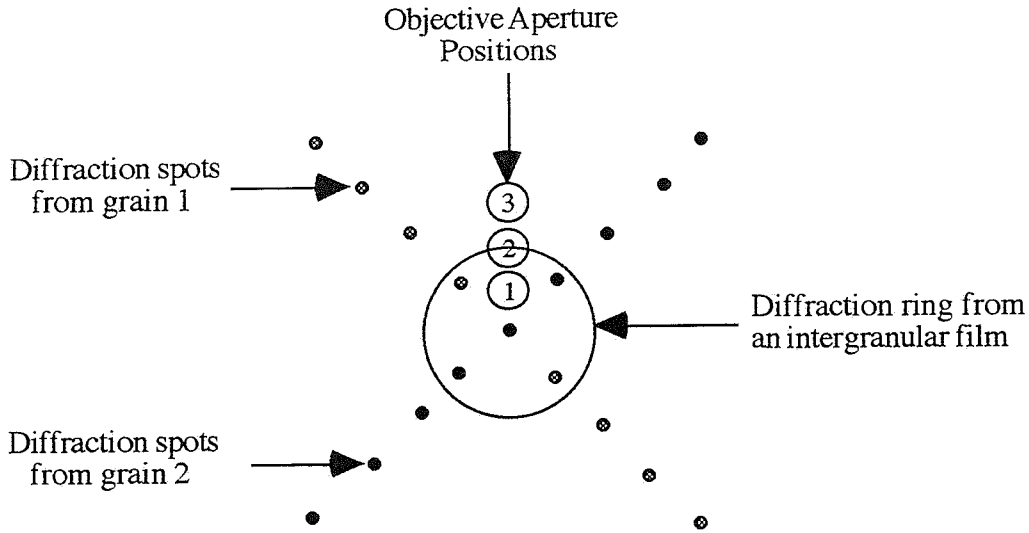

Fig. 2.7 Schematic diagram showing the positioning of the objective aperture required to form a diffuse dark field image of an intergranular film (after Clarke, 1979).

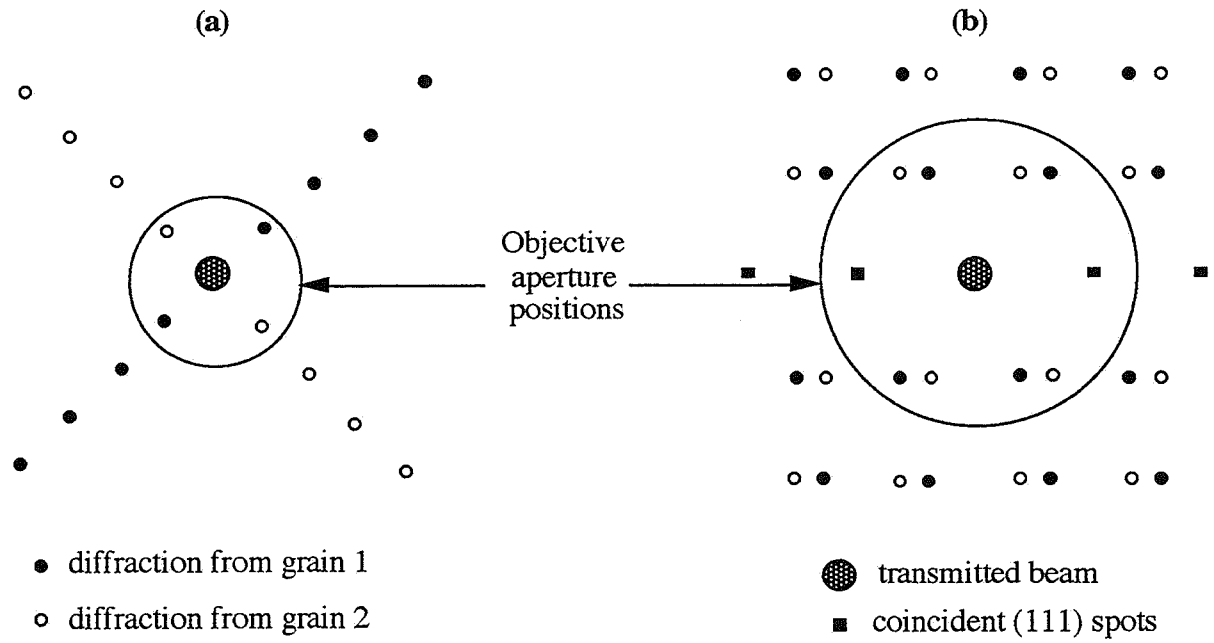

Fig. 2.8 Schematic of objective aperture positioning for the observation of interfaces using (a) axial lattice fringe imaging and (b) axial structure imaging technique of $\Sigma = 3$ twin boundary with a [111] twin axis in f.c.c. crystals.

is structured. This kind of effect for dislocations inclined to the electron beam (Boothroyd and Stobbs, 1984) and for a high angle end-on grain boundary in NiO have been reported (Rühle and Sass, 1984). More importantly, Simpson *et al.* (1986) observed Fresnel fringes at high angle edge-on alumina grain boundaries, but tilting away from the edge-on condition revealed the existence of dislocations. In addition, ion-beam thinning of specimens results in surface damage and interface grooving together with contamination during the long time required for careful interface alignment can confuse image interpretation. The interface grooving occurs because the atomic bonding at the interfaces are weaker than the perfect crystalline regions. However, not all the interfaces will groove. The grooving depends on the orientation of the interface relative to the surface of the specimen and the character of the interface (Simpson *et al.*, 1986). A schematic diagram of a grooved interface is shown in Fig. 2.9(a).

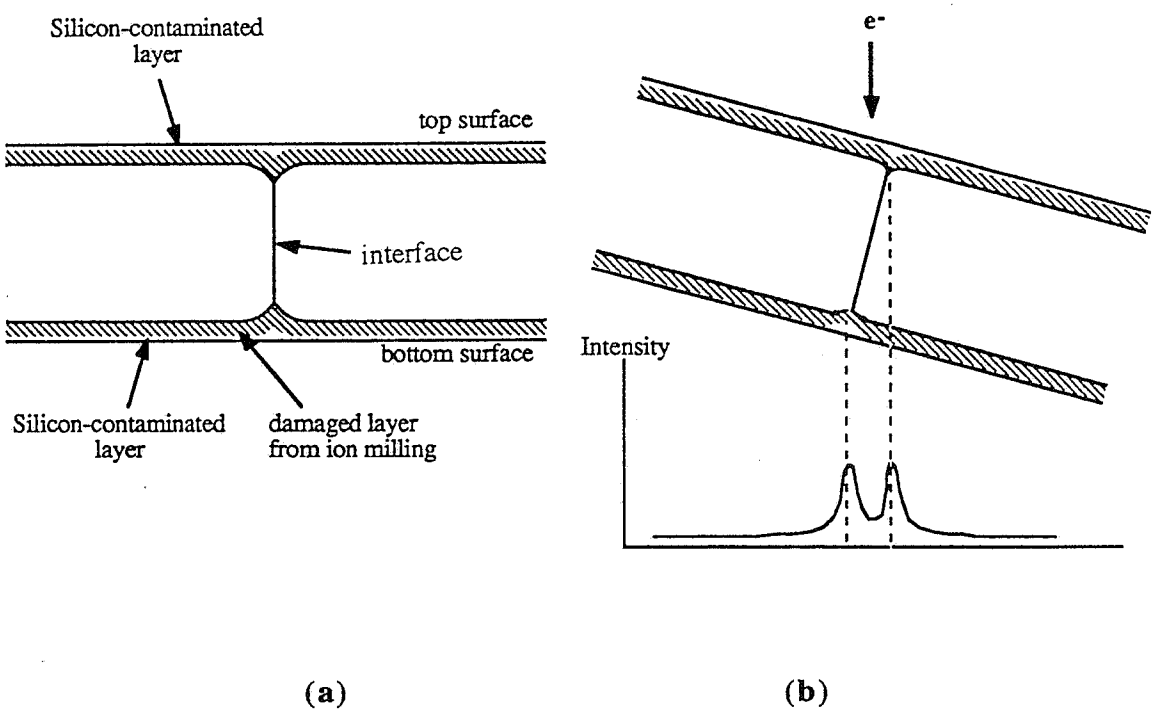

Fig. 2.9 (a) A schematic diagram of a grooved interface. Surface damage of the specimen due to ion beam thinning and silicon contamination from diffusion pump oil arise as a result of the preparation route. (b) In a tilted geometry the observation of two bright lines in diffuse dark field imaging can be due to amorphous materials filling the grooves at the top and bottom of the specimen at the interface (after Simpson *et al.*, 1986).

Thus, these observations show that Fresnel fringes can occur whenever the electron beam experiences a different mean inner potential under appropriate electron optical conditions. Therefore, care must be taken in interpreting the presence of the Fresnel contrast in terms of the presence of a thin film and a complementary technique such as diffuse dark field imaging and HREM has to be employed. The composition of the interfaces should also be identified for further confirmation.

The diffuse dark field imaging technique can be used to confirm the results of Fresnel fringe imaging showing the existence of an intergranular film. In addition, it can be used to distinguish whether the Fresnel and/or diffuse dark field contrast at the interface arises from an intergranular film or from interface grooving. The distinction can be made by tilting the interface away from the edge-on condition (Fig. 2.9(b)). If the supposedly intergranular film showing two distinct line, the contrast arises from grooving, otherwise it is a genuine amorphous intergranular film. The grooving effect can also be assessed by observing any scalloping effect at the edge of specimen.

As a result, the HREM technique is the most reliable to show the existence of intergranular films. However, care should be taken to show the absence of such films at the interfaces since Lou *et al.* (1978) showed that very small tilts ($\approx 0.2°$) are sufficient to cause enough grain overlap to obscure the presence of a thin intergranular film. Therefore, diffuse dark field imaging should also be employed since it could reveal the presence of an intergranular film even for slightly tilted interfaces. Susnitzky and Carter (1990) prepared a high angle 30° twist boundary (near $\Sigma = 13$) by hot pressing together two alumina monocrystals and investigated the interface structure. Although HREM image showed an intimate contact between the grains, WBDF showed the presence of dislocations.

The defocus sensitivity of the HREM technique was shown by Krivanek *et al.* (1979). Reliable information is produced at only one defocus value-Scherzer defocus. The major disadvantage of using HREM is that the region of interest should be thin. Adjacent grains must be oriented in strong diffraction conditions in order that high contrast images can be formed on both sides of the interface. This is a fairly difficult criterion to satisfy, particularly when it is also necessary to have the interface oriented in the edge-on condition. Even when all these conditions are satisfied simultaneously, extreme care must still be taken in the interpretation of the images.

2.5.1.5 Which is the best technique to measure intergranular film thickness?

Clarke (1987) was the first to argue that intergranular films adopt an stable equilibrium thickness as a result of two competing forces: attractive van der Waals dispersive forces and repulsive structural forces. The subject is going to be introduced and discussed in detail in Chapter 5. However, in order to confirm this, it is important to establish which of the above techniques is most reliable.

An early study on the measurement of intergranular film width and comparison of the results obtained by Fresnel fringe imaging technique and HREM was carried out by Clarke (1979). He concluded that measurements by Fresnel fringe imaging overestimate the thickness by up to 25 % in comparison to HREM measurements. Later, Ness *et al.* (1986) showed that the interface width changes according to which potential well is used in the simulations. There are various potential-well shapes used to simulate the presence of an amorphous intergranular film. Fig. 2.10 shows some of the different models which have been used for simulations.

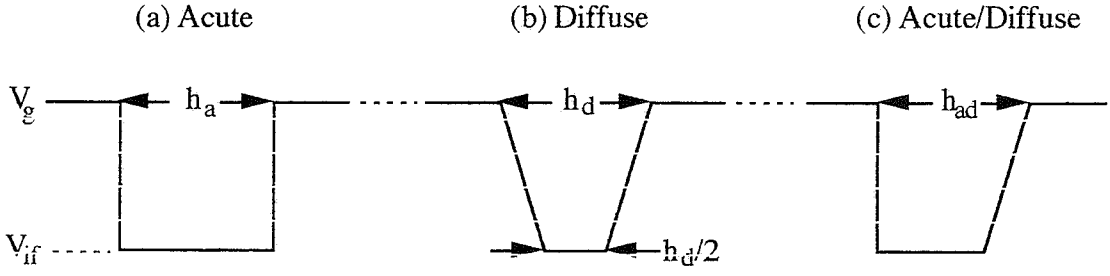

Fig. 2.10 A schematic representation of the three interface potential models used for simulations (after Ness *et al.*, 1986).

Each model exhibits the same potential drop across the grain boundary containing the intergranular film, $\Delta V_i = (V_g - V_{if})$ where V_g is the potential of the grains at either side of the interface and V_{if} is the potential of intergranular film, but has a different shape. Note that the potential drop will be different at interphase boundaries. The acute model represents a discrete amorphous/crystalline interface (with a sharp change in potential). The diffuse interface model approximates to an interface with a more gradual transition in potential between the crystals and the amorphous intergranular film. The third model is an artificial

combination of the first two models (AD). Ness *et al.* (1986) have examined the behaviour of all three models and have confirmed that the approach provides a reasonable measure of the intergranular film width in all cases. The acute and diffuse models give an overestimate and an underestimate respectively of the intergranular film width, while the AD model gives the most accurate value (but it was not used for image comparisons because of the asymmetry of the fringe intensities it yields). Later Ross (1989) found that the extrapolation causes a slight overestimate ($\approx 15\,\%$) of the intergranular film width.

However, the accuracies of *all* the techniques available for intergranular film thickness measurements have only been compared recently. Cinibulk *et al.* (1993) compared the results obtained from a single grain boundary using three different techniques, namely, diffuse dark field, defocus Fresnel fringe and HREM techniques on Si_3N_4 ceramics. They found that the HREM technique is the most accurate one.

For accurate measurements in HREM, the interfaces must be edge-on and, if possible, lattice fringes should be parallel to the interface, as this helps to identify accurately the edge of the grains. Even satisfying these conditions are not good enough to obtain accurate measurements. An overestimation of the width can arise from amorphisation of a small amount of grains at the interface in very thin regions during ion-milling. However, it is more likely that HREM will underestimate the film thickness, because the interface is not edge-on, the overlap in projection between the film and the grains either side will reduce the projected width of the film and in extreme cases completely obscure the existence of the film. If the interface is perfectly edge-on, an electron optical effect can cause a shift of the lattice fringes from the grain into the intergranular film (Krivanek *et al.*, 1979). The shift (r) is a function of the spherical aberration coefficient of the objective lens C_s, the electron wavelength λ, the interplanar spacing corresponding to the lattice fringes d and the defocus distance Δf given by the equation:

$$r = C_s(\lambda/d)^3 + \Delta F(\lambda/d) \qquad (2.4)$$

For the smallest shift (*i.e.*, highest accuracy for thickness determination) a small C_s, ΔF and d spacing and a high accelerating voltage are required. Cinibulk *et al.* (1993) calculated a shift value of ≈ 1 Å for the $\{10\bar{1}0\} = 6.6$ Å β-Si_3N_4 reflections in a microscope operated at

400 kV with a ΔF= - 500 Å, C_S = 1 mm and λ = 0.0164 Å. Obviously, the shift value is much smaller for {111} = 2.51 Å SiC planes which is calculated to be less than half of that one for $\{10\bar{1}0\}$ β-Si_3N_4 reflections. Therefore, if the microscope is operated very carefully, then an intergranular film thickness can be accurately measured to within ± 1 Å.

Cinibulk *et al.* (1993) assessed the possible overestimation from the other techniques by taking the HREM values as a standard. They found that diffuse dark field imaging yielded an overestimation by up to a factor of 2, whereas Fresnel imaging led to values 20% to 35% higher than those determined by HREM technique. The reasons for overestimation due to diffuse dark field imaging are a poor definition of where the intergranular film at interface starts and drift occurring during the long exposure times required for low intensity images especially when taken at high magnifications (low magnification images suffer more from enlargements).

The Fresnel fringe imaging also suffers from a number of experimental uncertainties which causes overestimation of an intergranular film thickness. These are the accurate location of first fringe maxima is difficult, curve fitting to the data is not always straightforward, extrapolation from high defocus values to Gaussian focus results in errors, low visibility of fringes at low defocus values. The fact that the overestimation due to Clarke (1979) is smaller than Cinibulk *et al.* (1993), could be because the use of a less sophisticated microscope with a higher C_S, ΔF and d spacing and lower accelerating voltage in turn decreases the accuracy of HREM measurements that Clarke (1979) was able to make. Although the results obtained by Cinibulk *et al.* (1993) give a first insight to the problem, their results are yet to be corroborated by others.

2.5.2 Characterisation of structured interfaces

If an interface is found not to have an intergranular film after all these techniques have been used, the complete structure of an interface can be established using HREM and weak beam dark field imaging techniques. The latter technique is described in Thomas and Goringe (1979). The Fresnel defocus imaging technique can also be used for such interfaces. As mentioned earlier, Rühle and coworkers successfully used this technique on the determination of a scattering potential value at dislocation cores in low angle end-on NiO grain boundaries.

If the interface is structured, the interface geometry should be described in terms of geometrical parameters; misorientation angle/axis and interface normal[@].

The determination of these three geometrical parameters involves basically two approaches. The first one is the analytical approach due to Young *et al.* (1973) where the misorientation characterised by a 3x3 matrix whose columns represent the direction cosines of grain 1 referred to grain 2. The second approach to yield a misorientation data relies on standard stereographic procedures where two pairs of diffraction patterns are required (Goux, 1961). This method is based on fact that the zone axes in both grains must be parallel. However, this is a fairly difficult criterion to meet in polycrystalline materials.

It is obvious that to find the values of these three parameters, the beam directions from each grains have to be known. The identification of beam directions involve the use of electron diffraction based techniques. Although HREM imaging of interfaces can enable us to study their atomic structure directly, in general if both the beam directions in adjacent grains are not known from the HREM data the diffraction information has to be obtained by using conventional microscopes. The diffraction data can be collected using TEM based techniques. Two techniques are available: convergent beam electron diffraction (CBED) and selected area diffraction (SAD). The CBED technique relies on the observation of three pairs of non-parallel Kikuchi lines to obtain an incident beam direction from each crystal and the orientation of a crystal can be done using the three pole solution. It is also necessary to obtain an HREM image from the interface to show the nature of it. Here lies a dilemma: HREM imaging requires very small specimen thicknesses whereas observations of Kikuchi lines require thicker specimens. Therefore, SAD technique becomes more useful to find the orientation-relationship between two crystals for cases involves HREM imaging of thin samples.

The CBED and the SAD techniques are described in Randle (1993) and Qing *et al.* (1989), respectively. The latter technique requires three diffraction patterns from each crystal to find the beam directions of each crystals with respect to one another. An improved version of the technique has developed and applied to $\Sigma = 3$ twin boundaries in cubic SiC grains by Turan

---

[@] *Ideally, it would be useful to identify the geometrical parameters for interfaces containing films to see whether they are wet because of the geometry of the interface.*

and Knowles (unpublished work)[#] who showed that the experimental results from cubic SiC grains and those used by Qing *et al.* (1992) are closer to theoretical values for the description of $\Sigma = 3$ twin boundaries than obtained in the algorithm used by Qing *et al.* (1989).

2.6 Summary

Although there has been intensive research on interfaces over a number of years, there is a continuing need for more detailed knowledge about the properties of individual interfaces and their dependence on parameters such as their interface crystallography and their chemical doping. More importantly, there is a need to incorporate this knowledge into models for the microscopic behaviour of polycrystalline ceramics (Clarke, 1990).

Therefore, the purpose of the study is to establish what type of interfaces exist and how often the different types occur. If amorphous intergranular films are present, how thick are they and are they specially oriented or randomly oriented? If structured interfaces are present, what is the geometry of the interface? In attempting to answer such questions, extreme care should be taken during the experiments and as many techniques as possible should be used to determine reliably the structure of the interfaces.

All the techniques have their advantages and disadvantages and can provide different information about an interface. For example, the presence of intergranular film is best determined by HREM, whereas the absence of the film is best determined by the combination of all the techniques. The film width should be determined by either Fresnel or HREM techniques and its composition and structure by diffraction pattern analysis techniques coupled with Fresnel imaging. The presence of any interface faceting should be determined by HREM and finally orientation relationships should be established from the diffraction patterns and direct structure imaging.

[#] *Computer programs are available for the determination of beam directions from three diffraction patterns and for the determination of Σ values and misorientation angle/axis pair.*

Chapter 3

General Microstructure of the Composites

3.1. Introduction

At the beginning of this Chapter, a justification of choice of materials and choice of fabrication technique will be made, after which the crystal structures and densification mechanisms of the chosen materials of silicon carbide and silicon nitride will be introduced. This will be followed by the discussion of how the composites studied in this work were produced and how their microstructures were characterised. The remaining part of the Chapter will concentrate on the experimental results obtained from density measurements, X-ray diffraction analysis and very basic transmission electron microscopy observations. The final part of this Chapter will be devoted to discussion, from which some preliminary conclusions will be drawn.

3.2. Justification of the choice of materials and processing route

3.2.1 Why ceramics?

Ceramic materials have become increasingly important in modern industrial and consumer technology. Ceramics can be divided into two groups: *traditional ceramics* (*e.g.*, glass, porcelain, cement) and *engineering ceramics* (technical, fine, structural and advanced ceramics are also terms used to describe these ceramics) which can be further loosely grouped into oxide ceramics (*e.g.*, alumina, zirconia) and non-oxide ceramics (*e.g.*, carbides, nitrides, borides). Note that an electronic ceramic (such as a dielectric or a superconductor) can be either a traditional or an engineering ceramic.

Typical properties of ceramic materials which make them potentially suitable for use in demanding environments are exceptional hardness, good stiffness, high strength in compression, strength retention at high temperatures, low density, high thermal shock resistance, high erosion resistance, high corrosion resistance and high oxidation resistance.

3.2.2 Why not ceramics?

The major drawbacks of engineering ceramics which generally prevent their exploitation are their lack of toughness (K_{IC} < 2-10 MPa.m$^{1/2}$), poor tensile strength reproducibility, reflected in their low Weibull moduli (*i.e.*, reliability), and difficulty of processing.

3.2.3 Why composites?

The inherent brittleness of ceramics can be overcome by the addition of reinforcing components such as fibres, whiskers and platelets into these brittle matrices. Such combinations can result in a tough composite material. There are two broad classes of ceramic matrix composite. The first class of composites is formed when particles or whiskers are dispersed randomly in a ceramic matrix. The second class is based on unidirectional fibre reinforcement of individual laminae stacked together to form laminates.

3.2.4 Why particulate reinforced composites?

Fibre-reinforced composite laminae have good toughness and superior mechanical properties in comparison with monolithic ceramics, but their properties are anisotropic. There are also a number of problems associated with their use, especially at high temperatures (*e.g.*, > 1000°C), in addition to the increased difficulty in their fabrication and in any reasonably complex near-net shaping (Prewo, 1986). Although whisker reinforced composites also have increased fracture toughness compared to monolithic ceramics, the toxicity of the whiskers limits their appeal. Therefore, particulate reinforced composites, and especially 'nanocomposites', continue to be of research interest. The particulate reinforced composites are also significantly cheaper to produce than other types of ceramic composites.

3.2.5 Why silicon nitride-silicon carbide composites?

Of the various ceramic materials available, SiC remains a promising candidate as a matrix material for high temperature composite material applications. SiC has many desirable properties such as good high temperature strength, chemical stability, sufficient thermal shock resistance (*i.e.*, low thermal expansion coefficient with good heat conductivity), as

well as hardness, abrasion resistance and low density. Hillig (1985) has examined the possible candidates for composites and among the materials considered SiC came out in first position to be one of the components in the most likely high temperature composite materials of the future.

Attempts to increase the fracture toughness and strength of SiC by the addition of particulates have met with some success (Lange, 1973, Wei and Becher, 1984, McMurtry *et al.*, 1987 & Buljan *et al.*, 1987). For example, titanium diboride (McMurtry *et al.*, 1987) additions to SiC matrices increase both the fracture toughness and the fracture strength of the composite relative to monolithic SiC matrix material. However, these additions can reduce the oxidation resistance of the SiC matrix (Janney, 1987) and as a result preclude the use of such composites at high temperatures. This is contrary to the methodology that a suitable reinforcement material should not only satisfy the requirements of ease of composite fabrication, but should also retain the useful superior mechanical and chemical properties of ceramics over other materials. Thus, in the composites investigated in this work, Si_3N_4 was selected as a suitable particulate reinforcement for SiC on the basis that in monolithic form Si_3N_4 has a higher strength and toughness than SiC, while SiC has the better oxidation resistance at high temperatures (≥1400°C).

3.2.6 Why hot isostatic pressing?

The choice of processing technique will have an effect on the mechanical properties of densified ceramic bodies. For example, uniaxial hot pressing produces anisotropic material, which is not necessarily desirable. Without sintering additives, pressureless sintering requires longer processing times than hot pressing. This can lead to significant grain growth and affect the mechanical properties by lowering mean strengths and also decreasing the reliability of nominally identical ceramic components. Thus, it is usual to incorporate sintering additives during pressureless sintering. These additives generate a sufficient quantity of liquid phase at the fabrication temperatures to enable liquid phase sintering mechanisms to operate effectively, reducing the required time for densification. However, liquid phases retained as amorphous intergranular films at interfaces and triple junctions at room temperature are able to creep at high temperatures, therefore limiting the temperature capability of the ceramic material.

Hot isostatic pressing has some advantages over both uniaxial hot pressing and pressureless sintering since it allows shorter densification times and/or lower densification temperatures which prevent grain growth and result in homogenous microstructure. It also allows densification without using sintering additives.

There are basically three hot isostatic pressing (HIP) techniques: Post-HIP, Sinter-HIP and Encapsulation-HIP (EHIP). In post-HIP, the material is pre-sintered to a density at which there is little or no interconnected or open porosity and then hot isostatically pressed. With Sinter-HIP the material is sintered *in situ* in the HIP equipment, possibly under vacuum, until a closed pore structure is formed and then hot isostatically pressed without removing it from the apparatus. The third method, EHIP, requires the material to be contained within a gas-tight envelope whilst still in the green state and then hot isostatically pressed. Each method has its advantages and disadvantages (Davidge *et al.*, 1988). The advantage of EHIP is that the material does not need pre-sintering to give a completely closed pore system, and therefore high levels of sintering aids are not required. The other advantage of EHIP is that a greater degree of microstructural control is obtained. After pre-sintering of material, HIP treatment will coarsen the grain structure whilst making only modest increases in theoretical density of the material.

3.2.7 Why deoxidation?

There have been some attempts to densify *(i)* SiC (Hermansonn *et al.*, 1986, Dutta, 1988 &1988a) and *(ii)* Si_3N_4 (Nezuka *et al.*, 1988 & Tanaka *et al.*, 1989) monolithic ceramics, *(iii)* Si_3N_4-25 vol% SiC-platelet (Pezzotti, 1993) and *(iv)* 5 to 30 vol% SiC-whisker reinforced Si_3N_4 (Takemura *et al.*, 1988) composites without using any sintering additives by hot isostatic pressing route. However, amorphous intergranular films were still detected at interfaces between Si_3N_4 grains (Nezuka *et al.*, 1988, Takemura *et al.*, 1988, Tanaka *et al.*, 1989 & Pezzotti, 1993) since Si_3N_4 powders contain thin surface films of silica. Interestingly, Lu *et al.* (1993) investigated the grain boundary structure of hot isostatically pressed laser synthesised Si_3N_4 powders without additives. They have observed intergranular films for the samples prepared from powders exposed to air, whereas these films were absent for the samples prepared from unexposed powders. It is of interest that the density of samples prepared from exposed powders (92 %) were much higher than that obtained from unexposed powders (70 %). Unfortunately, the electron microscopy investigations for hot isostatically pressed SiC materials produced without the addition of

sintering additives have not been reported, but it can be speculated that intergranular films at SiC-SiC grain boundaries would exist, on the basis that the elimination of surface silica requires the addition of carbon. Under hot isostatic pressing conditions, this would produce gaseous products of SiO and CO along with solid SiC (Lee and Cutler, 1975). Since SiO and CO cannot escape from the hot isostatic pressing apparatus, it is reasonable to conclude that on cooling from the hot isostatic pressing conditions amorphous intergranular phases will be produced.

There have also been attempts to crystallise these amorphous phases since they effect the high temperature properties of ceramic materials, but the attempts have only been partially successful, in that triple junction phases were crystallised, but not amorphous intergranular films. The recent work by Kleebe *et al.* (1993) showed that crystallising triple junctions does not solve the problem, since the impurities can be enriched at interfaces and lower the viscosity of the intergranular films even further. Thus, in this work, an alternative route was adopted to obtain dense and intergranular film free composites by the removal of surface silica films prior to densification process.

The hot isostatic pressing was conducted on both as-received powders as a *'control'* and deoxidised powder compacts where the surface silica had been reduced prior to full composite consolidation.

3.3 Introduction to silicon carbide and silicon nitride

3.3.1 Structure of silicon carbide and polytypism

The structure of SiC is composed of coordinating tetrahedra (either SiC_4 or CSi_4) which are arranged in such a way as to share corners, thereby satisfying the 4-fold coordination requirements of the carbon and silicon atoms.

SiC exhibits a form of one-dimensional polymorphism called polytypism. There are some excellent reviews on polytypism in SiC (Verma and Krishna, 1966, Baronnet, 1981 & Jepps and Page, 1983) and so here the subject is only introduced to cover enough information to understand the structure variations in SiC.

The many polytypes of SiC differ from one another only in the stacking sequence of double layers of Si and C atoms in tetrahedral coordination. Each double layer can be considered to consist of a plane of Si atoms in a close-packed arrangement (although the Si atoms do not touch one another) over a similar plane of close-packed C atoms; one Si atom lies directly over each C atom in a double layer. Each successive double layer is stacked on top of the previous double layer in such a way that there are only three possible relative positions for the double layers just as in close packed metals where there are only three possible relative positions for layers of close packed atoms. These positions are normally labelled A, B, and C. Depending on the stacking sequence, various structures (*i.e.*, cubic, hexagonal and rhombohedral) are produced.

Although several nomenclatures are in common usage to describe these polytypes (Verma and Krishna, 1966), the Ramsdell notation (Ramsdell, 1947) is the one in widespread use. In this number/letter notation, the number refers to the number of Si-C double layers in the unit cell and the letter to the crystal symmetry. Thus, 3C is a cubic polytype with a 3-layer repeat in the unit cell, whereas 6H and 15R have hexagonal and rhombohedral symmetry, respectively. 3C is the only polytype with cubic symmetry and it has become common practice to refer to the 3C polytype as β-SiC* and to refer to all the hexagonal and rhombohedral polytypes collectively as α-SiC.

There are an infinite number of possible polytypes (Verma and Krishna, 1966) but only a few are considered to be basic structures: 2H, 3C, 4H, 15R and 6H. All other structures being considered as sequences or intermixes of these basic units. The basic polytypes can be easily recognised by their electron diffraction patterns and the Ramsdell symbols can be deduced from the distribution of diffracted intensity along the $1\bar{1}0l$ reciprocal lattice rows which are visible in a $[11\bar{2}0]$ beam direction. All polytypes give a reflection corresponding to the fundamental layer spacing of 2.51 Å and the occurrence of other reflections from the origin to the fundamental layer is governed by the lattice type and space group. The most common SiC polytypes are listed in the Table 3.1 with several ways of designating the various structures and the models constructed from solid tetrahedra are shown in Fig. 3.1.

---

* *Note that the crystal structure of β-SiC is isostructural with the zinc-blende (sphalerite) structure.*

Ramsdell Notation	Stacking Sequence
3C	ABC/ABC...
6H	ABCACB/ABCACB...
15R	ABCBA/CABAC/BCACB/AB...
4H	ABAC/ABAC...
2H	AB/AB...

Table 3.1 The most common SiC polytypes.

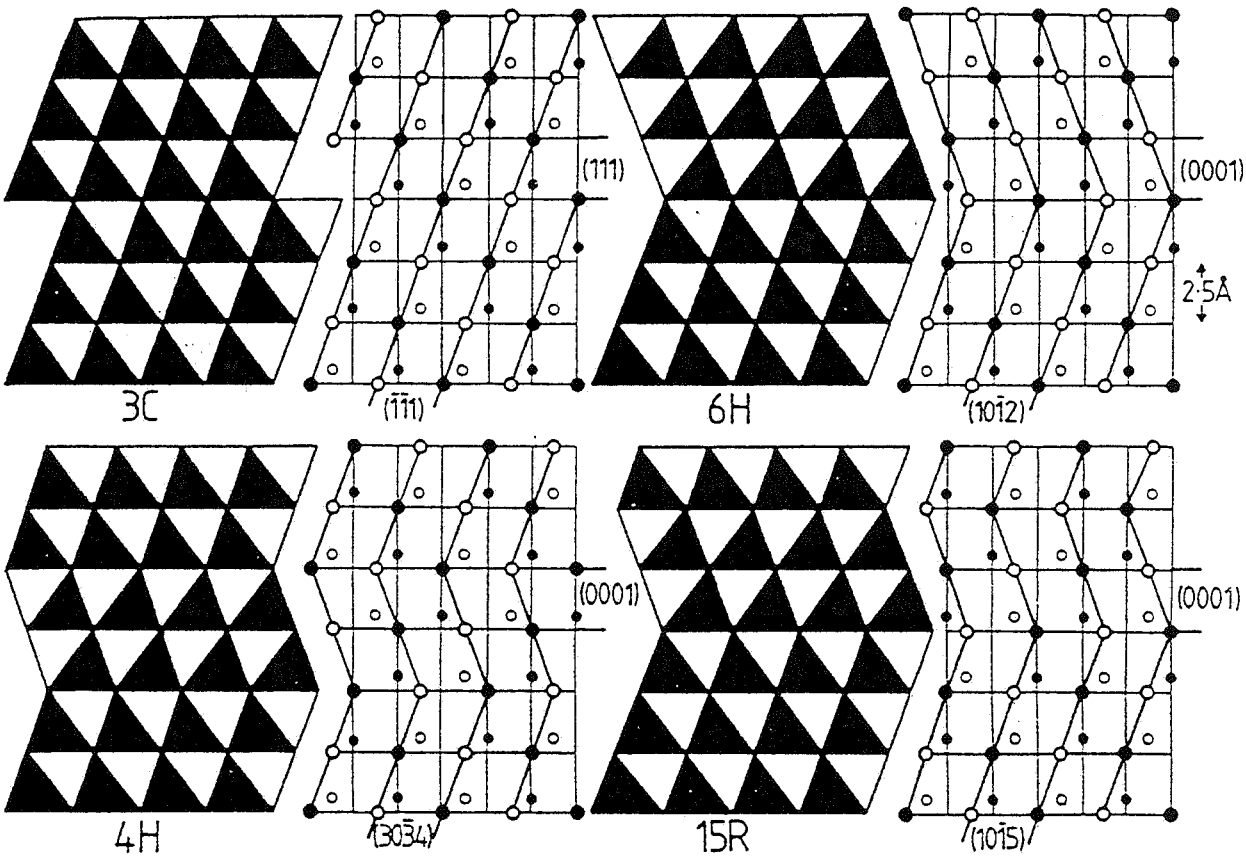

Fig. 3.1 Schematic of the four most common SiC polytypes represented by both tetrahedral structure unit diagrams and tramline structure diagrams (Jepps and Page, 1983). The stacking sequences may be visualised by considering the zig-zag sequence of non-basal-plane faces.

3.3.2 Structure of silicon nitride

Silicon nitride also exist in two different modifications, α and β. The structure of β-Si_3N_4 has been determined to be hexagonal (Hardie and Jack, 1957) and it is well accepted. In contrast, there has been disagreement over the crystal structure of α-Si_3N_4. Hardie and Jack (1957) concluded that it was hexagonal whereas Kato *et al.* (1975) has proposed a trigonal structure. On the other hand, some (*e.g.*, McColm, 1983) believe that α-Si_3N_4 is in fact an oxynitride and that therefore there is only one polymorph of Si_3N_4. However, Hiraga *et al.* (1983) have matched the experimental HREM images of α-Si_3N_4 with the proposed trigonal structure (Kato *et al.*, 1975) and a very good match was obtained suggesting that there are indeed two Si_3N_4 polymorphs.

The idealised structures can be described (Jack, 1983) as a stacking of Si-N layers along the *c*-axis in either an ..ABAB.. sequence (β-Si_3N_4) or an ..ABCD.. sequence (α-Si_3N_4) as shown in Fig. 3.2(a) and (b). The silicon atoms are located in the centre of irregular nitrogen tetrahedra, each nitrogen atom belonging to three tetrahedra.

In the hexagonal β-Si_3N_4 unit cell, SiN_4 tetrahedra are linked in such a way that the structure contains long, continuous hexagonal channels running parallel to the *c*-axis and centred at the *x* and *y* coordinates 2/3, 1/3. In α-Si_3N_4, the layers CD are identical with layers AB but is rotated by 180° on the *c*-axis (Hampshire, 1994). The continuous channels of β are replaced in α by two large, closed interstices centred at 1/3, 2/3, 3/8 and 2/3, 1/3, 7/8. Thus, in the α hexagonal unit cell containing $Si_{12}N_{16}$ there are two sites large enough to accommodate other atoms and ions. Although the Si-N layers in the actual β structure are almost identical with the "ideal" configuration, those in α are distorted and nitrogen atoms at heights of approximately 3/8 and 7/8 are pulled in toward the centres of the two respective interstices. The only significant difference between α- and β-Si_3N_4 modifications in terms of lattice parameter is that the crystallographic *c*-axis parameter of α-Si_3N_4 is about twice that of β modification (Fig. 3.2(c)).

The atomic arrangements of α- and β-Si_3N_4 differ considerably, but because of the similar *a* lattice parameters, the [0001] electron diffraction patterns are very similar although other zones such as $[11\bar{2}0]$ do allow a clear differentiation to be made.

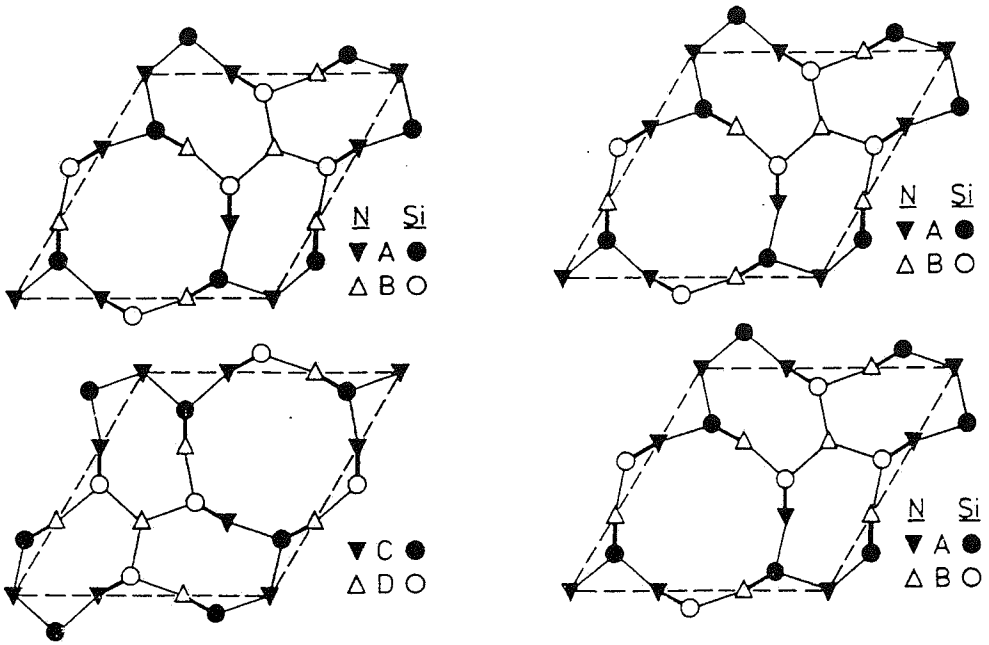

(a) **(b)**

Polymorph	*a*-axis (Å)	*c*-axis (Å)
α-Si_3N_4	7.76	5.62
β-Si_3N_4	7.60	2.91

(c)

Fig. 3.2 Idealised Si-N layers in (a) α-Si_3N_4 and (b) β-Si_3N_4 (after Jack, 1983). (c) Lattice parameters of α and β polymorphs of Si_3N_4.

3.3.3 Densification mechanism of silicon carbide

Some covalent substances such as carbon, boron, boron nitride, silicon, SiC, Si_3N_4 etc. do not sinter conventionally without sintering aids and/or the application of pressure. The reason for such behaviour has been attributed to the relatively poor vacancy diffusion caused by directional bonding (Popper and Davies, 1961).

Alliegro *et al.* (1956) were the first to sinter SiC successfully at high temperatures with the aid of suitable sintering additives. They found that the addition of Al either in elemental form or in the form of alumina was a suitable additive. However, they failed to explain the role of Al on the densification behaviour of SiC. Lange (1975) was the first to suggest that an alumina-calcia-silicate liquid phase* forms at high temperatures which dissolves the SiC particles and promotes densification by the solution-precipitation mechanism.

Omori and Takei (1982) have shown that a wide variety of rare-earth oxides can be used to densify SiC. Suzuki *et al.* (1982) produced material by pressureless sintering consisting of SiC and containing up to 35 wt% aluminium oxide. Recently, it has been shown that rapid sintering occurs at temperatures as low as 2000°C in the presence of liquid formed between Al_2O_3 and Y_2O_3 (Cutler and Jackson, 1989). The major problem associated with densification of SiC in the presence of oxide additives is the reaction between the SiC and oxide which results in the formation of volatile components and a substantial weight loss. Mulla and Krstic (1991) have claimed that a theoretical density of greater than 95 % can be obtained when pressureless sintering of β-SiC at temperatures between 1850 and 1950°C with Al_2O_3 and Y_2O_3 additions through a liquid phase sintering mechanism. They also claimed that volatilisation of the liquid phase and reactions between SiC and Al_2O_3 was reduced to less than 1 % at 1850°C. Liquid phase sintering of SiC has also been performed in the presence of a B_4C-SiC eutectic (Billington *et al.*, 1963), but in addition to the limited degree of densification (85-90 %) obtainable, the presence of a second phase on grain boundaries has a deleterious effect on high-temperature creep and strength. Therefore, for economic reasons, it would be advantageous to have a conventional way to sinter single phase covalent solids.

---

* *Alumina is added as a sintering aid, whereas calcia and silica are impurities from the starting SiC powder.*

These aims has been achieved by Prochazka (1973) who synthesised submicron β-SiC powders which then sintered after the addition of 1 wt% boron (B) and carbon (C) at 2050°C to 2150°C to densities of 95 to 98 % theoretical density. The absence of any detectable second phase (except C) in the sintered SiC led to Prochazka's conclusion that densification occurred by solid-state diffusion. Prochazka also suggested that neither the source of B nor its concentration (once it exceeds 0.3 %) affects the sintering behaviour.

Although sintered silicon carbide has been commercially available for a long time, the active sintering mechanism is still not well understood and the role of B and C in pressureless sintering of α and β-SiC has been a subject of continuing studies. There are several approaches to explain the sintering mechanism and also the role of C and B on the sintering of SiC. The models are based on thermodynamic (Prochazka, 1975) and kinetic arguments and liquid phase sintering (Lange and Gupta, 1976).

The first approach is based on thermodynamic arguments which propose that during the sintering of pure submicron powders of covalently bonded solids, densification is prevented by a hypothetically high ratio of grain boundary to solid-vapour surface energies, $\gamma_{gb} / \gamma_{sv}$ (Prochazka, 1974). In order that a pore surrounded by three grains (Fig. 3.3) can shrink to closure, the equilibrium dihedral angle (θ) must be $\geq 60°$ or $\gamma_{gb} / \gamma_{sv}$ must be ≤ 1.73, *i.e.*, concave interface will allow pore shrinkage (Fig. 3.3(a)). When θ, the equilibrium dihedral angle between two grains of the solid and their interfaces is less than 60° the solid-vapour interface is convex and will tend to move outward. Consequently such a pore cannot close (Fig. 3.3(c)). The critical ratio of $\gamma_{gb} / \gamma_{sv}$ (for the geometry shown in (Fig. 3.3(b)) is obtained from the Young's equation ;

$$\gamma_{gb} = 2 \gamma_{sv} \cos \theta/2,$$

The actual values for γ_{gb} and γ_{sv} of SiC are ≈ 3.5 Jm^{-2} and 5.4 Jm^{-2}, respectively. Applying the above model, SiC should in principle be sintered very easily, but in reality it does not because surface contamination reduces the actual value of γ_{sv} to ≈ 2 Jm^{-2} (F. L. Riley, private communication) and thus according to the above model the ratio of $\gamma_{gb} / \gamma_{sv}$ is too high and sintering is inhibited.

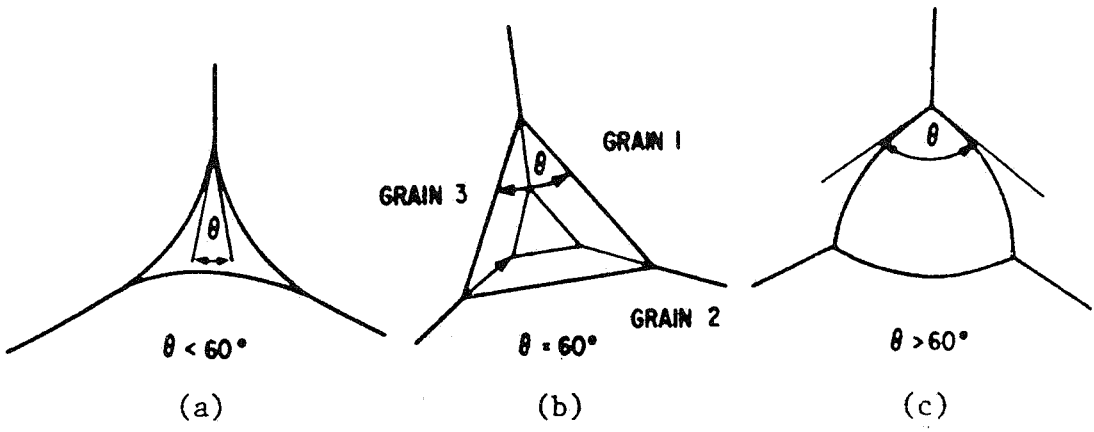

Fig. 3.3 Geometry of a three grain circuit in two dimensions as a function of the dihedral angle (after Prochazka, 1975).

Prochazka hypothesised that B segregates on grain boundaries and reduces the grain boundary energy (γ_{gb}), whereas C deoxidises the surface of SiC particles and increases the surface energy (γ_{sv}), and hence the ratio γ_{gb} / γ_{sv} decreases and permits densification.

In contrast, Greskovich and Rosolowski (1976) have proposed a kinetically-controlled process of sintering where the addition of B to SiC containing C retards surface and/or vapour-phase transport (in contrast to the volume and grain boundary diffusion) and retards grain growth at lower temperatures, resulting in enhanced densification at elevated temperatures.

The hypothesis of grain boundaries rich in B has received support from Lange and Gupta (1976). However, they did not conduct TEM work either to confirm or deny the presence of an intergranular film. The kinetic argument of Greskovich and Rosolowski (1976) has also found a support from the results of subsequent research of Suzuki and Hase (1979) & (1980) although these investigators suggested that material transport through a B-C liquid film caused densification by solid state sintering as long as the additives existed as a film which disappeared above 2000°C by dissolution in the SiC. Suzuki and Hase advocated this since the most frequently observed dihedral angle was 92° in a 1900°C-fired compact of pure β-SiC rather than expected value of 60° from thermodynamic equilibrium. The pictorial

evidence used to support this shows a highlighted film, but the lattice fringes of the adjoining grain continue through this boundary region and possess the same SiC (111) spacing. Following this, Rühle and Petzow (1981) reported that no amorphous film exists at the grain boundaries of (B, C)- and (Al, C)-doped SiC using EELS, EDX and STEM.

The importance of C as a deoxidant has also been demonstrated by Stutz *et al.* (1985) who could not find any evidence of liquid formation at the sintering temperature. This supports the results of Hamminger *et al.* (1983) who deduced that grain boundaries were free of any intergranular film after using high resolution Auger electron spectroscopy on ultra high vacuum fracture surfaces of pressureless sintered α-SiC containing B and C.

Davis *et al.* (1987) concluded from results of TEM and Auger analysis on a sample of Hexoloy SiC sintered with B and C that the absence of any evidence for the existence of a secondary amorphous or crystalline phase, even at high temperatures, in the α-SiC strongly indicates that sintering of this material occurs by solid-state transport when both B and C are present as sintering aids. However, a satisfactory explanation for the role of B (and perhaps the complete role of C) in enhancing densification has not yet been postulated.

It is also relevant to note that all the above models are based on analyses obtained from the final sintered products.

In contrast to these analysis, Wrobleska *et al.* (1990) & Wrobleska and Hamminger (1991) investigated at room temperature the microstructure of B and C doped SiC after various stages of sintering. TEM observations revealed the existence of 10 nm thick layers on SiC grains at 1773 K. From EELS measurements it was found that the layers consisted of a mixture of amorphous SiO_2, amorphous carbon and traces of B. At 1773 K, the Gibbs free energy change is zero for the reaction between SiO_2 and C. Auger spectra exhibited the elements Si, C and O from samples which had reached 2123 K. The reduction of SiO_2 was not complete and B was not detected. However, graphite layers were seen by TEM in the samples from 2123 K. At approximately 2446 K, silica reacts with carbon forming secondary SiC particles while the carbon layer becomes significantly thinner and is almost entirely depleted of B and O. The fully densified samples at 2423 K reveal grain boundaries which are free of intergranular films. The final, dense material was found to consist of B-enriched SiC and polycrystalline carbon inclusions.

This study implies that a combined deoxidising and volume-diffusion enhancing sintering mechanism is active. Wrobleska and Hamminger concluded that these analysis did not confirm the hypothesis of Lange and Gupta (1976) who suggested a B-rich liquid phase arises during sintering of SiC, but that instead their results agree with the measurements of Carter *et al.* (1988) that boron promotes sintering by an acceleration of the reduction process of silica. The reduction of silica can also be accelerated if the sintering process is carried out in vacuum, but the addition of boron is still necessary for full densification (Wrobleska and Hamminger, 1991).

Therefore, it is claimed that B promotes the sintering of SiC by the generation of C-vacancies, leading to an increase of the diffusion coefficients of C and Si which then affect the densification process (Birnie, 1986). This is a reasonable claim since B has not been detected at the grain boundaries, but inside the SiC grains instead. B is soluble in SiC; Murata and Smoak (1978) quoted a value of 0.4 wt% at 2473 K whereas Davis *et al.* (1984) quoted a smaller value of 0.14 wt% at a lower temperature (2373 K).

In summary, there has been quite a research effort devoted to finding B at grain boundaries after sintering at very high temperatures. That nobody has succeeded to date indicates that it is either dissolved in SiC (evidence for such an explanation is that More *et al.* (1986) found B_4C precipitates inside SiC grains after annealing pressureless sintered α-SiC) or it forms gaseous species (such as boron oxide which forms when the sintering atmosphere is CO) and leaves the system (Greskovich and Prochazka, 1987).

The other general conclusion reached was that densification of pressureless sintered SiC doped with B and C takes place by solid state sintering (Prochazka, 1975 & Davis *et al.*, 1987), but the effect of surface silica on the densification behaviour of SiC has not been discussed other than proposing that surface silica prevents SiC densification. However, a clever experiment carried out by Wrobleska and Hamminger (1991) altered my own opinion on the densification mechanism of SiC. Although they did not suggest it, their experiments could be interpreted as demonstrating that an incomplete liquid phase sintering mechanism at low temperatures followed by a solid state sintering mechanism at high temperatures is responsible for the full densification of pressureless sintered SiC doped with B and C.

3.3.4 Densification mechanism of silicon nitride

Classical sintering processes are not applicable to Si_3N_4 because of its high degree of covalent bonding. As a result, densification aids are necessary to assist liquid phase sintering and to enable full densification. Frequently used sintering additives are MgO, Y_2O_3 and $Y_2O_3 + Al_2O_3$.

In contrast to the densification mechanism of SiC, the densification mechanism of Si_3N_4 is well understood and can be described in the following way (Ziegler *et al.*, 1987). The sintering additive reacts with the phases containing oxygen, silica or silicon oxynitride, which are always present on the surfaces of commercially available powders, and these form the liquid phase. If the amount of liquid phase is high enough and the viscosity at the sintering temperature is sufficiently low, a particle rearrangement process will occur, induced by capillary forces. The degree of densification in this stage is dependent mainly on the particle size and shape and the amount and viscosity of the secondary phase. With increasing temperature, the solution-diffusion-precipitation process starts and is superimposed on the rearrangement process. The driving force at this stage is the higher solubility at the contact points of the particles caused by capillary forces as well as the differences in the chemical potentials between small and large particles which leads to an enhanced solution of small particles. If the starting powder is α-Si_3N_4 which becomes thermodynamically unstable at temperatures greater than 1400°C and tends to transform into the more stable β form, further enhanced solution of small particles occur.

According to current opinion (Lee and Rainforth, 1994), α-Si_3N_4 is a more energy-rich metastable form and the formation of α-Si_3N_4 seems to be associated with certain reaction routes during nitridation of silicon, such as the gas phase reaction of silicon vapour or SiO with nitrogen (Henderson and Taylor, 1975).

In the following Sections, the material preparation carried out under the light of findings reported in the literature and summarised so far in this Chapter and experimental techniques available for the characterisation of composite microstructure will be described.

3.4 Materials

Although the microstructure of few different SiC and mullite based materials (monolithic SiC and mullite, graphite interlayered-SiC, TiB_2-SiC, Si_3N_4-SiC and SiC whisker reinforced mullite composites) are characterised throughout this study, the vast majority of the results reported in this dissertation were obtained from the Si_3N_4-SiC composites. Therefore, powder characteristics and material preparation routes will only be discussed for Si_3N_4-SiC composites and the others will be described whenever they are mentioned or appropriate references will be given instead.

The range of Si_3N_4-SiC composites supplied by "B.P. Chemicals" had been prepared by mixing commercially available powders of pure Lonza UF15 SiC powder and Starck LC10 Si_3N_4 powder without the addition of any sintering aids. The batches contained either 10 or 20 wt% of Si_3N_4 additives.

The characteristics of starting powders according to the manufacturers are as follows. Lonza UF15 SiC powder has a mean particle size of 0.5 μm with 15 m^2/g surface area; the impurity content of SiC powder has been found to be 0.81 wt% oxygen (corresponding to 3 wt% silica) and 0.39 wt% carbon, with the other major impurities of Al, Fe and Ti totalling 1200 ppm; the surface area of Starck LC10 Si_3N_4 powder is also 15 m^2/g and major impurities are 0.17 wt% of carbon and 3 wt% of silica. Therefore, in order to eliminate the surface silica, two of the green compacts from the batches containing 10 and 20 wt% Si_3N_4 were deoxidised briefly in a graphite furnace at 1900°C by the addition of carbon resin. The rationale for the choice of 1900°C for the deoxidation was that the reduction of silica would go to completion quickly and efficiently without any discernible densification of the green compacts taking place during the short time hold at this temperature (S. M. Winder, private communication).

The green compacts were encapsulated in tantalum cans. Tantalum forms tantalum carbide under most conditions of hot isostatic pressing by reacting with SiC. In order to prevent this unwanted reaction between SiC and tantalum, the internal surface of the cans were sprayed with colloidal boron nitride. The cans were evacuated down to 10^{-7} atm prior to sealing. The encapsulated and sealed green compacts were then hot isostatically pressed at 2100°C for one hour under a pressure of 200 MPa. A flow chart of how the composites were produced is presented in Fig. 3.4.

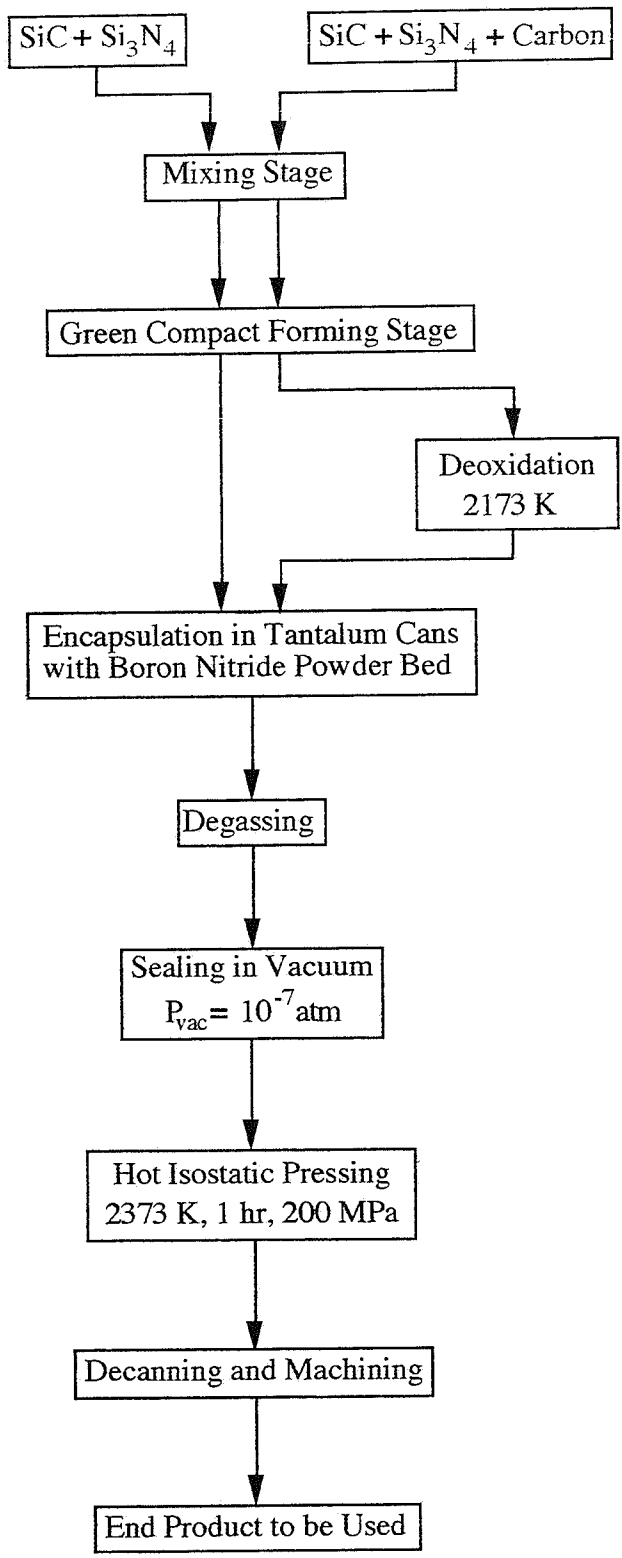

Fig. 3.4 The schematic of flow chart for processing Si_3N_4 particulate reinforced SiC matrix composites. Note that initial batches contain either 10 or 20 wt% Si_3N_4.

3.5 Experimental procedure

3.5.1 Density measurements

The densities of the hot isostatically pressed samples were measured by the Archimedes method in distilled water at room temperature. The theoretical densities of composites were calculated using the rule of mixtures taking the density of SiC as 3.21 gm cm^{-3} and Si_3N_4 as 3.19 gm cm^{-3} using the lattice parameter data in the relevant JCPDS files.

3.5.2 X-ray diffraction

The crystalline phases and their relative proportions in the bulk materials and starting powders were identified by X-ray diffraction using Cu K_α radiation at a scanning rate of 1° 2θ per min with a 0.2° receiving slit and a 1.0° divergent slit. Samples from each batch were powdered to eliminate any preferred orientation effect.

A quantitative estimate of the different phases in the composite would only be of limited accuracy since calculations cannot account for all factors influencing X-ray intensities such as stacking faults, twinning, particle size effects and textures (Ruska *et al.*, 1979). Further difficulties arise from the overlapping of diffraction peaks, the different degrees of crystallinity, and particle size and strain effects associated with the crystals. However, a crude qualitative analysis still supplies insight into the understanding of phase transformations and the formation of new phases in these composites. Therefore, the common procedures for SiC (Ruska *et al.*, 1979 & Frevel *et al.*, 1992) and Si_3N_4 (Gazzara and Messier, 1977) were used for quantitative calculations.

3.5.3 Transmission electron microscope analysis

Samples were prepared for transmission electron microscopy (TEM) examination by cutting thin slices from the bulk material using a slow speed diamond saw. These slices were polished to 1 μm diamond finish and were finally thinned by ion beam thinning. The thinned samples were examined uncoated by TEM using a Philips EM400ST at 120 kV, a Philips

CM30 at 300 kV and a JEOL 2000FX at 200 kV. The latter two microscopes were each fitted with an windowless energy dispersive X-ray analyser (WEDX) and a parallel electron energy loss spectroscopy (PEELS). The PEELS spectrometers on 2000FX at 200 kV and on CM30 at 100 kV have an energy resolution of 3 eV and 1.2 eV respectively. A JEOL 4000EX-II at 400 kV, which has a C_S of 1 mm and a point-to-point resolution of $\approx$ 1.7 Å, was used for high resolution transmission electron microscopy (HREM) analysis.

The TEM techniques and their applications to the characterisation of interfaces were discussed in Chapter 2. Here, the analytical techniques to deduce the composition of intergranular phases will be discussed briefly. There are four main techniques to do this: PEELS, WEDX, Auger and secondary ion mass spectroscopy (SIMS). However, the latter two are not available here in Cambridge and so were not used.

For the basics and the comparisons of PEELS and WEDX techniques the reader should refer to the book by Budd and Goodhew (1988). The most important advantage of PEELS over WEDX is that low atomic number elements can be easily detected down to lithium by PEELS, whereas even with the best WEDX it is difficult to detect boron. The other advantage of PEELS is that structural information can be deduced from PEELS spectra and also comparing the experimental spectra with the spectra in PEELS atlases. However, only a small energy range will be displayed in the PEELS spectra and PEELS spectra have to be collected quite a few times to obtain information about large number of elements. Information about a large number of elements can be easily obtained by WEDX, but unlike PEELS this does not contain any structural information.

3.6 Experimental results

3.6.1 Density measurements

The densities of the hot isostatically pressed composites are shown in Table 3.2. These show that near-full densities were obtained for 10 and 20 wt% Si_3N_4 particulate reinforced composites using the as-received powders, while significantly lower densities (93 and 80 % of theoretical densities) were achieved using the deoxidised powder compacts.

3.6.2 X-ray diffraction results

X-ray diffraction (XRD) patterns obtained from SiC and Si_3N_4 starting powders are shown in Fig. 3.5(a) and (b), respectively. Analysis of the XRD patterns showed that the UF15 SiC starting powder is in the form of α-SiC with the predominant polytype being 6H in the Ramsdell notation (Ramsdell, 1947). Analysis of the LC10 Si_3N_4 starting powder using a well accepted method (Gazzara and Messier, 1977) showed that it contains ≈ 97 % α-Si_3N_4 and ≈ 3 % β-Si_3N_4.

XRD patterns from composites containing 10 and 20 wt% Si_3N_4 prepared from as-received powders and deoxidised compacts are shown in Fig. 3.6. The major and minor crystalline phases identified are summarised in Table 3.2.

Interestingly, the composites made from the as-received powders had β-SiC (3C) as the major SiC phase with a small amount of α-SiC phase, mainly 6H, while α-SiC remained the major form of SiC in the composites made from the deoxidised compacts. The detailed analysis of XRD patterns to show the presence and/or absence of some common SiC polytypes will be discussed in Chapter 7.

Almost all the α-Si_3N_4 transformed into β-Si_3N_4 in the composites made from the as-received powders, while in the composites made from deoxidised powder both α-Si_3N_4 and β-Si_3N_4 phases were present in significant quantities. In addition, silicon oxynitride is identified in both types of composites.

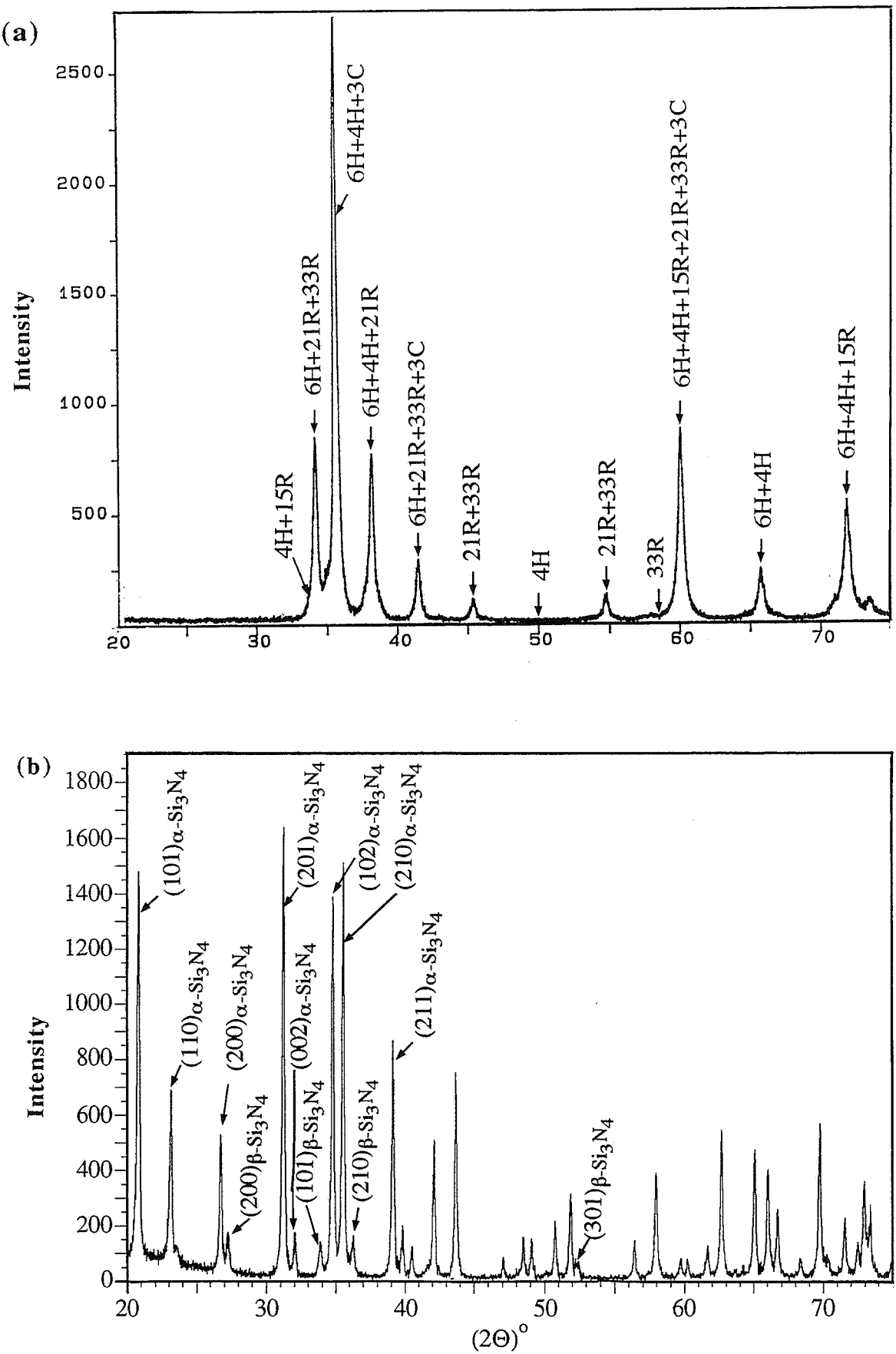

Fig. 3.5 X-ray diffraction patterns of starting powders: (a) UF15 SiC and (b) LC10 Si_3N_4.

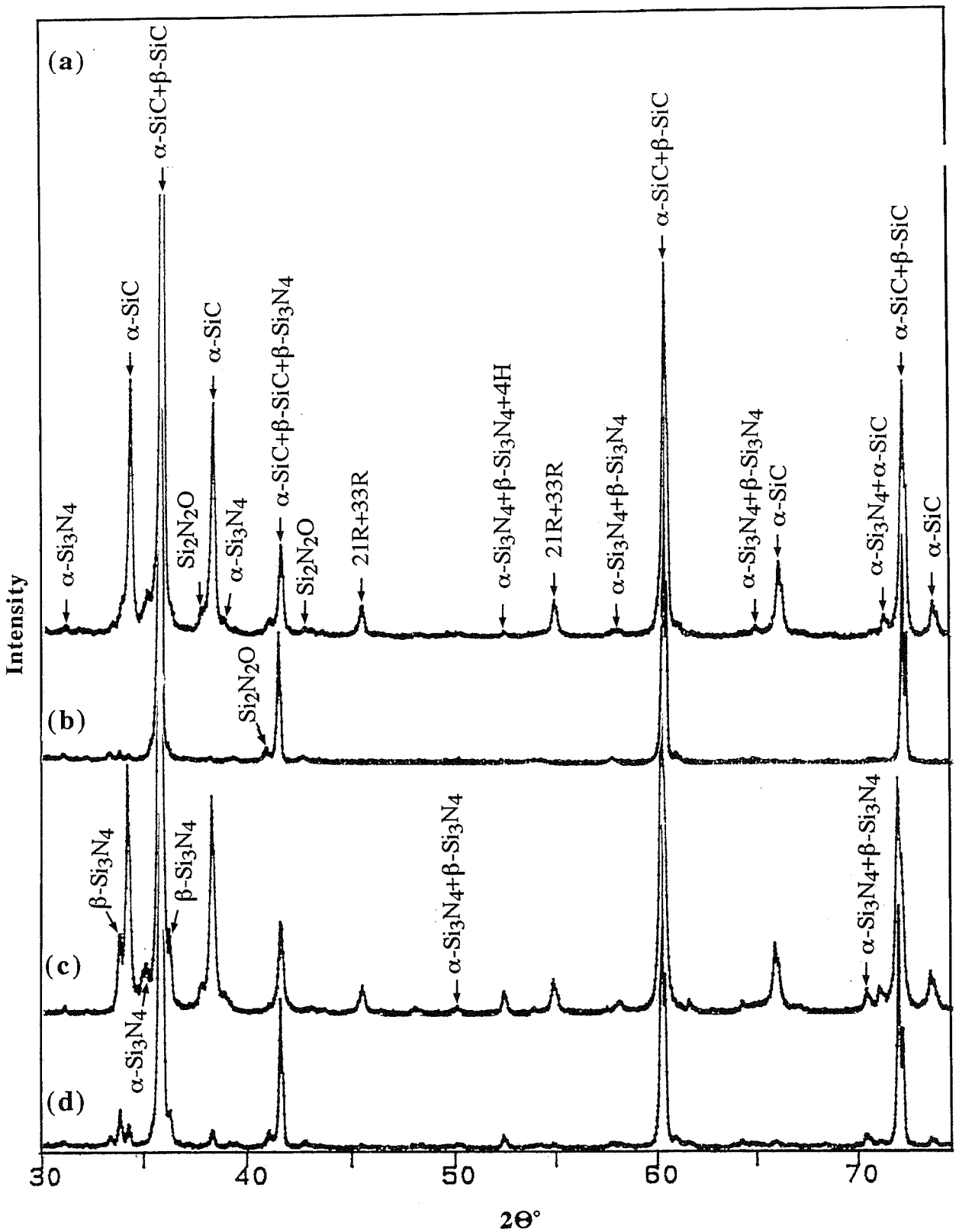

Fig. 3.6 Comparison of X-ray diffraction patterns from composites denoted as 10D (a), 10A (b), 20D (c) and 20A (d). Where D and A refer to deoxidised and as-received whereas 10 and 20 refer to the wt% of Si_3N_4 content.

Type	Relative density (%)	Major crystalline phases	Minor crystalline phases
A10	99	β-SiC; β-Si_3N_4	α-SiC; α-Si_3N_4; Si_2N_2O
A20	100	β-SiC; β-Si_3N_4	α-SiC; α-Si_3N_4; Si_2N_2O
D10	93	α-SiC; β-Si_3N_4; α-Si_3N_4	β-SiC; Si_2N_2O
D20	80	α-SiC; β-Si_3N_4; α-Si_3N_4	β-SiC; Si_2N_2O

Table 3.2 Relative densities and the crystalline phases detected after hot isostatic pressing of the Si_3N_4 reinforced SiC composites. A10 and A20 composites are fabricated from as-received powders while D10 and D20 composites are fabricated from deoxidised green compacts. 10 and 20 signify that the composites contain 10 or 20 wt% Si_3N_4, respectively.

It is generally believed from thermodynamic considerations that α- and β-Si_3N_4 are low and high temperature polymorphs respectively with α transforming to β at about 1420°C (Lee and Rainforth, 1994). It should also be emphasised that while the thermodynamics are reasonably understood the kinetics may dominate and unless a liquid is present to lower the activation energy for transformation very little α to β transformation occurs until much higher temperatures (the value of the high temperature is not given in Lee and Rainforth, 1994).

Although in this study, a temperature of 2100°C is used, the α to β transformation was not complete in the absence of liquid phases when deoxidised green compacts were hot isostatically pressed. Therefore, the transformation most probably took place during the deoxidation stage when the liquid phases were available and a further but a limited amount of transformation occurred during hot isostatic pressing. This point could not be clarified since XRD analysis have not been carried out on the deoxidised samples before hot isostatic pressing.

3.6.3 Microstructure of composites made from as-received powders

The microstructure of the composites prepared from as-received powders consisted of grains of β-SiC, α-SiC, β-Si_3N_4, α-Si_3N_4, Si_2N_2O, fine Si_3N_4 precipitates, sub-micron graphite-like inclusions and residual intergranular phases.

An analysis of the electron diffraction patterns from the composites confirmed the XRD analysis that β-SiC and β-Si_3N_4 were the predominant phases. A small amount of α-SiC could be identified, mostly in the form of 6H SiC, with other long period polytypes of α-SiC seen less frequently.

A typical aspect of the microstructure within the 20 wt% composite is shown in the through-focal series in Fig. 3.7. There is evidence for thin intergranular films present at all the interfaces, *i.e.*, both the 3C-α SiC interphase boundaries and the grain boundary between two α-SiC grains, from the behaviour of the Fresnel fringes at the interfaces as a function of defocus. As discussed in Chapter 2, Ness *et al.* (1986) & Ross and Stobbs (1989) showed that when the mean inner potential of the film is lower than the adjacent grains, the film will appear as a central bright fringe, with adjacent dark fringes when imaged using an underfocused lens. The contrast reverses if an overfocused lens is used, despite the contamination evident on all the microstructure seen in Fig. 3.7. It can therefore be inferred that the intergranular films in Fig. 3.7 had a lower mean inner potential than those of surrounding grains. The large regions of amorphous phase at the triple junctions seen in Fig. 3.7 are also a characteristic of the observed microstructure.

A significant amount of twinning in the 3C SiC grains on (111) planes was observed during TEM observations (Fig. 3.8). Easily recognisable $\Sigma = 3$ twin diffraction patterns were obtained in the transmission electron microscope when the electron beam was parallel to a $[1\bar{1}0]$ 3C SiC zone axis common to both grains. A small inclusion inside twinned 3C SiC grain is also evident in Fig. 3.8. It was also observed that the internally twinned 3C SiC grains were generally elongated in shape, whereas the α-SiC grains had more irregular morphologies. As seen in Fig. 3.7, the contact area of α-SiC grains with triple junction phases are semi-circular whereas the 3C SiC grains were flat at the contact points.

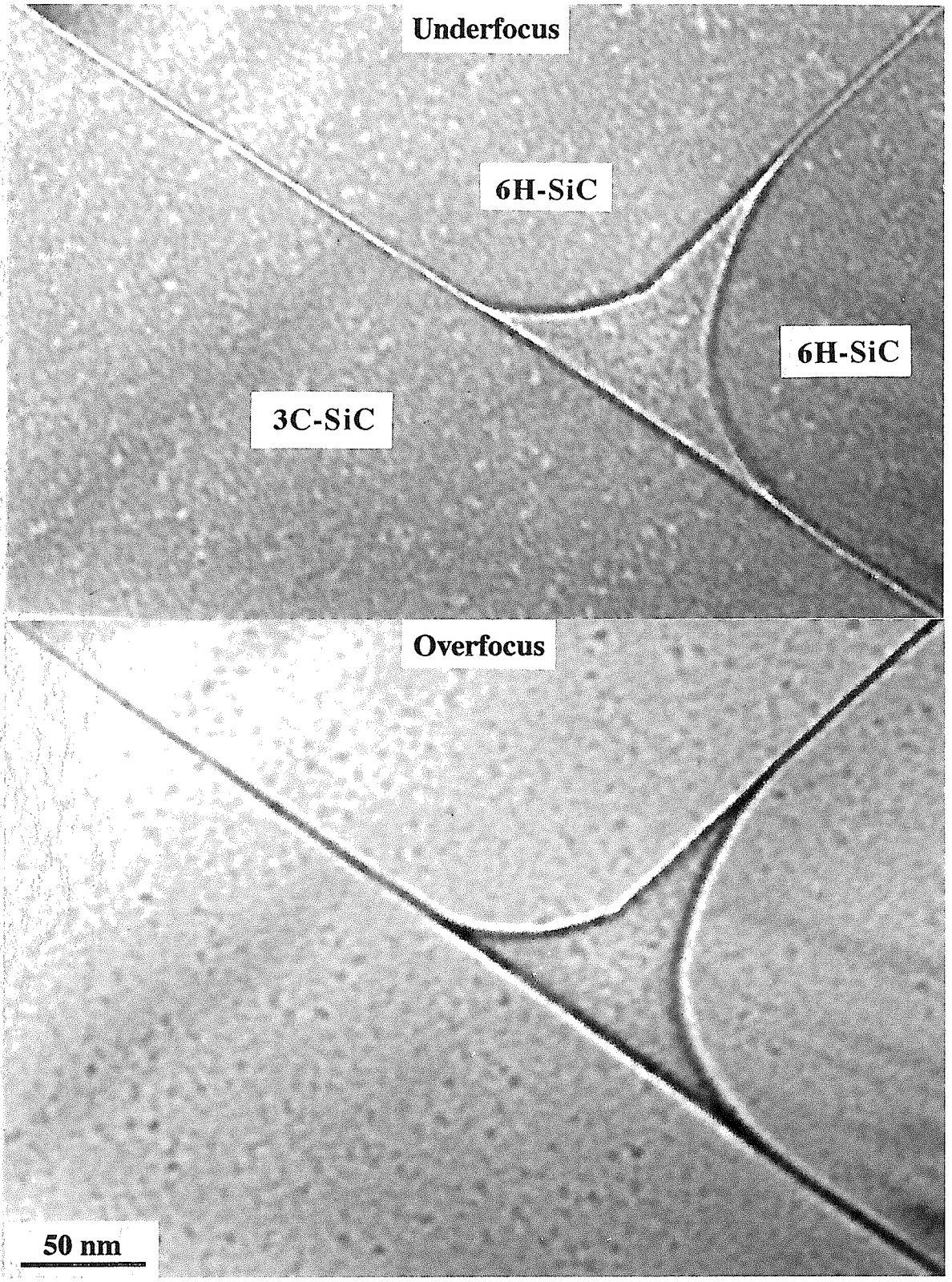

Fig. 3.7 A typical aspect of the microstructure of 20 wt% Si_3N_4 particulate reinforced SiC composites prepared from as-received powders. The reverse Fresnel contrast at all three interfaces indicate the existence of amorphous intergranular films whose mean inner potentials are lower than the adjacent SiC grains.

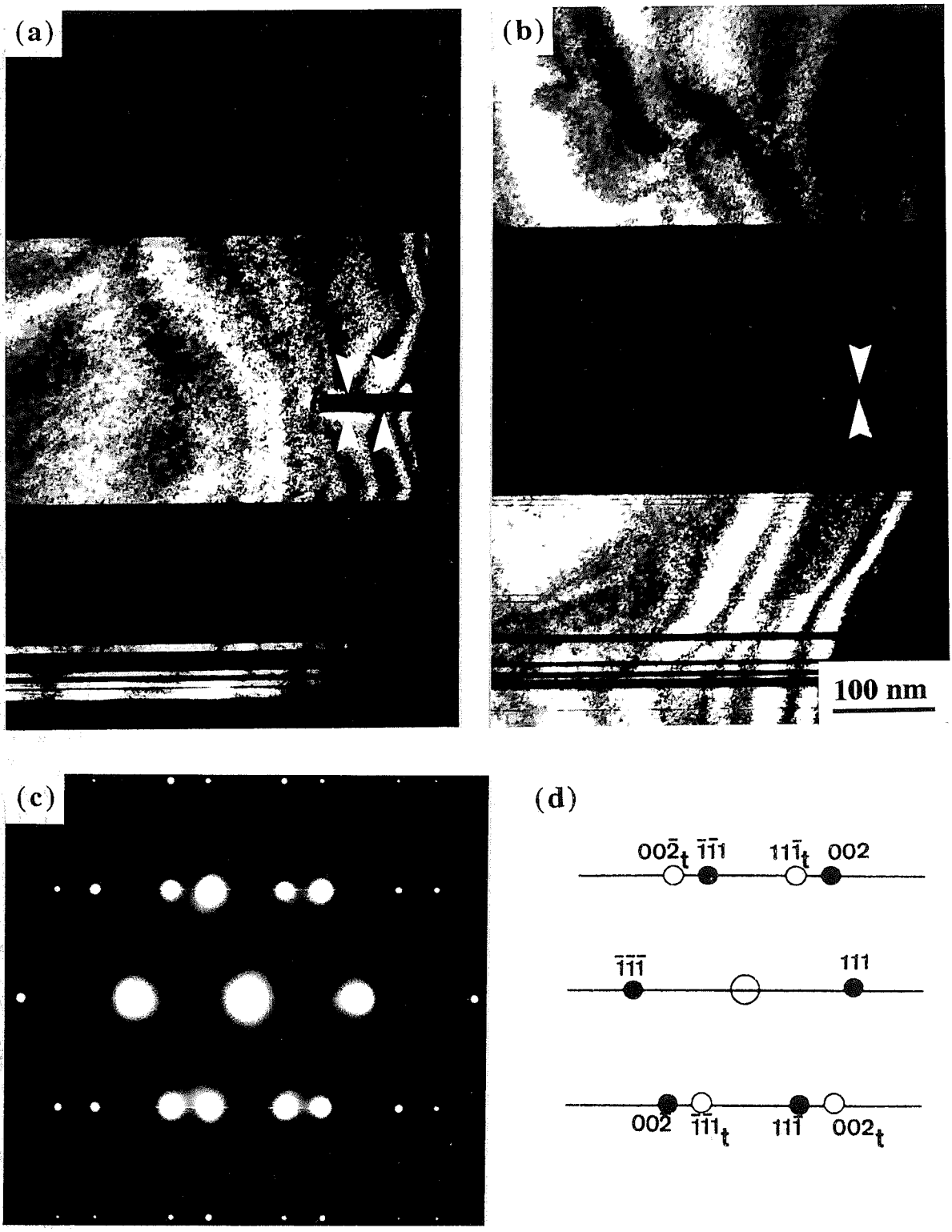

Fig. 3.8 (a) A dark field electron micrograph of a (111) twinned β-SiC particle using the $(11\bar{1})$ twin spot, (b) the same area using the (002) matrix diffraction spot, (c) the $[1\bar{1}0]$ diffraction pattern of the twinned grain and (d) its schematic representation. A graphite-like inclusion is arrowed which is out of contrast in both the micrographs due to the imaging conditions used.

In comparison with SiC, Si_3N_4 grains were more equiaxed and a few of them were observed to be faceted (Fig. 3.9(a)). The grain shown in Fig. 3.9(a) is identified as β-Si_3N_4 by tilting it away from [0001] towards the [11$\bar{2}$0] zone axis which gives a different diffraction pattern in comparison to the same direction in α-Si_3N_4. The size of the faceted grains were in the region of 1.0 to 1.5 μm.

A large number of Si_3N_4 precipitates finer than 500 nm in size were found to be distributed inside SiC grains. The shapes of the precipitates were variable – in projection some were circular or hexagonal in shape, whereas others could be seen to be elongated with round ends. An example of a β-Si_3N_4 precipitate is shown in Fig. 3.9(b). Note the size of the precipitate is only ≈ 275 nm wide and 400 nm long.

TEM observations of samples broken accidentally showed that these small Si_3N_4 precipitates, twinned SiC grains and graphite-like inclusions actually help to deflect cracks along the interfaces.

3.6.4 Microstructure of composites made from deoxidised compacts

The general microstructure of the 10 wt% Si_3N_4 composite prepared from deoxidised powder compacts is shown in Fig. 3.10(a) and (b) at relatively low magnifications. Even though these micrographs are from thin foils, the porous nature of the composite is evident. Most of the SiC grains are full of stacking faults characteristic of α-SiC. In some areas, very large 10 μm long 6H grains were detected, indicative of significant grain growth having been possible during processing, although the average grain size is smaller than the composites made from as-received powders. In addition, graphite-like inclusions were also observed (see the arrowed features in Fig. 3.10(a)), as in the composites prepared from as-received powders, but Si_3N_4 precipitates in SiC grains were not found.

TEM analysis revealed that the amorphous phases are largely absent at interfaces and triple junctions in these series of composites. Instead, the amorphous phases at triple junctions (Fig. 3.7) in the composites made from as-received powders are replaced with pores (Fig. 3.10(a)). The detailed analysis of interfaces in both type of composites have been discussed in Turan and Knowles (1995) and will be discussed in details in Chapters 5, 6 and 7.

3.7 Discussion

3.7.1 Relative densities of the composites

The density measurements showing that near-full densities were obtained for composites fabricated from as-received powders, in contrast to the much lower densities obtained from the deoxidised material, merit comment.

3.7.1.1 The effect of deoxidation on the densification behaviour

The generally accepted model of the densification of SiC (Prochazka, 1975) is that densification occurs in the solid state, with carbon added as a sintering aid to deoxidise the particle surfaces and increase the surface energy. However, during hot isostatic pressing gaseous products are unable to escape from the system, which is why a deoxidation process to remove surface silica was carried out prior to hot isostatic pressing for some of the composites produced in this work.

If the role of carbon is simply as a deoxidant in order to obtain dense SiC, it would have been expected that full densities would have been achieved in the composites made from deoxidised powders, in contrast to results reported in Section 3.7.1. Instead, observations of intergranular films in the composites made from as-received powders (Turan and Knowles, 1995) are entirely consistent with a liquid phase sintering route, as favoured by monolithic Si_3N_4. The implication is that the presence of the Si_3N_4 overrides any barrier to densification offered to monolithic SiC by its native oxide of silica, presumably by creating enough liquid for the solution-reprecipitation process to go to completion in Si_3N_4 at the same time as inducing densification of the SiC through liquid phase sintering.

It is reasonable to assume that by comparison relatively little liquid phase would have been available during hot isostatic pressing of the deoxidised powder compacts. This is in agreement with HREM observations (Turan and Knowles, 1995) of relatively little intergranular films seen at room temperature in the composites made from the deoxidised material. On this basis, the solution of α-Si_3N_4 into the liquid and its subsequent precipitation into β-Si_3N_4 would be expected to be relatively incomplete. During hot isostatic

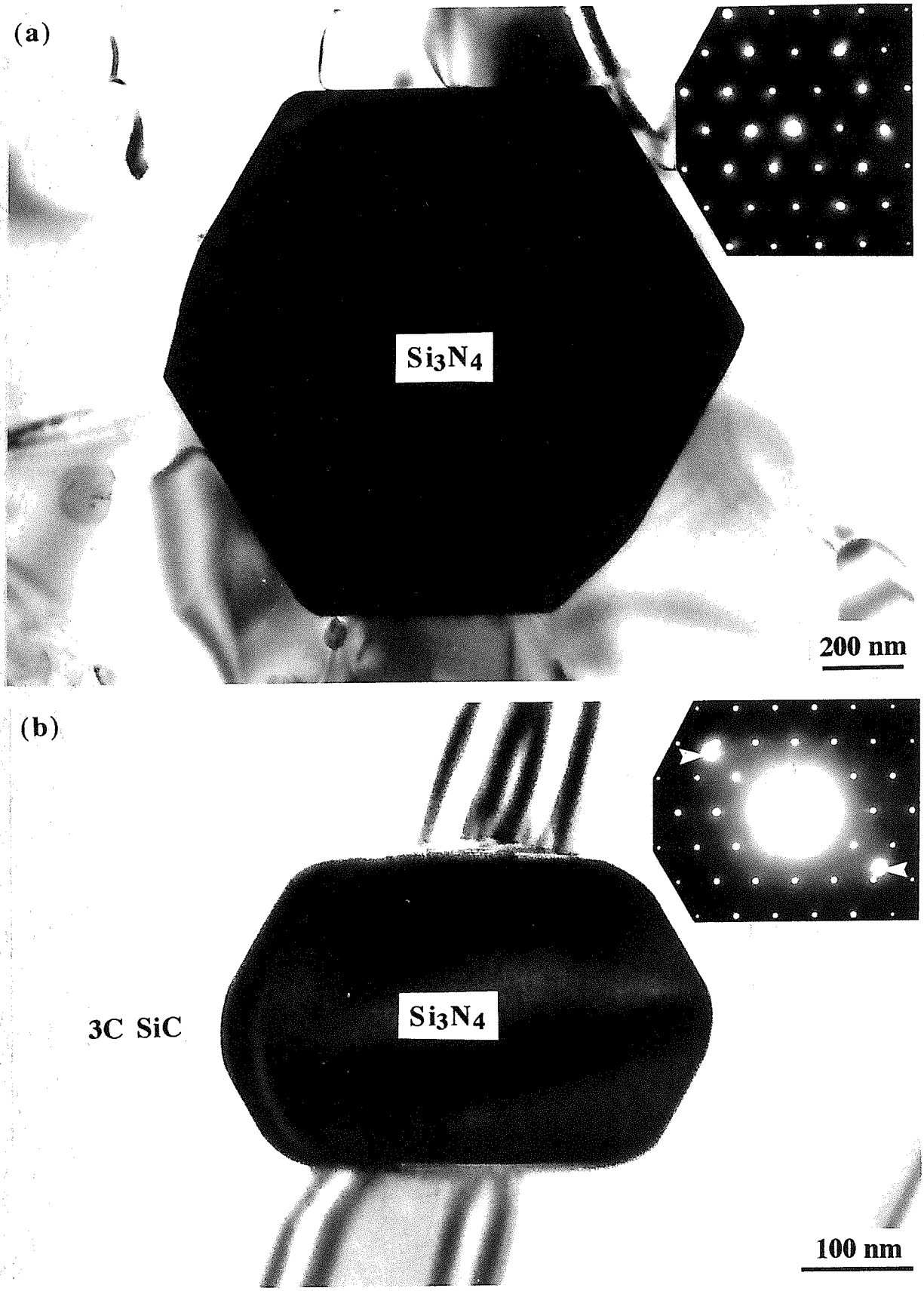

Fig. 3.9 An example of a hexagonally shaped β-Si_3N_4 grain (a) and an elongated β-Si_3N_4 precipitate in a 3C SiC matrix grain (b). The insets show the diffraction patterns in [0001] β-Si_3N_4 direction. SiC matrix spots are arrowed in (b).

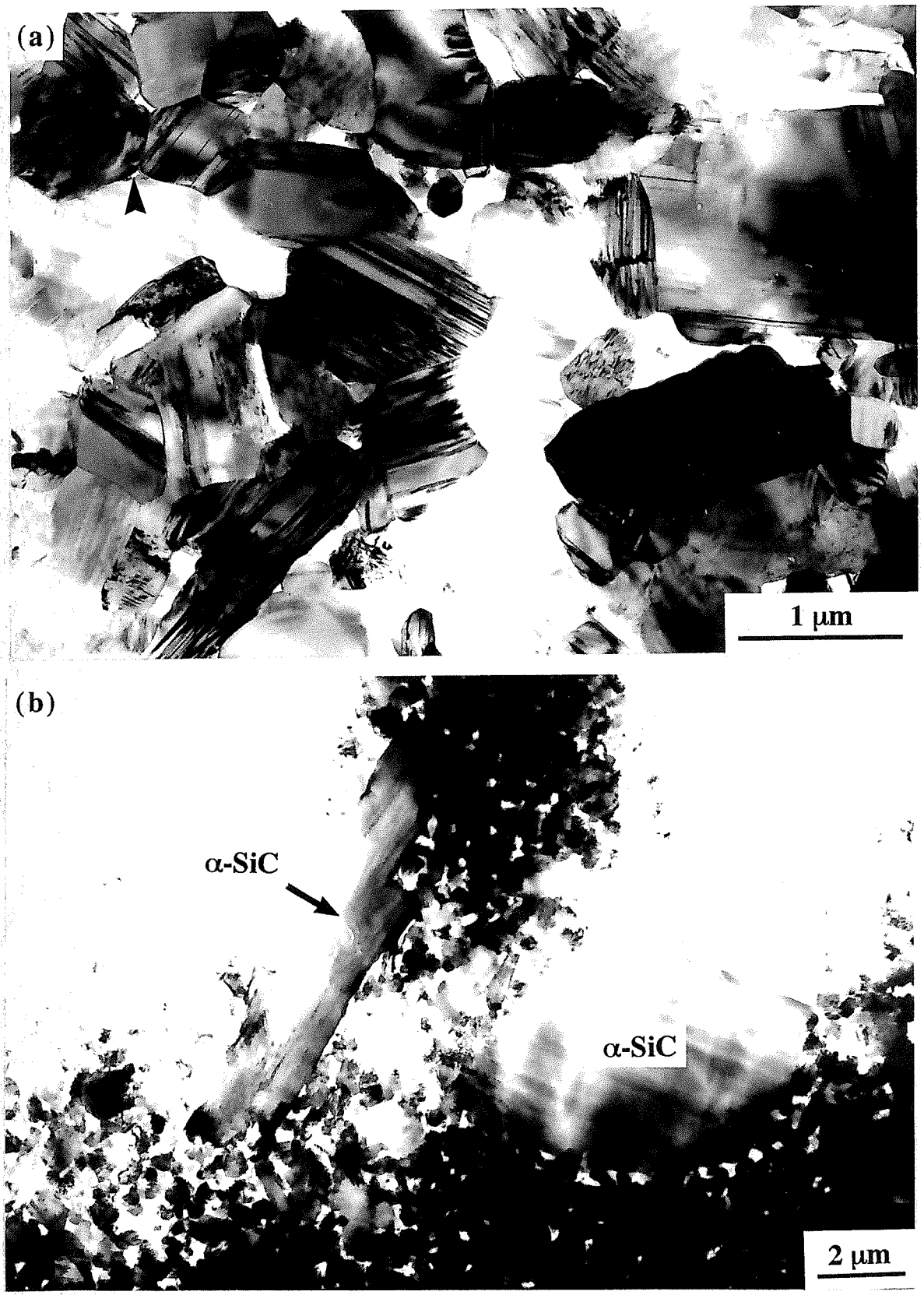

Fig. 3.10 A typical microstructure of a 10 wt% Si_3N_4 reinforced SiC composite prepared from deoxidised powders (a) and a localised region of large grains from the same material (b). The arrowed feature in (a) is a graphite-like inclusions.

pressing, the limited amount of liquid present would have the effect of producing a skeleton of solid material that could only densify further through slower solid state diffusion process. It is also conceivable that the deoxidation step itself contributed to the attainment of a low final density by enabling some densification to occur, thus forming the basis for a solid skeleton during hot isostatic pressing.

This also explains why the near theoretical densities for SiC produced by hot isostatic pressing is possible even without the addition of densification aids. For example, Dutta (1988) hot isostatically pressed α-SiC powder to 97 % theoretical density at 2100°C without the addition of sintering aids. Hermansson *et al.* (1986) obtained 96 % density by hot isostatic pressing of the same powder (UF15) at 1900°C under 160 MPa without additives. They concluded that for complete densification of SiC powders using glass EHIP technique no sintering aids are necessary even below 1900°C if well defined powders are used. The main powder treatment involves removal of large grains by sieving or sedimentation techniques. Watson *et al.* (1985) managed to obtain high density (>95 % theoretical) SiC specimens in argon under 138 MPa pressure for 2 hours using hot isostatic pressing and observed an increase in the room temperature strength of up to 20 %, an increase in the strength at 1200°C of up to 50 %, and a Weibull modulus increase of up to 100 % relative to monolithic SiC ceramics produced by pressureless sintering. Interestingly, no abnormal grain growth was seen. Tanaka *et al.* (1989) have also hot isostatically pressed highly pure Si_3N_4 to near full theoretical density without additives.

Despite the fact that the sintering additives were not introduced explicitly in the composites made from as-received powders (also the examples observed in the literature), there was enough liquid phase at the fabrication temperatures from the surface silica to produce the desired densification behaviour. These are all indicating that the surface silica does play an important role before it is removed by the carbon addition even during the so-called solid state sintering of SiC and obviously during hot isostatic pressing of SiC (Dutta, 1988) and Si_3N_4 (Tanaka *et al.*, 1989) without the help of sintering additives.

The role of silica can be assigned as follows; silica does not react with carbon until the high temperatures (1600-1650°C) reached (Lee and Cutler, 1975) and the reaction will not complete even at 1900°C (Wrobleska and Hamminger, 1991) although the reaction is

favourable thermodynamically over 1520°C. Also note that above 1500°C[#], vitreous silica melts (Rochow, 1973). Therefore, during the temperature rise, surface silica melts and helps the densification by the first stage of liquid phase sintering which is particle rearrangement. In the first stage as discussed by German (1985), there is rapid initial densification due to the capillary force exerted by the wetting liquid on the solid particles and the elimination of porosity occurs as the system minimises its surface energy. In most of the cases, this initial stage overlaps with the second stage of the solution-precipitation of particles. In spite of the short duration, the changes induced in the initial stage are often the most significant. Dramatic microstructural changes occur during the initial stage. The events are solid state sintering, coalescence, liquid spreading, capillary attraction, particle sliding, diffusional homogenisation, and particle disintegration and fragmentation (German, 1985). The liquid formation and associated capillary force cause rearrangement and clustering in the microstructure.

These results indicate strongly that the densification of as-received powders during hot isostatic pressing took place by liquid phase sintering. In addition, it has an implication that SiO_2 does play an initial role before it is removed by carbon even during the so-called solid state sintering of SiC.

In support of above proposal, it is relevant to recall that the recent experimental observations by PEELS analysis of Wrobleska *et al.* (1990) discussed in 3.3.3 have revealed that a thin (>10 nm) uniform layer forms on the SiC particles at 1500°C, which contains amorphous silica, amorphous carbon and traces of B. Although the PEELS spectra presented does not indicate structural information about whether B was in the form of boron oxide or elemental boron, their experiment clearly shows the existence of a liquid phase containing boron at some stage of sintering. Sintering at 2123 K for 5 minutes did not increase the density of the green compacts. They found that the reduction of silica was not complete at these conditions despite the high heating rates (20 K/min). However, they did not detect any B. Further sintering experiments at 2473 K did not reveal the existence of any liquid phase. (Note that they achieved 97 % density for 5 minutes sintering whereas 97.5 % density was achieved for 1 hr sintering).

[#] *The melting temperature will be lower in the presence of other impurities.*

It seems that the densification of SiC takes place in the early stages by liquid phase sintering and at the later stages this is coupled with solid state sintering rather than densification taking place by the previously proposed solid state sintering mechanism for B and C doped SiC, since vitreous silica is liquid above 1500°C and is not removed efficiently until higher temperatures (1900°C) are reached.

3.7.1.2 The effect of silicon nitride content on the densification behaviour

The interesting point to note here is that increasing the amount of Si_3N_4 does not effect the final density of the composites made from as-received powders. Buljan *et al.* (1987) observed that increasing the content of SiC particulates decrease the densification rates of Si_3N_4. This is due to the increasing content of SiC increasing the densification temperature of Si_3N_4 since typically α-Si_3N_4 powder densifies at 1900°C whereas SiC densifies at temperatures around 2100°C. However, the opposite should be expected from Si_3N_4 reinforced SiC since the increase in Si_3N_4 content should lower the densification temperature. Therefore, this theoretical argument is in agreement with the experimental observation in the composites made from as-received powders that the densities obtained with the increasing Si_3N_4 content should not decrease.

However, the same argument cannot be applied to the composites made from deoxidised compacts because lower densification rates were observed with increasing content of Si_3N_4 addition in contrast to the above expectation. The observation of a decrease in density for the composites made from deoxidised compacts cannot be due solely to the increase in the Si_3N_4 content. There are other effects to be considered on the densification rates. Hermansson *et al.* (1986) showed experimentally that removal of few large particles significantly enhances the densification rate and this was especially pronounced for α-SiC powder. They achieved fully dense SiC products by hot isostatic pressing of green bodies, obtained by cold isostatic pressing of sedimented α-SiC powder at 300 MPa, at temperatures below 1900°C under 160 MPa pressure without sintering aids. Without the removal of the large particles but under same experimental conditions only 96 % density was achieved. Therefore, the observation of a decrease in density for deoxidised composites with an increase in Si_3N_4 content could be due to a bad batch containing large SiC and/or Si_3N_4 grains which hinder the densification of 20 wt% Si_3N_4 particulate reinforced composite made from deoxidised compacts. In the absence of liquid phases the effect of large grains could be even significant since rearrangement is going to be difficult.

The second explanation for this behaviour is that the densification rate of Si_3N_4 is generally effected by the $\alpha \rightarrow \beta$-Si_3N_4 phase transformation which requires liquid phases at the fabrication temperatures (Hampshire and Jack, 1981). Due to the fact that there is supposedly no liquid phases during the hot isostatic pressing of deoxidised compacts, the transformation will not occur. Therefore, the higher the amount of Si_3N_4, the lower the densification rate. However, this effect should not be too significant so there must be some additional parameters to account the lower densification rate for higher amount of Si_3N_4 addition.

Silicon nitride does not melt, but instead decomposes at 1900°C at 1 atm nitrogen pressure. The decomposition of Si_3N_4 results in the escape of Si_3N_4 in the form of gaseous species* during the deoxidation stage. This could increase the porosity and cause lower densification rates of composites made from deoxidised compacts in comparison to composites made from as-received powders. This would also help to account for the lower densification rate of 20 wt% Si_3N_4 reinforced composite compared to 10 wt% Si_3N_4, since the higher Si_3N_4 content would increase the amount of Si_3N_4 decomposition and as a result could decrease the value of density.

The other possibility could be the $\alpha \rightarrow \beta$ reverse phase transformation of SiC, but so far noone has claimed any effect of this transformation on the densification behaviour of SiC.

3.7.2 Comparison of general microstructure

General microstructural observations showed that the composites prepared from as-received powders contain amorphous intergranular phases. By contrast, the composites prepared from the deoxidised material were free of such intergranular phases. TEM micrographs also showed the porous nature of the composites prepared from the deoxidised material. In comparison, low magnification micrographs from the composites prepared from as-received powders did not reveal any porosity. Graphite-like inclusions were detected in both type of the composites. However, Si_3N_4 precipitates were only found in the composites prepared from as-received powders.

---

* *Lange (1982) proposed that Si_3N_4 weight loss can occur as a result of (i) the decomposition of Si_3N_4 to $Si_{(g)}$ and $N_{2(g)}$, (ii) the active oxidation of Si_3N_4 to form $SiO_{(g)}$ and $N_{2(g)}$ and (iii) the reaction between Si_3N_4 and SiO_2 to form $SiO_{(g)}$ and $N_{2(g)}$. Above 1850°C, the first reaction dominates whereas below 1850°C, the third reaction dominates.*

Large grains of α-SiC grains were detected in the composites prepared from deoxidised compacts, whereas the large grains were 3C SiC in the composites prepared from as-received powders. The fact that the inclusions were almost all detected at the interfaces and the absence of precipitates in the composites prepared from deoxidised compacts indicate that the grain growth was not as substantial in these composites as in the composites made from as-received powders. This is also supported by the observations of peak broadening, which is caused by the small size grains, in the XRD patterns of the composites prepared from deoxidised compacts. Peak broadening was absent in the XRD patterns of the composites prepared from as-received powders.

3.8 Conclusions

X-ray diffraction and transmission electron microscope techniques have been used to investigate the microstructure of SiC-Si_3N_4 composites fabricated from as-received powders and from deoxidised compacts. The densities of the composites were measured using the Archimedes method.

The observed densities of composites prepared from deoxidised powder compacts were significantly lower than those of the composites prepared from as-received powders.

X-ray diffraction and transmission electron microscope analysis enabled the identification of an unexpected near-complete phase transformation of α-SiC into β-SiC in composites prepared from as-received powders, while α-SiC remained untransformed in the composites prepared from deoxidised material. An incomplete transformation of α-Si_3N_4 into β-Si_3N_4 was found in the deoxidised compacts, but this transformation went to near completion in the composites made from as-received powders. The α-Si_3N_4 to β-Si_3N_4 transformation is well established as is the β → α-SiC transformation, but there are still some unknown parameters responsible for the occurrence of α → β-SiC reverse transformation which will be discussed in Chapter 7.

The existence of intergranular phases in composites prepared from as-received powders and the relative absence of such films in composites prepared from deoxidised powder compacts, coupled with the much lower densification rates for composites prepared from deoxidised

powders both suggest strongly that densification took place efficiently in the composites made from as-received powders because of liquid phase sintering. The answers to the questions of *whether or not the amorphous phases at triple junctions extend to the interfaces or whether or not some of the interfaces are free of such films, if the films are present what are their thicknesses and compositions, what controls the existence of a film and a film thickness at an interface* will be attempted in Chapters 5 and 6.

Graphite-like inclusions were detected in the both type of composites. The questions arise are: *are they graphite?; if they are, do they contain any other impurities?; and how do they form?* These questions will be answered in the next Chapter.

Chapter 4

TEM Observations of Graphite-like Inclusions

4.1 Introduction

In the course of work characterising hot isostatically pressed Si_3N_4 particulate reinforced SiC composites produced without the use of sintering aids, sub-micron size, graphite-like inclusions were regularly found at grain boundaries, at interphase boundaries and within SiC and Si_3N_4 grains.

Graphite and/or carbon rich inclusions have been commonly observed in SiC-based materials. For example, inclusions were detected in *(i)* pressureless sintered SiC doped with B and C by Hamminger (1989), Braue and Carpenter (1990) & Turan and Knowles (unpublished report), *(ii)* in SiC whisker-reinforced Si_3N_4 and SiC platelet-reinforced Si_3N_4 composites by Braue (1992), *(iii)* in hot pressed SiC-AlN composites by Xu *et al.* (1992) and *(iv)* in hot isostatically pressed SiC samples, one without sintering additives and the other with 0.2 % Al addition, by Braue *et al.* (1989). Kleebe *et al.* (1990) have also observed carbon clusters in hot isostatically pressed Si_3N_4 composites reinforced with carbon coated SiC whiskers as well as, unexpectedly, in uncoated SiC whisker reinforced Si_3N_4 composite. In one isolated case, in addition to the carbon inclusions, B_4C precipitates were found in annealed α-SiC (which was produced by pressureless sintering) in a graphite furnace (More *et al.*, 1986).

It is important to study the existence and character of these inclusions for the following reasons. Such inclusions can be related to failures under thermal cycling and creep test conditions due to the cavities and microcracks associated with them (Tighe *et al.*, 1986). On the other hand, inclusions were found to be grain growth controllers (Prochazka, 1974), but they have to be considered detrimental if they are distributed inhomogeneously as this can lead to the occurrence of agglomerate type critical flaw dimensions (Hamminger, 1989). Inclusions may also influence crack deflection as well as slow crack growth at high

temperatures. Braue *et al.* (1989) investigated the correlation of subcritical crack growth and microstructure in hot isostatically pressed SiC and concluded that compared to the impact of non-crystalline phases, the influence of graphite inclusions on subcritical crack growth is regarded as of minor importance. There is evidence for even healing of microcracks within the graphite layers during annealing (Tighe *et al.*, 1986). Graphite inclusions are also claimed (Mieskowski *et al.*, 1984) to effect the oxidation behaviour of SiC by forming gas bubbles and increasing the material transportation. In fact, Gourbilleau and Nouet (1993) showed by using TEM that the bubbles and the channels are indeed associated with the graphite inclusions. It can be concluded from these that the inclusions can control the microstructure developed during the densification and consequently can have an effect on a number of properties of SiC materials.

In this Chapter, transmission electron microscopy results on the structure and chemistry of these inclusions will be reported and the reasons for their occurrence in terms of possible chemical reactions that can occur during composite fabrication will be discussed.

4.2 Experimental results and discussions

4.2.1 Observation of inclusions

Despite the composites having been made without sintering aids, highly defective disc-shaped inclusions were detected at grain boundaries, interphase boundaries and within grains of SiC and Si_3N_4. High resolution transmission electron microscope images of two particular inclusions within a twinned β-SiC grain and a Si_3N_4 grain are shown in Fig. 4.1.

Using high resolution transmission electron microscopy, conventional electron diffraction techniques and by comparing the morphology of these inclusions with graphite inclusions reported in the literature and cognisant of the report of the presence of carbon as an unwanted inclusion in Si_3N_4 hot isostatically pressed without additives (Nezuka *et al.*, 1988), the inclusions could be readily identified as graphite inclusions. In addition, from the known rotation of the diffraction pattern with respect to the image and also from high resolution transmission electron microscopy of the characteristic ≈ 3.4 Å (0002) planes of graphite, the thin direction of the inclusions could be identified as the graphite [0001] direction.

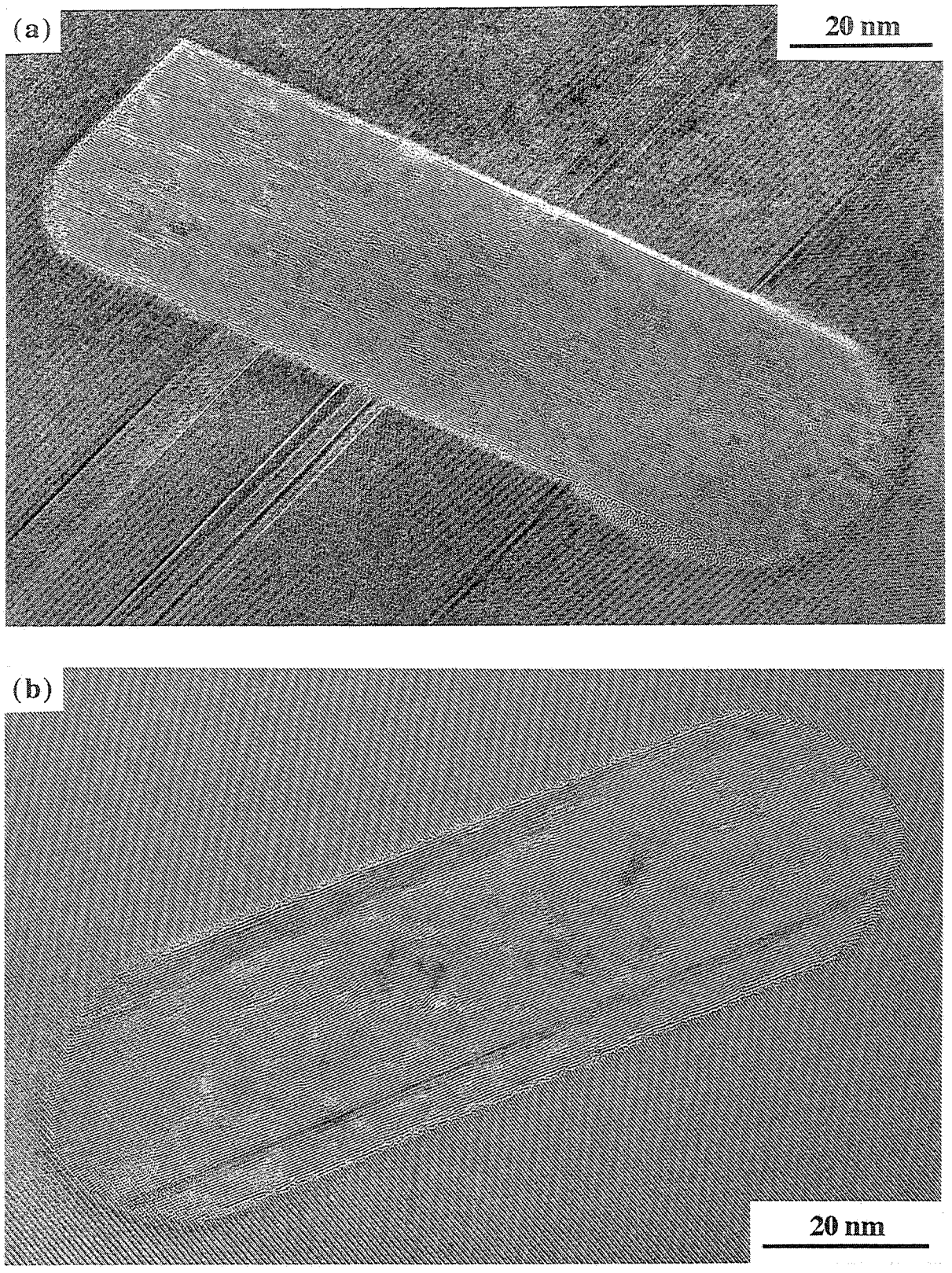

Fig. 4.1 Low magnification HREM images taken around Scherzer defocus showing the disc-like morphology of inclusions in a Si_3N_4-SiC particulate composite made from as-received powders, (a) inside SiC and (b) inside Si_3N_4 grains.

However, supposedly confirmatory elemental analysis by PEELS failed to show that the inclusions were graphite, as expected. Instead it was apparent that the inclusions contained boron and nitrogen in the form of hexagonal graphite-like BN. An example of a stripped B *K*-edge from a PEELS spectrum of a typical inclusion is shown in Fig. 4.2, with the N *K*-edge at an energy loss of 400 eV.

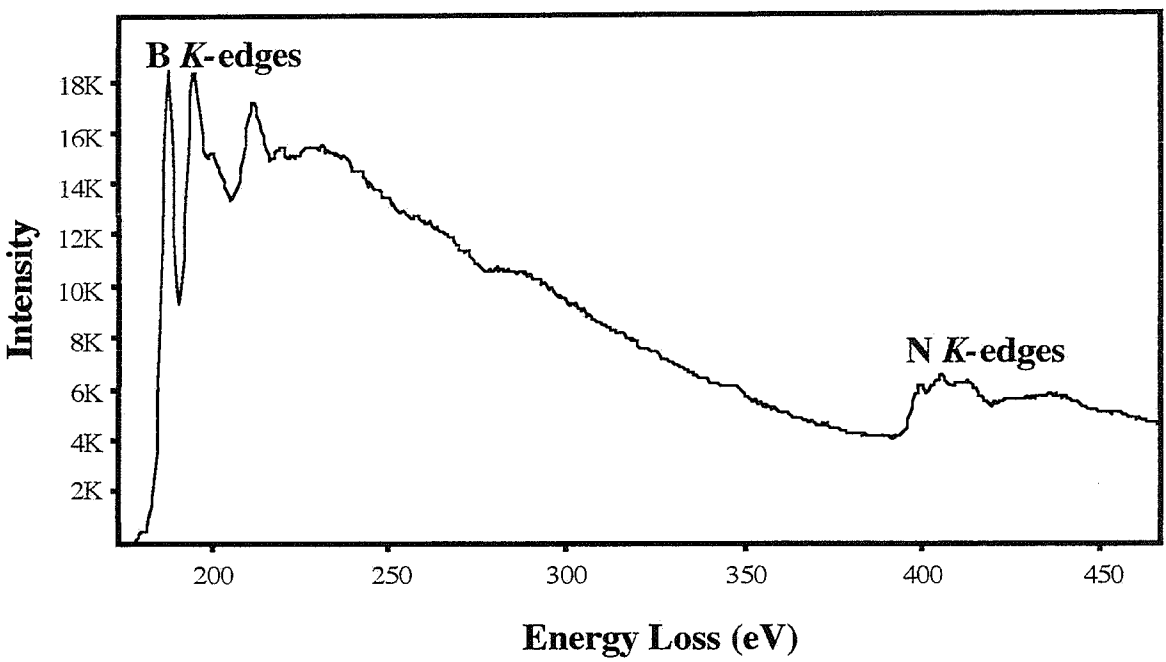

Fig. 4.2 Stripped B *K*-edge from an inclusion together with the N *K*-edge.

The similarity of both the structures and lattice parameters of graphite (a = 2.47 Å, c = 6.70 Å) and hexagonal BN (h-BN: a = 2.50 Å, c = 6.66 Å) evident from Fig. 4.3 gives rise to this ambiguity in microstructural interpretation if confirmatory chemical analysis is not used. Both structures have a layered hexagonal structure consisting of hexagonal rings of atoms within the (0001) planes, either all carbon or alternating boron and nitrogen as appropriate, but whereas graphite has an ..ABAB.. hexagonal stacking sequence in the c-direction, h-BN has an unusual ..AAAA.. stacking sequence (Pease, 1952). The similarity of the (0002) interplanar spacings (3.35 Å for graphite and 3.33 Å for h-BN) means that both electron diffraction and high resolution transmission electron microscopy are inappropriate techniques to deduce the nature of these inclusions unambiguously. A consequence of the low atomic number of boron is that it is not easily detectable by windowless energy dispersive X-ray analysis (WEDX), and so it is fortunate that it is readily detectable by PEELS.

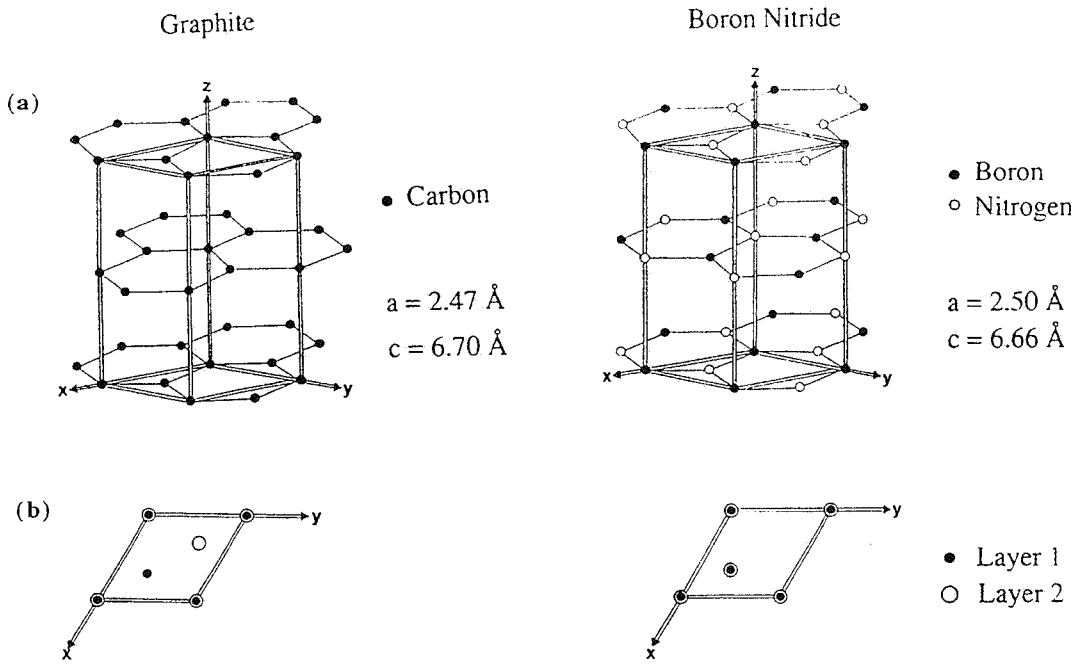

Fig. 4.3 (a) A comparison of the crystal structures of graphite and hexagonal BN, (b) a comparison of the projections of the graphite and h-BN structures along [0001].

4.2.2 PEELS analysis of boron nitride inclusions

In Fig. 4.4, a bright field TEM image taken when the [110] 3C SiC zone axis was parallel to the electron beam shows two different orientations of the disc-like BN inclusions within a 3C SiC grain. These two different orientations can be described as one being edge-on and the other end-on to the electron beam. Diffraction pattern analysis showed that the *c*-axis of the inclusion is perpendicular to the electron beam when the inclusion is viewed edge-on whereas the *c*-axis of the inclusion is parallel to the electron beam when it is viewed end-on. The edge-on orientation is most commonly observed whereas the circular shape in the end-on orientation is not commonly observed, presumably because of the way in which ion beam thinning will tend to remove the latter in thin sections.

PEELS spectra were collected from both the inclusions in both the above orientations and are shown in Fig. 4.5(a) and (b). The stripped B and N *K*-edges of the inclusion on the left in Fig. 4.4 are shown as dotted lines in Fig. 4.5(a) and (b) whereas the full lines in Fig. 4.5(a) and (b) are the stripped B and N *K*-edges for the inclusion on the right in Fig. 4.4. It can be seen that the relative intensities of B and N peaks are differ considerably.

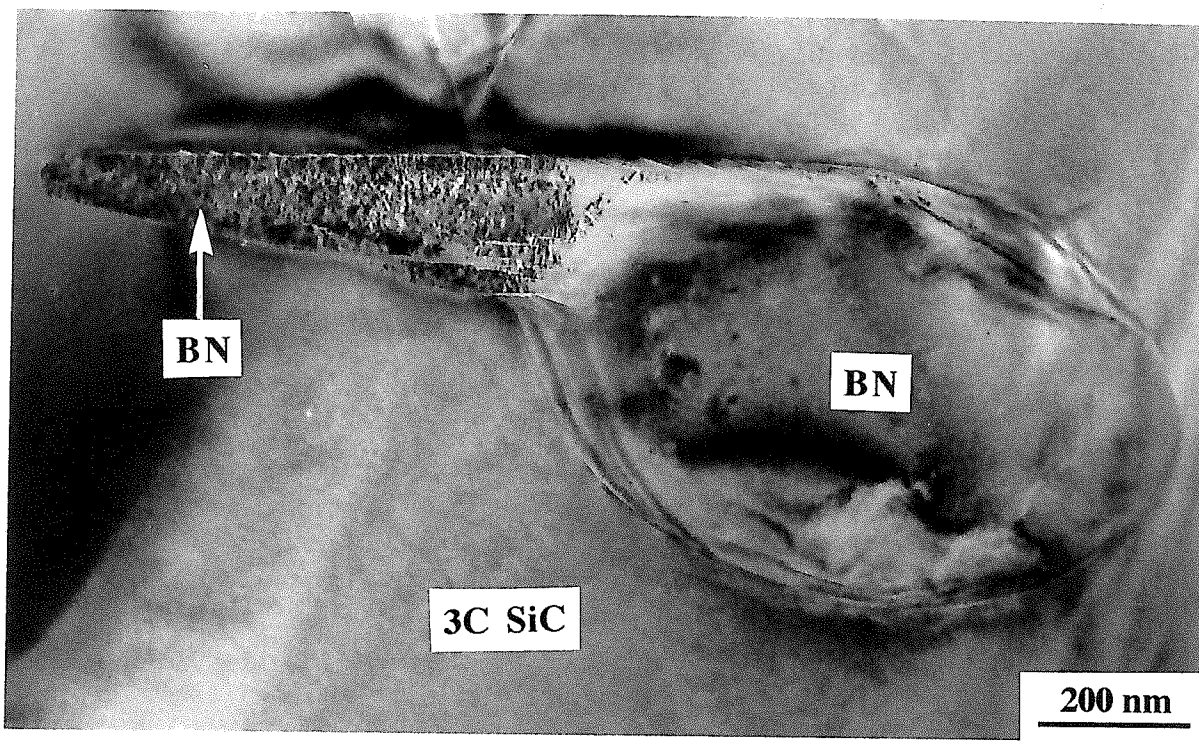

Fig. 4.4 A bright field TEM image showing the disc-like morphology of the inclusions in two orthogonal directions.

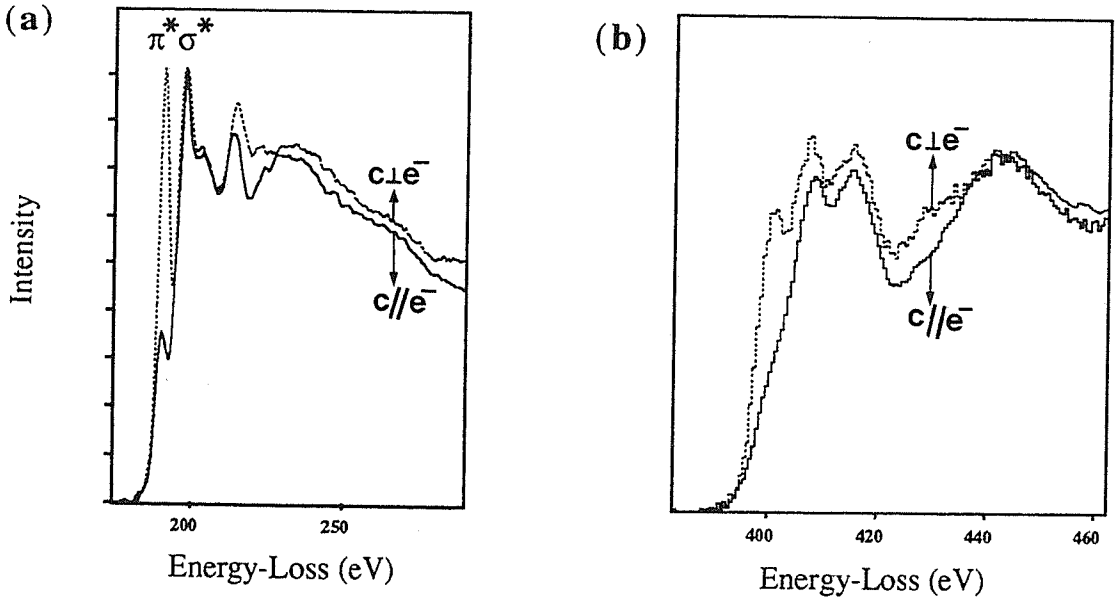

Fig. 4.5 (a) Stripped B *K*-edges and (b) stripped N *K*-edges of the inclusions shown in Fig. 4.4. The full line spectra are from the inclusion to the right in Fig. 4.4 and the dotted line spectra from the inclusion on the left in Fig. 4.4.

Such a difference in the PEELS spectra could arise from a difference in the crystallographic structure (Hosoi *et al.*, 1982) or specimen orientation in that the core-edge fine structure in electron energy loss spectra of thin anisotropic crystals depend on the orientation of the crystal with respect to the electron beam or a detector (Leapman and Silcox, 1979 & Stephen and Brown, 1981). These possibilities will be examined, starting with the crystallographic structure effect.

As discussed at the beginning of this section, the crystal structure of the inclusions are the same. This eliminates the first possibility and reinforces the second possibility that the alignment of crystal axes with respect to the electron beam and/or the detector causes the observed difference in the spectra.

The peaks observed in the spectra of any given material are related to the arrangements of atomic orbitals. It is illustrated schematically in Fig. 4.6(a) how the π- and σ-orbitals are aligned in a graphite crystal. It can be seen that the π-orbitals extend along the *c*-axis, while the σ-orbitals lie in the hexagonal plane. These two states produce two distinct peaks separated in energy in the energy loss spectra. The intensity of the peaks can be increased or decreased depending on how the crystal and collector aperture are oriented with respect to the electron beam. If the configuration of crystal and collector aperture is chosen to favour the momentum transfer (q) parallel to the π bond (q // c), the corresponding π^* peak will be more intense whereas if the configuration favours the momentum transfer in the hexagonal plane, π^* will be less intense with respect to the σ^* peaks (Colliex *et al.*, 1985). Bearing this in mind, a few extreme geometries can be envisaged which could enable the exploitation of this feature to explore the near-edge structure of particular atomic species, such as graphite and h-BN.

The first geometry is shown in Fig. 4.6(b) where the *c*-axis of graphite crystal is aligned at 45° to the electron beam. This has been explored by (Disko *et al.*, 1982) who collected two spectra in a STEM by adjusting the beam deflection so that the spectrometer collected electrons scattered through θ = 1.4 mrad (to give q // c) and θ = - 1.4 mrad (to give (q $\perp$ c)). In this geometry, when (q // c) the π^* peak is more intense, whereas when (q $\perp$ c) the σ^* peak is more intense (Fig. 4.6(b)).

Stephens and Brown (1981) took a different approach (second extreme geometry) that a difference in the spectra can be obtained by physically tilting a crystal from one extreme (c // e^-) to the other (c ⊥ e^-) when the collection angles are the same at these two extremes. However, this is very difficult since it requires a tilt of 90° and therefore they collected a spectrum when *c*-axis of h-BN was parallel to the electron beam (c // e^-) and a second spectrum collected by tilting the sample by 45° to this position. Their STEM results on h-BN showed that when (c // e^-) the intensity of π^* peak is **less** than σ^* peak and at the tilted position the intensities are rather similar@. Obviously, if they have tilted the crystal further and collected a spectrum, the π^* peak would have been even less intense. This is in contrast to the results obtained by Disko *et al.* (1982).

The second extreme geometry is fully explored independently firstly by Turan and Knowles (1993) in h-BN and secondly by Cullen *et al.* (1993) in carbon nanotubes wherein the *c*-axis of graphite at the edge of nanotube make an angle of ≈ 90° with the *c*-axis of graphite at the centre of nanotube. The PEELS spectra obtained by Turan and Knowles (1993) reproduced in Fig. 4.5(a) and (b) were collected from the inclusions shown in Fig. 4.4. Both sets of workers first collected a spectrum when the *c*-axis of the crystal parallel to [0001] direction, which in both cases favours the σ^* peak, whereas when a second spectrum was collected when the *c*-axis of the crystal was perpendicular to the electron beam the π^* peak was favoured. In both cases, very similar spectra were obtained for the same orientations. However, Cullen *et al.* (1993) did not comment on the disagreement between their results and other researchers (*e.g.*, Disko *et al.*, 1982).

The third extreme geometry can be achieved in TEM by tilting the *c*-axis of the crystal parallel to the electron beam and collecting spectra in a similar way to that of Disko *et al.* (1982) in STEM. However, in TEM, all the diffracted spots in the [0001] zone will all favour the σ^* peak. In this case, the intensity of π^* and σ^* peaks can be altered by changing the magnitude of the camera length used to collect a PEELS spectrum in diffraction mode. An increase in the camera length decreases the scattering angle of a beam which is allowed to go through a given spectrometer entrance aperture.

@ *Note that figure captions of (a) and (b) in Fig. 5 in Stephen and Brown (1981) should be exchanged if Fig. 2 is collected when the electron beam was parallel to the c-axis of BN .*

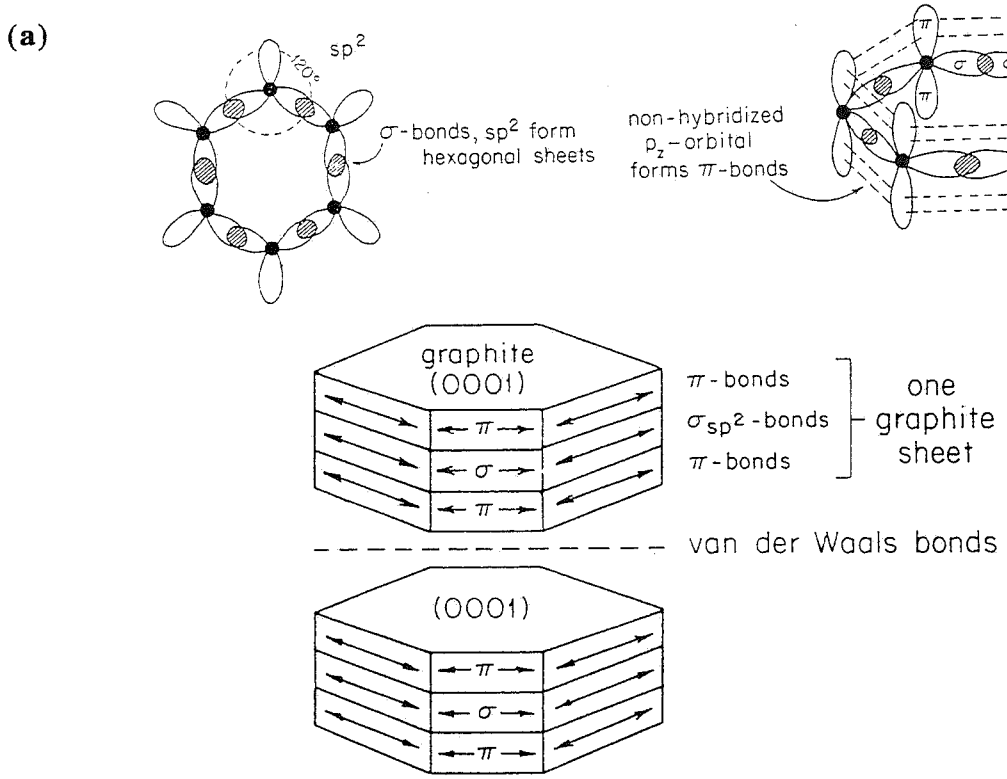

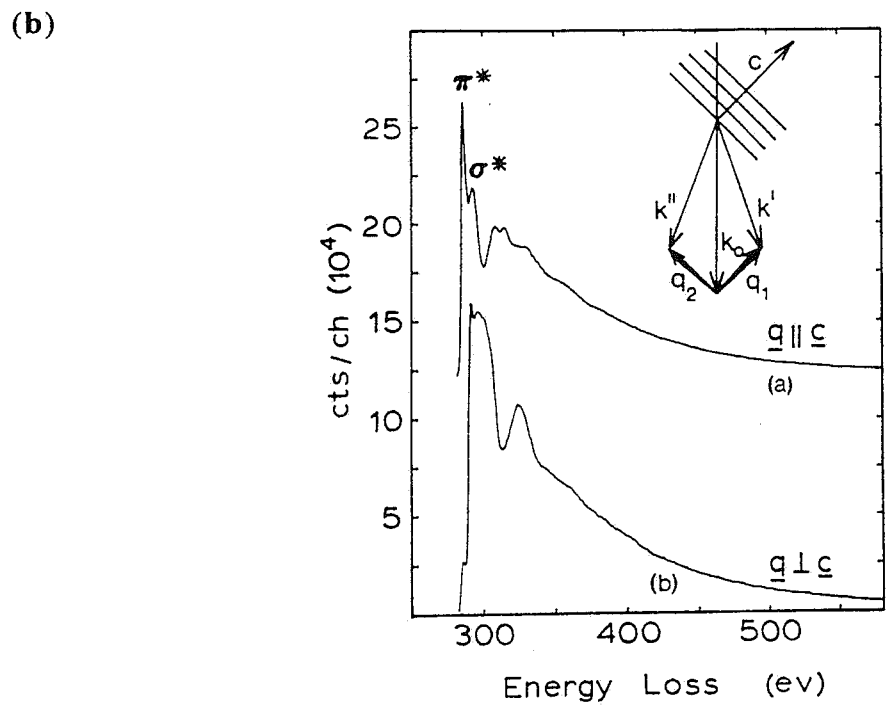

Fig. 4.6 (a) Graphite structure in terms of bonding chemistry (after Jaffe, 1988); (b) PEELS spectra from graphite at two different collection angles. Inset shows the scattering and collection geometry (after Disko *et al.*, 1982).

It is also clear from the above discussions that none of the PEELS spectra in the literature were collected when the *c*-axis of a h-BN crystal was physically perpendicular to the electron beam and the spectra collected from different diffracted beams favouring different peaks (the fourth extreme geometry). This geometry is explored in one of the h-BN crystal tilted parallel to $[11\bar{2}0]$ zone axis which contains (0001) type planes parallel to the electron beam, *i.e.*, ($c \perp e^-$). The indexed diffraction pattern is shown in Fig. 4.7(a). In Fig. 4.7(b) and Fig. 4.7(c), the spectra were collected when a small objective aperture was placed on the, the 0002 spot (Fig. 4.7(b)) and the $1\bar{1}00$ spot (Fig. 4.7(c)). The spectrum in Fig. 4.7(d) was collected without an aperture. The intensity of the π^* peak when the spectrum was collected from the 0002 spot was higher than when it was collected from $1\bar{1}00$ spot. Under the same collection conditions, the intensity of the π^* was the same for 0002 and $000\bar{2}$ spots. This shows that the intensity of σ^* and π^* peaks can be altered by choosing different diffracted beams in a similar way to methodology used by Disko *et al.* (1982) when the crystal is aligned parallel to $[11\bar{2}0]$.

The results for BN obtained throughout this study and the results reported in the literature for h-BN and graphite are summarised in Table 4.1.

The PEELS spectra shown in Fig. 4.5(a) were compared with BN spectra in the literature. The B *K*-edge from the circular inclusion showed that the π^* peak is at a lower height than the σ^* peak which is at a slightly higher (≈ 6 eV) energy loss. This was found to be identical *(i)* with a BN standard (obtained from a BN particle) in Ahn and Krivanek (1983), *(ii)* with the data reported by Hosoi *et al.* (1982) for hexagonal BN with the *c*-axis oriented parallel to the incident beam and *(iii)* with data taken at zero scattering angle by Leapman and Silcox (1979) on an h-BN specimen tilted at 45° to the *c*-axis. The B peak for disc-like inclusion (in which the intensities of π^* peak is at a similar height to the σ^* peak) is the same as the PEELS spectrum shown for a BN film in the standards published by Reimer *et al.* (1992). Unfortunately, the structure of test samples and the beam directions were not given in both the PEELS atlases (Ahn and Krivanek, 1979 & Reimer *et al.*, 1992), but most probably the structure of BN samples used were hexagonal since the PEELS spectrum from a cubic BN crystal does not show a π^* peak (Hosoi *et al.*, 1982).

Crystal orientation	π^* / σ^* ratio		Resolution	References
	>1	<1	(eV)	
q // c (C)§	√			Disko *et al.* (1982)
q ⊥ c (C)§		√		Disko *et al.* (1982)
c // e (C)	√		1.4	Leapman *et al.* (1983)
c // e^- (C)		√	2	Hosoi *et al.* (1982)
Thin C-film		√	2.1	Reimer *et al.* (1992)
c // e^- (C)		√	0.5-0.6	Cullen *et al.* (1993)
c ⊥ e^- (C)		slightly	0.5-0.6	Cullen *et al.* (1993)
q // c (BN)§	√			Leapman & Silcox (1979)
q ⊥ c (BN)§		√		Leapman & Silcox (1979)
BN particle		√		Ahn & Krivanek (1983)
c // e^- (h-BN)		√	4.5	Stephens & Brown (1981)
Tilted 45° (h-BN)	equal	equal	4.5	Stephens & Brown (1981)
c // e^- (h-BN)		√	2	Hosoi *et al.* (1982)
c // e^- (h-BN)	√		1.4	Leapman *et al.* (1983)
c // e^- (h-BN)	√		0.6	Martin *et al.* (1988)
BN-film	√		2.5	Reimer *et al.* (1992)
c ⊥ e^-	equal	equal	3	Fig. 4.5
c // e^-		√	3	Fig. 4.5

Table 4.1 Summary of ratios between π^* and σ^* peaks for graphite-like boron nitride (h-BN) and graphite (C) obtained by different researchers. Some available experimental details are also presented.

§ *The crystal c-axis is oriented 45° to the electron beam.*

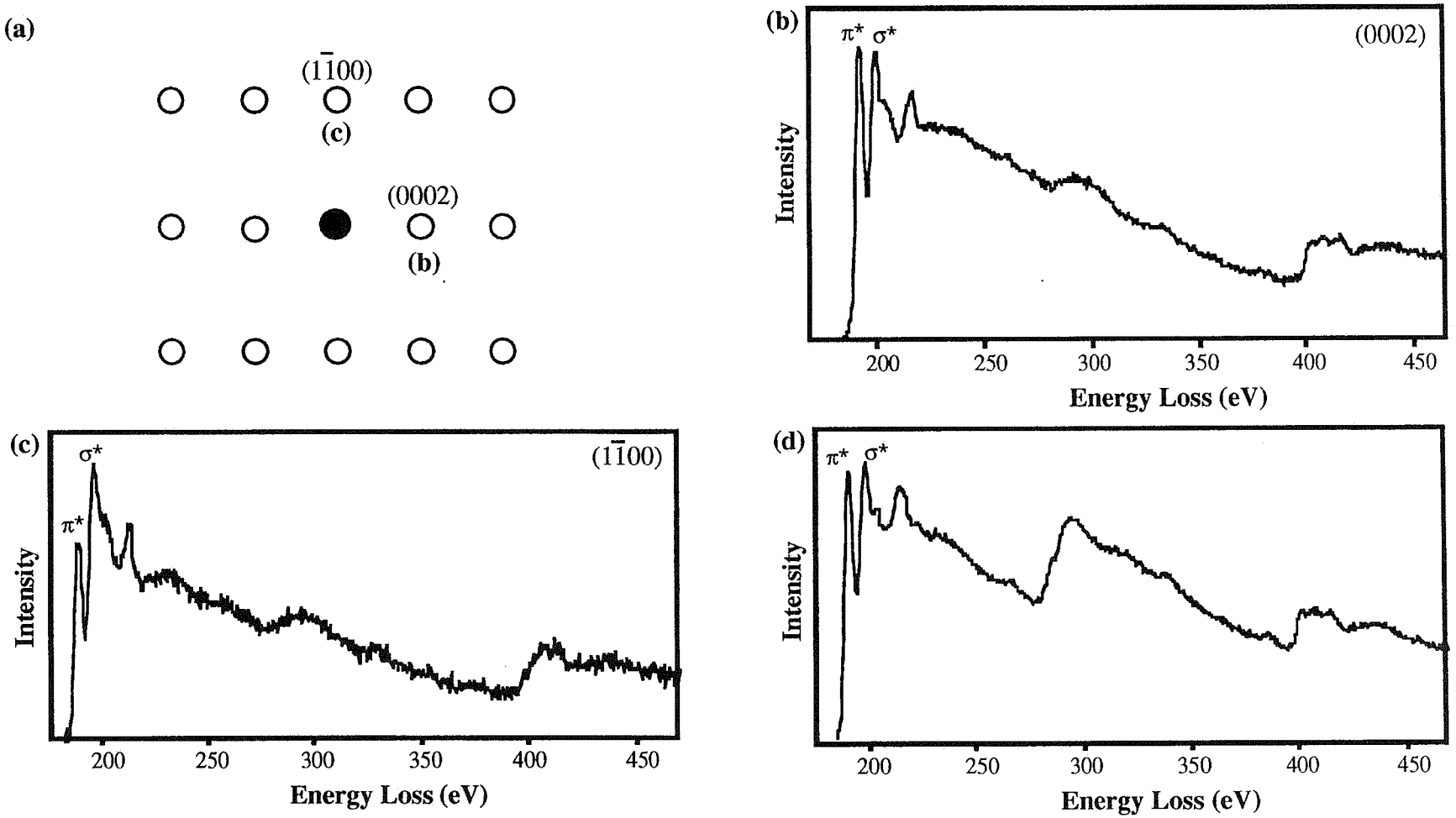

Fig. 4.7 (a) An indexed schematic [11$\bar{2}$0] diffraction pattern from an h-BN inclusion. PEELS spectra collected when the objective aperture was just covering the (0002) spot (b) and the (1$\bar{1}$00) spot (c), whereas (d) was collected without an aperture.

Hosoi *et al.* (1982) only obtained EELS spectra when the *c*-axis of graphite and h-BN was oriented parallel to the electron beam. Their result on h-BN is similar to the one obtained by Stephens and Brown, but the graphite spectrum is again opposite to that of Disko *et al.* (1982). Martin *et al.* (1988) studied the structure of h-BN when the *c*-axis of BN was parallel to the electron beam and found that the π^* peak is higher than the σ^* peak, in contradiction to Stephen and Brown (1981) & Hosoi *et al.* (1982).

In summary, these results show the effect of specimen orientation on the relative heights of the π^* and σ^* peaks, with the π^* peak increasing in intensity as a consequence of having the *c*-axis of the inclusion perpendicular to the electron beam under the same experimental conditions. The discrepancy on the relative intensities of the π^* and σ^* peaks summarised in Table 4.1 arise because of the different experimental conditions adopted in different studies. Unfortunately, in most of the cases all the details about the experimental parameters used are not given.

The parameters that could effect the relative intensities of the π^* and σ^* peaks are the crystal orientation with respect to the electron beam, the size of the spectrometer collection aperture (Colliex *et al.* (1985) mentioned that a large acceptance angle of the spectrometer mixes both the contributions), the magnitude of the camera length used if the spectra are collected in diffraction mode and the scattering angle used (Disko *et al.*, 1982). It is also worth noting that increasing the specimen thickness increases the background intensity at the same time as decreasing the peak intensity, but that multiple scattering caused by the increased specimen thickness will not contribute to the intensities of π^* and σ^* peaks (Colliex *et al.*, 1985 & Hall, 1992).

From these analysis, it is clearly established that only the hexagonal form of BN exists in the composites and that the B peaks in the PEELS spectra of h-BN exhibit a strong orientation dependence which is reasonably well understood.

4.2.3 Carbon layers in h-BN inclusions

The larger h-BN inclusions adjacent to SiC grains were found by high resolution transmission electron microscopy to be composed of a number of separate thin h-BN inclusions separated by layers with a partially disordered structure, an example of which is shown in Fig. 4.8(a). PEELS spectra collected on these layers are shown in Fig. 4.8(b) and Fig. 4.8(c) show carbon *K*-edges similar to those reported in the literature from evaporated amorphous carbon (Reimer *et al.*, 1992), but it is apparent from the structure of these layers shown in the high resolution electron microscope image in Fig. 4.8(a) that this carbon is more properly described as turbostratic carbon (Franklin, 1951). Note that the expected features in the near edge structure of turbostratic carbon was probably lost due to the poor energy resolution of the spectrometer. In contrast to these observations, no carbon layers were found adjacent to the h-BN inclusions if they were in contact with Si_3N_4 grains.

This result leads to the question *why BN is in graphite-like form while carbon is in turbostratic form?* The observation of turbostratic carbon and graphite-like BN is explicable in terms of the chemistry of these two materials.

Boron nitride exists in a variety of different crystal structures (graphite-like, zinc blende, wurtzite, turbostratic, *etc.*), but only the layered hexagonal turbostratic BN (t-BN) and graphite-like BN (h-BN) forms are stable at the fabrication temperature (2100°C) and pressure (200 MPa) of the Si_3N_4–SiC composites according to the pressure-temperature phase diagrams of BN (Bundy and Wentorf, 1963). Even if the structure of BN formed initially in the composite is t-BN, the transformation from t-BN to h-BN is favourable, since it has been shown in the literature (Thomas *et al.*, 1963) that when t-BN is heated at a high enough temperature ($\approx$ 2000°C), the structure evolves towards h-BN, analogous to the graphitization process in turbostratic disordered carbons. In the case of t-BN, the temperature of transformation to h-BN can be lowered by the presence of trace B_2O_3 (Thomas *et al.*, 1963). After cooling from the hot isostatic pressing temperature of 2100°C, h-BN is therefore the favoured form of BN.

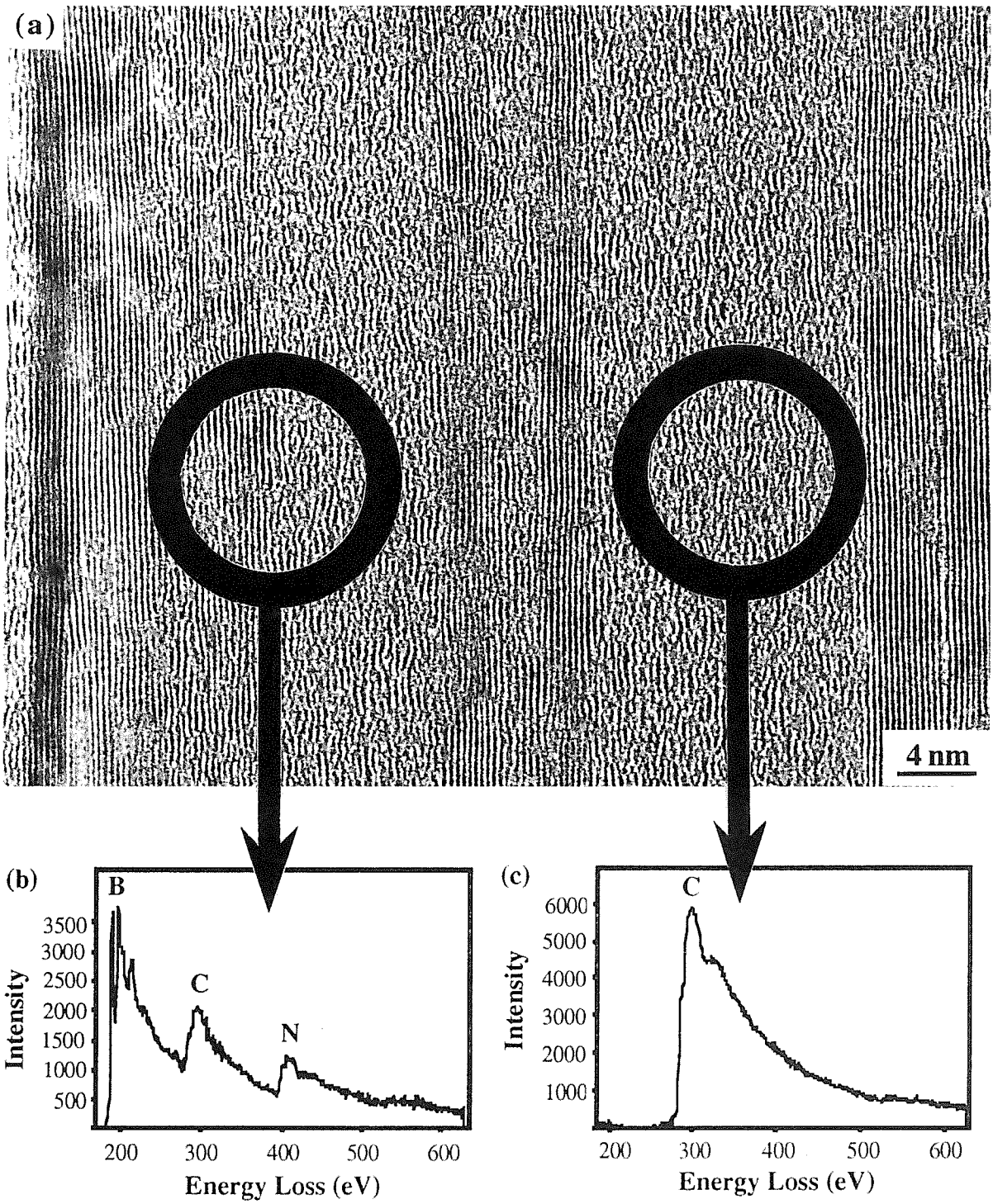

Fig. 4.8 (a) High resolution transmission electron microscope image at Scherzer defocus of a large BN inclusion containing turbostratic carbon layers;
(b) PEELS spectrum from a region including h-BN and the carbon layers;
(c) PEELS spectrum from the carbon layers alone.

Graphitization of carbonised materials takes place between 1000°C and 3000°C depending on the type of carbon, chemical composition and applied pressure during graphitization (Pacault, 1971). The graphitization experiments of Rouzaud and Oberlin (1989) on a highly graphitizing anthracene-based semi-coke showed that a microstructure similar to the one shown in Fig. 4.8(a) is obtained at temperatures up to 1500°C and that above 2100°C defect free flat graphite layers were obtained. Therefore, at the fabrication temperatures of the composites, completely graphitized defect free carbon layers would be expected. However, the ability for a carbonaceous material to graphitize increases as oxygen to hydrogen ratio of the carbon decreases. Thus, while complete graphitization is obtained from anthracene coke at 2100°C, the graphitization temperature is 3000°C for saccharose coke which is rich in oxygen (Rouzaud and Oberlin, 1989). While the hydrogen content of the composites is unknown, the presence of oxygen in the composite as an impurity will not be conducive to the formation of graphitic carbon and instead is more likely to favour the formation of turbostratic carbon, as has been observed.

4.2.4. Morphology and size of the inclusions

The most prominent features of the inclusions are their long fibrous morphology. The diameters of the inclusions varied considerably between 0.1 μm and 1.5 μm, although most lay in the 0.5 – 0.7 μm range. The thickness of the inclusions ranged between 30 – 250 nm, with most in the 60 – 100 nm range. The inclusions shown in Fig. 4.1(a) and (b) are thus two of the smaller inclusions observed. Their thickness were more stable than their diameter throughout the composite suggesting that the growth is faster in the *a*-axis direction than in the *c*-axis direction.

Whenever two inclusions found together, they were morphologically twinned, *i.e.*, their thickness and the diameters were nearly the same. The inclusions found in pressureless sintered commercial SiCs (Hexoloys) have irregular shapes and are mostly situated at triple junctions (Fig. 4.9). These observations shown in Figs. 4.1 and 4.9 agree well with the literature reports that the inclusions have disc-like morphology in hot isostatically pressed SiC-based materials (Braue *et al.*, 1989 & Braue, 1992), whereas they have irregular morphology in pressureless sintered materials (Hamminger, 1989 & Braue and Carpenter, 1990).

4.2.5 Stacking faults and dislocations in h-BN inclusions

HREM images of h-BN inclusions exhibited a highly faulted structure. It was also evident in the diffraction patterns of h-BN that {0002} type diffraction spots were streaked and that they were extended and curved perpendicular to the streaking direction. From the occurrence of streaks in the diffraction pattern (Fig. 4.10(a)) it is apparent that the h-BN crystal has one-dimensional disorder similar to graphite, *i.e.*, the stacking of the sheets are imperfect. The curves at {0002} type spots indicate that the crystal is not fully ordered and that there are rotations between the successive layers. Fig. 4.10 is a typical example of such a diffraction pattern obtained from an inclusion, together with the corresponding HREM image of the same inclusion. Stacking faults can be easily seen in the image, but they are not regular and this results in the streaking effect parallel to $g = 0002$.

In layered structures, the binding forces between atoms in the layers are much stronger than the binding forces between atoms in adjacent layers. For example, in graphite, slip occurs readily in planes parallel to the layers and is almost impossible in non-layer planes. Therefore, the dislocation arrangements and Burgers vectors are confined mainly to the layer planes. The weak binding between layers can also result in stacking faults of low energy and hence unit dislocations are usually widely dissociated into partial dislocations (Hull and Bacon, 1984). For example, in graphite, packing faults consisting of random displacements of the layers perpendicular to the *c*-axis have been observed (Hoffman and Wilm, 1936).

Due to the stacking arrangement of graphite crystals (..ABAB..), there is an alternative position for the B atom to position itself over a A atom - a C position (since the stacking of A on A has prohibitively high energy and will not occur) and so graphite can contain a region of crystal arranged in the rhombohedral stacking sequence.

It is the usual practice to relate the behaviour of BN to graphite. However, this resemblance often fails. For example, h-BN does actually take the ..AAAA.. stacking sequence which will never occur in graphite because of the high energy associated with it. This gives even more alternative positions for the second layer atom resting on a first layer A atom, *i.e.*, B and C positions.

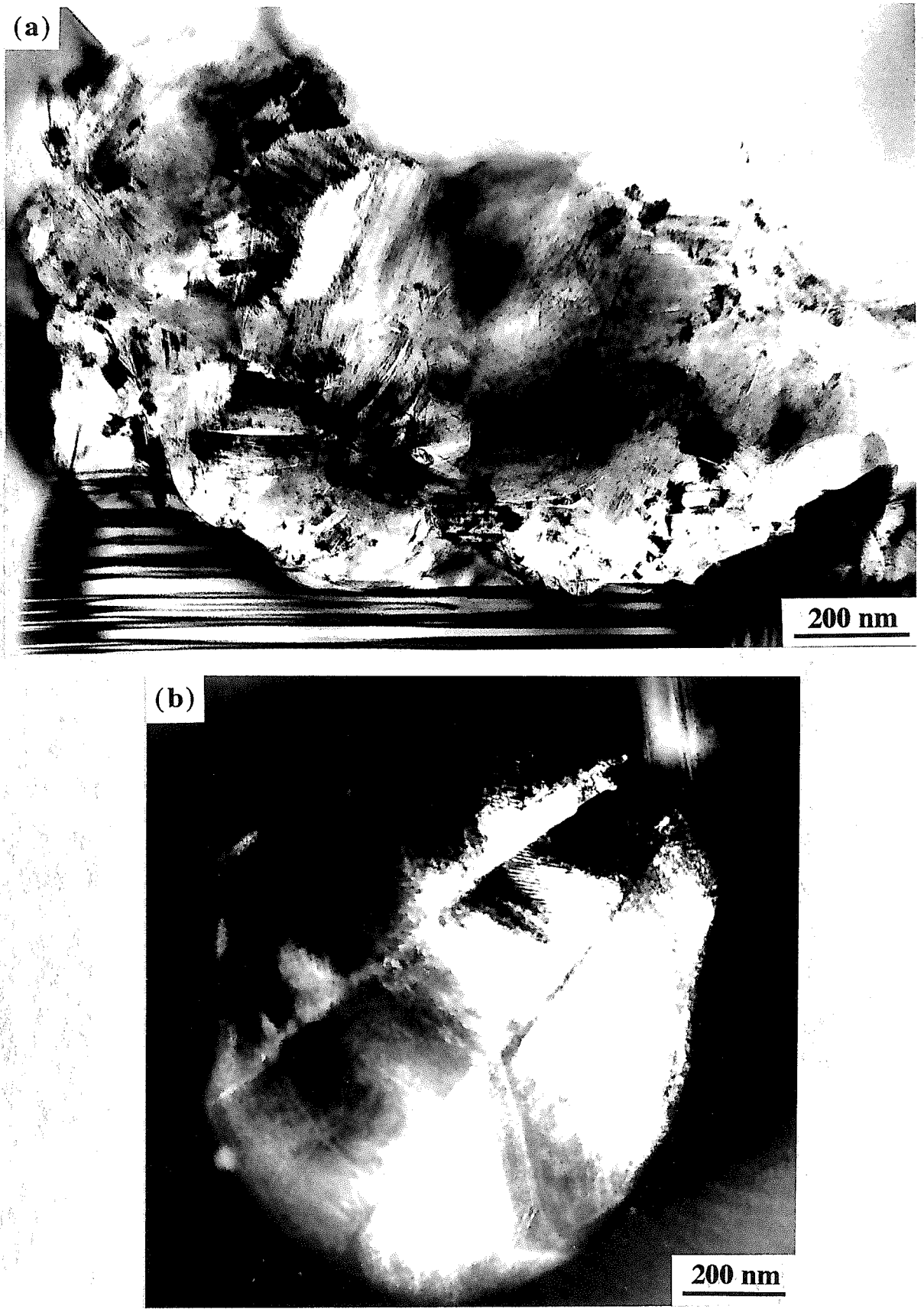

Fig. 4.9 (a) Bright field and (b) dark field TEM images of graphite inclusions observed in pressureless sintered Hexoloy SA SiC ceramics.

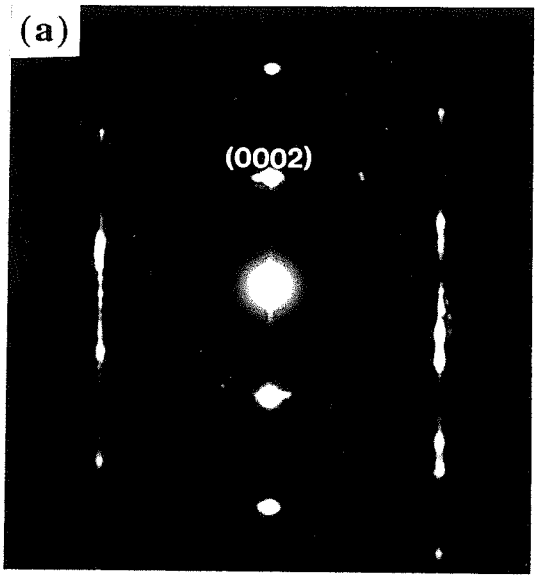

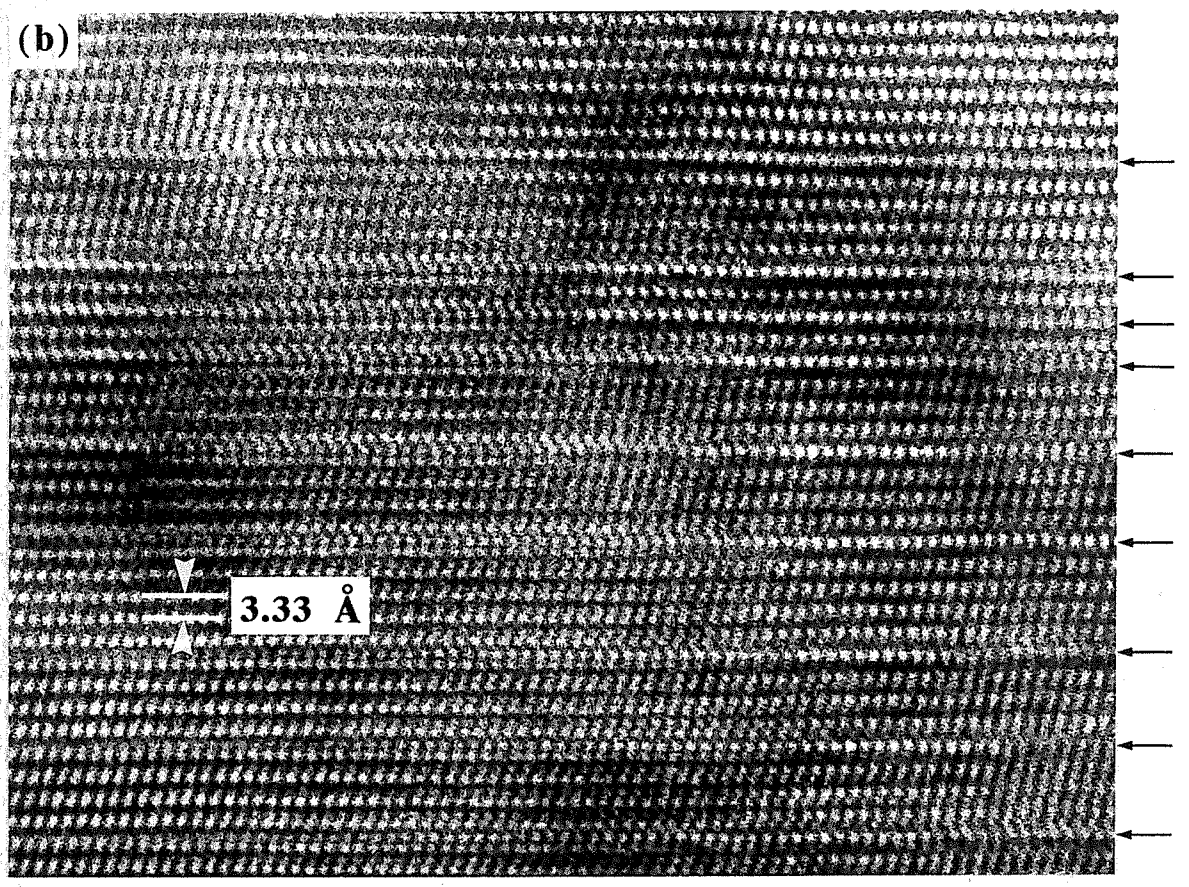

Fig. 4.10 (a) A diffraction pattern from a BN inclusion when the electron beam is parallel to [11$\bar{2}$0] zone axis where the streaking along {0001} type of planes and curvatures perpendicular to streaking direction can be clearly seen; (b) a HREM image obtained from the same inclusion showing the stacking faults marked by arrows.

4.2.6 Delamination Cracks

The other feature of the inclusions is that they show a delaminated fibrous texture with delamination voids separating the fibres and with strands consisting of few basal planes connecting the fibres together (Fig. 4.11(a)). The tilt angle between (0001) planes of the fibre and strands seen in 4.11(a) is 25°. In Fig. 4.11(b), the delamination cracks have been observed with thicker strands holding the delaminated fibres. In this case, the angle is 41°.

The delamination cracks might originate during crystal growth or under the subsequent compression or shear stresses. The stresses can be created by the linear thermal expansivity differences between SiC/Si_3N_4 and h-BN as well as due to the anisotropic linear thermal expansion behaviour of h-BN (Pease, 1952), since the thermal expansion coefficient (α) of h-BN in *c*-axis is 40.5×10^{-6} /°C and zero along *a*-axis at 770°C (and only 0.95×10^{-6} along *a*-axis at 2100°C). The thermal expansion coefficients of 6H-SiC between 0-423°C in the *a*- and *c*-axis directions are 4.2 and 4.68×10^{-6} K^{-1} respectively, whereas those of β-Si_3N_4 between 0-1000°C are 3.23 and 3.73×10^{-6} K^{-1}, respectively (Lee and Rainforth, 1994). Therefore, on cooling down from the fabrication temperatures of the composite, h-BN inclusions would undergo a considerable contraction in *c*-axis direction relative to the basal plane. The resultant effect of this anisotropic contraction is the delamination and microcracking of h-BN discs during cooling after sintering. However, during service conditions, the expansion of the discs along *c*-axis due to the rapid temperature changes can be accommodated by closure of the gaps between them and little change in the thermal expansion of the bulk specimen is expected and the composite can absorb the stress energy.

This property of h-BN could be used to improve the thermal shock resistance of the matrix. Indeed, it has been shown that the addition of more than 5 vol% h-BN into ceramic matrices like mullite, alumina (Goeuriot-Launay *et al.*, 1986) and Si_3N_4 (Lutz and Swain, 1992) have increased the thermal shock resistance of the ceramic matrix composites by having a little change in the expansion of the composite since the expansion can be accommodated by the closure of the cracks formed upon cooling. Both sets of researchers also found that thermal shock resistance of the composites increases with the increasing vol% of h-BN addition. Such cracks in h-BN grains were observed in BN related composites like BN-SiC, BN-SiAlON, BN-Si_3N_4 (Sinclair and Simmons, 1987) and BN-B_4C (Ruh *et al.*, 1992). However, one should not forget the possibility that the cracks could have been introduced during the sample preparation stage.

The other reason to incorporate h-BN into matrices is to improve the fracture toughness of the matrix material because of its high temperature stability and inertness against C and CO and most other ceramics up to 1800°C. Because of its non-wetting properties it is also stable to attack by molten glass, molten Si, B, nonoxidising slags, molten salts and reactive metals like Al, Fe, Cu and Zn. In addition, its high electrical resistivity and high thermal conductivity make h-BN a very attractive material to be used in the fields of semiconducting components and ceramic matrix composites. h-BN is also a very promising material to replace graphite since the oxidation of h-BN in air starts at 800°C, whereas that of graphite is already significant at 600°C. For example, it has been shown (Lowden and More, 1990) that h-BN could be used as an interface material, *i.e.*, as a thin film, between the fibre and the ceramic matrix, acting as a mechanical fuse to protect the fibre against the notch effect due to microcracking arising in the matrix. The h-BN interface has a mechanical behaviour similar to pyrolytic carbon with a much higher resistance to the environmental parameters.

The addition of h-BN has also been shown to improve the fracture toughness of oxide matrix composites by microcracking and or crack-particle interaction mechanisms (Rice *et al.*, 1980, Lewis *et al.*, 1981 & Lewis and Rice, 1981). The h-BN flakes have an easy cleavage plane, and elastic and thermal mismatches with the matrix produce high local residual stresses providing crack-particle interaction and the potential for microcracking. In contrast, the fracture toughness of Si_3N_4 matrix composites decrease with the addition of h-BN due to the increasing porosity associated with h-BN content (Lutz and Swain, 1992).

Fracture toughness of the Si_3N_4-SiC composites studied in this work are quoted (S.M. Winder, private communication) to be higher than monolithic SiC (Hexoloy SA) and lower than TiB_2 particulate reinforced SiC (Hexoloy ST). The fracture toughness of Hexoloy SA and ST are 4.6 and 8.0 $MPam^{-1/2}$, respectively (data taken from the introductory leaflet of Hexoloy materials from Carborundum). Although the increase in fracture toughness is attributed to the thermal expansion differences between SiC and Si_3N_4, the difference is not really high enough to cause an increase in the fracture toughness of the composite.

The fracture toughness measurements have not been undertaken in this study because of the very small nature of the supplied materials, but observations of accidentally broken TEM samples revealed very interesting results. Disc-like h-BN inclusions, Si_3N_4 precipitates and

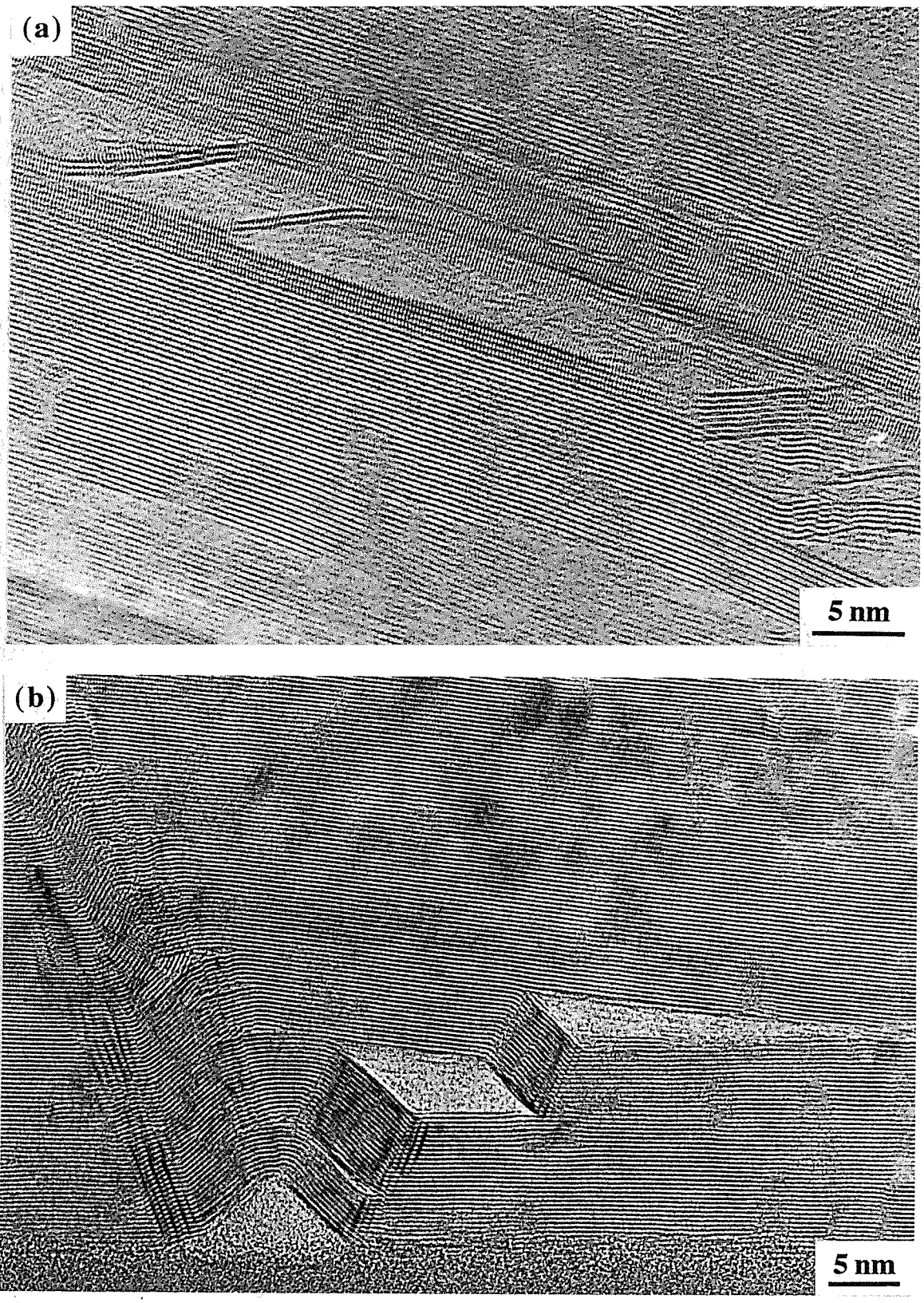

Fig. 4.11 (a) and (b) High resolution transmission electron microscope images at Scherzer defocus of h-BN inclusions show the examples of delamination cracks. The composition of the material filling the cracks is unknown.

twinned SiC grains were found to be deflecting the cracks along their elongation axis. A TEM micrograph showing this phenomenon clearly for an inclusion is shown in Fig. 4.12. Crack deflection at the interfaces can increase the fracture toughness of the composite and the inclusions can act as effective crack blunting elements and make the material tougher. Toughening by crack deflection can be achieved with long enough disc-like grains embedded in a matrix with a weak interface to allow crack deflection at the same time strong enough to transfer the load from matrix to the reinforcing agent. It is found (Tighe *et al.*, 1986) that although h-BN additions may contribute to the toughness, the thermal, mechanical and corrosion stresses will cause strength degradation since h-BN is unstable in oxidising atmospheres.

It is also obvious in Fig. 4.12 that BN planes are bent the same as the cracks and strands observed in Fig. 4.11(a and b). This raises the question as to whether *these so-called misorientation bands have special crystallographic features associated with the internal structure of h-BN.*

These misorientation bands could be identified as deformation bands, kink bands or deformation twins depending on the morphology and the crystallography between the bands and the main inclusions. Therefore, it is relevant to review the differences between possible misorientation bands to establish the identity of the bands observed in this study.

4.2.7 Introduction to misorientation bands

4.2.7.1 Deformation bands

Inhomogeneous deformation results in regions of different orientation called deformation bands (Dieter, 1986). The tendency to form deformation bands is greater in polycrystalline specimens because the restraints imposed by the interfaces make it easy for orientation differences to arise in a grain during deformation. Deformation bands generally appear irregular in shape but are elongated in the direction of principal strain. The outline of the bands is generally indistinct and poorly defined, indicating a general fading out of the orientation difference. Deformation bands have been observed in both f.c.c. and b.c.c. structures but not in h.c.p. metals.

4.2.7.2 Twinning

Twinning results when a portion of the crystal takes up an orientation that is related to the orientation of the rest of the untwinned lattice in a definite crystallographic manner. The twinned portion of the crystal is a mirror image of the parent crystal with the plane of the mirror is called the twinning plane. Twins may be produced during growth from vapour, liquid or solid, by mechanical deformation or as the result of annealing following plastic deformation. Twinning occurs in a definite direction on a specific crystallographic plane for each crystal structure and generally occurs when the slip systems are restricted or when the critical resolved shear stress is increased so that the twinning stress is lower than the stress for slip. A formal description of twinning crystallography will be presented in Appendix 4.1.

4.2.7.3 Kink bands

Consideration of the equation for critical resolved shear stress shows that it will be difficult to deform a hexagonal crystal when the basal plane is nearly parallel to the crystal axis (Dieter, 1986). Orowan (1942) found that if a cadmium crystal of this orientation is loaded in compression it would deform by a localised region of the crystal suddenly snapping into a tilted position with a sudden shortening of the crystal. This phenomenon is called buckling or *kinking*. Distortion of the crystal is essentially confined to the kink band. Hess and Barrett (1949) concluded that the interfaces of a kink correspond to a localised and symmetric bending of the structure about an axis that lies in the slip plane and normal to the slip direction and that kink bands can be considered to be simple types of deformation bands. In h.c.p. crystals slip predominantly occur on the (0001) $<11\bar{2}0>$ system, and the kinking (bending) axis will be $[1\bar{1}00]$ and the habit plane of the symmetric kink is initially $\{11\bar{2}0\}$ although as the bending increases the composition plane will depart from this orientation (Crocker and Abel, 1976).

Kinking is a secondary process being initiated by slip and in many cases occurs as an accommodation mechanism for twins (Crocker and Abel, 1976). It also helps to relieve stresses set up by twin formation. Kinking, therefore, occurs as a secondary deformation mechanism in the crystals of any symmetry class. For example kink bands were observed in

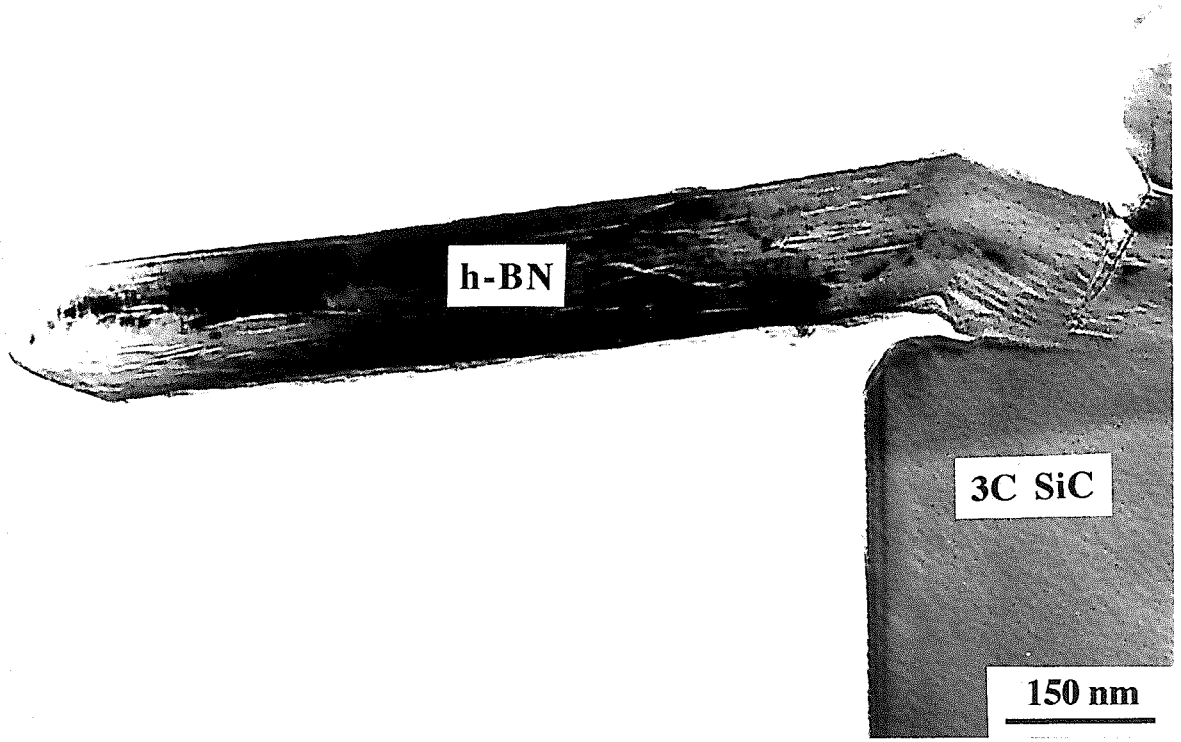

Fig. 4.12 A TEM image of an accidentally broken sample showing the crack deflection ability of h-BN inclusions.

metals of h.c.p., f.c.c. and b.c.c. structures, ceramics such as 6H-SiC (Suematsu *et al.*, 1991), rock forming minerals (Nicolas and Poirier, 1976), ore forming minerals like graphite and fibre reinforced composites. Materials with a layered structure very frequently exhibit kink bands when subjected to deformation. The morphology of kinks is less well defined than that of slip lines and twins. The misorientation bands which end in the material are wedge shaped. The wedge shaped misorientation bands is provided by the accommodation layer of neighbouring twin boundaries. It is also considered that kink bands are special forms of deformation bands in which slip take place on a single plane (Carter *et al.*, 1964).

Although the most important deformation modes of slip and twinning are well established and have their crystallographic descriptions (Christian, 1975), the crystallography of kinking has had very little attention. The kinking models have been developed by a number of researchers. A general theory of kinking was developed that a pair of kink band boundaries is composed of single walls of dislocations of opposite sign (Frank and Stroh, 1952). Starkey (1968) developed a simple geometrical model and this model later was extended to cover coincident site lattice model of grain boundaries (Baronnet and Olives, 1983). Crocker and Abel (1976) have tried to describe kink bands in the same way as deformation twins are formally described and they established compound type kinking in h.c.p. crystals. However, the models are based and tested in sharp kink interfaces observed by optical microscope images. Optically very sharp kink interfaces may be characterised by a more gradual, continuous change in orientation on the microscale.

Starkey established that the angle (δ) between the planes of host crystal and the kink interface plane is the same as the angle (ε) between kink band planes and the kink interface plane and determined by:

$$\mathrm{Tan}\,\delta = \frac{dT}{\frac{1}{2}(n.vt)} \qquad (4.1)$$

where dT is the lattice spacing of the plane, vt is the lattice vector parallel to the compression axis and n is an integer. A representative diagram of Starkey's model is shown in Fig. 4.13.

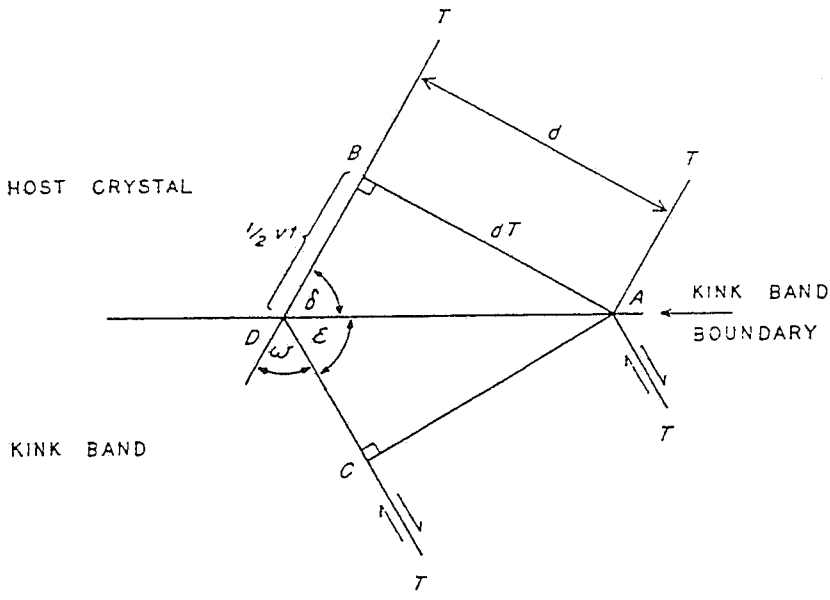

Fig. 4.13 The idealised geometry at a kink boundary (after Starkey, 1968).

The geometry proposed by Evans and Adler (1978) is shown in Fig. 4.14. According to this geometry a kink inclination angle (α) should be equal to about twice the kink boundary orientation (β), with β ranging between 20 and 30°. They have detected three principal modes of kinking in C-C composites, which are kinking due to longitudinal compression, lateral displacement (shear) and lateral compression. The kink morphologies for longitudinal compression and lateral displacement are found to be very similar.

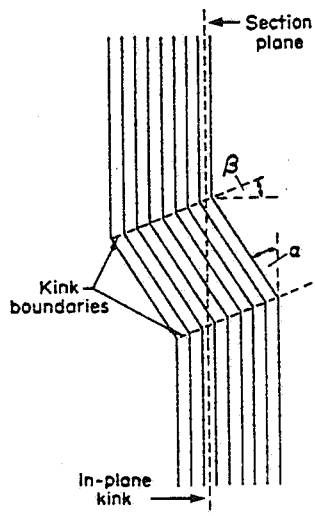

Fig. 4.14 A schematic indicating the morphology of kinks. The kink orientation (α) and the interface orientation (β) are indicated (after Evans and Adler, 1978).

In summary, twin boundaries are well defined and have special orientation-relationships, whereas deformation bands appear irregular and the interfaces are poorly defined. On the other hand, kink bands are neither well defined nor poorly defined and the crystallography is not well established in comparison to twinning. A comparison of these three principal misorientation mode is shown in Fig. 4.15.

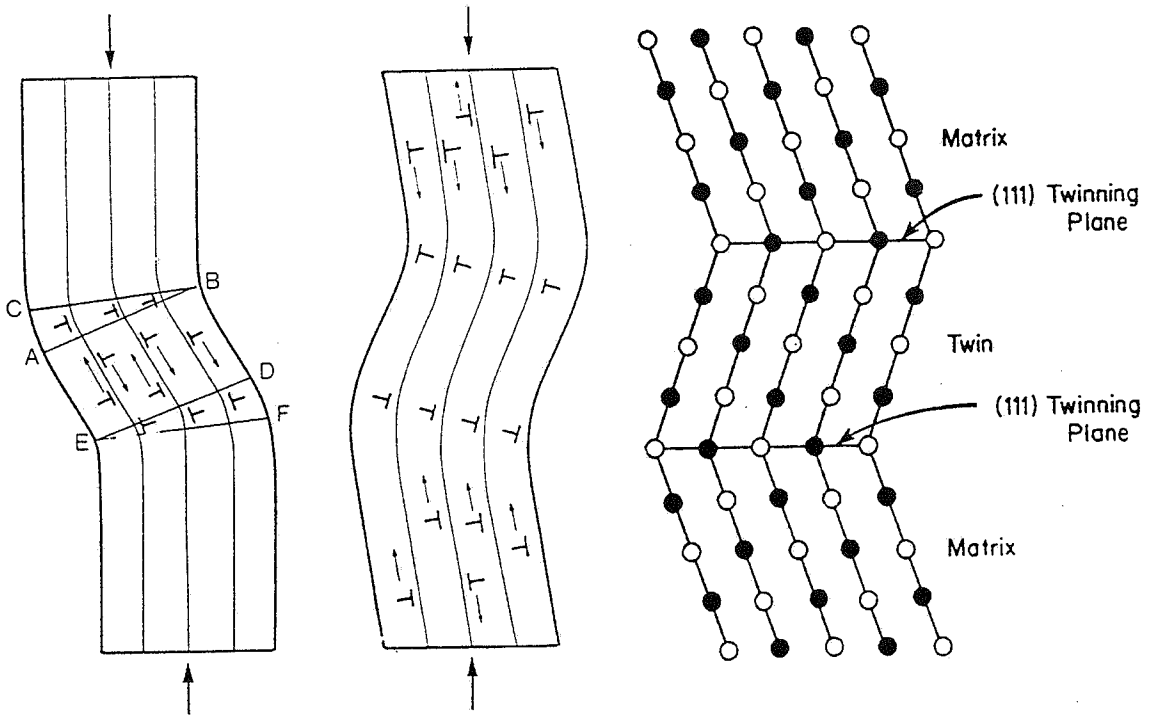

Fig. 4.15 Structures of an ideal (a) kink band; (b) deformation band and (c) twin band in f.c.c. structure.

4.2.7.4 Observations of Misorientation Bands

Delamination voids (or cracks) of various types have been observed in h-BN crystals as shown in Fig. 4.11. Similar voids but on the macroscale have been observed in graphite by Freise and Kelly (1963) & Soule and Nezbeda (1968). Freise and Kelly used Stroh's argument (Stroh, 1958) to explain the origin of these cracks that any attempt to produce a shear on the basal planes across a bend plane or across a twin must for geometrical reasons open up a crack. This supports their experimental observations that the cracks were generally observed at twinned regions. On the other hand, Soule and Nezbeda (1968) proposed that

the origins of the voids can be divided into two categories. Examples of delamination voids in layered crystals are shown in Fig. 4.16(a, b, c and d). The first category (a) might be created during crystal growth and the second category (b, c and d) might have been caused by subsequent compression or shear stresses.

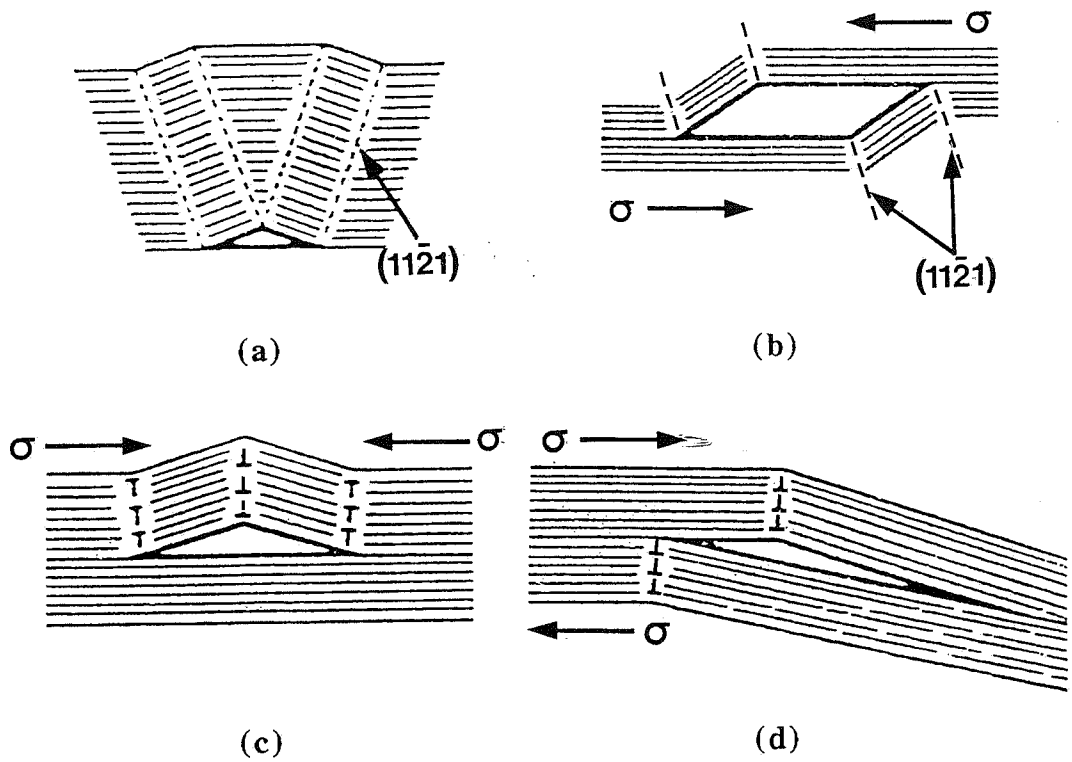

Fig. 4.16 Examples of delamination voids in graphite as viewed parallel to the basal plane. (a) is formed by the triangular confluence of (11$\bar{2}$1) double twins during crystal growth (Palache, 1941); (b) is caused by the separation of a (11$\bar{2}$1) double twin under a shear stress (Freise and Kelly, 1961); (c) can be produced by compressional stress or by a stress where one side is pinned down by an impurity or other imperfection; (d) this type is due to Stroh (1958).

Examples of misorientation band formation associated with cracks from my own work are shown in Fig. 4.11(b) and 4.17. The schematic view of Fig. 4.11(b) is shown in Fig. 4.18. These bands are called triangular conjugate bands due to their shapes. The fact that both the misorientation bands in Fig. 4.18 make an angle of 139° with respect to the basal planes and that this is the same as in Fig. 4.11(b) indicates that these bands are likely to have certain crystallographic orientation relationship.

Twinning occurs in graphite. Freise and Kelly (1961) determined precisely the angular relationship between the graphite parent lattice and its twin. They found that the two lattices can be derived one from another by a rotation of 20.48° about an axis parallel to $[1\bar{1}00]$. The twin plane is found to be $(11\bar{2}1)$. The twin components for graphite are;

$$K_1 = (1\bar{2}11),\ \eta_1 = [\bar{1}2\bar{1}6],\ K_2 = (0001),\ \eta_2 = [\bar{1}2\bar{1}0],\ g = 0.37$$

The twins correspond to regions separated from the matrix by bend planes of a specific angle and a low energy. Bend planes with the axis of bending lying in the basal plane are produced when a crystal is deformed. The twins are not formed by a shear parallel to the composition plane but parallel to the K_2 plane conjugate to this. In such layered structures, twinning based on the motion of dislocations would not occur other than in the basal planes since it is necessary to break the strong bonds between the atoms in the same layer in order for shear to take place. Therefore, the formation of twins was attributed to a shear parallel to K_2 rather than K_1.

Although the twinning in graphite has been studied in detail, there have been relatively few studies on the twinning of h-BN. The structural difference between h-BN and graphite suggest that the twinning laws need not be the same. Indeed, Kurdymov *et al.* (1976) showed that the twinning plane of h-BN is different from that of graphite and the twinning plane is $(1\bar{2}12)$. This generates an obtuse angle of 139° between the (0001) planes of the h-BN matrix and the (0001) planes of its twin (and therefore a tilt angle of 41°). The twin components for h-BN are;

$$K_1 = (1\bar{2}12),\ \eta_1 = [\bar{1}2\bar{1}3],\ K_2 = (0001),\ \eta_2 = [\bar{1}2\bar{1}0],\ g = 0.75.$$

A projection of the structure of h-BN and its twin on the $(1\bar{1}00)$ plane is shown in Fig. 4.19.

Bonnet *et al.* (1981) used the n-CSL concept to interpret the twin relations in graphite. They found a $\Sigma = 17$ around [210] description with 40.12° for a $(c/a)^2$ of 15/2 for the twin relation described by Freise and Kelly (1961). Following this, Knowles (unpublished work) produced n-CSL data for h-BN by adopting the same procedure applied by Bonnet *et al.* (1981). His analysis showed that the twin relation proposed by Kurdymov *et al.* (1976) can be identified as a $\Sigma = 8$ around [210] with 41.38° for a $(c/a)^2$ of 7.0639.

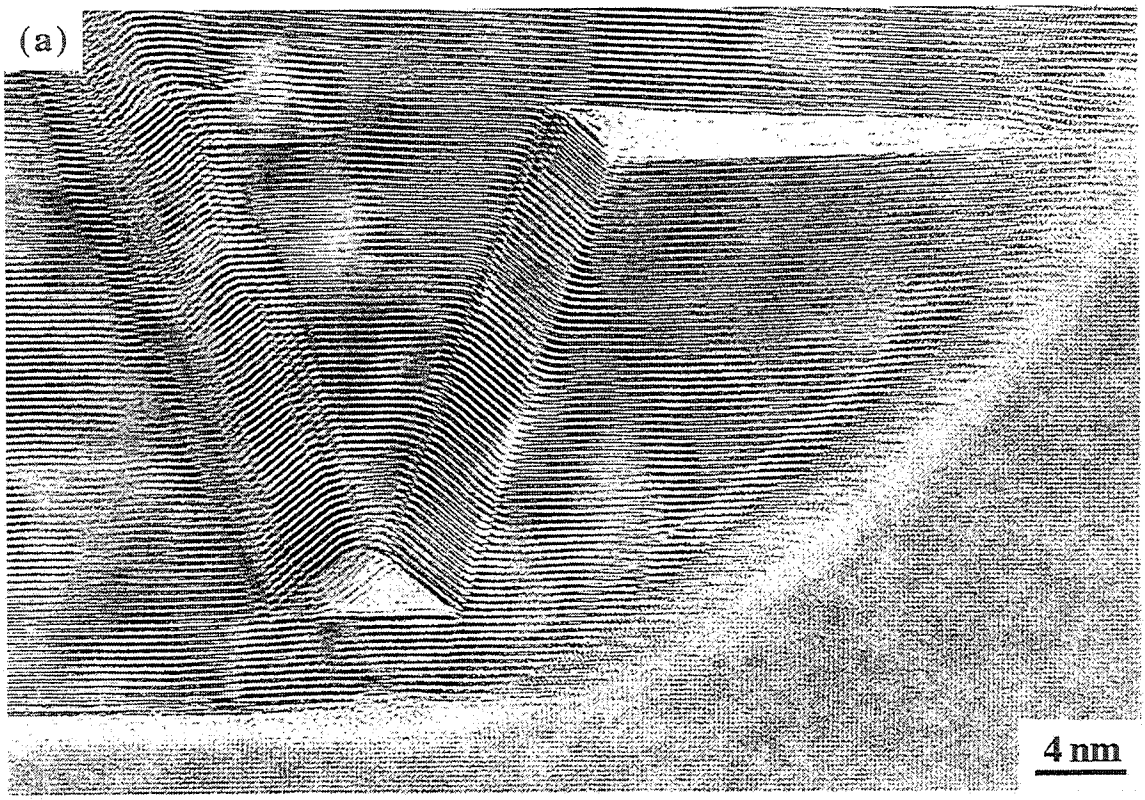

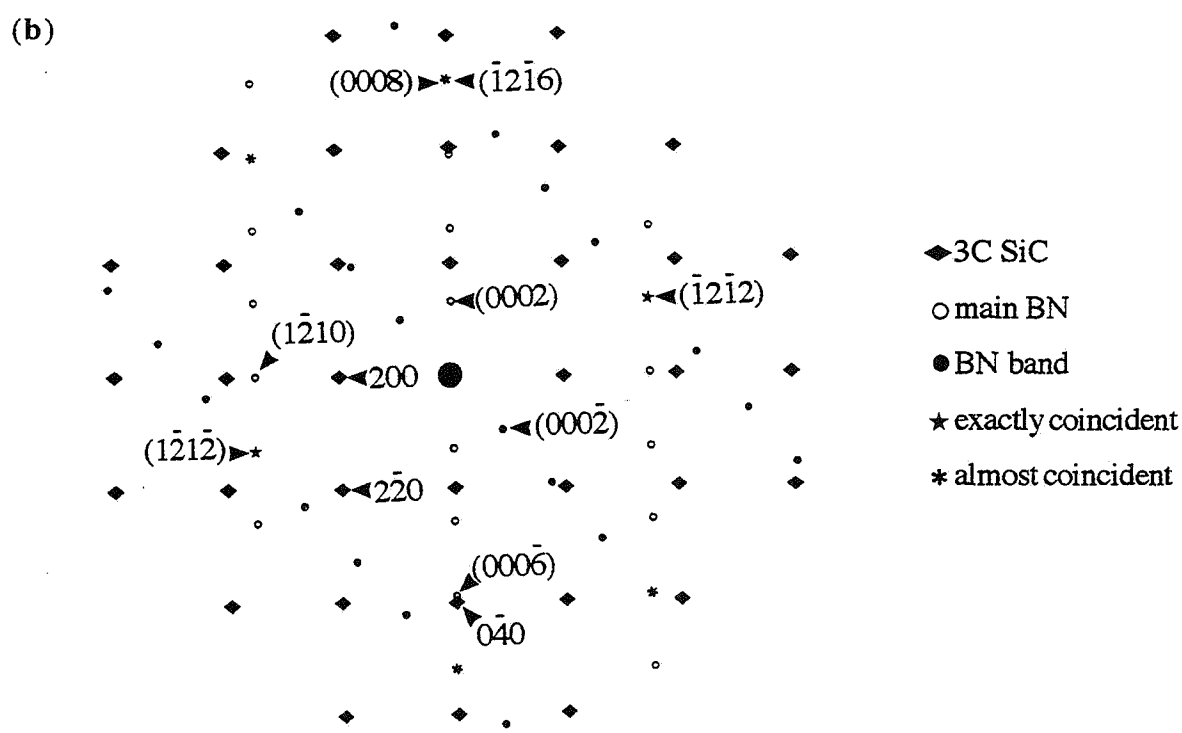

Fig. 4.17 (a) Other example of delamination voids and misorientation bands observed in h-BN inclusions surrounded with SiC. (b) Indexed schematic diffraction pattern from the bands and the surrounding 3C SiC grain.

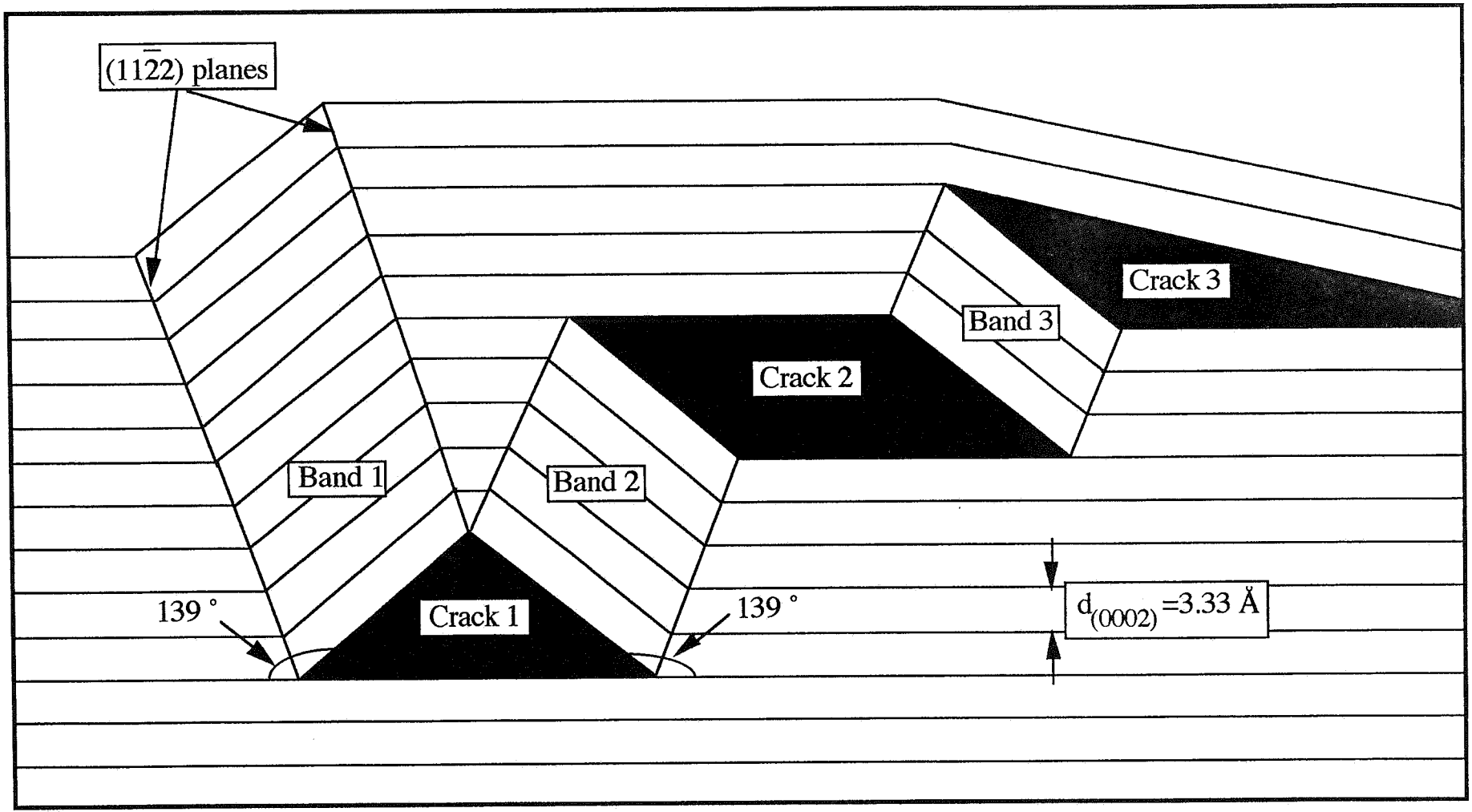

Fig. 4.18 Schematic representation of cracks and misorientation bands observed in h-BN inclusions in Figs. 4.12(b) and 4.17(a).

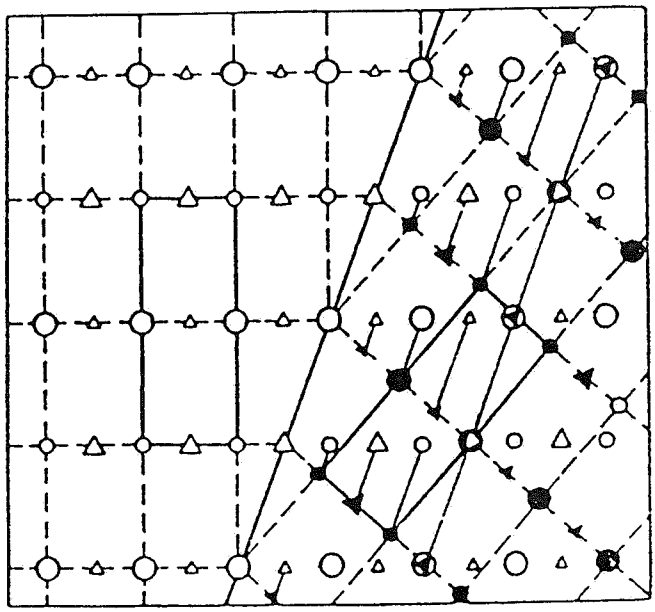

Fig. 4.19 Twinning scheme in h-BN as proposed by Kurdymov *et al.* (1976). The light circles and triangles of smaller dimensions give the positions of the B atoms, the larger ones represent the N atoms in the original structure. The dark symbols give the positions of the same atoms after shear.

The experimental observations of Fig. 4.11(b) match very well with the above analysis of twin relationships in h-BN that the (0001) type planes of bands have an angle of 139° with the (0001) planes of main inclusion as expected theoretically. The experimental analysis of possible kink band formation in line with Starkey's analysis showed that the theoretically expected kink angle calculated using the lattice parameters of h-BN in equation 4.1 is 139° which is the same as the twinning angle. The h-BN inclusion in Fig. 4.17 is aligned parallel to $[1\bar{1}00]$ zone axis which contains (0002) planes perpendicular to $(11\bar{2}0)$ planes. The 1.25 Å *d*-spacings of $(11\bar{2}0)$ planes are below the resolution limit of the microscope (≈ 1.7 Å) and so they cannot be imaged in the electron microscope. From these analysis the bands can be identified as either conjugate kink bands or conjugate twin bands.

Theories of kinking of anisotropic rocks have been discussed by Price and Cosgrove (1990). Cobbold *et al.* (1971) produced conjugate kink bands experimentally by compressing a multilayer of plasticine parallel to the layering and suggested that initiation of kink bands occurs at a local irregularity in the layering. They concluded that kink bands will develop in materials with a high mechanical anisotropy. Such irregularities exist in h-BN

inclusions in the form of dislocations where the Burgers vector is perpendicular to the layering. This leaves behind an unanswered question of *how the compression develops parallel to the layering in these inclusions.*

Consideration of Fig. 4.16 reveals that the bands in Figs. 4.11(b) and 4.17 could form during the growth process or due to the compressive stresses developed during the cooling from the fabrication temperatures. Although the crack shapes are the same in Fig. 4.16(a) and (b), the resulting bands have different shapes in that the interfaces formed due to the new geometry are parallel to each other in Fig. 4.16(a), whereas the interfaces are growing apart from each other in Fig. 4.16(b). If the bands develop because of the compressive stresses during cooling then their formation would be unavoidable in every single inclusion. This was not found to be the case experimentally, but it is important to note that in order to observe these bands the inclusion should be aligned parallel to the $[1\bar{1}00]$ zone axis. Therefore, the void indicated as *crack 1* in the schematic of Fig. 4.18 is formed by the triangular confluence of $(11\bar{2}2)$ double twins (conjugate twinning). The twinning plane $(11\bar{2}2)$ gives an angle of 139° between the (001) planes of the matrix and twin. Freise and Kelly (1963) postulated that a high concentration located at the internal tip of this configuration should nucleate a cleavage crack as is observed in the both experimental micrographs. However, the crack shapes are different in the micrographs. In summary, h-BN inclusions have been observed and distinguished from being graphite using PEELS technique. These h-BN inclusions displayed a strong orientation dependence in the PEELS spectra, the ability to form microcracks and the ability to deflect cracks at the interfaces. The microcracks are associated with twin and kink bands.

While all these observations are interesting, boron nitride is not deliberately added to the composite either as a sintering additive or to improve the properties of the composite material (S.M. Winder, private communication). Therefore, it is relevant to discuss how these inclusions arise.

4.2.8 Possible formation mechanisms of h-BN inclusions

The fabrication of particulate ceramic matrix composites usually involves hot isostatic pressing which is mostly used to obtain a dense composite body with a uniform microstructure and isotropic properties without the need to use additives which remain at the interfaces and be deleterious for high temperature applications. The green shaped compacts have to be encapsulated either in metals or quartz prior to hot isostatic pressing. In both encapsulation techniques, BN powder is placed between the sample and the encapsulation material in order to prevent any reaction taking place between the encapsulation and the sample. BN is chosen as a barrier layer because of its relative chemical inertness and non-sinterability (Greenwood, 1973). This was the only source of boron in the production of the Si_3N_4-SiC composites. Therefore, a number of mechanisms which could lead to the presence of h-BN inclusions need to be carefully considered.

In accounting for the presence of the h-BN inclusions in the composites, it is important to record firstly that the areas of composite observed in the transmission electron microscope were not from the peripheries of the composite and secondly that there was no obvious evidence of white powder indicative of residual BN from the barrier layer on the parts of the samples used for transmission electron microscopy.

The first possibility is that delogged BN particles are transported into the material by liquid phases formed during hot isostatic pressing without involving any reaction. This is unlikely since the morphologies of the inclusions were indicative of epitaxial growth from a melt. For example, a number of cases were found where {0001} planes of the h-BN inclusions were parallel to {111} planes of neighbouring β-SiC grains, despite the occurrence of thin $\approx$ 1 nm intergranular films between the inclusions and the grains (Turan and Knowles, 1993). Thus, while there is the possibility that the h-BN inclusions observed were simply delogged particles transported into the centre of the composite from the colloidal spray, presumably by unwanted liquid phases formed during the hot isostatic pressing operation, it must be considered to be very unlikely.

A second possibility, by analogy with the $\alpha \rightarrow \beta$ transformation in Si_3N_4 is that BN undergoes a solution-reprecipitation reaction, using liquid available at the hot pressing temperature. However, while this is obviously possible in principle, this would have

difficulty in accounting satisfactorily for the observations of carbon layers in the h-BN inclusions next to SiC grains (Fig. 4.8) and the observations of the absence of carbon layers next to Si_3N_4 grains. It would also be unable to account for the fact that h-BN inclusions are also found in composites made with deoxidised compacts where liquid phases were nearly eliminated (Turan and Knowles, 1995) and the observation that the h-BN inclusions are distributed throughout the composites.

A third possibility is that at the temperature and external pressure used during the hot isostatic pressing process, BN in the powder bed is able to dissociate to elemental boron and nitrogen. Gaseous products such as nitrogen formed in and around the powder compact are unable to escape from the encapsulant and will be able to diffuse throughout the compact relatively efficiently, either through open pores during the early stages of densification or through the solid state during later stages of densification. The degree of dissociation experienced by the BN will be determined by the equilibrium vapour pressure of the gaseous nitrogen.

Extrapolating from data in the JANAF tables (Stull and Prophet, 1971), at 2373 K, we have:

$$BN_{(s)} \rightarrow B_{(s)} + {}^1/_2\, N_{2(g)} \qquad \Delta G^\circ_{2373\ K} = +\ 43\ kJ\ mol^{-1} \qquad (4.1)$$

for the decomposition of BN. Thus, the equilibrium partial pressure of nitrogen for the decomposition of solid BN into solid boron and nitrogen gas at 2373 K and unit activities of boron and BN is 0.013 atm. Therefore, in an environment where the internal pressure in the tantalum can is 10^{-7} atm prior to hot isostatic pressing, it would be expected that the BN could readily decompose at 2373 K.

However, this is not the only possible decomposition reaction. The composite also contains Si_3N_4, which from the JANAF tables can be seen to begin to be able to dissociate at a lower temperature (1240 K) than that of BN (1620 K) for an original nitrogen partial pressure within the can of 10^{-7} atm. Since the temperature is necessarily increased gradually in a hot isostatic pressing run, the dissociation of Si_3N_4 is favourable thermodynamically at an internal can pressure of nitrogen of 10^{-7} atm when the temperatures of 1240 K is reached, although it should be recognised that at this temperature the kinetics of dissociation will be

slow. Possible gaseous products formed in the powder cannot escape at any significant rate through the tantalum can and are therefore contained by the encapsulation supported by the external high pressure gas. As soon as the equilibrium vapour pressure of nitrogen is reached at a particular temperature within the can, decomposition will cease. A gradual increase in the temperature causes more and more Si_3N_4 dissociation to occur, since the equilibrium partial pressure of nitrogen increases with temperature. The partial pressure of nitrogen in the can will therefore increase. This will in turn increase the temperature at which the dissociation of BN will begin. As a result, it is reasonable to expect that any significant dissociation of Si_3N_4 will prevent the dissociation of BN during the hot isostatic pressing run. Thus, decomposition of BN and the diffusion of nitrogen and boron through the compact (whether as a vapour (Singh and Wiedemeir, 1991) or in solid form) and the subsequent chemical reaction between boron and nitrogen to form h-BN, either to attain equilibrium at the hot isostatic pressing temperature or on cooling the composite after hot isostatic pressing, is also unlikely to be the source of the h-BN inclusions that have been observed.

The remaining and the most likely, possibility is that the h-BN inclusions are the product of a chemical reaction between Si_3N_4 and/or SiC and boric oxide (B_2O_3) which exists as an unwanted contaminant in the sub-micron size colloidal BN spray. B_2O_3 occurs at room temperature as a thin film on the surface of BN, arising from the chemical reaction:

$$4\,BN_{(s)} + 3\,O_{2(g)} \rightarrow 2\,B_2O_{3(s)} + 2\,N_{2(g)} \qquad \Delta G^{\circ}_{298\,K} = -1483\ kJ\ mol^{-1} \qquad (4.2)$$

just as thin films of silica (SiO_2) are able to exist on Si_3N_4 and SiC powder surfaces at room temperature and atmospheric pressure. B_2O_3 has a very low melting point and is liquid above 723 K and a gas above 2316 K at atmospheric pressure (Stull and Prophet, 1971). The possibility of B_2O_3 becoming a gaseous species within the tantalum can should therefore also be considered. The temperature at which the equilibrium vapour pressure of boric oxide is 10^{-7} atm can be calculated to be 1275 K using a suitably integrated form of the Clausius-Clapeyron equation (Tabor, 1991):

$$\ln \frac{P_1}{P_2} = \frac{L_e}{R}\left(\frac{1}{T_2} - \frac{1}{T_1}\right)$$

where L_e is the average latent heat of evaporation over the temperature range T_1 to T_2 , taken here to be 380 kJ mol^{-1} using data from the JANAF Tables (Stull and Prophet, 1971) and P_1 and P_2 are the equilibrium vapour pressures at T_1 and T_2 respectively, here taking T_2 to be the boiling point of 2316 K at atmospheric pressure. This temperature of 1275 K is almost the same as the dissociation temperature of Si_3N_4, implying that at and above this temperature B_2O_3 will volatilise while Si_3N_4 will dissociate until the respective equilibrium vapour pressures are attained.

It is therefore reasonable to expect that during the hot isostatic pressing run, any B_2O_3 originally present on the surface of the colloidal BN particles in the barrier layer is able to evaporate and penetrate the porous green compact during the early stages of densification, reacting with either Si_3N_4 and/or SiC:

$$Si_3N_{4(s)} + 2\ B_2O_{3(l,\ g)} \rightarrow 4\ BN_{(s)} + 3\ SiO_{2(l)} \qquad (4.3)$$

$$3\ SiC_{(s)} + 2\ N_{2(g)} + 2\ B_2O_{3(l,\ g)} \rightarrow 4\ BN_{(s)} + 3\ SiO_{2(l)} + 3\ C_{(s)} \qquad (4.4)$$

Both these reactions are favourable thermodynamically up to 2373 K, even allowing for the vaporisation of B_2O_3 and the ability for Si_3N_4 to decompose at sufficiently high temperatures. Thus, for example, calculations from data in the JANAF Tables show that for reaction (4.3) $\Delta G^\circ_{2300\ K} = -196$ kJ mol^{-1} and $\Delta G^\circ_{2400\ K} = -120$ kJ mol^{-1} after the decomposition of Si_3N_4 has been taken into account. At lower temperatures where SiO_2 is solid and Si_3N_4 has not decomposed, this reaction is even more favourable thermodynamically, *e.g.*, $\Delta G^\circ_{1200\ K} = -375$ kJ mol^{-1} and $\Delta G^\circ_{1800\ K} = -309$ kJ mol^{-1} if the silica is assumed to be in the form of cristobalite. For reaction (4.4) similar calculations with SiC in the form of α–SiC give $\Delta G^\circ_{1800\ K} = -290$ kJ mol^{-1}, $\Delta G^\circ_{2300\ K} = -90$ kJ mol^{-1} and $\Delta G^\circ_{2400\ K} = -25$ kJ mol^{-1}.

It should be noted of course that these thermodynamic calculations do not necessarily imply that kinetically these chemical reactions will take place at a particular temperature, however high. In this context Coblenz and Lewis (1988) concluded that, on the basis of X-ray diffraction work alone, they were unsuccessful in attempting to synthesise BN–SiO_2 composites from Si_3N_4 and B_2O_3 after hot pressing in BN-washed dies at 1900 K and 35 MPa.

Nevertheless, it might still be expected that sub-micron h-BN inclusions such as the ones have been observed in this study might well arise in encapsulated and subsequently hot isostatically pressed materials containing Si_3N_4 if BN has been introduced as a barrier layer in the hot isostatic pressing process and high processing temperatures have been used. A simple calculation based on the dimensions of the tantalum can and the dimensions of the powder compacts prepared for hot isostatic pressing for the samples investigated in this work suggests that for a volume fraction of B_2O_3 of 5% in BN spray (Riley, 1983) (as would arise for 50 Å thick films on 0.6 μm diameter spheres), the volume fraction of the BN that can arise from the surface B_2O_3 is of the order of 0.5% by volume. This would be well below the detection limit for X-rays, but consistent - at least qualitatively - with TEM observations. Note that it is also very difficult to detect an even higher percentage of BN in the presence of both α and β-Si_3N_4, silicon oxynitride, silica and SiC polytypes due to overlapping main peaks.

The observations of carbon layers in the h-BN inclusions next to SiC grains (Fig. 4.8) and the observations of the absence of carbon layers next to Si_3N_4 grains are consistent with the premise that the h-BN inclusions formed as a result of the chemical reactions (4.3) and (4.4). In support of this, quite regularly h-BN inclusions found to be with Si_3N_4 precipitates inside SiC grains and an example of this case is shown in Fig. 4.20. The intragranular h-BN inclusions in SiC and Si_3N_4 grains were initially formed at porous regions but were most probably trapped inside grains during rapid grain growth.

It might be also thought that, in addition to the chemical reactions (4.3) and (4.4), SiC and B_2O_3 will react to form boron carbide (B_4C). However, this reaction is not favourable thermodynamically, and reassuringly no B_4C inclusions were detected in the composites.

The observation of carbon inclusions in SiC pressureless sintered with the addition of carbon and in SiC whisker reinforced composites with carbon coated whiskers is expected, but there is no reason for the observations of carbon inclusions other than the existence of carbon in the starting powder as a contamination when it is not deliberately added. Therefore, if BN is used as a packing material or release agent in SiC and Si_3N_4 production processes, it is possible that inclusions reported to date as being carbon inclusions in such materials could be h-BN and at least merit re-examination by energy loss spectroscopy or windowless energy dispersive X-ray analysis to confirm that they are indeed carbon, rather than h-BN.

4.3 Conclusions

Small sub-micron graphite-like boron nitride inclusions have been detected unambiguously in silicon nitride particulate-reinforced silicon carbide composites hot isostatically pressed in tantalum cans with a boron nitride barrier layer sprayed onto the internal surface of the can to prevent the tantalum reacting with the silicon carbide. The inclusions were first of all thought to be graphite which is the usual inclusion observed in the SiC based ceramics, but they were identified as h-BN by PEELS analysis.

The occurrence of the BN inclusions in the composite is obviously a consequence of the introduction of colloidal BN into the hot isostatic pressing process since the composite did not include any additive containing boron. Consideration of the possible ways in which these inclusions can arise in the composite suggests that they are formed from boron oxide present as a thin surface film on the boron nitride particles in the barrier layer. While it is unlikely that BN particles diffuse into the composite during hot isostatic pressing, surface boron oxide, B_2O_3, on the particles will be molten during the hot isostatic pressing operation and be able to diffuse rapidly to the centre of the powder compact. Reaction of Si_3N_4 and B_2O_3 to form silica and h-BN, the stable form of BN at the hot isostatic pressing temperature and pressure, is favourable thermodynamically, as is the chemical reaction of SiC with N_2 (present from the tendency of Si_3N_4 to decompose under the hot isostatic pressing conditions used) and B_2O_3 to form h-BN, silica and carbon. These chemical reactions are consistent with the observation of carbon layers with h-BN inclusions adjacent to SiC, whereas such layers have not been observed when the h-BN inclusions are adjacent to Si_3N_4.

Note that in addition to unavoidable surface B_2O_3, more B_2O_3 could form during the degassing and subsequent sealing steps before hot isostatic pressing. During this process, the can containing BN powder bed and the green compacts are generally heated up to high temperatures to get rid of the unwanted species. For example, Dutta (1988) outgassed the tantalum cans containing SiC green compacts wrapped with BN for 6 to 8 h at 1100 to 1200°C and then vacuum sealed. This treatment could increase the amount of B_2O_3 in the can through the oxidation of BN (Oda and Yoshio, 1993).

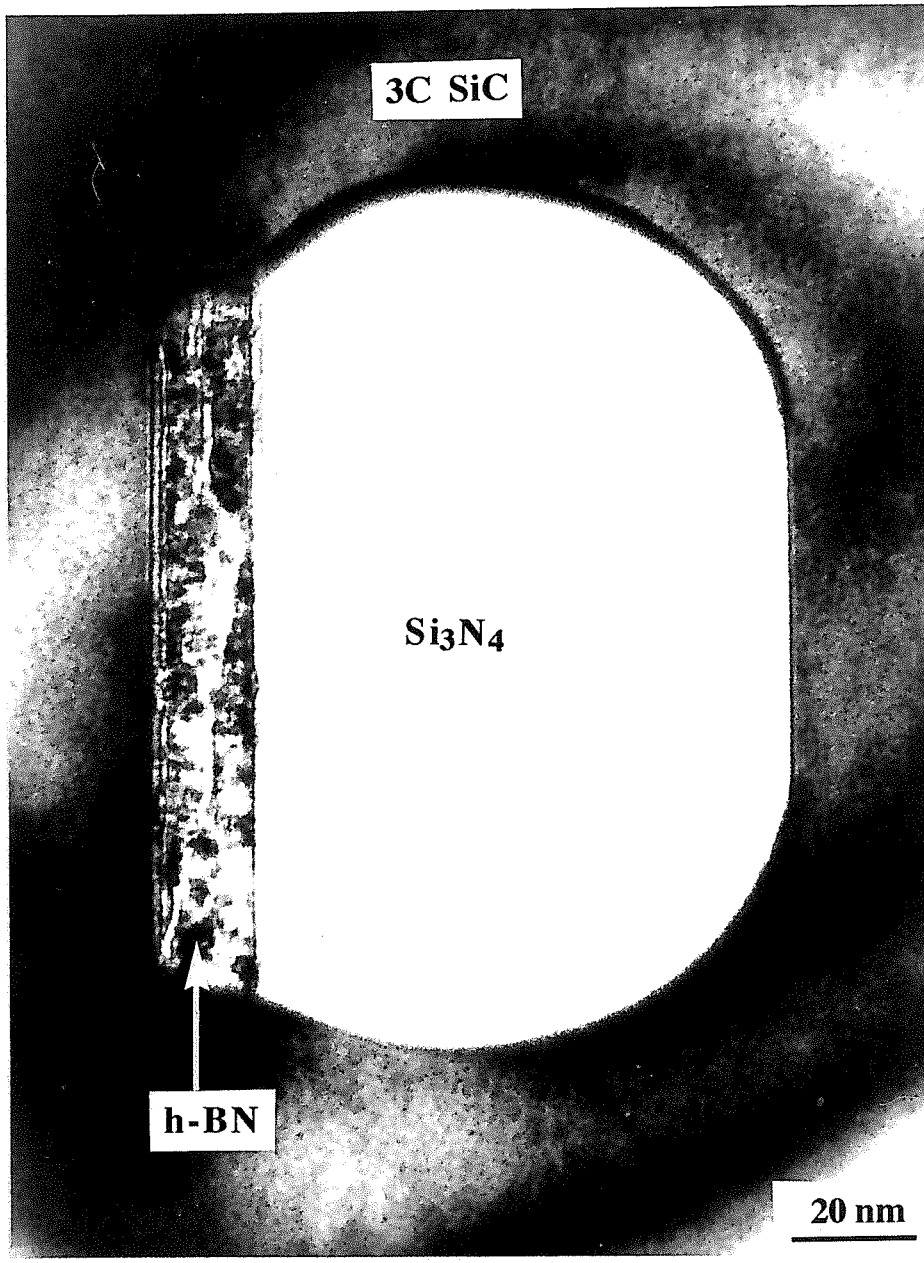

Fig. 4.20 A bright field TEM image of a h-BN inclusion between 3C SiC matrix grain and a Si_3N_4 precipitate.

It is suggested that such inclusions may be more prevalent in sintered, hot pressed and hot isostatically pressed ceramic materials whenever boron nitride is used as a barrier layer than has been recognised to date. Inclusions identified as graphite from electron diffraction and bright field imaging without the use of WEDX and/or PEELS elemental analysis techniques in hot isostatically pressed and hot pressed Si_3N_4 materials may be h-BN after all.

Most of the h-BN inclusions were elongated and thin in the [0001] direction. This is consistent with the literature that hot isostatic pressing result in well defined shapes whereas sintering result in inclusions with irregular shapes.

PEELS analysis of inclusions in different crystallographic directions revealed the direction dependency of PEELS spectra in that the intensities of π^* and σ^* peaks are determined by the relative alignment of *c*-axis of the crystal with respect to the electron beam and also by other experimental parameters, such as, size of the spectrometer collection aperture, the magnitude of the camera length in diffraction mode and the scattering angle used for collection. The comparison of PEELS spectra with the results in the literature was found to be of limited use since so many factors can effect the intensities of π^* and σ^* peaks and unfortunately in most of the literature these factors are not all reported.

In large h-BN inclusions, carbon containing regions were identified by PEELS and in conjunction with HREM imaging the structure of such layers identified them as turbostratic carbon. The fact that carbon is in turbostratic structure whereas h-BN is crystalline is consistent with the results reported in the literature.

Delamination cracks formed as a result of thermal expansion difference between h-BN and SiC and/or Si_3N_4. Some of these cracks were associated with misorientation bands some which found to have special orientation relationship with the parent crystal. In few occasion, the angle between the (0001) planes of main inclusion made an angle of 139° which is the angle proposed in the literature as a twinning angle for h-BN. Twins of h-BN can be imaged in the HREM when BN crystal is parallel to $[1\bar{1}00]$ zone axis. Such twins identified as $\Sigma = 8$ in terms of coincident site lattice model. The grain boundaries formed between two BN grains and interphase boundaries formed between h-BN and SiC and/or Si_3N_4 will be discussed in detail in Chapter 6.

Appendix 4.1

Formal description of twinning crystallography

A formal description of twinning crystallography can be found in any metallurgical text book (*e.g.*, Christian, 1975). Therefore, only the basic nomenclature relating to the theory will be given. This is:

K_1 = the twinning plane, composition plane or the first undistorted plane
K_2 = the second undistorted plane
η_1 = the shear direction
η_2 = the direction defined by the intersection of the plane of shear with K_2
s = plane of shear which is the plane that is mutually perpendicular to K_1 and K_2 and contains η_1 and η_2.
γ = the shear and equals the shear strain
g = the magnitude of shear.

The relationship between K_1, K_2, η_1, η_2 and *plane of shear* is graphically illustrated in Fig. 4.21.

There are three types of twins: type I, type II and a compound twin. A type I twin occurs when K_1 is a rational plane and η_2 is a rational direction. A type II twin occurs when K_2 is a rational plane and η_1 is a rational direction. A compound twin occurs when all four elements K_1, K_2, η_1, η_2 are all rational. The compound twin is the most common twinning mode in f.c.c. and h.c.p. crystal structures.

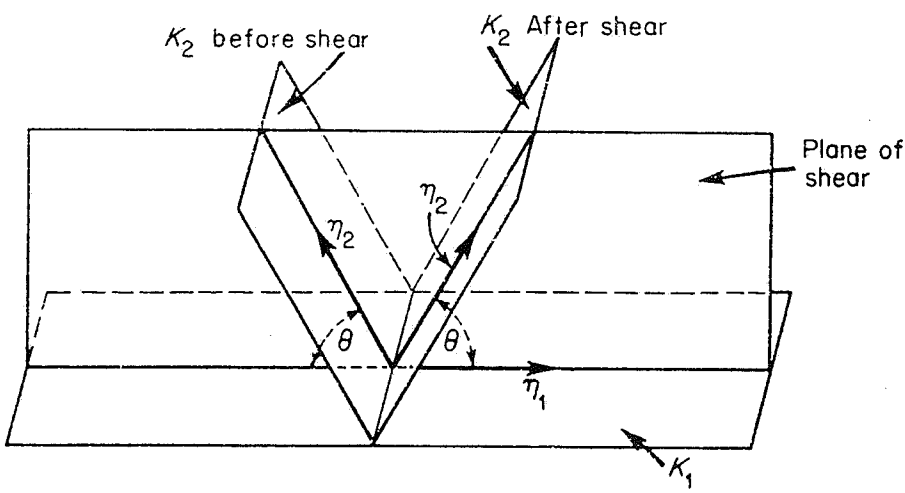

Fig. 4.21 A schematic showing the relationship between the twinning elements (after Reed-Hill and Abbaschian, 1992).

Chapter 5

Equilibrium Film Thicknesses at Interfaces in Engineering Ceramics and Ceramic Matrix Composites

5.1 Introduction

Over the last few decades, there has been a great deal of theoretical and experimental research focused on the determination of the character and properties of interfaces. This is because almost all mechanical, physical, chemical, electronic and high temperature properties of the materials are influenced by the structure and properties of the interfaces as has been described in Chapter 2. For example, it is found (Kargol and Albright, 1977 & Kurishita and Yoshinaga, 1989) that the fracture resistance is inversely proportional to the grain boundary energy, being a maximum for low angle and 'special' grain boundaries and a minimum for high angle grain boundaries.

This Chapter is preliminary to the work presented in Chapter 6. It consists of *(i)* a literature survey on the wetting behaviour of interfaces and on the existing theories of stable equilibrium film thicknesses together with extensions of these theories where necessary in order to explain the experimental observations, *(ii)* a critical review of the results reported in the literature and *(iii)* some of my own experimental results.

5.2 Wetting behaviour of interfaces

Transmission electron microscope investigations using Fresnel, diffuse dark field and high resolution electron microscopy techniques have revealed that, while most of the interfaces in ceramic bodies are covered with intergranular films (Clarke, 1979), some interfaces are not (Schmid and Rühle, 1984). The HREM image of a SiC region of a hot isostatically pressed Si_3N_4-SiC composite in Fig. 5.1 taken during the course of this work shows almost all the possible configurations of interfaces that can exist in ceramic materials. It can be seen that

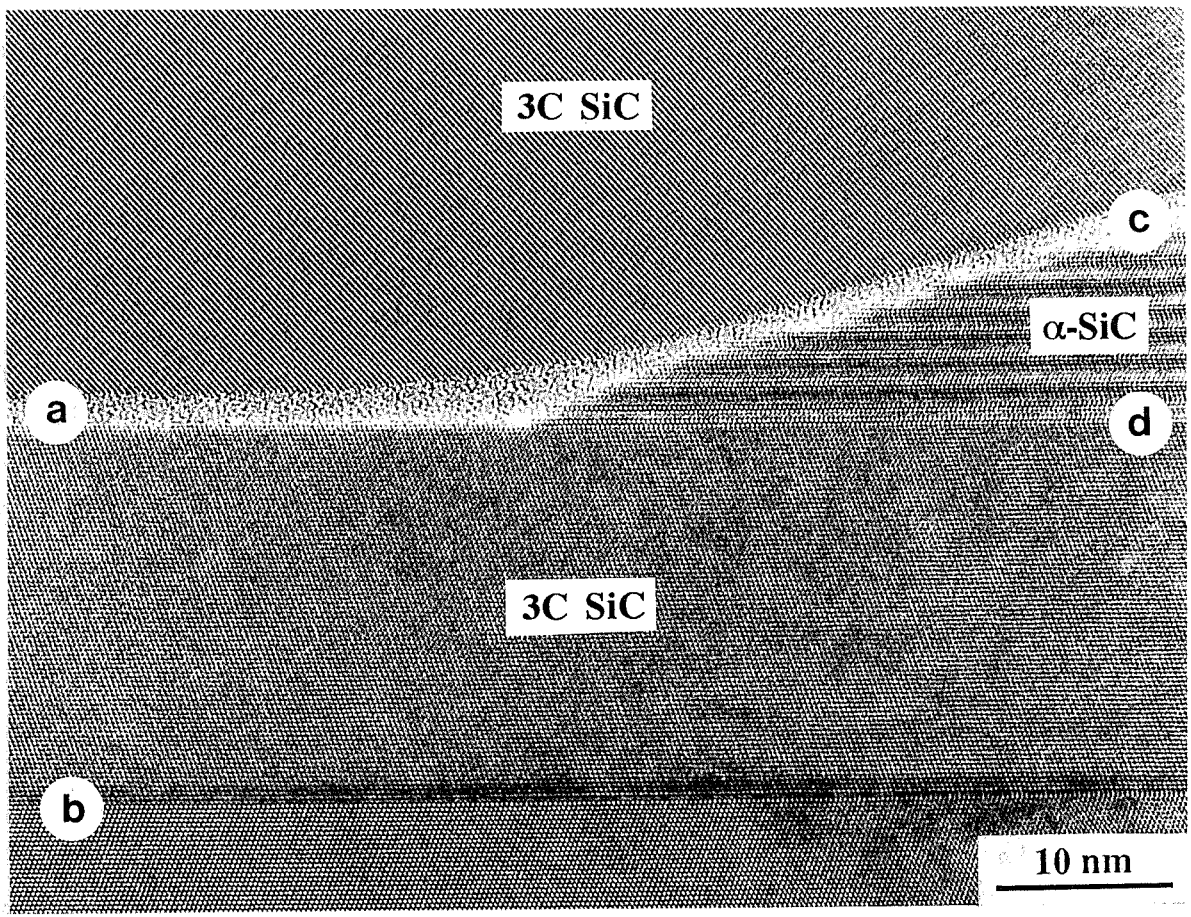

Fig. 5.1 HREM image of Si_3N_4-SiC composite prepared from as-received powders. This shows the anisotropic wetting behaviour of grain (*a* and *b*) and interphase (*c* and *d*) boundaries in ceramic materials. The interfaces labelled as (*a*) and (*c*) contain intergranular films whereas interfaces (*b*) and (*d*) are free of such films. Note that the interface labelled as (*c*) is faceted although an intergranular film exists at the interface.

well as two wetted interfaces (*a* and *c*) and two unwetted interfaces (*b* and *d*). The twin boundary (*b*) and the interphase boundary (*d*) between 3C SiC and α-SiC are not wetted with intergranular films, while the high angle 3C SiC–3C SiC grain boundary and the 3C SiC–α-SiC interphase boundary are both wetted with a film.

The first question arises from these observations is *what is the condition for an intergranular film to spread and cover an interface between two media?*

The simplest statement concerns the energies involved (Raj, 1981), *i.e.*:

$$2\gamma_{SL} < \gamma_{SS} \tag{5.1}$$

where γ_{SL} and γ_{SS} are the energies of a crystal-liquid and crystal-crystal interfaces respectively. A schematic diagram for such a condition is shown in Fig. 5.2.

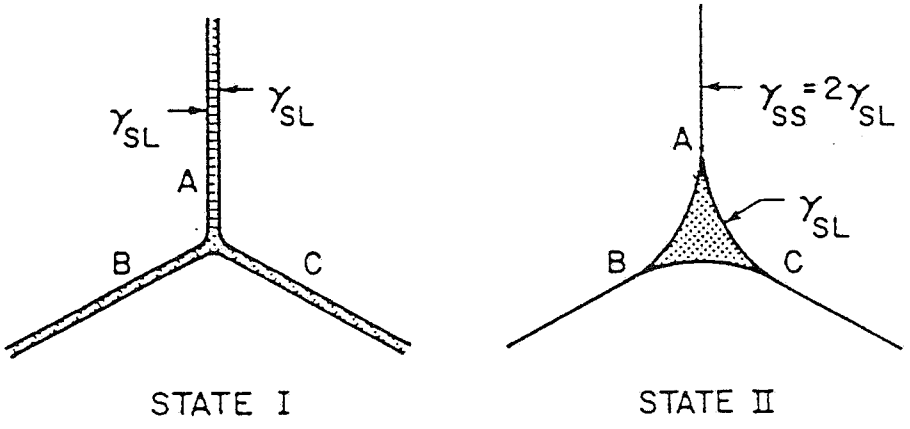

Fig. 5.2 End point configurations for comparing the energies of interfaces wet (state I) and not wet (state II) by an intergranular film. Redrawn after Raj (1981).

This model assumes that the interfacial energies are isotropic. However, it is well known (Kingery *et al.*, 1976) that the surface energy of solids is dependent on the crystallographic orientation. Therefore, Clarke (1985) has taken a different approach of plotting the energy of

grain boundaries as a function of misorientation for crystalline and wetted[@] grain boundaries (Fig. 5.3). Note that the graph is not constructed in any quantitative manner – this has to wait until interatomic potential based computations of all the energies involved are available for particular systems (and then it will be for misorientations about specific axes [UVW] for, *e.g.*, symmetrical tilt boundaries). Nevertheless a plot of this kind can still be useful. The plot indicates that, in line with experiment, most interfaces should be covered with an amorphous intergranular film to lower their interfacial energies. However, in a number of cases no intergranular film is detected since these cases have lower interfacial energies than those interfaces containing intergranular films. These are widely believed to be low angle grain boundaries, interfaces of special misorientations such as a coherent twin boundary (*e.g.*, $\Sigma = 3$ CSL f.c.c. grain boundary) and the (111) 3C SiC–(0001) α-SiC interphase boundary, both of which are shown in Fig. 5.1. However, this approach would imply that all the grain boundaries in pressureless sintered SiC are either low angle boundaries or special high angle boundaries or, if not, $2\gamma_{SL} > \gamma_{SS}$, because SiC intergranular films in these ceramics have not been reported to date.

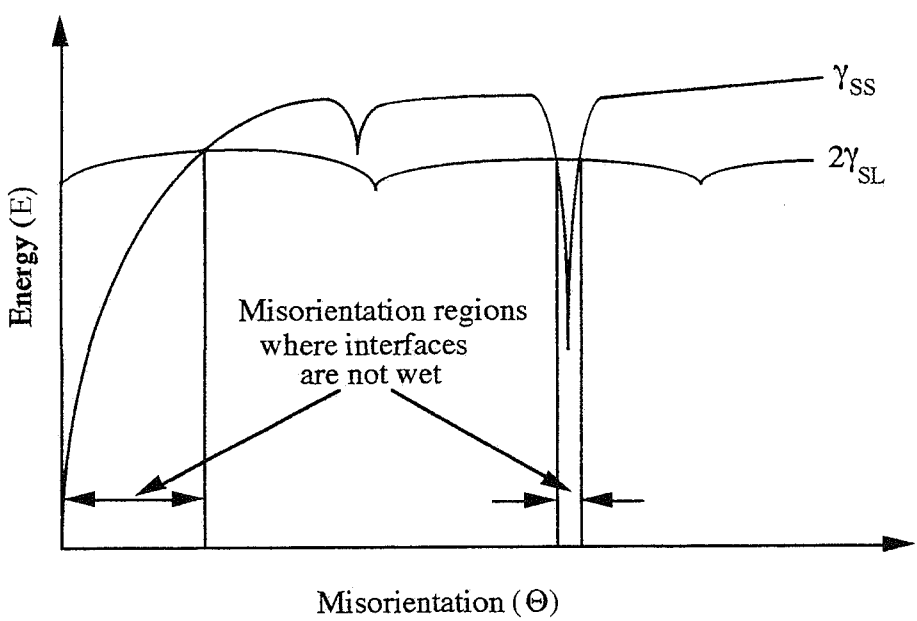

Fig. 5.3. Schematic misorientation vs. energy diagram of interfaces showing that interfaces will only be free of intergranular films if their energy is lower than that of a wetted interface. Redrawn after Clarke (1985) & Clarke and Gee (1992).

[@] *Although the term wetting is largely used in connection with intergranular films, the correct terminology to describe the process is spreading of the film on the interface since the contact angle is 0°.*

The situation described so far pertains to the behaviour of ceramic materials at fabrication temperatures, typically ≥1500°C. However, the transmission electron microscopy investigations are mostly done at room temperatures. *How then does the temperature change effect the wetting behaviour?*

As the material is cooled to room temperature from fabrication temperatures the wetting behaviour may be altered (Clarke, 1985). It is reasoned that, in general, the wetted interface will have a greater temperature dependence than that of its crystalline counterpart since the entropic contribution to the free energy of a liquid is expected to be larger than a crystalline interface. This is schematically shown in Fig. 5.4. The important feature of this graph is that some of the interfaces observed to be free of intergranular films at room temperature could have been wet at the fabrication temperatures. This possibility will be explored in the proposed liquid phase transformation mechanism to explain the $\alpha \rightarrow \beta$ reverse SiC phase transformation in Chapter 7. Clarke also concluded that a wetted interface will not spontaneously dewet unless a finite nucleation barrier is overcome.

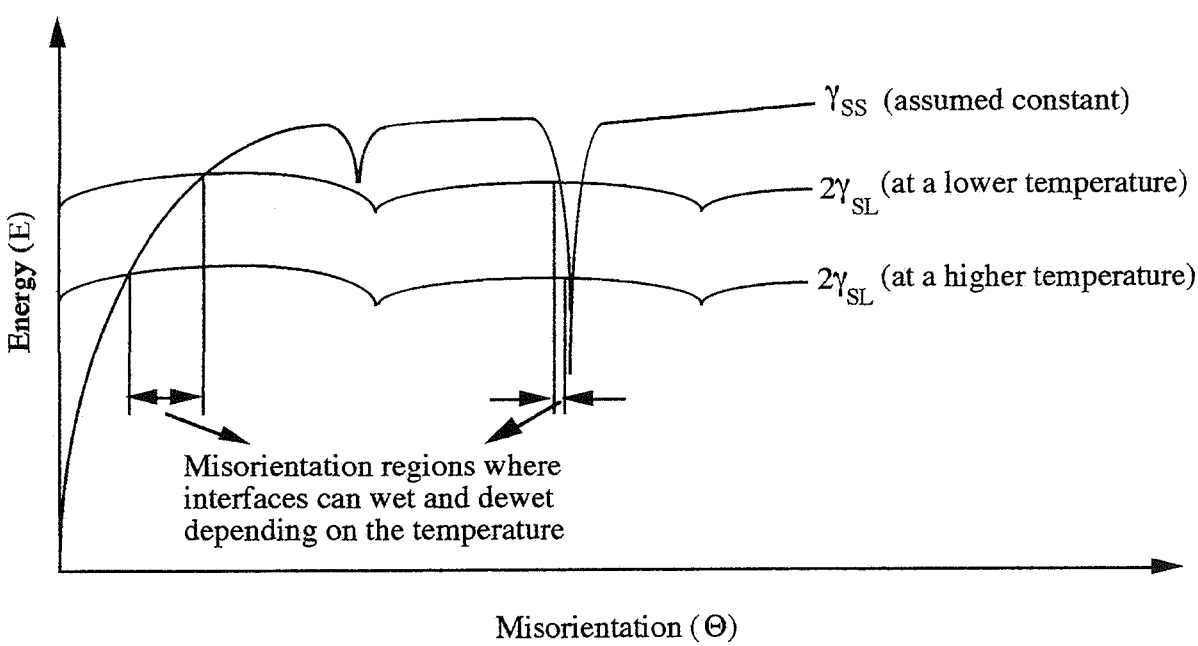

Fig. 5.4. Schematic diagram showing that when the material is cooled down to room temperature some interfaces which are wet at high temperatures will be favoured energetically to dewet at lower temperatures. Note that for clarity it is assumed that the energy of the crystalline interface does not change with temperature. Redrawn after Clarke (1985) & Clarke and Gee (1992).

In addition to the temperature effect on the magnitude of the γ_{SL}, the effect of impurities also has to be considered (Kingery *et al.*, 1976). If a small amount of low surface tension impurity is added, it tends to concentrate in the surface layer and decrease the surface energy (γ_{SL}) sharply even with a small amount of addition. Conversely a high surface tension impurity tends to concentrate in the surface layer to a lesser extent and has only a minor effect on γ_{SL}. The surface energy does not change linearly with the additives. Of course, it should never be forgotten that every single material has a different value of γ_{SL} and γ_{SS}.

5.3 Equilibrium film thickness

The other striking TEM observation is that the thickness of intergranular films seems to be relatively constant from one interface to another in any given sample, but that it varies from material to material. There are a number of approaches to explain *why the liquid remains at the interfaces and why it adopts an equilibrium thickness.*

Lange (1982a) applied a squeeze film analysis and predicted that a finite film thickness remains within the experimental time frame where it is energetically favourable. Using an electron diffraction technique, Marion *et al.* (1987) showed that the intergranular films are more highly ordered than the glass in the triple grain pockets. This experiment suggests that the stress distributions in the liquid layer needed to maintain the chemical potential gradient are associated with some structure in the liquid. However, the liquid film thicknesses were not defined as a function of the sintering parameters.

Kwon and Messing (1991) found the opposite to Marion *et al.*, in that an epitaxial arrangement of the liquid at the solid-liquid interface is not necessary to maintain a stable liquid film between two grains during solution-precipitation. They derived two different equations to calculate equilibrium film thickness for diffusion controlled and interface reaction controlled solution precipitation. The equation for the diffusion controlled case indicates that the equilibrium film thickness is a function of material properties, such as solubility, in a system where the Stokes-Einstein relationship holds true, and it predicts that the same equilibrium film thickness will be maintained for materials sintered under pressure. The equilibrium film thickness will depend on the thermal history of materials during liquid phase sintering since the solubility increases with increasing temperature. For interface

reaction control, the thickness is predicted to vary rapidly as a function of heating and cooling due to additional temperature dependent parameters (such as solubility). For example, in support of the theory developed by Kwon and Messing (1991), a thicker amorphous intergranular film was observed (Clarke, 1989 and Cinibulk *et al.*, 1993a) in rapidly quenched Si_3N_4 ceramics from above the eutectic temperature than in normally, more slowly, cooled samples. However, Lee *et al.* (1994) observed a constant film thickness for rapidly and normally cooled samples.

Probably the most important theory of all is the one developed by Clarke (1987) who showed that for a stable film thickness to exist the attractive force due to the long range van der Waals dispersion interactions between the grains must be balanced by a net repulsive long range structural interaction. This theoretical approach has been recently extended (Clarke *et al.*, 1993) to include a possible effect of a repulsive electrical double layer force at the interface.

5.4 The theory of the equilibrium film thickness by Clarke's model

It is instructive to examine how an equilibrium film thickness can be envisaged theoretically using Clarke's approach. Clarke (1987) employed two different continuum approaches to show the existence of equilibrium film thickness between two intervening phases separated by a third intermediate phase.

The first one is based on the interfacial energy approach and the second one is based on simple force balance approach. In the following section, the second approach is going to be described with its advantages and drawbacks since it is the one accepted in the field of ceramics.

5.4.1 Force balancing approach

For a stable equilibrium intergranular film thickness to exist it is a necessary condition that the net normal force acting to draw two adjacent grains together and thin the film should be equal to zero. This condition is satisfied by the following:

$$P_E + P_C + \Pi = 0 \tag{5.2}$$

where P_E is the externally applied pressure, P_C is the capillary pressure due to the concave curvature at the three and four-grain junctions, and Π may be termed the disjoining pressure following Derjaguin *et al.* (1978). The disjoining pressure consists of the contributions such as those due to van der Waals forces (Π_{DISP}), electrical double layer interactions (Π_{EDL}), interactions resulting from solute adsorption on the two grain surfaces (Π_{ADS}), hydrogen bonding forces (Π_{HB}) and any structural or steric forces (Π_{ST}). Thus, the disjoining pressure can be formally expressed as:

$$\Pi = \Pi_{DISP} + \Pi_{ST} + \Pi_{EDL} + \Pi_{ADS} + \Pi_{HB} \tag{5.3}$$

Neglecting some of the contributions since there is no experimental evidence for their existence in ceramic materials at high temperatures*, the net normal force acting across a thin intergranular film may be written as:

$$P_E + P_C + \Pi_{DISP} + \Pi_{ST} + \Pi_{EDL} = 0 \tag{5.4}$$

Some of these terms have to be negative, *i.e.*, repulsive acting to make the film thicker whereas the others have to be positive, *i.e.*, attractive and acting to thin the intergranular film. Now, it will be shown *how these terms can be calculated and how they can effect the film thickness, starting with attractive forces.*

5.4.2 Attractive forces

5.4.2.1 External pressure

If extraordinarily large compressive stresses are applied, the film thickness can be lowered, as for example could occur during hot isostatic pressing (Clarke, 1987) where the liquid is literally squeezed out from the interfaces. This will only arise if the liquid is free to flow out of the composite material and if the applied pressure exceeds the pore pressure. However, the hot isostatic pressing of materials is generally done in an encapsulant which is impermeable, and so, in practice, this method of lowering the stable intergranular film thickness would not take place.

---

* *In the original paper the contribution of electrical double layer is neglected, but later on Clarke et al. (1993) extended the theory to include this contribution.*

5.4.2.2 Van der Waals forces

Van der Waals forces between atoms or molecules can be separated into orientation, induction and dispersion forces. Of these long-range van der Waals forces, the component amenable to analysis is the dispersion force, which is conventionally referred to as the London dispersion force. This contribution has as its origin the electromagnetic interaction between fluctuating dipoles in the different phases (Mahanty and Ninham, 1976). The fluctuations involved tend to have frequencies in the ultraviolet region of the spectrum and are instrumental in determining the optical dispersion characteristics of the phases, hence the term dispersion forces. In comparison to isolated atoms or molecules, the dispersion force interaction between solid phases is of much longer range, and varies much more slowly with distance as Hamaker (1937) first showed. The Lifshitz (1956) quantum theory to the calculation of the London dispersion force was extended by Dzayloshinski *et al.* (1961). For a medium β sandwiched between phases α and γ (Fig. 5.5), their result can be expressed as (Clarke, 1987):

$$\Pi_{DISP}(h) = \frac{\mathsf{h}}{8\pi^2 h^3}\int_0^{\infty}\sum_{n=1}^{\infty}\frac{1}{n^3}\left[\left(\frac{\varepsilon_\alpha - \varepsilon_\beta}{\varepsilon_\alpha + \varepsilon_\beta}\right)\left(\frac{\varepsilon_\gamma - \varepsilon_\beta}{\varepsilon_\gamma + \varepsilon_\beta}\right)\right]^n d\zeta \qquad (5.5)$$

where ε_α, ε_β and ε_γ are the dielectric permittivities of the three media (α, β and γ) as a function of the imaginary frequencies $i\zeta$, h is Planck's constant divided by 2π, h is the equilibrium film thickness, and the summation n is over the frequencies $\zeta_n = n(2\pi kT/\mathsf{h})$.

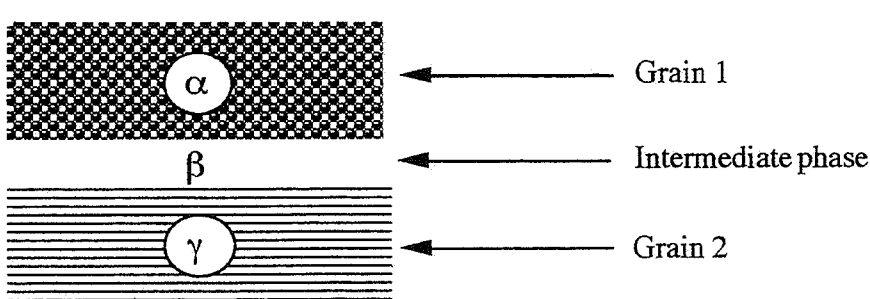

Fig. 5.5 A schematic representation of an interface where two phases, (α) and (γ) are separated by a third phase (β).

This equation indicates that the dispersion force can be either attractive or repulsive depending on the relative values of the dielectric permittivities of the three phases. The only condition for the dispersion force to be repulsive can be stated as being when the order of the dielectric constants is changing monotonically across the interface (*i.e.*, $\varepsilon_\alpha > \varepsilon_\beta > \varepsilon_\gamma$). For the symmetrical case in which the grains (α and γ) either side of the intergranular film (β) are the same, the above equation reduces to the simpler approximate form of:

$$\Pi_{DISP} = \frac{h}{8\pi^2 h^3}\int_0^\infty \left[\left(\frac{\varepsilon_\alpha(i\zeta) - \varepsilon_\beta(i\zeta)}{\varepsilon_\alpha(i\zeta) + \varepsilon_{\beta(i\zeta)}}\right)\right]^2 d\zeta = \frac{H_{\alpha\beta\alpha}}{6\pi h^3} \qquad (5.6)$$

where $H_{\alpha\beta\alpha}$ is the Hamaker constant.

In this symmetrical case, the dispersion force will always be attractive and thin intergranular films cannot be stable against the attractive forces unless there exists a repulsive structural or steric force of sufficient strength to balance the long-range van der Waals force.

5.4.3 Repulsive forces

5.4.3.1 Structural or steric forces

The notion of a steric force was introduced by Derjaguin and Churaev (1974), but Clarke (1987) was the first to give it a direct physical embodiment. He proposes that, unlike bulk phases, the structure of a liquid for microscopic thicknesses (*e.g.*, an intergranular film) is not random and that it exhibits a form of spatially varying orientational order close to each grain. The structural force can be visualised as follows (Clarke, 1987a): consider two solids separated by a liquid having a random structure. Assume that the first layer of liquid molecules have a preferred orientation on the solid surfaces and that to accommodate this alignment the liquid molecules in the gap arrange themselves to match the orientation of the monolayers on either solid. When the size of the gap is large this is a minor concern, the bulk of the liquid remains randomly oriented, and the distortion adds little to the overall energy of the system. As a result of the free flowing of the liquid out from the gap, the solid surfaces can be brought closer. As the gap gets closer the configurational matching becomes more difficult and the orientation of the liquid molecules less random. In turn the energy of the system rises and this will act to resist the grains being brought together. The magnitude

of the force increases as the distortion increases when the grains are brought closer. Although the magnitude of the van der Waals forces depends on the dielectric constants of the adjacent grains and the film, the repulsive structural term will only depend on the conformational distortion of the molecules in the intergranular film.

If the correlation length associated with orientational fluctuations is ξ, the orientational order imposed upon the liquid phase structure by the adjacent grains will extend a distance of the order of ξ into the intergranular film. Clarke (1987) derived an equation for the calculation of steric forces:

$$\Pi_{ST} = a\eta_0^2 / \sinh^2(h/2\xi) \tag{5.7}$$

where the product $a\eta_0^2$ is the free energy difference between intergranular liquid with and without structural ordering.

5.4.3.2 Electrical double-layer forces

Since there is no experimental evidence for the existence of electrical double layers between crystalline grains separated by a liquid film at high temperatures, this effect was neglected in Clarke's first model on the possible equilibrium thicknesses of intergranular films. However, recently Clarke *et al.* (1993) extended the model to include this interaction. A possible electrical double layer effect can be expressed as;

$$\Pi_{EDL} = \frac{16k_BT}{z^2\pi b_L h^2}\tanh^2\left[\frac{ze\Psi_s}{4k_BT}\right]\kappa^2 h^2 e^{-kh} \tag{5.8}$$

where Ψ_s is the potential at the surface of the grains, $1/\kappa$ is the Debye screening length, k_BT is the Boltzman constant times absolute temperature, z is the ion charge and b_L is the Bjerrum length:

$$b_L = e^2 / 4\pi\varepsilon\varepsilon_o k_BT \tag{5.9}$$

where e is the proton charge (1.602×10^{-19} C), ε is the dielectric constant of the intervening media and ε_o is the permittivity of free space (8.854×10^{-12} Fm^{-1}).

5.5 Estimate of the equilibrium film thickness by Clarke's model

The equilibrium thickness of an intergranular film between two identical bodies in the absence of any applied and capillary stresses can be calculated as the solution of the equality between the attractive dispersion forces and the repulsive disjoining forces:

$$\Pi_{DISP} = \Pi_{ST} + \Pi_{EDL} \tag{5.10}$$

$$\frac{H_{\alpha\beta\alpha}}{6\pi h^3} = 4a\eta^2 \exp(-h/\xi) + \frac{16k_BT}{z^2\pi b_L h^2}\tanh^2\left[\frac{ze\Psi_s}{4k_BT}\right]\kappa^2 h^2 e^{-kh} \tag{5.11}$$

In order to solve this equation, the values of three principal parameters are required: the dielectric permeabilities of the adjacent materials and the separating film, a value for the preexponential constant, $4a\eta_o^2$ and the parameters effecting the electrical double layer contribution.

Evaluation of the Hamaker constant requires, in principle a complete knowledge of the dielectric permeabilities over all frequencies. However, a good approximation can be computed following the procedures described by Hough and White (1980) from relatively few experimental data. The required data include the principal relaxation frequencies and oscillator strengths, and in particular the optical constants. The calculations of Hamaker constants by this method is almost limited to alumina-alumina grain boundaries containing silica films because of the lack of availability of these parameters for ceramics. Nevertheless, an estimate less accurate than the procedures described by Hough and White (1980) can be made by using the Tabor-Winterton (1969) approximation to the Hamaker constant based on Lifshitz theory. This method requires the use of relatively well known terms such as refractive indices and the static dielectric constants. If the absorption frequencies (υ_e) of both the media are assumed to be the same and in the UV, the following approximate expression will be obtained for the non-retarded Hamaker constant for two same macroscopic phases (α) interacting across a medium (β):

$$H_{\alpha\beta\alpha} = \frac{3}{4}kT\left(\frac{\varepsilon_\alpha - \varepsilon_\beta}{\varepsilon_\alpha + \varepsilon_\beta}\right)^2 + \frac{3h\nu_e}{16\sqrt{2}}\frac{\left(n_\alpha^2 - n_\beta^2\right)^2}{\left(n_\alpha^2 + n_\beta^2\right)^{3/2}} \tag{5.12}$$

where ε_α and ε_β are the zero frequency dielectric constants of the macroscopic phase and the intergranular film respectively and n_α and n_β are the refractive indices in the visible of the respective phases. This is known as the symmetrical case where two phases either side of the interface are the same (Israelachvili, 1992), *i.e.*, grain boundaries.

It should be noted that this analysis applies to what are normally referred to as dielectric or non-conducting materials.

Israelachvili (1992) also noted the very good agreement between the calculated Hamaker constants using equation (5.12) and those computed more rigorously by solving the full Lifshitz equation (Hough and White, 1980).

5.6 Is Clarke's theory sufficient to explain the experimental observations?

The first conclusion to be drawn from Clarke (1987) is that the value of calculated equilibrium thickness of intergranular films with a constant silica composition for grain boundaries decreases with an increasing value of Hamaker constant. One important result obtained using this argument is that SiC-SiC grain boundaries would not be wet since the calculated theoretical equilibrium thickness is zero because of its very high refractive index, resulting in a very high value of Hamaker constant. However, high angle-non special Al_2O_3-Al_2O_3 and Si_3N_4-Si_3N_4 grain boundaries should be covered with intergranular films. These predictions have been confirmed experimentally. Intergranular films were commonly observed at Al_2O_3-Al_2O_3 (Hansen and Philips, 1983) and Si_3N_4-Si_3N_4 (Kleebe *et al.*, 1992) grain boundaries while SiC-SiC grain boundaries were found to be free of such films (Davis *et al.*, 1987). Carpenter *et al.* (1991) employed this argument to explain their experimental observations of film-free grain boundaries between SiC grains in liquid phase sintered SiC-10 wt% Al_2OC material.

However, in contrast to the theoretical calculations and experimental observations, Sigl and Kleebe (1993) & Turan and Knowles (1995) showed recently that some SiC-SiC interfaces are covered by intergranular films. Sigl and Kleebe did not comment on why they observed

intergranular films at SiC-SiC interfaces, despite the fact that the theoretical calculations to date indicate the opposite.

It is well known (Rahaman *et al.*, 1986) that SiC and Si_3N_4 powders contain a small amount of silica as surface contamination and that subsequently, at elevated temperatures, surface silica becomes liquid. In SiC, the silica phase has to be removed by the addition of carbon to facilitate the full densification process, while in addition to silica other liquid making agents are added to Si_3N_4 to enable liquid phase sintering, the $\alpha \rightarrow \beta$ phase transformation and, as a result, the near-theoretical densification. Thus, it is entirely possible that intergranular films have not been observed in sintered SiC materials while intergranular films are largely observed in Si_3N_4 materials because of the lack of sintering additives in the former, implying that the absence of experimental evidence of intergranular films at SiC-SiC grain boundaries is nothing to do with the high Hamaker constant of SiC-SiC grain boundaries. The fact that the films were absent even in the liquid phase sintered SiC material examined by Carpenter *et al.* (1991), who attributed the absence of films at the interfaces to the high Hamaker constant of such interfaces, would appear to be contrary to the above explanation of the absence of liquid phases. However, they also concluded that all the liquid phase has been crystallised during cooling, not leaving behind any liquid phase to spread on grain boundaries.

The possible effect of the presence or absence of a liquid phase has been explored in my work by the hot isostatic pressing of SiC-Si_3N_4 composites prepared from as-received powders and deoxidised compacts and by subsequent HREM investigations of the interfaces. The microstructural investigations revealed that most of the grain and interphase boundaries were wetted by intergranular films in the composites prepared from as-received powders (Fig. 5.1) while most of the interfaces found to be free of intergranular films in the composites prepared from deoxidised green compacts (*e.g.*, Fig. 5.6). This will be discussed in detail in Chapter 6 (also see Turan and Knowles, 1995).

In addition, the thickness of intergranular films for mullite-mullite grain boundaries should be higher than all the above mentioned grain boundaries because of the very low Hamaker constant of these grain boundaries. However, experimental observations showed that

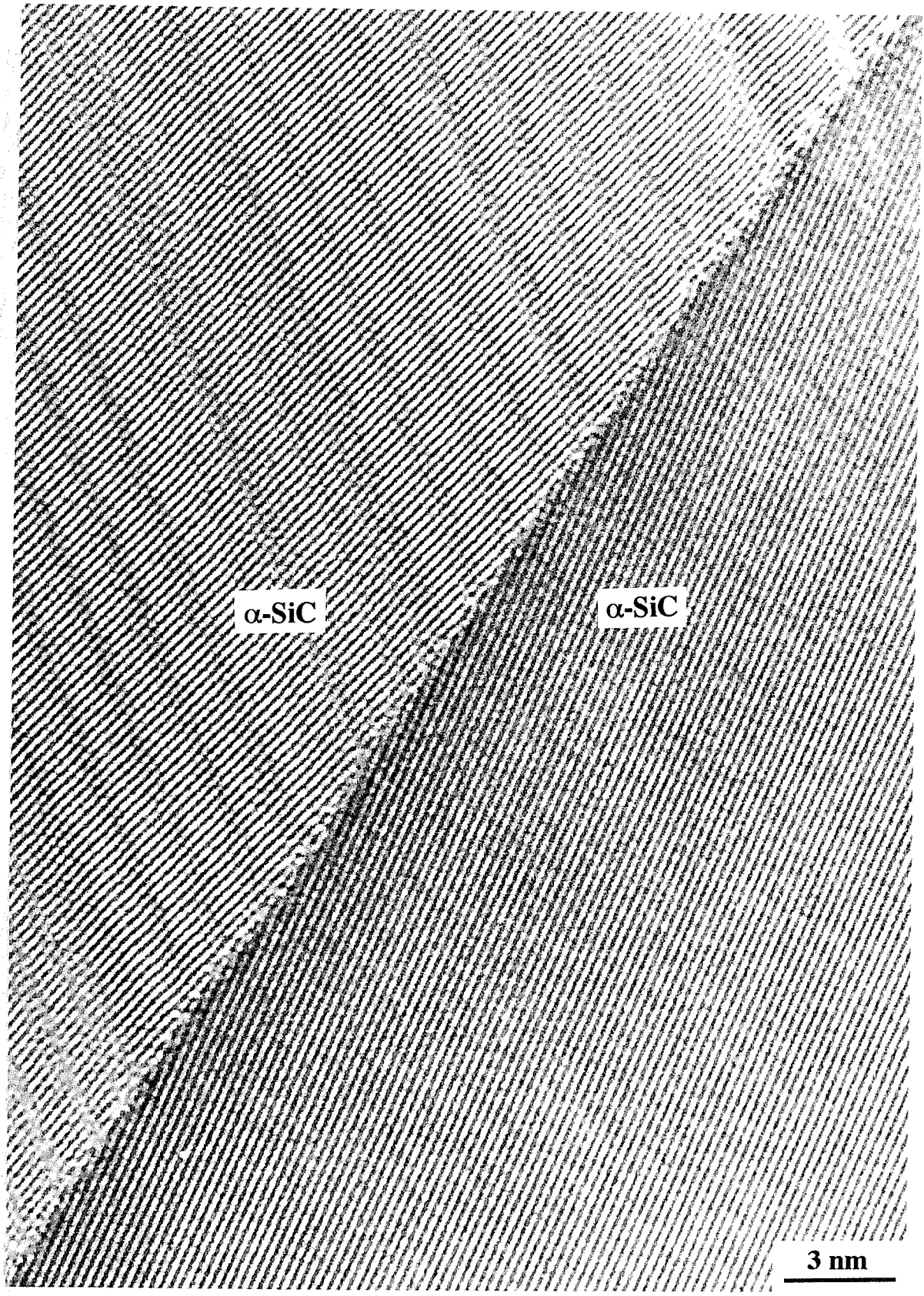

Fig. 5.6 An example of an intergranular film free grain boundary between two α-SiC grains in the 10 wt% Si_3N_4-SiC composite made from deoxidised compacts.

mullite-mullite grain boundaries do not contain intergranular films (Fig. 5.7)@. The interface in Fig. 5.7(a) appears to be semicoherent. The mismatch between the (230) 2.12 Å planes of upper grain and the (001) 2.88 Å planes of bottom grain is 35.85%. This mismatch is reduced substantially by joining every 15 planes from the upper grain to 11 planes of bottom grain. Due to these reasons, it may not be energetically favourable to wet the interface shown in Fig. 5.7(a) with amorphous phases. Examination of diffraction pattern, in which the top and bottom grains are oriented parallel to $[13\bar{4}]$ and $[1\bar{1}0]$ zone axes respectively, for the case shown in Fig. 5.7(b) showed that none of the diffraction spots are overlapping. A set of $(1\bar{1}1)$ planes from both grains make an angle of 11.5°. Also $(11\bar{1})$ (2.542 Å) planes of bottom grain are parallel to (401) (1.578 Å) planes of upper grain with a large misfit of 61%. These indicate that the orientation relationship between these two grains is not special and that therefore energetically the interface should be wet unlike the observation of Fig. 5.7(a). Other HREM observations on mullite-mullite grain boundaries also revealed that there are no films at the grain boundaries, irrespective of interface crystallography. In this case, it was found (Kara, 1994) that by using more than the stoichiometric amount of alumina to form mullite, the possibility of intergranular film formation can be eliminated, as otherwise alumina loss during crystallisation leaves behind unreacted silica that wets the interfaces.

All these results obtained during the TEM studies of SiC, Si_3N_4 and mullite ceramics underline an important, but obvious, point that to have an equilibrium film thickness there should, first of all, be liquid forming elements inside the material.

The second important conclusion of Clarke and co-workers (Clarke, 1987 & Clarke *et al.*, 1993) is that the equilibrium film thickness is dominated by the dielectric constants of the adjacent grains. This statement has been used to explain why the thickness of an intergranular film at a grain boundary has a different, smaller value than that of an interphase boundary (Clarke, 1987). However, the experimental evidence for the difference in the film thickness is not very strong since the technique of diffuse dark field used for the comparisons is not reliable (Cinibulk *et al.*, 1993). Secondly, a close examination of the micrograph (Fig. 1 in Clarke, 1987) shows that there is an apparent thickness variation between the interphase boundaries which could arise naturally if not all the interfaces are parallel to the oncoming electron beam. Sigl and Kleebe (1993) observed that the film thickness at grain boundaries are smaller than at interphase boundaries and concluded that

---

@ *Production of the mullite ceramic from which the TEM samples prepared is described in Kara (1994).*

this is consistent with Clarke's theoretical approach which states that in such asymmetric cases there is still an attractive van der Waals interaction but since it is weaker the net equilibrium separation will be wider. However, Clarke (1987) did not discuss how to calculate the equilibrium thickness of intergranular films at interphase boundaries where the dielectric properties of the grains either side of the interface are different (Fig. 5.5). The theory has been only established for grain boundaries (the symmetrical case). Composite materials are gaining considerable research interest and therefore there is a need to know the controlling factors of the equilibrium film thicknesses at the interphase boundaries in addition to the grain boundaries.

The other conclusion reached by Clarke (1987) using equation (5.12) was that the dominant effect of the dielectric constants means that equilibrium film thickness is not affected by the crystallographic misorientations across the interface. Although this has been confirmed by HREM investigations on Si_3N_4-Si_3N_4 grain boundaries (Cinibulk *et al.*, 1993a) and SiC-SiC grain boundaries (Fig. 5.8), it is relevant to my experimental results to discuss these conclusions in some detail.

5.7 The calculation of Hamaker constants of interphase boundaries

In order to calculate Hamaker constant of a interphase boundary, the approximate equation suggested by Israelachvili (1992) should be used instead of equation (5.12).

$$H_{\alpha\beta\gamma} = H_{\upsilon=0} + H_{\upsilon>0} \tag{5.13}$$

where $H_{\upsilon=0}$ is the purely zero-frequency contribution and

$$H_{\upsilon=0} = \frac{3}{4}kT\left(\frac{\varepsilon_\alpha - \varepsilon_\beta}{\varepsilon_\alpha + \varepsilon_\beta}\right)\left(\frac{\varepsilon_\gamma - \varepsilon_\beta}{\varepsilon_\gamma + \varepsilon_\beta}\right) \tag{5.14}$$

whereas $H_{\upsilon>0}$ is the dispersion energy contribution and

$$H_{\upsilon>0} = \frac{3h\upsilon_e}{8\sqrt{2}}\frac{\left(n_\alpha^2 - n_\beta^2\right)\left(n_\gamma^2 - n_\beta^2\right)}{\left(n_\alpha^2 + n_\beta^2\right)^{1/2}\left(n_\gamma^2 + n_\beta^2\right)^{1/2}\left\{\left(n_\alpha^2 + n_\beta^2\right)^{1/2} + \left(n_\gamma^2 + n_\beta^2\right)^{1/2}\right\}} \tag{5.15}$$

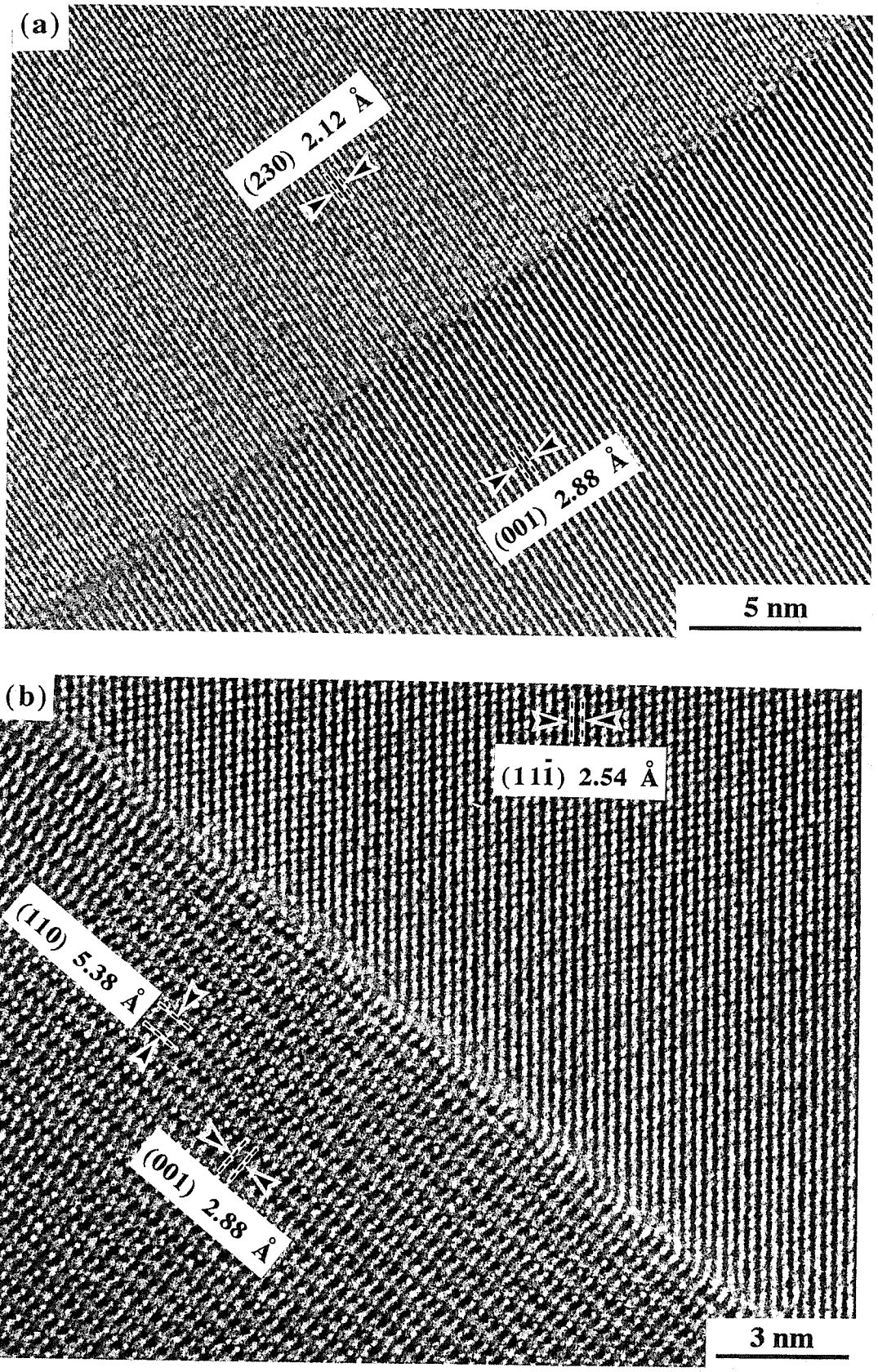

Fig. 5.7 Intergranular film free grain boundaries in monolithic mullite ceramics prepared from a non-stoichiometric mixture of alumina and silica.

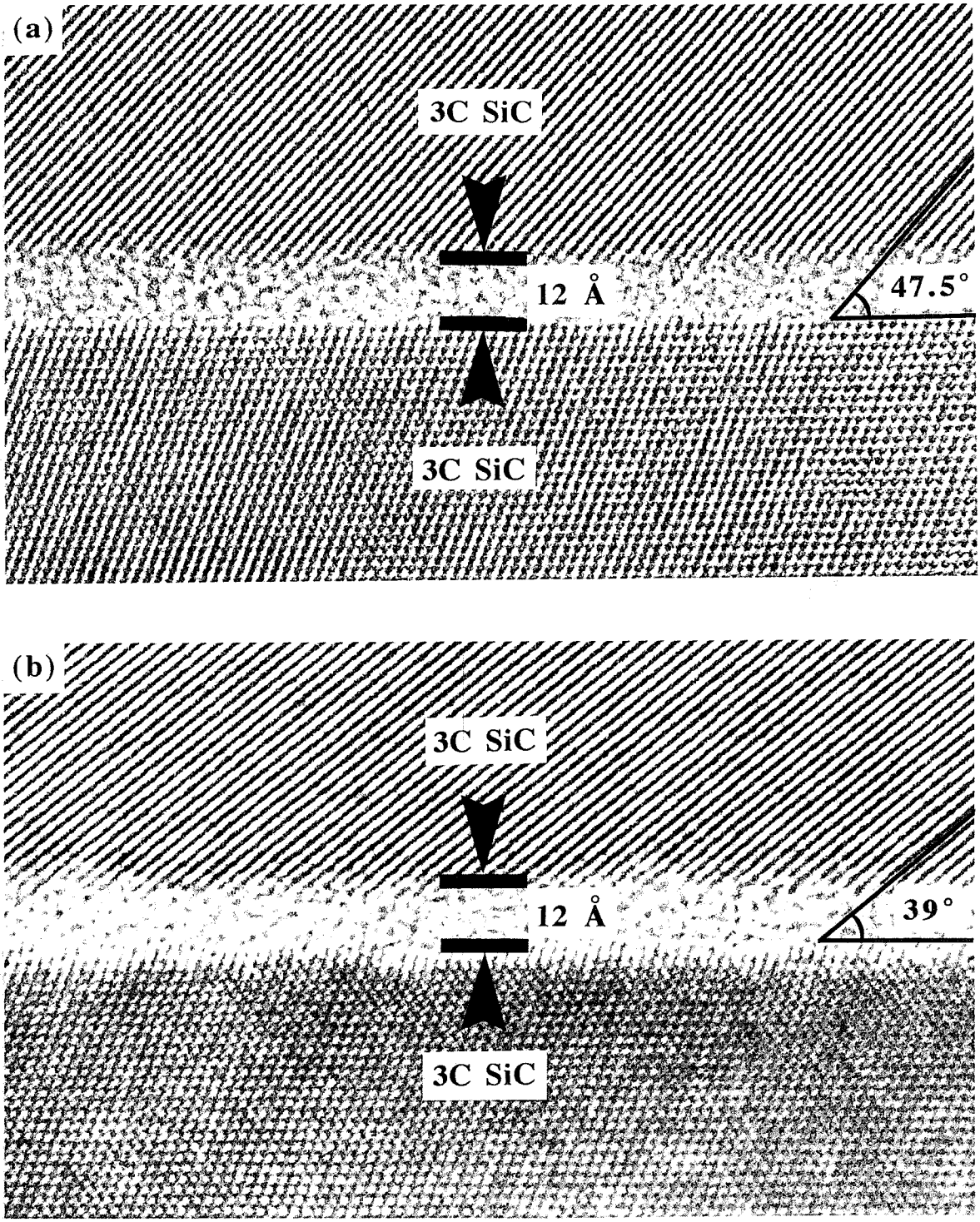

Fig. 5.8 HREM images of two 3C SiC-3C SiC grain boundaries in Si_3N_4-SiC composite prepared from as-received powders show that the film thickness at the interfaces are the same despite the fact that both interfaces have different misorientations across the interface.

where the n_i are the refractive indices and the ε_i are the static dielectric constants of the adjacent grains and the film. υ_e is the characteristic absorption frequency which is assumed to be the same for all three materials, with a value $\approx 3 \times 10^{15}$ s^{-1}. If $H_{\alpha\beta\gamma}$ is positive, the van der Waals force is attractive, otherwise the force is repulsive. The relative magnitudes of these two terms ($H_{\upsilon=0}$ *and* $H_{\upsilon>0}$) at room temperature and at a typical sintering temperature (*e.g.*, 2000°C) will be discussed in Section 5.8.1.

Although the calculations of Hamaker constants at interphase boundaries where the phases α, β and γ are all isotropic are straightforward using equation (5.12), a difficulty arises if the crystals forming the interphase boundary* are anisotropic.

As established (*e.g.*, Moulson and Herbert, 1990), at optical (visible) frequencies the principal dielectric constants (ε) of a material depend on its principal refractive indices (n) according to the following equation:

$$\varepsilon \approx (n)^2 \tag{5.16}$$

The principal refractive indices are determined by the crystal structure. While cubic crystals are isotropic, non-cubic crystals are anisotropic and have different refractive indices depending on the crystallographic direction. Anisotropic materials show either two (hexagonal, trigonal and tetragonal crystals) or three (orthorhombic, triclinic and monoclinic crystals) "principal" refractive indices.

From the above discussion, it can be deduced that the magnitude of Hamaker constant and therefore the equilibrium film thickness will be determined depending on how the anisotropic crystal is oriented with respect to the interface. In other words, misorientation across the interface will effect the equilibrium film thickness. Before any detailed calculations made it is relevant to note that in relation to any effects of misorientation, the dielectric constant and the refractive index normal to the interface are the dominant factors determining the magnitude of the Hamaker constant.

---

* *In addition to its usual usage, the term interphase boundary is used here to describe two dissimilarly oriented grains of chemically and crystallographically the same material but having an orientation dependence of refractive index and dielectric constants.*

In the light of the discussion earlier in this Section, Equation (5.13) can then be used to calculate the equilibrium film thickness between two grains of anisotropic crystal where different orientations of the grain have a different static dielectric constant and refractive index normal to the interface. While this is at best a first approximation to model the effects of crystal anisotropy (and note that this is different from the geometry considered by Parsegian and Weiss (1972) for HgCl crystals), the dominance of the magnitude of the square of the optical refractive index normal to the interface in any calculation of van der Waals dispersion forces ensures that this approximation is not unreasonable.

5.8 Results and discussion

The calculated Hamaker constants taking the values of dielectric constants and refractive indices from Table 5.1(a) and (b) and using equation (5.13) are tabulated in Table 5.2.

The results indicate that the difference in the equilibrium film thickness with changing orientation may well be inside experimental errors for anisotropic crystals with relatively similar dielectric constants and refractive indices in different directions, for example, Al_2O_3 and Si_3N_4. However, the equilibrium film thickness for crystals with large differences in dielectric constants and refractive indices in different directions *e.g.*, rutile (TiO_2) will depend strongly on the dielectric properties of the adjacent grains and therefore crystallographic misorientation across the interface. This is because the difference in the dielectric constant of TiO_2 in different directions creates large differences in Hamaker constant and therefore should create a difference in the stable equilibrium film thickness.

5.8.1 Equilibrium film thickness at interphase boundaries

The findings of larger equilibrium film thicknesses for interphase boundaries in comparison to grain boundaries in a given system has led to a conclusion (Clarke, 1987 & Kleebe *et al.*, 1992) that in such asymmetric cases, there is still an attractive van der Waals interaction but since it is weaker, the net equilibrium separation will be wider.

Compound	Dielectric constant (ε)	Refractive index (n)	Reference[@]
Silica	3.81	1.448	Clarke (1987)
Flint glass*		1.700	Wood (1993)
Boron Oxide		1.485	Bansal & Doremus (1986)
Na-Ca-Si-O		1.510	Sakka *et al.* (1983)
Na-Ca-Si-O-N		1.550	Sakka *et al.* (1983)
47%Si+41%O+12%C	4.40	1.580	Renlund *et al.* (1991)
Silicon oxynitride		1.810	Calculated value
Anorthite (crystalline)		1.585	Kingery *et al.* (1976)
Carbon (amorphous)		2.000	Wood (1993)
Garnet		1.820	Wood (1993)
Yttria (amorphous)		1.920	Kingery *et al.* (1976)
		1.890	Ohring (1992)

(a)

Compound	Dielectric constant (ε)		Refractive index (n)		Reference[@]
	ε // *c*-axis	ε ⊥ *c*-axis	*e* // *c*-axis	*o* ⊥ *c*-axis	
Quartz	4.62	4.4	1.553	1.544	McCrone *et al.* (1978)
Graphite	3.28	2.61	1.810	2.150	Ergun (1968)
Silicon Nitride	8.00		2.060		Clarke (1987)
6H-SiC	10.0	9.70	2.697	2.654	McCrone *et al.* (1978)
h-BN	2.21	4.32	1.65	2.130	Ishii & Sato (1983)
Alumina	11.4	9.49	1.76	1.768	McCrone *et al.* (1978)
Rutile	165.0	83.7	2.903	2.616	McCrone *et al.* (1978)
Mullite	6.80	6.00	1.638	1.642	McCrone *et al.* (1978)

(b)

Table 5.1 The static dielectric constants and refractive indices in the visible of some amorphous and cubic materials (a) and anisotropic crystalline materials (b).

[@] *The references given here are for the refractive index values.*

Interface type	Hamaker Constant (10^{-21}J)	
	pure silica film	47% Si + 41% O + 12% C
Rutile (c // c)@	333	
Rutile (a ⊥ c)	282	
Rutile (a // a)@	240	
SiC-SiC	249-263	198-211
3C SiC-h-BN (⊥ c)	150	
SiC-Si_3N_4	142-146	98-101
SiC-$Y_2Al_5O_{12}$	92	
Si_3N_4-h-BN (⊥ c)	89	
h-BN-h-BN (a // a)@	86	
Si_3N_4-Si_3N_4	82	
SiC-Al_2O_3	78	40
h-BN-h-BN (a ⊥ c)	74	
h-BN-h-BN (c // c)@	64	
3C SiC-h-BN (// c)	50	
SiC-Mullite	49	13-14
Si_3N_4-h-BN (// c)	29	
Al_2O_3-Al_2O_3	24.5-25.5	8*
Mullite-Mullite	11	

Table 5.2 The calculated Hamaker constants for some important grain and interphase boundaries are displayed in decreasing values of Hamaker constants for interfaces containing pure silica and silicon oxycarbide intergranular films. The latter can arise by the solution of carbon into silica liquid at high temperatures and as illustrated in this table could alter the magnitude of Hamaker constant.

@ *These cases are exaggerated, obviously at this condition an interface would not exist and the material would be a single crystal.*

* *Anorthite as an intergranular film.*

However, Hamaker constant (which is the measure of the strength of attractive van der Waals forces across the interface) calculations for numerous interphase boundaries (Table 5.2) using equation 5.13 show that the attractive forces at interphase boundaries are not necessarily smaller than at grain boundaries on the basis that they both contain the same intergranular film. For example, the attractive forces at a SiC-Si_3N_4 interphase boundary are larger than a Si_3N_4-Si_3N_4 grain boundary, but smaller than at a SiC-SiC grain boundary (Table 5.2). Therefore, all other factors being unchanged, the equilibrium film thickness at an SiC-Si_3N_4 interphase boundary should be between those arising at SiC-SiC and Si_3N_4-Si_3N_4 grain boundaries. This is also consistent with the experimental observations that intergranular films at interphase boundaries between Si_3N_4 and $Y_2Si_2O_7$ (Cinibulk and Kleebe, 1993), between Si_3N_4 and $Yb_2Si_2O_7$ (Vetrano *et al.*, 1993) in Si_3N_4 ceramics and between SiC and garnet in SiC ceramics (Sigl and Kleebe, 1993) have been found to be thicker than films at grain boundaries between the matrix grains in the corresponding ceramics.

The other consequences of equation 5.13 discussed by Clarke (1987) and Israelachvili (1992) is that the Hamaker constant will be only negative when the static dielectric constant of the intervening medium is intermediate between those of the two interacting media, *i.e.*, $\varepsilon_\alpha > \varepsilon_\beta > \varepsilon_\gamma$. This condition is thought to be unlikely to be satisfied in practice (Clarke, 1987) since the dielectric constants of the ceramic materials are generally higher than that of silica (likely to be the major constituent in the amorphous film).

However, an example of such a condition can be envisaged between two grains of hexagonal boron nitride (h-BN) which have different dielectric constants in different directions. The dielectric constant of h-BN parallel to *c*-axis is 2.21 while perpendicular to *c*-axis it is 4.32 (Xu and Ching, 1991). The static dielectric constant of silica ($\varepsilon = 3.81$) falls between the dielectric constants of h-BN in two different orthogonal directions. Therefore, if an amorphous SiO_2 film exists between two h-BN grains whose *c*-axes are aligned perpendicular to each other, then the Hamaker constant and the film thickness will be expected to be dominated by repulsive forces since the condition of $\varepsilon_\alpha > \varepsilon_\beta > \varepsilon_\gamma$ ($4.32 > 3.81 > 2.21$) is satisfied (Clarke, 1987 and Israelachvili, 1992).

The theoretical calculations for these particular cases showed that the Hamaker constants are not negative (Table 5.2). Evaluation of equation (5.13) is indicating that it is only negative

when $\varepsilon \approx (n)^2$, an equality which does not apply to most ceramic materials. In practice, for ceramics the refractive index of the intervening medium should be intermediate to those of two interacting media, *i.e.*, $n_\alpha > n_\beta > n_\gamma$ to be able to have negative Hamaker constant and therefore a repulsive force. This is because the dispersion energy contribution always dominates over the entropic zero-frequency contribution in equation 5.13. The effect of zero frequency contribution on the absolute value of Hamaker constant is shown to be very small (Table 5.3).

The temperature effect on the value of Hamaker constant is also displayed in Table 5.3. It can be seen that a pronounced temperature effect on the Hamaker constant occurs only if the material has a very large static dielectric constant (*e.g.*, TiO_2) or a very low refractive index (*e.g.*, Al_2O_3). Therefore, during the Hamaker constant calculations zero frequency term ($H_{\upsilon=0}$) can be ignored for materials such as, SiC, Si_3N_4 and BN to a very good approximation.

Interface type	Hamaker constant with $H_{\upsilon=0}$		Hamaker constant without $H_{\upsilon=0}$	Accumulated error (%) arising between the terms	
	at 25°C	at 2000°C		25-2000°C	with & without $H_{\upsilon=0}$
3C SiC-SiO_2-3C SiC	249.6	253.6	248.95	1.83	0.26
TiO_2-SiO_2-TiO_2	333.0	352.4	330.0	5.5	0.90
Al_2O_3-SiO_2-Al_2O_3	24.55	29.90	23.78	17.89	3.13

Table 5.3 The effect of dielectric constants and temperature on the Hamaker constant and therefore on the film thickness for three different material, one having a high refractive index, the second one having a high dielectric constant and the last one having a low dielectric constant as well as a low value of refractive index.

Thus, the intergranular film thickness is actually determined by the refractive indices of grains and the separating films rather than by the static dielectric constants as established earlier by Clarke (1987). Theoretical and experimental results on a case study are now going to be discussed to show the misorientation effect on the film thickness.

5.8.2 Case study: Effect of misorientation on the film thickness

H-BN is a very interesting material for the study of the possible effect of misorientation on the film thickness at grain and interphase boundaries. Theoretical considerations yield an interesting point for the interphase boundaries between h-BN and SiC containing SiO_2 film. Imagine that there are four possible interphase boundary configurations with different misorientations between 3C-SiC and h-BN as shown in Fig. 5.9.

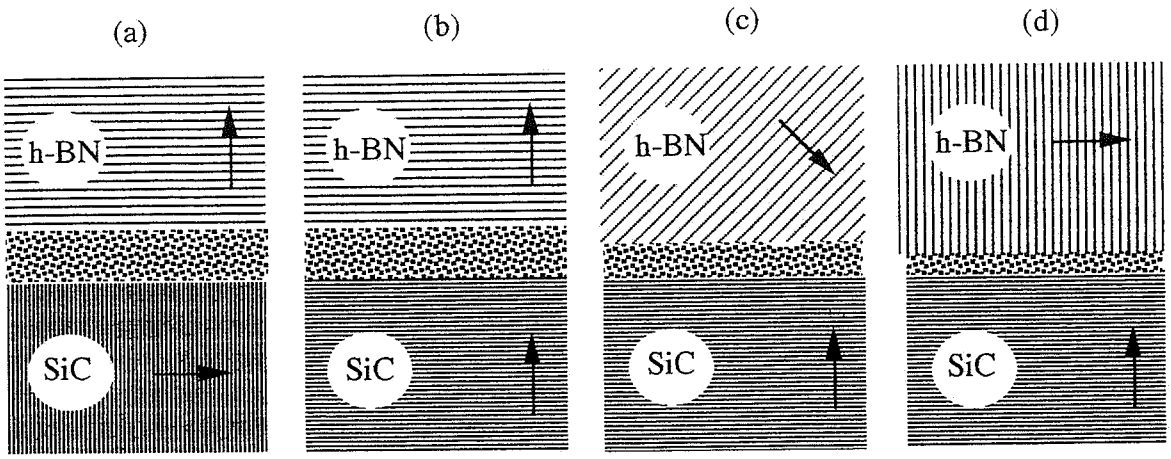

Fig. 5.9. Representative diagrams of some of the possible interphase boundaries between h-BN and SiC. The arrows indicate the stacking direction of (0002) planes of h-BN and (111) planes of SiC, respectively.

The calculations of Hamaker constants revealed that the intergranular film thicknesses in Fig. 5.9(a and b) should be the same although the misorientation is different that in (a) (111) SiC planes are parallel to (0002) h-BN planes while in (b) perpendicular to (0002) h-BN planes. In comparison with these, the film thickness in Fig. 5.9(d) should be thinner since the intergranular film thickness between the *a*-axis direction of h-BN and SiC will be dominated by attractive forces and *c*-axis direction by less attractive forces (see the Hamaker constant values in Table 5.2). Finally, thickness of the film in Fig 5.9(c) where there is an angle between both the orthogonal directions of h-BN and SiC should be intermediate to the extreme misorientations in (a), (b) and (d).

Interphase boundaries oriented similar to the cases illustrated in Fig. 5.9(a)-(c) have been observed in my work and are shown in Fig. 5.10. The film thicknesses are measured to be 12 Å for both the interfaces in Fig. 5.10(a) and (b). This would appear to confirm the theoretical considerations (Clarke, 1987) and experimental results (Cinibulk *et al.*, 1993 and Fig. 5.8 in this Chapter) that the thickness of intergranular films do not depend on the misorientations of the grains if either the interfaces consist of isotropic grains* either side of the interface or as in Fig. 5.9(a) and (b), an isotropic grain is misoriented with respect to the fixed anisotropic grain.

In contrast, the film thickness is smaller, *i.e.*, $\approx$ 6.6 Å in Fig. 5.10(c). In this case, there is a 70° angle between the h-BN planes and the interface. The refractive index normal to the interface of the h-BN grain in this orientation can be calculated from the indicatrix to be 2.05. Therefore, an estimate of the Hamaker constant for the interphase boundary for this particular misorientation can be determined using equation (5.15). Comparison of the Hamaker constant values strongly suggest that the film thickness should be smaller than those observed in Fig. 5.10(a) and (b), as experimental results have suggested.

These experimental observations strongly support the theoretical considerations raised throughout this Chapter that the thickness of intergranular films should be dependent on the misorientation across the interface when the dielectric constants and in particular the refractive indices of the substances are different in different directions, and refutes Clarke's theoretical considerations (Clarke, 1987) which states that the "equilibrium film thicknesses do not depend on the crystallographic misorientations but rather depend on the dielectric properties of the adjacent grains".

In summary, it is theoretically and experimentally established that some interfaces having 'special' misorientations will not be wet. The thicknesses of the films depend on the crystallographic misorientation and also depend on the refractive indices of the adjacent grains and the separating films rather than their dielectric constants. In the following section other factors effecting the film thickness will be examined.

---

* *It is either isotropic or very close to isotropic, e.g., in silicon nitride and alumina.*

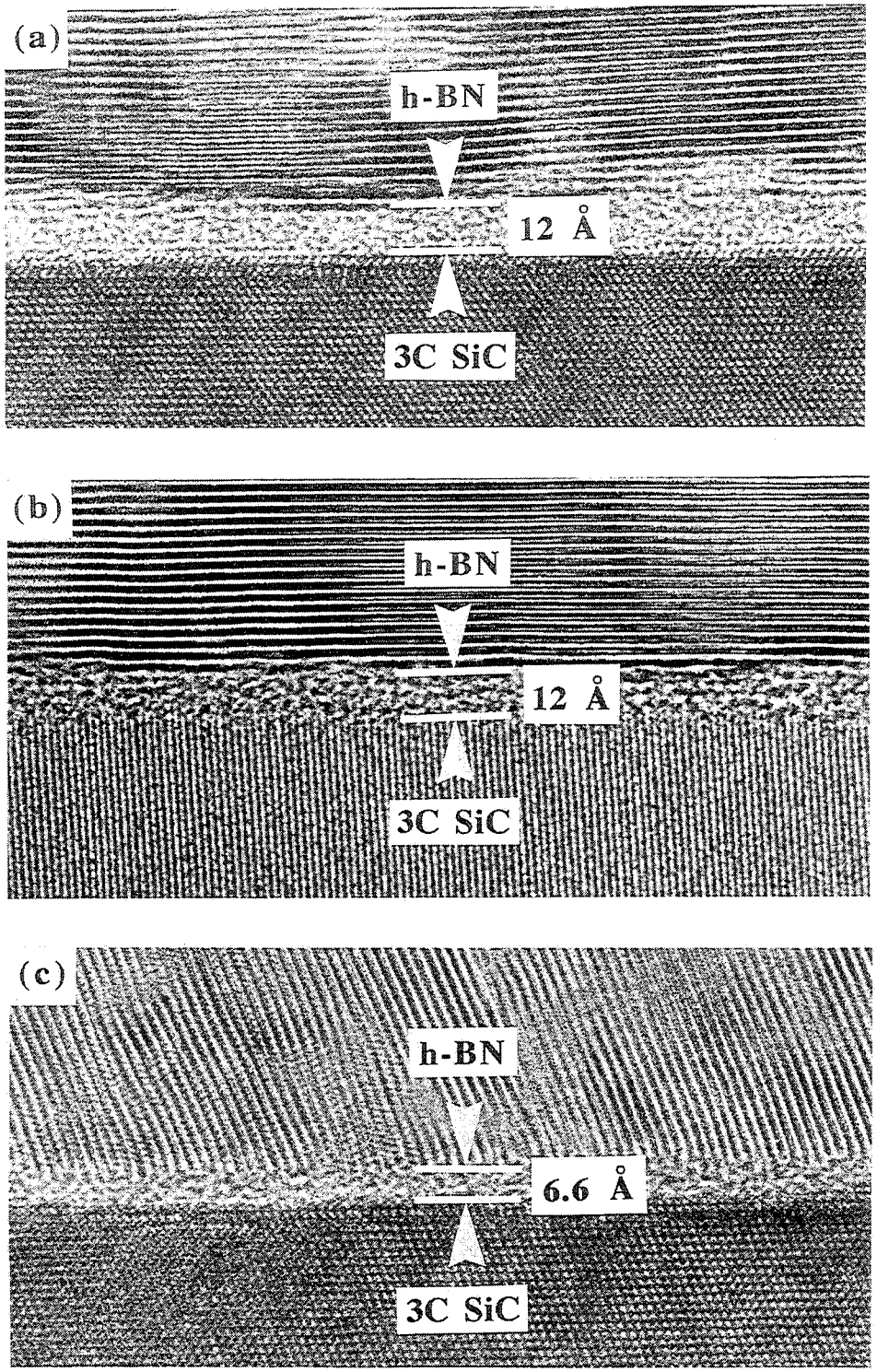

Fig. 5.10 Three differently misoriented interphase boundaries between h-BN and SiC grains showing the effect of misorientation on the film thickness.

5.8.3 Other parameters effecting the equilibrium film thickness

5.8.3.1 The effect of film composition

Examination of the equations (5.10 and 11) reveals that equilibrium film thickness increases with the decreasing ratio of $H_{\alpha\beta\gamma}$ / (Π_{ST} + Π_{EDL}), *i.e.*, the higher the Hamaker constant the lower the equilibrium film thickness. *So, what is affecting the Hamaker constant?*

It has already been shown that the contribution from the zero frequency term, which includes dielectric constants and the temperature effects, does not effect the value of Hamaker constant unless the operating temperatures and dielectric constants are very high. Therefore, there is only one remaining parameter that could effect the Hamaker constant of a particular interface, *i.e.*, the refractive index of the film. It is obvious from equation (5.15) that the higher the refractive index of the film the lower the Hamaker constant and in turn the higher the equilibrium film thickness. An example for SiC-SiC grain boundaries having two different intergranular film compositions is shown in Table 5.2.

The refractive index of the film is determined by its chemical composition. Although the exact chemical compositions of intergranular films have to be known for accurate Hamaker constant calculations, experimental limitations of both interference with adjacent grains and beam broadening during chemical analysis in the electron microscope have in practice meant that this has not been possible to ascertain these with confidence. The chemical analysis that has been undertaken by other workers (*e.g.*, Clarke *et al.* (1981) in Si_3N_4 ceramics) has shown that most of the films in ceramics are amorphous silica mixed with very small amount of Fe, Al, Ca, etc. contamination from the starting powders. In addition, there are some indications that intergranular silica films can, and will, contain some amount of other elements from sintering additives and incomplete reaction elements. For example, nitrogen and yttrium enrichment in silica would be expected in an intergranular film between Si_3N_4 and $Y_2Si_2O_7$ grains, Si-O-C between SiC grains or Si-C-O-N between SiC and Si_3N_4 grains.

In theory, assuming that the exact composition of the film is known, it is then possible to calculate the refractive index and a zero frequency dielectric constant for a mixture of elements in the amorphous intergranular film and then to use these values in the Hamaker constant calculations. There are some calculation methods (Scaife, 1989 and Wakino *et al.*,

1993) of the dielectric constant of a mixture, but dielectric constants can be assumed to be unchanged with changing composition since as established in Section 5.8.1 the contribution from entropic zero frequency on the value of Hamaker constant is very small and can be ignored.

A simple rule of mixtures can be used for the calculation of a refractive index (Babcock, 1977).

$$n_f = n_a a + n_b b + \ldots \tag{5.17}$$

where n_f is the refractive index of the film containing elements a and b with refractive indices of n_a and n_b, whereas a and b are the mol% of constituents of the film.

Thus, according to equation (5.17), the refractive index of mullite (which is a mixture of 3 mol of alumina and 2 mol of silica) is calculated to be 1.67 using the refractive indices of alumina and crystalline silica from Table 5.2. Comparing this calculated value with the measured refractive index of mullite (1.65) indicates that there is not much difference and suggests that equation (5.18) can be used at least for some useful comparisons. The calculated value is higher than the refractive index of amorphous mullite (1.597). However, if the refractive index of one of the constituent material is not known, for example, crystalline Y_2O_3 and Yb_2O_3 which are commonly used sintering aids to densify Si_3N_4 ceramics, then a different approach has to be used to calculate the refractive index of $Y_2Si_2O_7$ and $Yb_2Si_2O_7$ which are the common second phases in liquid phase sintered and heat treated Si_3N_4 materials. So, *what else is determining the ultimate refractive index of a material?*

It is known (Bloss, 1971) that the denser polymorph of a material always has a higher refractive index than the less dense one and that higher atomic weight elements are more effective in slowing light. Therefore, compounds containing high atomic weight elements usually have higher refractive indices (McCrone *et al.*, 1978). For example, Wickersheim and LaFever (1961) reported an refractive index data for amorphous yttria of 1.91 and for yttria mixed with lanthana crystals as 1.95. Note that the atomic weight of lanthanum (139) is higher than yttrium (89). From these considerations it can be assumed that $Yb_2Si_2O_7$ should have a higher refractive index than $Y_2Si_2O_7$ since Yb (173) is heavier element than Y and also the density of Yb_2O_3 (9.17) is higher than Y_2O_3 (5.01).

The effect of nitrogen content on the refractive index of M-SiAlON glasses is reproduced from Lewis (1989) in Fig. 5.11. It is clear that when the nitrogen content increases the refractive index of the glass also increases. This seems to be in contrast to the above approach, (McCrone *et al.*, 1978) that the higher the atomic weight, the higher the refractive index of the glass, since the refractive index of M-SiAlON glasses increases despite nitrogen replacing the slightly heavier element oxygen. However, in this case the replacement of oxygen by nitrogen increases the density of the glass which in turn increases the refractive index (Bloss, 1971). It is believed (Lewis, 1989) that nitrogen by replacing oxygen increases the density of SiAlON materials because nitrogen has a superior ability for cross linking the network structure of oxynitride glass. Note that nitrogen atoms are capable of bridging three network tetrahedral groups whereas oxygen atoms are capable of bridging only two.

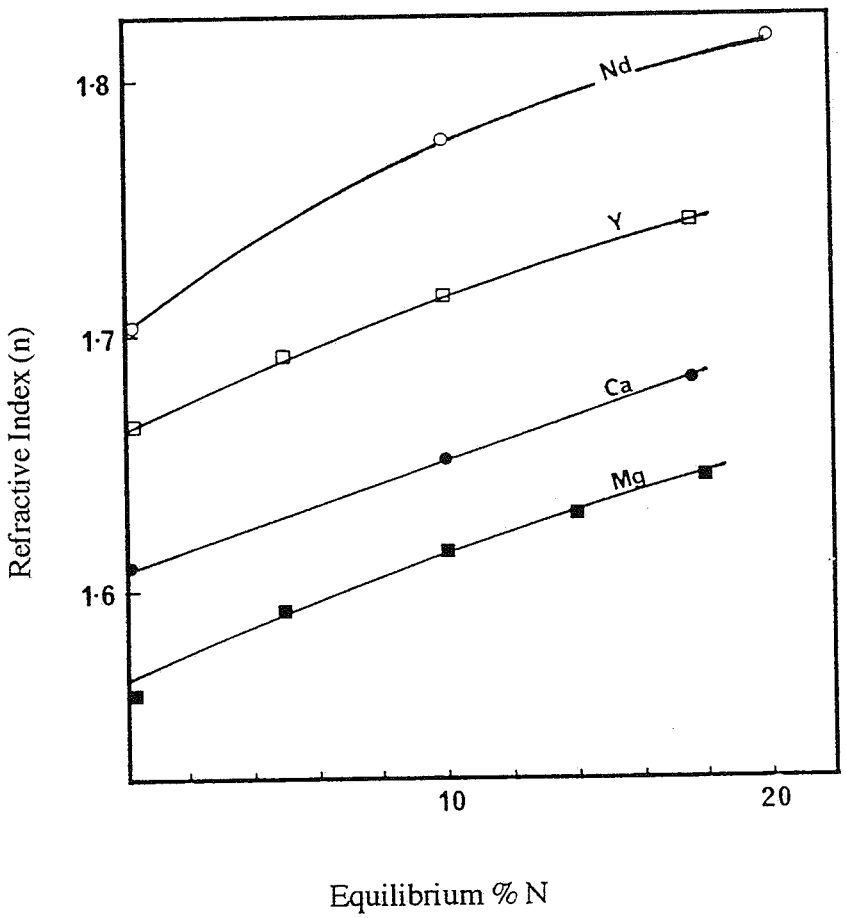

Fig. 5.11 Change in the refractive index of M-Si-Al-O-N as a function of equilibrium nitrogen percentage (after Lewis, 1989) where M = Mg, Ca, Y and Nd. Note also that for a fixed percentage of nitrogen the refractive index of SiAlON glasses increases with increasing atomic weight of the element from Mg to Nd.

It is relevant to examine a case where two Si_3N_4 grains are separated by a supposedly pure silica film and to assume that 10% nitrogen is in it, but undetected, as has been claimed by Vetrano *et al.* (1993). They carried out EDS analysis of amorphous phases in sintered Si_3N_4 doped with 5 vol% Yb_2O_3 and detected a high level of oxygen but no nitrogen. On the basis of a detection limit determined here due to overlap with carbon (from a coating) and the high level of oxygen, they concluded that at least 10 at% nitrogen could exist in the amorphous film. From Fig. 5.11 the effect of 10% nitrogen is to increase the refractive indices of the SiAlON glasses by $\approx 4\%$. This increases the refractive index of silica from 1.45 to 1.51 and in turn decreases the Hamaker constant from 82 to 65×10^{-21} J. This indicate that a small amount of nitrogen enrichment in the film can effect the film thickness significantly.

How do these theoretical considerations relate to experimental observations?

Some of experimental observations on the thickness of intergranular films are summarised in Table 5.4. The immediate conclusion arising from the results is that film thicknesses at interphase boundaries are always larger than the film thicknesses at grain boundaries.

One of the most studied materials by TEM is sintered Si_3N_4 with the addition of Y_2O_3 as a sintering aid. It has been observed that the film thicknesses at interphase boundaries between $Y_2Si_2O_7$ and Si_3N_4 are higher than the film thicknesses at the grain boundaries between two Si_3N_4 grains (Cinibulk and Kleebe, 1993). Although Clarke's proposal is not always true according to the Hamaker constant calculations and the experimental observations reported in this Chapter, in this case this result is expected. From the theoretical Hamaker constant calculations, the film thickness at the interphase boundary between $Y_2Si_2O_7$ and Si_3N_4 should in theory be wider than a Si_3N_4-Si_3N_4 grain boundary, assuming that the film is amorphous silica and that the refractive index of crystalline $Y_2Si_2O_7$ is ≈ 1.67 (calculated using equation 5.17 using the refractive indices of amorphous Y_2O_3 and crystalline SiO_2).

Sigl and Kleebe (1993) observed that the thickness of intergranular films at SiC-SiC grain boundaries were slightly less than at SiC-$Y_3Al_5O_{12}$ interphase boundaries in pressureless sintered α-SiC powder mixed with yttrium aluminium garnet to promote densification. This is also expected from the Hamaker constant calculations (Table 5.2).

Interface type•	Flux used	Film composition (+SiO_2)	Film thickness (Å)	
			GB*	IB@
Si_3N_4-$Yb_2Si_2O_7$(1)	5 vol% Yb_2O_3 + 0.5 vol% Al_2O_3	Yb = Si	10	25
Si_3N_4-$Yb_2Si_2O_7$(1)	10 vol% Yb_2O_3 + 0.5 vol% Al_2O_3	Yb at GB	10	25
Si_3N_4-Si_3N_4(2)	5 vol% Yb_2O_3 + 0.25 vol% CaO		13	
Si_3N_4-Si_3N_4(3)	5 vol% Yb_2O_3 + 0.5 vol% Al_2O_3§	Yb/Si < $Yb_2Si_2O_7$	10	
	after oxidation		8	
Si_3N_4-$Y_2Si_2O_7$(3)	5 wt% Y_2O_3 + 1 wt% MgO	N, Mg, Al, Y	12	
	after oxidation	≈ SiO_2	9	30
Si_3N_4-Si_3N_4(2)	1 wt% Y_2O_3 + 0.2 wt% Al_2O_3		10	
Si_3N_4-Si_3N_4(2)	10 wt% Y_2O_3 + 2 wt% Al_2O_3		15	
Si_3N_4-Si_3N_4(2)	5 wt% Y_2O_3		15	
Si_3N_4-Si_3N_4(2)	5 wt% Nd_2O_3		15	
Si_3N_4-?(2)	5 wt% Sc_2O_3		15	25-30
Si_3N_4-Si_3N_4(2)	5 wt% ZrO_2	no Zr	5	
Si_3N_4-Yb_2SiO_5(2)	10 vol% Yb_2O_3	Yb at GB	10	35-40
Si_3N_4-Si_3N_4(4)	5 wt% CeO_2 + 1 wt% Al_2O_3	CeSiAlON	9	
Si_3N_4-Si_2N_2O(5)	2 wt% MgO		8	15
SiC-$Y_2Si_2O_7$(6)	6 wt% Y_2O_3 + 1.5 wt% Al_2O_3	YSiAlO		50-100
SiC-Si_3N_4(6)	6 wt% Y_2O_3 + 1.5 wt% Al_2O_3	Higher Al, no Y		10-20
SiC-$Y_3Al_5O_{12}$(7)	5 or 10 vol% $Y_3Al_5O_{12}$		10	12

Table 5.4. The experimental film thicknesses of some important grain and interphase boundaries in monolithic ceramics and ceramic matrix composite materials.

• *(1) Vetrano et al. (1993); (2) Kleebe et al. (1992); (3) Cinibulk and Kleebe (1993); (4) Kleebe and Cinibulk (1993); (5) Cinibulk et al. (1993a); (6) More et al. (1991); (7) Sigl and Kleebe (1993).*

* *Grain boundary between matrix grains.*

@ *Interphase boundary between a matrix grain and a secondary phase.*

? *Secondary phase is not given.*

§ *Heat treated at 1250°C under 0.1 MPa N_2 for 12 h to devitrify the secondary phase.*

The observed film thicknesses at interphase boundaries between $Y_3Al_5O_{12}$-SiC (12 Å) and $Y_2Si_2O_7$-Si_3N_4 (> 30 Å) are quite different although the film thicknesses at the grain boundaries between SiC-SiC and Si_3N_4-Si_3N_4 are almost the same (≈ 10 Å) as shown in Table 5.4. This difference could have arisen due to different crystallisation effect. If there was any garnet dissolved in the film at the $Y_3Al_5O_{12}$-SiC interphase boundary, the film thickness should have been much greater than that between SiC-SiC which could mean that most of the sintering additive crystallised as $Y_3Al_5O_{12}$. On the other hand, in the case of Si_3N_4-$Y_2Si_2O_7$ interphase boundary the film could contain some dissolved Y that the sintering additive has not been completely crystallised. Bearing this in mind, further calculations assuming that some amount of Y incorporated to the silica film which could increase the refractive index of silica (Fig. 5.11) showed that the film thickness at Si_3N_4-$Y_2Si_2O_7$ interphase boundaries should be higher than a film at $Y_3Al_5O_{12}$-SiC interphase boundary, as experimentally observed.

Kim *et al.* (1994) also observed very thick anorthite films between sapphire bicrystals, but they did not comment on why the films were thicker than the silica films between alumina grains (Hansen and Philips, 1983). Anorthite is composed of CaO, Al_2O_3 and $2SiO_2$. The refractive indices of both alumina and calcia are higher than that of silica. This will increase the refractive index of the film from 1.448 for silica to over 1.60 if the film is anorthite and substantially decrease the value of Hamaker constant (Table 5.2) leading to an increase in the film thickness as observed by Kim *et al.* (1994).

Most significantly, Tanaka *et al.* (1994) showed that the addition of Ca^+ to Si_3N_4 increases the equilibrium film thickness in comparison to undoped material. Doped samples contained 80, 220 and 450 ppm Ca and the film thickness was found to be 10 Å for undoped material and 7, 11 and 15 Å for the doped samples, respectively. They calculated the CaO concentration in the film from PEELS analysis which showed that the 80 ppm doped sample had a $CaO/(CaO+SiO_2)$ ratio of 1.5 mol%. Again this result can be explained in terms of the magnitude of the Hamaker constant. It can be predicted that replacing Si with Ca^+ in silica can increase the refractive index of the film since Ca is a heavier element. In fact, increases in the refractive index of silica with increasing amount of CaO is presented in Bansal and Doremus (1986). Any increase in the refractive index of the film is going to decrease the Hamaker constant and hence increase the film thickness as experimentally observed by

Tanaka *et al.* (1994). However, a very small addition of CaO may not effect the refractive index and it is also obvious here that 80 ppm doping decreased the film thickness unlike the expectations. An alternative explanation to this special case will be reviewed in Section 5.8.3.2 (also see Tanaka *et al.*, 1994).

5.8.3.2 Combined effect of repulsive forces ($\Pi_{ST} + \Pi_{EDL}$)

In addition to changes in the Hamaker constant $H_{\alpha\beta\gamma}$, the degree of epitaxial alignment (η_o=1 for perfect alignment) can also change the equilibrium film thickness. Smaller values of η_o will decrease the value of the equilibrium thickness. For example, Clarke (1987) showed that if η_o is decreased from 1 to 0.5, the film thickness decreases from $\approx$ 2 nm to 1.5 nm.

As shown in Fig. 5.12, the higher the structural correlation length (ξ), the higher the equilibrium film thickness. Some elements like Ca^+ can disrupt the degree of epitaxy of the intergranular film to the attached grains and can decrease the correlation length and decrease the strength of repulsive steric forces. This will decrease the equilibrium film thickness.

The other parameter which can effect the value of steric forces is a. The value of this term which is the free energy difference per unit volume between the ordered and disordered (amorphous) structure can be assigned knowing the heat of melting of the intergranular film, found by using the JANAF tables (Stull and Prophet, 1971). The heat of melting cristobalite to form amorphous silica has the value of 400 MJm^{-3}. The heat of melting of impure intergranular silica films will be determined by the composition of the intergranular film and the refractoriness of the constituents. As a result more refractory constituents can lead to an increase in the film thickness.

The composition of films can effect the formation of an electrical double layer at the interfaces in addition to changing the refractive index value of the film. A film composition close to stoichiometry will reduce space charge effects (electrical double layer) in the film thus lowering the repulsive forces acting across the interface. The incorporation of impurities will lead to a higher space charge in the film and thus higher repulsive forces which stabilise a film with larger thickness (Kleebe *et al.*, 1992).

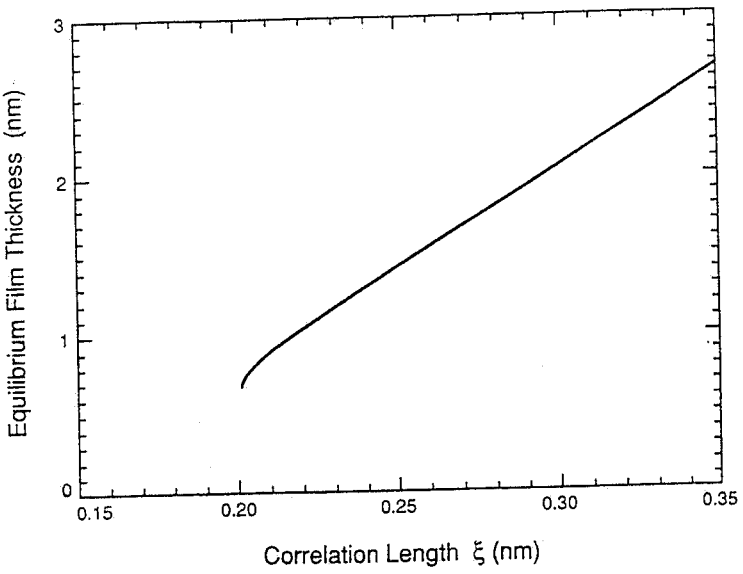

Fig. 5.12 Equilibrium film thickness as a function of the structural correlation length.

It can also be deduced that the higher the value of Π_{EDL} (which is inversely proportional to the Bjerrum length (b_L) in equation 5.8) the higher the equilibrium film thickness. The rearranged equation of 5.9 for a easy calculation of (b_L) is:

$$b_L = \frac{1.670658\text{x}10^{-5}}{\varepsilon T} \tag{5.18}$$

The parameters that can change the Bjerrum length are the composition of the film and the operating temperature, *i.e.*, the higher both the dielectric constant of the film and the fabrication temperature, the lower the Bjerrum length and the higher Π_{EDL}, and as a result the equilibrium thickness increases. For example, the Bjerrum length is 2.18 nm for silica at 2000 K, whereas it is 1.9 nm for silicon oxycarbide. Therefore, if the composition of amorphous phase between two SiC grains is close to silicon oxycarbide the film thickness would be higher than that of containing a pure silica film. It can therefore be concluded that an increase in the refractive index of a film has a double effect on the equilibrium film thickness *(i)* by decreasing the Hamaker constant and (ii) by decreasing the Bjerrum length, both which serve to increase the film thickness.

Recently, the electrical double layer effect on the film thickness has been shown (Tanaka *et al.*, 1994). Although they have not discussed the contribution from dispersion forces, they proposed that the addition of Ca^+ to the film has a dual effect. The first one is that Ca^+ can disrupt both the network structure of the silica film and the degree of epitaxy to the silicon nitride grains, decreasing the structural correlation length and hence decreasing the magnitude of the steric repulsive forces. Secondly, Ca^+ can provide a charged species to the material, provided it absorbs to the grain surfaces. This may result in the formation of an electrical double layer. Since Ca^+ is known to be a silica network modifier and since small additions of Ca^+ (less than 1 mol%) cause a decrease in viscosity of several orders of magnitude, it might be expected that the strongest effect of minor Ca^+ addition will be to decrease the steric force and cause a reduction in the film thickness. Further additions of absorbed Ca^+ can be expected to increase the repulsive electrical double layer forces, leading to increases in film thickness.

The effect of surface potential on the equilibrium thickness with increasing values of inverse Debye length is shown in Fig. 5.13 (from Tanaka *et al.*, 1994). The magnitude of Debye length (the effective thickness of the double layer, $1/\kappa$) depends solely on the properties of the liquid (Israelachvili, 1992). The relation between inverse Debye length and electrical double layer term has been presented in equation 5.8.

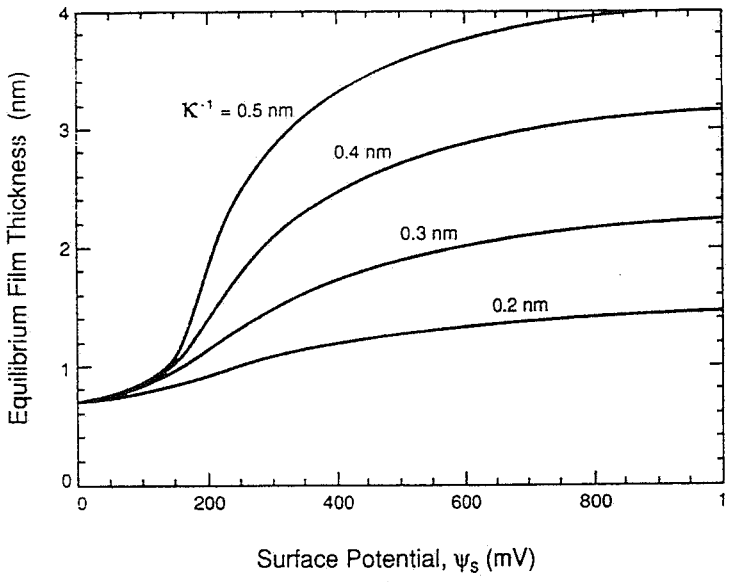

Fig. 5.13 Equilibrium film thickness as a function of the surface potential.

5.8.3.3 The effect of liquid volume on the film thickness

Clarke's model predicts that the equilibrium film thickness should be independent of the amount of additives used for processing. The studies of Greil and Weiss (1982) support this prediction, in that the intergranular film thickness is rather insensitive to the content of amorphous secondary phase. Greil and Weiss found that as the liquid phase volume was increased, the volume of second phase at the triple junctions was increased whereas the film thickness remained almost the same.

In contrast to these trends, Alexander *et al.* (1990) observed thicker interfacial films (>3 nm) for yttria and magnesia doped SiC whisker reinforced alumina composites in comparison to zirconia-doped composites where thinner interfacial films (<1 nm) were observed. They attributed the reason to the increase in the amount of liquid phase.

Turan and Knowles (1995) also reached a similar conclusion that the thickness of the intergranular films depends on the amount of liquid phase retained after cooling to room temperature by comparing the film thicknesses in the composites prepared from as-received powders and the composites prepared from the deoxidised compact which was supposed to have far less amount of liquid making agents. The thickness of the film in the composite prepared from deoxidised compact was $\approx$ 7.5 Å, less than the thickness of intergranular films ($\approx$ 12 Å) seen in the composites made from the as-received powders without any deoxidation step. Although these results are in disagreement with the results obtained by Greil and Weiss (1982), it is relevant to note that the diffuse dark field technique used by Greil and Weiss to measure the equilibrium film thickness has recently been shown to be very unreliable (Cinibulk *et al.*, 1993). Thus, in order to explore in a systematic way the possible effect of liquid phase content on the intergranular film thickness, it is necessary to use relatively sophisticated techniques such as HREM and/or Fresnel fringe imaging. The results obtained from such techniques will be discussed in detail in the next Chapter.

The effect of zero volume content of liquid/glass is the obvious one that the film thickness would be zero as observed in pressureless sintered SiC doped with B and C although it should be remembered that Clarke (1987) proposed a high refractive index of SiC causing a high Hamaker constant value and thus no film at the interface. On the other hand, mullite-mullite grain boundaries should contain the thickest intergranular films among the important ceramic materials, but as shown in Fig. 5.7.

Probably the most important study to determine the liquid volume effect was done by Kleebe *et al.* (1992). They investigated the film thickness variation as a function of liquid volume by preparing two Si_3N_4 materials with different amount of sintering additives. Both the materials contained identical Y_2O_3 / Al_2O_3 ratio of 10, but two specimens were fluxed with 1 wt% Y_2O_3 + 0.2 wt% Al_2O_3 and with 10 wt% Y_2O_3 + 2 wt% Al_2O_3, respectively. They found that the film thickness increased from 10 Å to 15 Å with an increase in liquid volume content. However, they concluded that the film thickness is effected by the composition of the film rather than the amount of available liquid since the Y and Al concentration in the film would be greater for the specimen containing higher amount of sintering additives. The concentration of heavy elements in the film would increase the refractive index of the film and this in turn would decrease the Hamaker constant value which would result in higher film thickness as observed.

Due to the strong effect of film composition on the equilibrium film thickness, it is very difficult to determine the volume effect unless the composition of the film is more accurately known than at present.

5.9 Conclusions

In this Chapter, Clarke's theory which states that "the equilibrium thickness of intergranular films are dependent of the dielectric constants of the constituents but does not depend on the crystallographic misorientation of the boundary" has been discussed and put to a test to see whether or not it can explain the experimental observations.

As a result, the above statement is once more experimentally proven to be true for isotropic crystals and/or anisotropic crystals with small differences in different directions in the dielectric constants and refractive indices.

Since Clarke's theory is only established for the calculations of the equilibrium film thicknesses of grain boundaries, by accepting Clarke's theory is valid for isotropic crystals, his theory can be extended to enable the calculation of Hamaker constants of interphase boundaries and grain boundaries in anisotropic crystals on the assumption that the refractive index of the anisotropic material normal to the interface is important in the determination of

the Hamaker constant. Both the experimental and theoretical results showed that the equilibrium film thicknesses are also dependent on the misorientation of the interface, since the dielectric properties of the anisotropic crystals change with misorientation.

It is also established that the thickness of the film could only be dominated by the repulsive forces when the refractive index rather than the dielectric constant of the intergranular film is intermediate to the refractive indices of the interacting media since the approximation $\varepsilon \approx (n)^2$ is not valid for engineering ceramic materials. In addition, the static dielectric constants do not contribute significantly to the value of Hamaker constant and their contribution can be ignored.

For a given interface, the lower the ratio of $(H_{\alpha\beta\gamma} / \Pi_{ST} + \Pi_{EDL})$, the higher the equilibrium film thickness. A high equilibrium thickness will arise when the refractoriness and the refractive index of the intergranular film increases.

In summary, Clarke's statement should be modified as "*The equilibrium film thickness depends on the refractive indices of the adjacent grains and is largely effected by the refractive index of the intergranular film. The film thickness also depends on the misorientation across the interface for systems containing highly anisotropic crystals separated by a given composition*".

Chapter 6

Characterisation of Interfaces in Si_3N_4 - SiC Composites

6.1 Introduction

In this Chapter, experimental results on the structure of individual interfaces that occur between SiC-SiC, Si_3N_4-Si_3N_4, SiC-Si_3N_4, SiC-BN and Si_3N_4-BN in the Si_3N_4-SiC composites will be presented and discussed.

To recap, the composites were received in four different batches. Two batches were prepared from as-received starting powders containing 10 and 20 wt% Si_3N_4 and two batches were prepared from deoxidised green compacts containing 10 and 20 wt% Si_3N_4. The general microstructure of the composites presented in Chapter 3, 4 and 5 showed that the composites prepared by the same route but containing different amount of Si_3N_4 were essentially the same except for their densities. In contrast, the microstructure of composites made from as-received powders and deoxidised green compacts were significantly different. Therefore, two main sections of this Chapter will be devoted to the characterisation of interface structure in these two different families of composites.

The microstructural observations showed that amorphous intergranular films tend to be present at the interfaces. The thickness of these films has to be measured to establish the existence of equilibrium film thickness and the factors effecting the thickness. Hence, before discussing the structure of individual interfaces, it is necessary to test the accuracy of three main techniques (HREM, Fresnel fringe defocus and diffuse dark field (DDF) imaging techniques) available for the detection of intergranular films at the interfaces.

6.2 Assessment of accuracy of TEM techniques on the detection and measurement of film thickness

HREM, Fresnel and DDF imaging techniques have been tested by Cinibulk *et al.* (1993) who concluded that the HREM technique gives ± 1 Å accuracy on the intergranular film thickness measurements and that the Fresnel technique measures the thickness 20 to 35 % higher than the HREM technique, whereas diffuse dark field measurements are 50 to 100 % higher than those measured by HREM. This is the only work of its kind although Clarke (1979) carried out a similar study, but at his time the resolution of the microscopes were not as good as the current generation of microscopes. Hence, there is a need to carry out a similar work either to support the results obtained by Cinibulk *et al.* (1993) or to deny it.

For this purpose, a SiC-SiC interface was imaged using Fresnel defocus imaging, diffuse dark field imaging and HREM techniques. The Fresnel series and the diffuse dark field image of the entire interface are shown in Fig. 6.1(a, b and c). The HREM images in Fig. 6.2 show (a) a small part of the grain boundary between two 3C SiC grains and (b) the interphase boundary between 3C and α-SiC grains. All techniques indicate the presence of an intergranular amorphous film at the interface. Note that the images shown in Fig. 6.1 and 6.2 were taken using two different microscopes since the JEOL 4000-EX high resolution electron microscope did not have a small enough objective aperture to obtain high contrast Fresnel and diffuse dark field images. First the interface was aligned edge-on to the electron beam on the JEOL 4000-EX while the crystals were tilted to low index zone axes to obtain a high quality HREM image. Fresnel and diffuse dark field images from the same interface were obtained subsequently on a JEOL 2000-FX[@]. Cinibulk *et al.* (1993) also obtained the images from a single Si_3N_4-Si_3N_4 grain boundary, but instead of showing Fresnel fringe images of the ***same*** grain boundary as the HREM image they presented a Fresnel series from a different grain boundary. Therefore, it is difficult to comment on their results.

In this study, the thickness of the film is measured to be approximately 13±1 Å from HREM images using the methodology described in Section 2.6.1, but varies as a function of position along the interface, particularly at a region that can be described as a small triple junction (indicated with an arrow in Fig. 6.1(a)).

[@] *It is advisable to apply the HREM technique first since the limited specimen tilts on the HREM and stringent conditions of the technique do not always enable good HREM images to be obtained.*

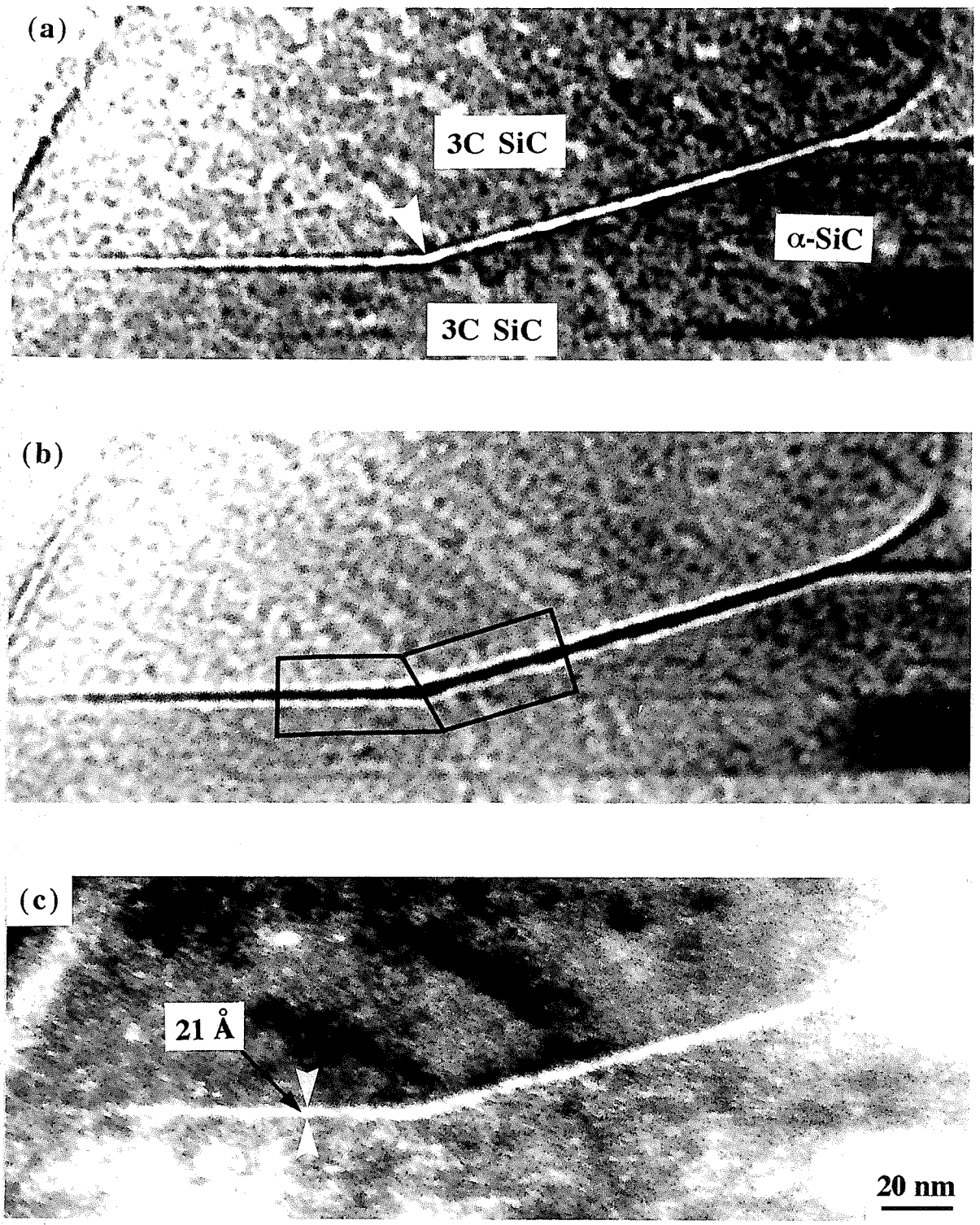

Fig. 6.1. (a) underfocus, (b) overfocus Fresnel fringe images obtained from an edge-on interface between SiC grains and (c) a diffuse dark field image from the same interface. Notice that the contamination and damage evident in above figures arises due to the lengthy times required for the edge-on alignment of the interface and also because of the high voltages used in HREM.

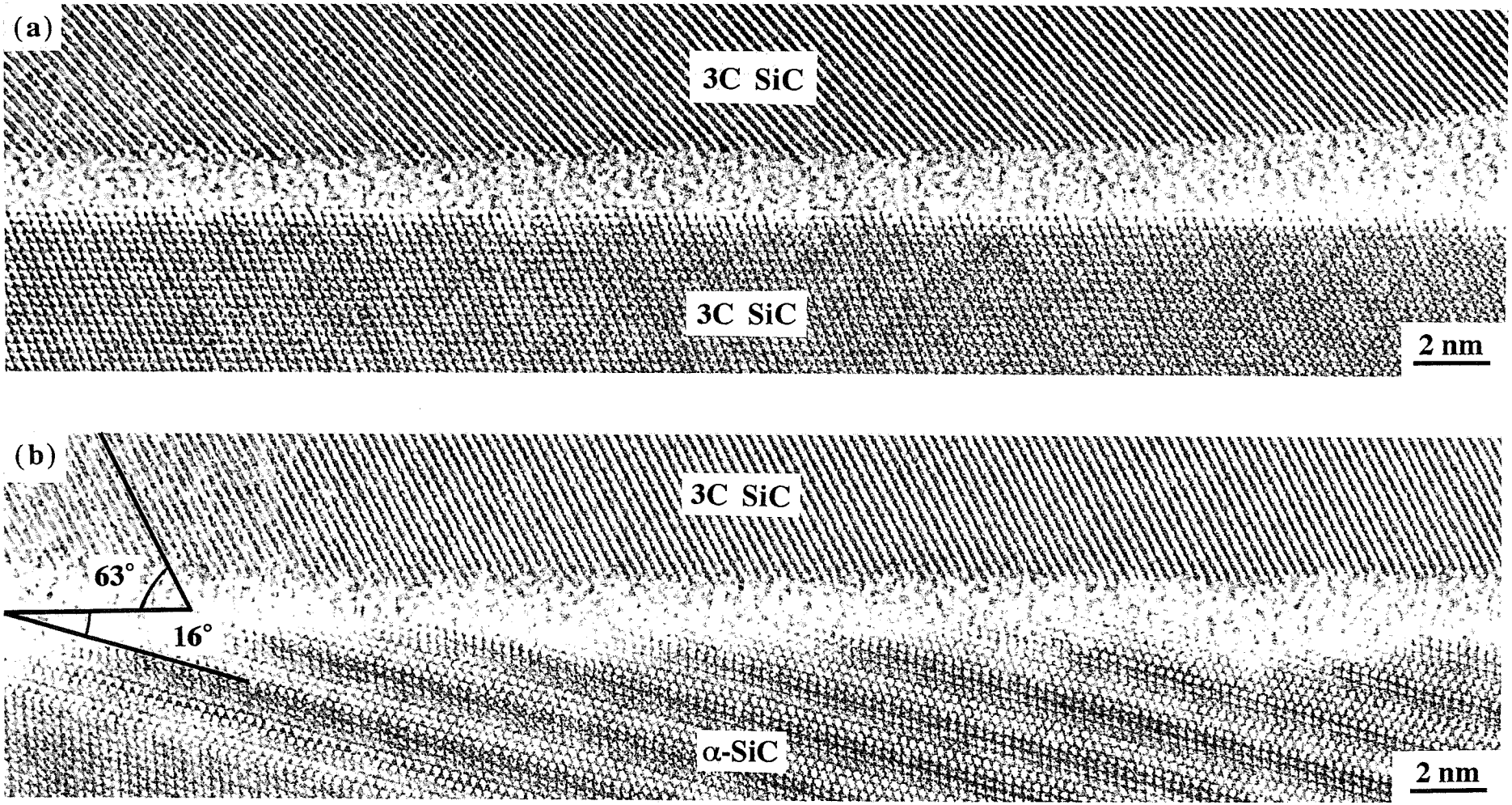

Fig. 6.2 The HREM images of interfaces from boxed areas shown in Fig. 6.1. Note that the entire interface is cut into two parts: (a) shows the grain boundary between two 3C SiC grains whereas (b) shows an interphase boundary between 3C and α-SiC grains.

Here, one of the advantages of HREM over the other techniques in measuring the intergranular film thickness accurately is that an internal calibration for every single negative is possible while for the other techniques one has to rely on rather general calibration methods. Bearing this in mind, rather fortunately the composite also contains 6H SiC whose principal interplanar-spacing is ≈ 15 Å which is easily within the resolution limit of current transmission electron microscopes. More importantly, its lattice fringes are visible at the typical magnifications (100000-150000) of Fresnel imaging conditions. Therefore, this can be used to calibrate the magnifications used during Fresnel imaging of the interfaces and during the subsequent printing.

Fresnel imaging technique was performed using a JEOL 2000FX fitted with a LaB_6 filament. This provides a good coherence and brightness at the low beam convergences necessary to give good Fresnel fringe visibility and also enables short exposure times to minimise specimen drift. The through focal series contained 21 negatives in total taken from underfocus (ΔF = - 3830 nm) to overfocus (ΔF = + 3830 nm). From the through focal series fringe spacings were measured and plotted against corresponding defocus values (Fig. 6.3). Although there should be 21 data points, only 15 of them were measured since most of the negatives were taken around the Gaussian focus *in order to find the exact position of the Gaussian focus* (where ΔF = 0 nm) and low fringe visibility at low defocus values prevented accurate measurements of Fresnel fringe spacings.

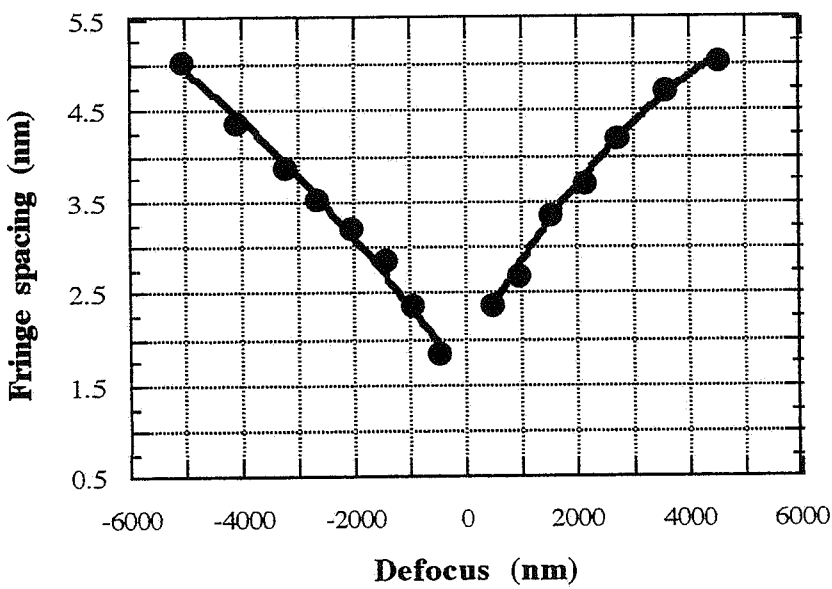

Fig. 6.3 A plot of Fresnel fringe spacing against defocus for a part of the interface where two 3C SiC grains are separated with an intergranular film shown in Fig. 6.2.

The film thickness obtained by extrapolating the high defocus values to low defocus values and fringe spacing at a defocus where the underfocus and overfocus curves meet corresponds to the film thickness, which is ≈ 16 Å. This is ≈ 23 % higher than the value obtained from HREM measurements. From the plot, it can be seen that there exists two different film thicknesses that, by separately extrapolating underfocus and overfocus values, to be 14 Å and 18 Å, respectively. The value obtained from underfocus measurements is within the experimental errors and deviates 1 % from HREM measurements whereas the overfocus measurements deviates by 38 %.

Although these results are obtained from one grain boundary, it can be deduced from these results that thickness measurements using the methodology of Ness *et al.* (1986) gives a higher film thickness in comparison to the methodology used to measure film thickness from HREM micrographs (Cinibulk *et al.*, 1993). Ness *et al.* (1986) showed that the use of low defocus values ($\Delta F < 300$ nm) measures the film thickness more accurately, but as pointed out earlier the fringes are not visible at low defocus values. Although digitisation of experimental images can help to find the first fringe maxima, Cinibulk *et al.* (1993) showed that digitisation does not improve the deviation from HREM results.

The film thickness measured as ≈ 21 Å from DDF images which deviates ≈ 60 % from that of HREM measurements and is in line with the results obtained by Cinibulk *et al.* (1993).

In summary, although the thickness value obtained from HREM is probably the most reliable technique, Fresnel imaging technique can be used reliably when the HREM technique is not available. The advantage of the Fresnel technique is that it can be performed in any transmission electron microscope. In particular, if the underfocus data alone is extrapolated to Gaussian focus, the results come close to HREM measurements. This could also save time and negatives if the Fresnel technique is solely used for thickness measurements. In this work, diffuse dark field technique on thickness measurements have not been performed since the earlier examinations (Clarke, 1979 & Cinibulk *et al.*, 1993) as well as the above experiment showed that it gives much higher values in comparison to the other techniques, but it was nevertheless used as a complementary technique whenever it was possible.

6.3 Interface structures in the composites made from as-received powders

6.3.1 Interfaces between SiC grains

There are basically three types of interfaces between SiC grains: the first two are grain boundaries between either two α-SiC grains or two β-SiC grains and the third type is an interphase boundary between β and α-SiC grains.

The application of TEM techniques revealed that most of these interfaces are wet with intergranular films, while some are free of these films. Examples of intergranular films at 3C-3C SiC grain boundaries have already been shown in Fig. 5.7. and Fig 6.1. Further observations at different interfaces showed consistently that the thickness of intergranular films are around 13±1 Å, but as can be seen in Fig. 6.2(a), the thickness of the film is as high as 30 Å towards the triple junction (to the right edge of the Figure). Therefore, the thickness measurements are obtained at points away from these triple junctions. Intergranular-film-free interfaces were also observed at 3C SiC-3C SiC grain boundaries and were generally $\Sigma = 3$ coherent twin boundaries (*e.g.*, the interface labelled as *b* in Fig. 5.1).

The interphase boundaries between 3C and α-SiC grains were mostly wetted with films apart from 'special' interphase boundaries between 3C SiC and α-SiC grains. An example of latter case is also evident in Fig. 5.1 (labelled as *d*) where the {0001} planes of the α-SiC grain are parallel to a set of {111} planes of the neighbouring β-SiC grain.

The HREM image of the interphase boundary shown in Fig. 6.2(b) shows that the α-SiC grain is faceted. This results in a varying film thickness along the interface. Here, the dense {0001} α-SiC planes make an angle of 47° with the {111} planes of 3C SiC grain and are parallel to the interface in the orientation shown in Fig. 6.2(a). The average interface plane makes an angle of ≈ 63° with the {111} planes of 3C SiC in Fig. 6.2(b) whereas the {0001} α-SiC planes make an angle of 16° with the interface plane.

The Fresnel technique was also applied on different interphase boundaries (Fig. 6.4 and also see Fig. 3 in Turan and Knowles, 1995). The fringe spacings obtained from these interfaces are plotted in Fig. 6.4(c) (data shown with (o) are from interface shown in Fig. 6.4 and data

with (●) from interface shown in Fig. 3 in Turan and Knowles, 1995). The extrapolation of underfocus values to zero defocus showed that the film thickness varied between 16 and 18 Å. In Fig 6.4, the angle between {111} planes of 3C SiC and {0001} α-SiC grains are $\approx 60°$ and so this interface can be identified as an high angle interphase boundary. It is also interesting in these series of micrographs that the interface at the left corner (arrowed) shows reverse Fresnel contrast similar to the observations reported by Rühle and Sass (1984) on 12° low angle tilt boundaries in NiO when the dislocations were aligned end-on to the oncoming electron beam. Interestingly, there is a small angle of 8° between (111) planes of 3C and {0001} planes of α-SiC grains. Tilting experiments showed the faceted nature of the interface.

A number of low angle boundaries were also observed to be free of intergranular films. An example is shown in Fig. 6.5 where a α-SiC grain is surrounded by a 3C SiC grain. The α-SiC grain is separated from the main 3C SiC grain with a slab of 3C SiC. The orientation relationship between them is such that when the main 3C SiC grain is parallel to a [110] zone axis, the α-SiC grain is only 3° off the $[11\bar{2}0]$ zone axis and the [110] zone axis of the 3C slab is parallel to the $[11\bar{2}0]$ axis. The dark field image in Fig. 6.5(a) is formed when the beam direction was parallel to the $[11\bar{2}0]$ zone axis whereas the weak beam dark field image in Fig. 6.5(b) was obtained by tilting 5.5° away to a g-3g condition on the main 3C grain. Both images at the interface between the 3C grain and the 3C slab display strain contrast, whereas the interface between the 3C slab and α-SiC grain is flat. The latter type of interfaces were shown to be coherent interfaces using HREM (*e.g.*, see Fig. 5.1).

Further applications of Fresnel technique on the interphase boundaries revealed some interesting results. In the first example, shown in Fig. 6.6, dislocation contrast at an interface is revealed by the Fresnel imaging. The bright field image shows that the interface is faceted (Fig. 6.6(a)). The spacing between the facets are smaller between the points *A* and *B* and also facets are more regular in comparison to a region between *B* and *C*. The diffraction pattern obtained from the interface (Fig. 6.6(b)) indicated that the orientation relationship at this interface is close to:

$[211]_1 \parallel [110]_2$ with (111) planes of both the grains making an angle of 13° with one another

The Fresnel fringes shown in Fig. 6.6(c) and (d) obtained from the inclined interface shows the ledges as lines.

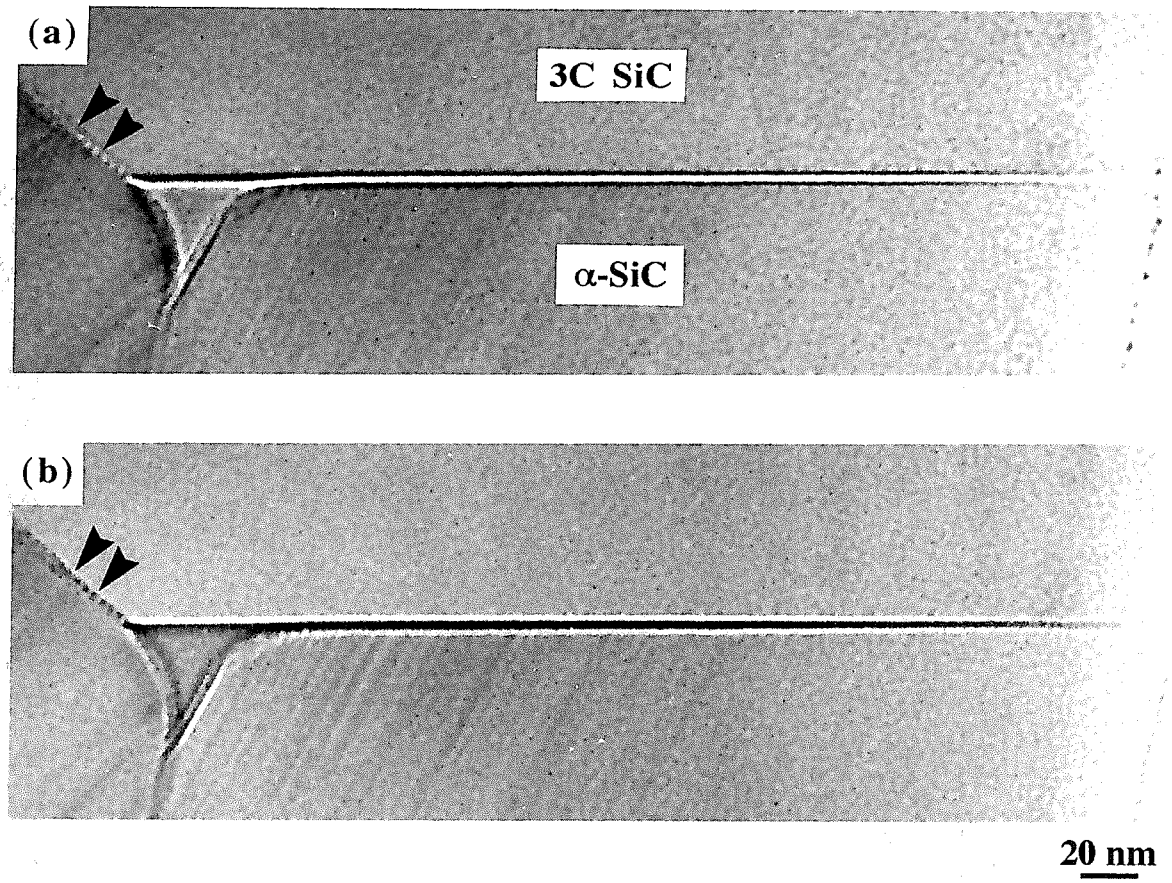

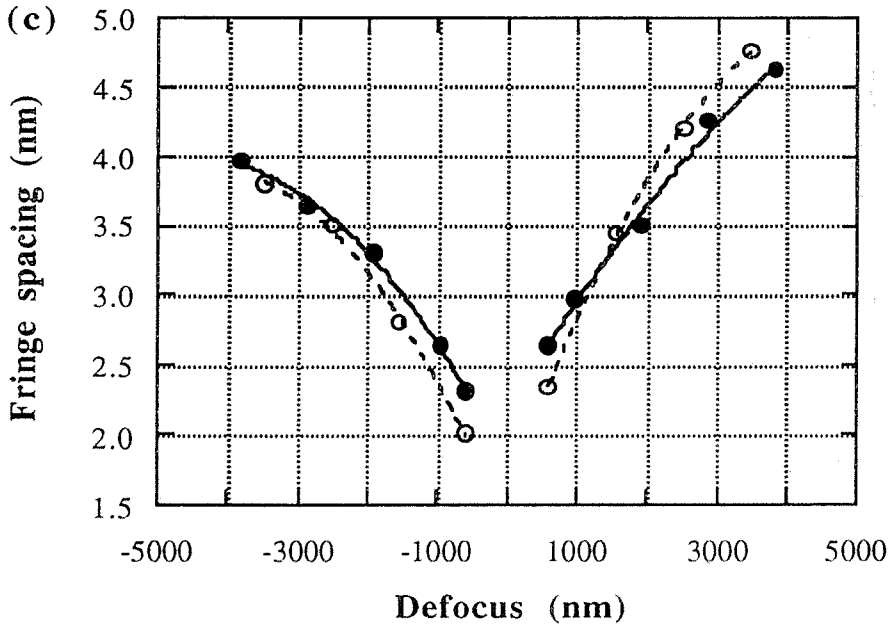

Fig. 6.4. (a) Underfocus (ΔF = - 2500 nm), (b) overfocus (ΔF = + 2500 nm) Fresnel fringe images of an edge-on interphase boundary between α and β-SiC grains. (c) A plot of Fresnel fringe spacings against defocus for two of interphase boundaries between α-SiC and β-SiC.

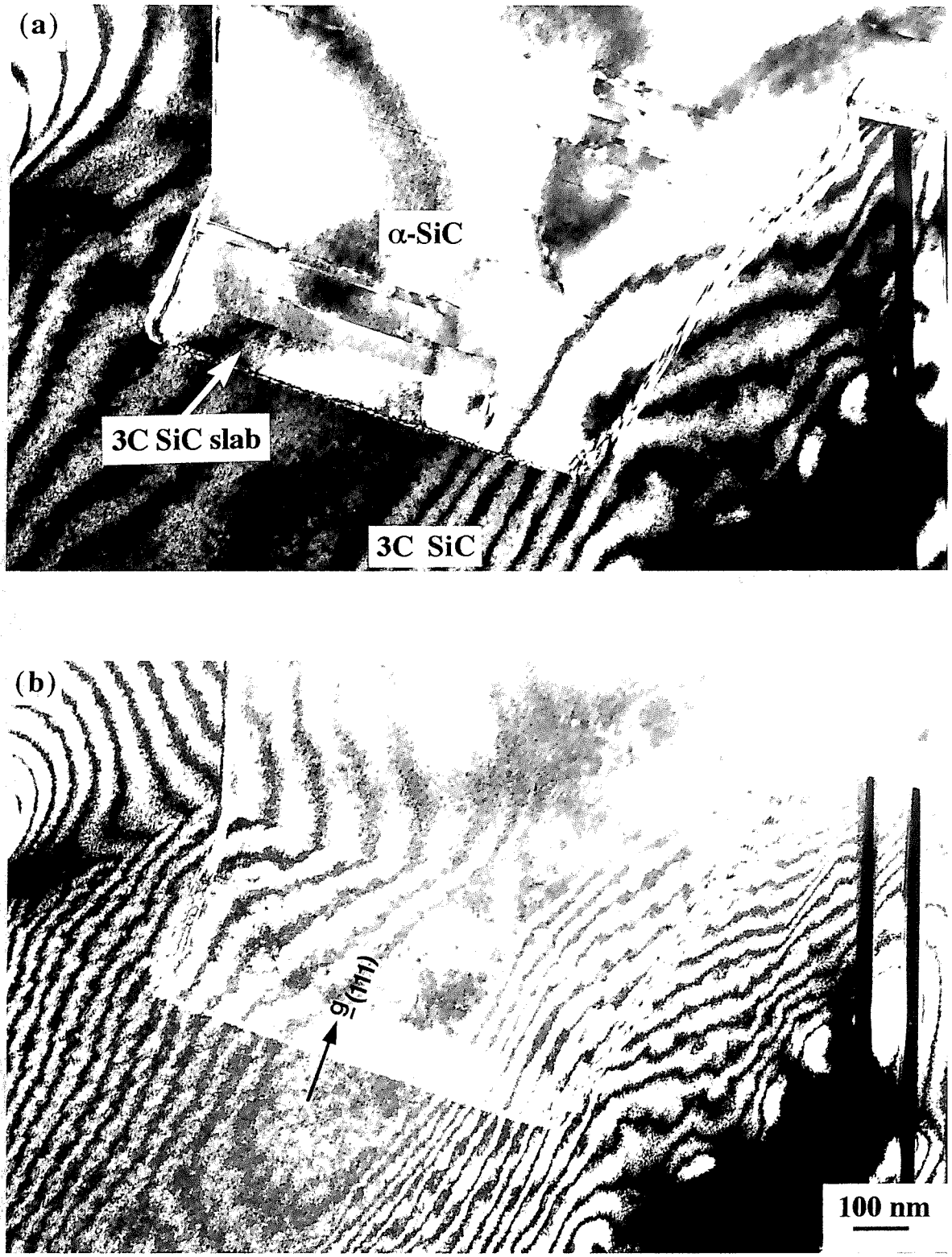

Fig. 6.5 (a) A dark field image from g = (111) and (b) a g–$3g$ weak beam dark field image of a SiC-SiC interface. The image in (a) was obtained when the beam direction of α-SiC was parallel to $[11\bar{2}0]$ whereas the image in (b) was obtained after tilting by 5.5° to obtain a g–$3g$ condition.

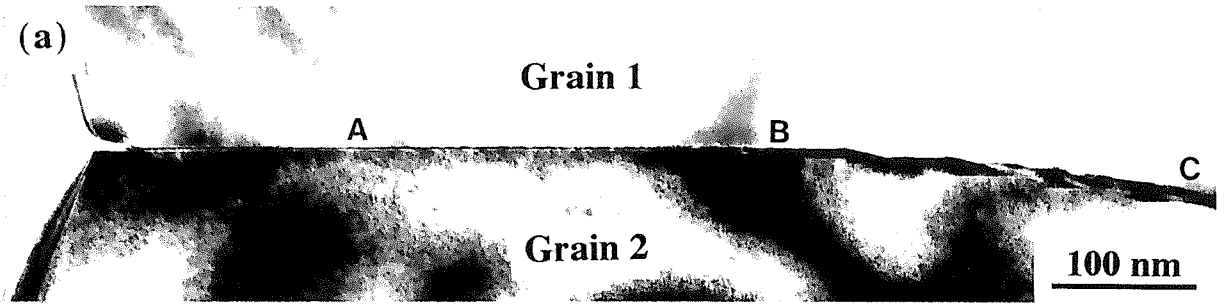

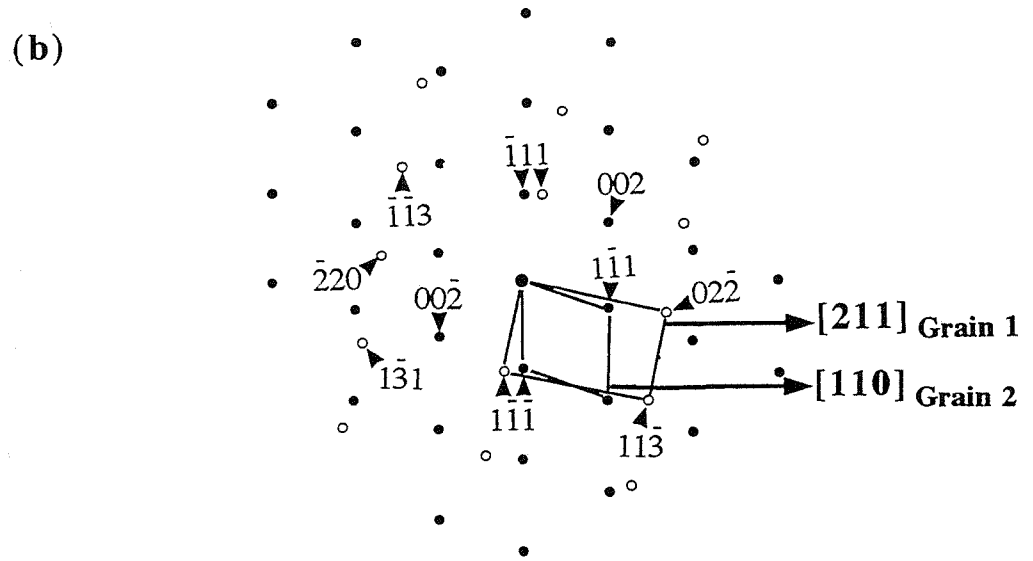

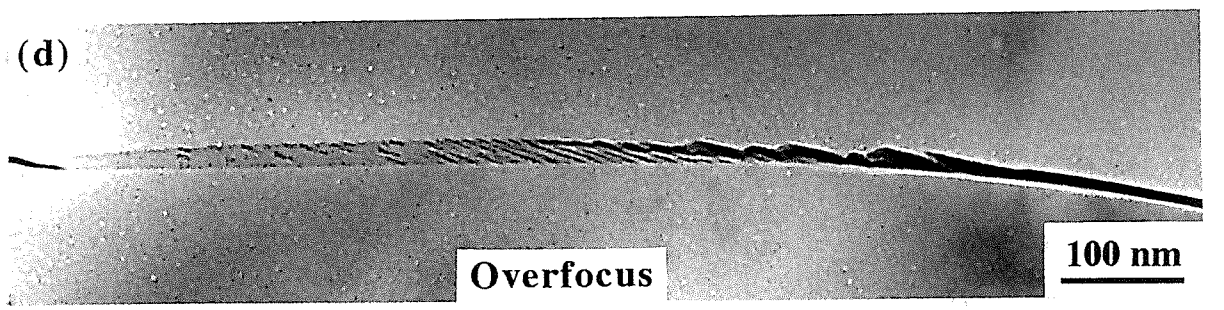

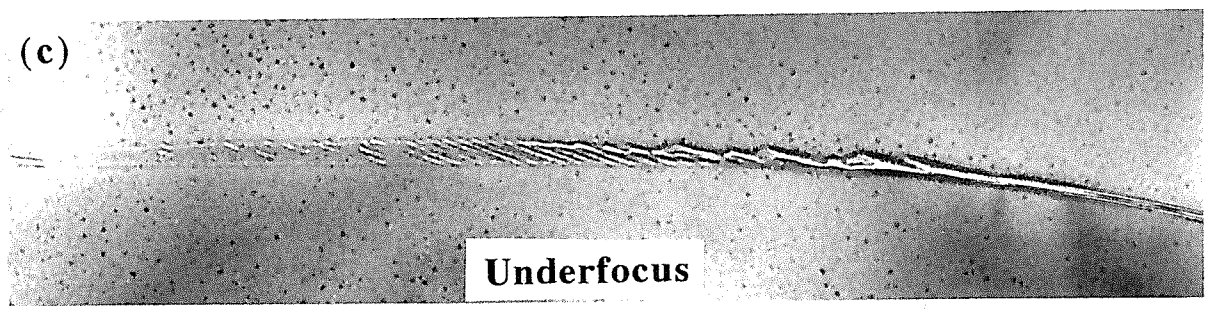

Fig. 6.6 (a) A bright field image of [211] ‖ [110] 3C SiC-3C SiC interface; (b) schematic of indexed diffraction pattern obtained at the imaging conditions used in (a); (c), (d) and (e) same as (a) but after tilting away to weak diffracting conditions.

In Fig. 6.7(a) and (b), a different edge-on interface between two SiC grains shows that the interface contains an amorphous intergranular film. Tilting away from this condition the interface still shows Fresnel reverse contrast (Fig. 6.7(c) and (d)). In the second condition, the interface contains a set of regularly spaced fringes instead of a smooth intergranular film at the interface. In order to reveal the structure of the interface weak beam dark field (Fig. 6.7(e)) and lattice fringe imaging (Fig. 6.7(f)) techniques were applied. Both techniques showed that the upper grain (α-SiC) is faceted at the interface. The shape of the interface in weak beam image indicates that the Fresnel contrast arises at this interface in the second condition from the facets whereas in the first condition contrast arises due to an amorphous phase filling the voids between these facets since the diffuse dark field image showed a faint bright line indicative of amorphous film. It is also interesting that a second interface connected to the same triple junction has an intergranular film (see Fig. 7.9). This again shows the anisotropic wetting behaviour of the interfaces.

From Figs. 6.2(b), 6.4, 6.6 and 6.7, it can be concluded that when {111} or {0001} SiC planes make an angle smaller than $\approx 20^{\circ}$ with the average interface plane, the grain is faceted at the interface even though the interface is still wetted with an intergranular film.

6.3.2 Grain boundaries between Si_3N_4 grains

Two different types of grain boundaries were observed between Si_3N_4 grains. In the first type, such as the example shown in Fig. 6.8, an amorphous triple junction phase could be clearly detected by HREM. In this particular case none of the grains were oriented parallel to any low index direction with respect to the electron beam. It is apparent from the micrograph that the amorphous phase is extending from the triple junction along at least one of the grain boundaries, having a film thickness there of approximately 10 Å. It is possible that the amorphous triple junction phase may also be extending along the other grain boundaries in this micrograph, but since they are not edge-on it is not possible to deduce whether they have thin intergranular films or whether they are free of such films.

The thickness of the intergranular films were also measured using the Fresnel defocus imaging technique (Fig. 6.9(a) and (b)). The results obtained from Fresnel analysis were almost the same as HREM results in that the thickness of the film is $\approx$ 12 Å (Fig. 6.9(c)).

The examples of Fresnel images shown in Fig. 6.9(a) and (b) demonstrate the existence of an intergranular film at this interface. An insufficient number of grain boundaries between Si_3N_4 grains have been observed in my work to draw firm conclusions on the presence and absence of intergranular films, but at general Si_3N_4-Si_3N_4 interfaces, the data available in the literature is quite large and conclusive that grain boundaries between Si_3N_4 grains generally contain intergranular films with a thickness of 10 to 15 Å (see various work by Rühle and co-workers).

In the second type of grain boundaries, the interfaces do indeed appear to be free of intergranular films when oriented edge-on to the electron beam. The first, and more interesting, example, shown in Fig. 6.10(a), is from an asymmetrical high angle tilt boundary with the electron beam in each grain very near to [011] and with a tilt angle of 56° between the two grains about this common direction. A superimposed diffraction pattern from this interface is shown in Fig. 6.10(b). The trace of the 'macroscopic' average interface plane makes an angle of 21.5° with the (100) planes of grain 1 and an angle of 34.5° with the (100) planes of grain 2. However, the interface appears to facet on (100) planes of grain 1 and elsewhere it has the characteristics of a symmetrical tilt grain boundary with the interface plane $(5\bar{1}1)$ common to both grains.

The orientation relationship between the two grains deduced from the electron diffraction pattern is a Type 1 twinning operation with $K_1 = (5\bar{1}1)$. The twinning plane is drawn in Fig. 6.10(b).

An equivalent description is that the orientation relationship is close to a $\Sigma = 9$ near-coincident site lattice (K.M. Knowles).

The contrast at the grain boundary in the enlarged view of the interface is shown in Fig. 6.11 highlights one of the difficulties posed in interpreting HREM images of interfaces – while any amorphous phase is obviously very thin indeed, and less than the spacing of the (100) planes (6.58 Å), further detailed interpretation of the image requires an assumption about the interface either being accurately edge-on to the electron beam or being sufficiently close to edge-on that the loss in detail at the interface can be interpreted entirely in terms of the grains

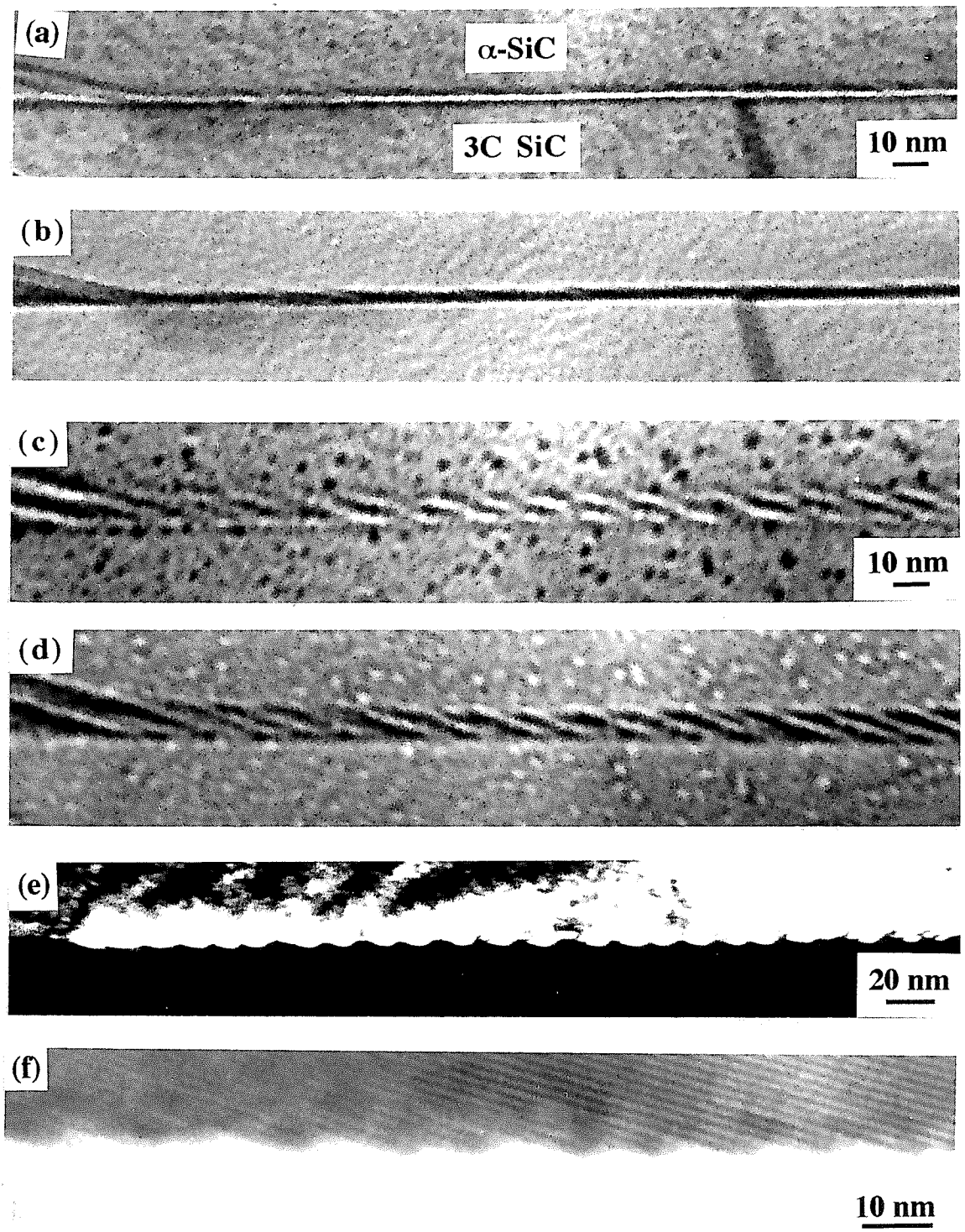

Fig. 6.7 An edge-on interface between α and 3C-SiC showing Fresnel reverse contrast indicating an amorphous intergranular film at the interface ((a) and (b)). After tilting away from the conditions used in (a) and (b) the interface still shows Fresnel reverse contrast ((c) and (d)). A weak beam (e) and a lattice fringe (f) images of α-SiC grain show the faceted character of the interface.

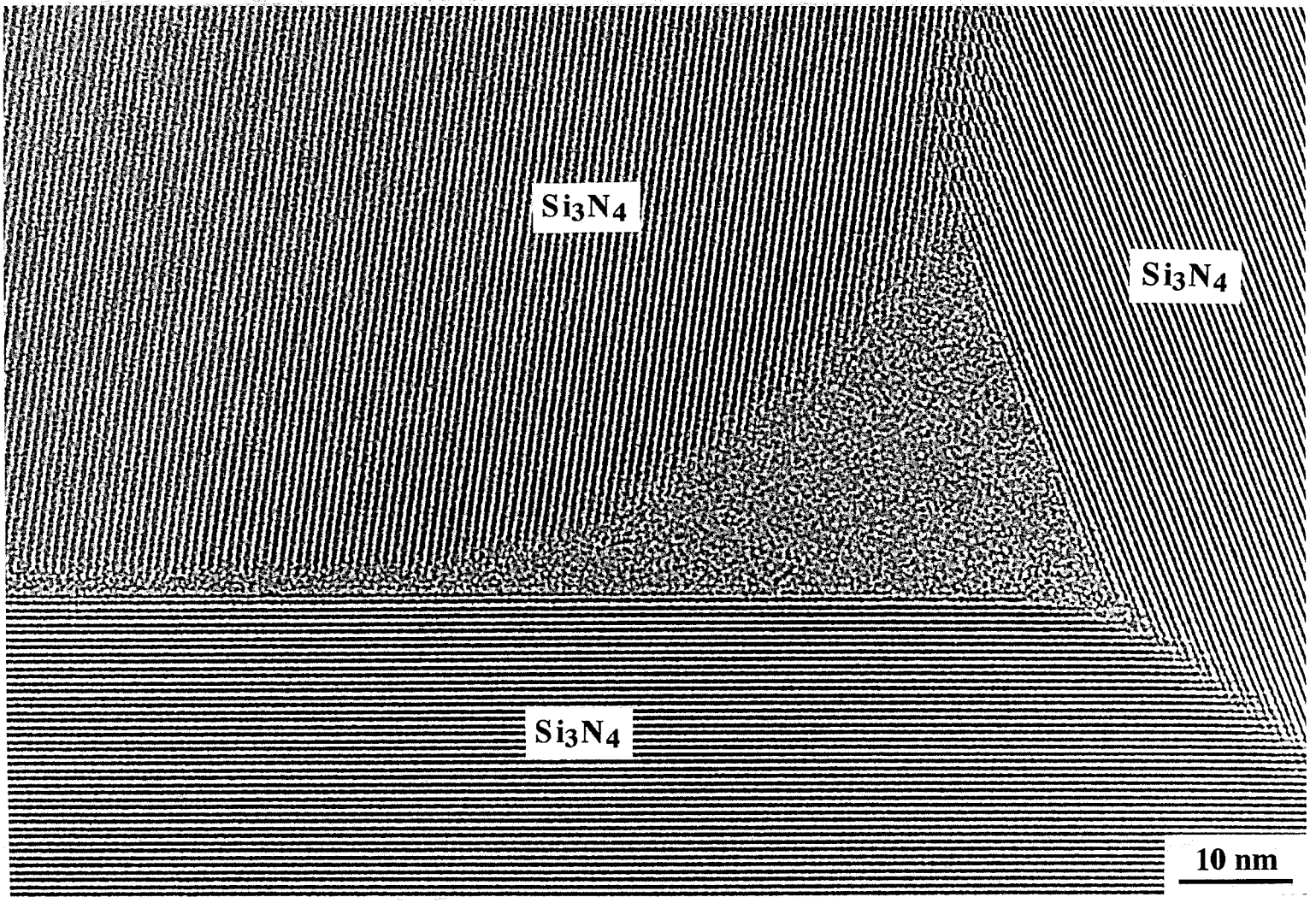

Fig. 6.8 An example of an amorphous phase trapped at a triple junction between three Si_3N_4 grains, with the extension of this phase into at least one of the grain boundaries with a thickness there of ≈ 10 Å.

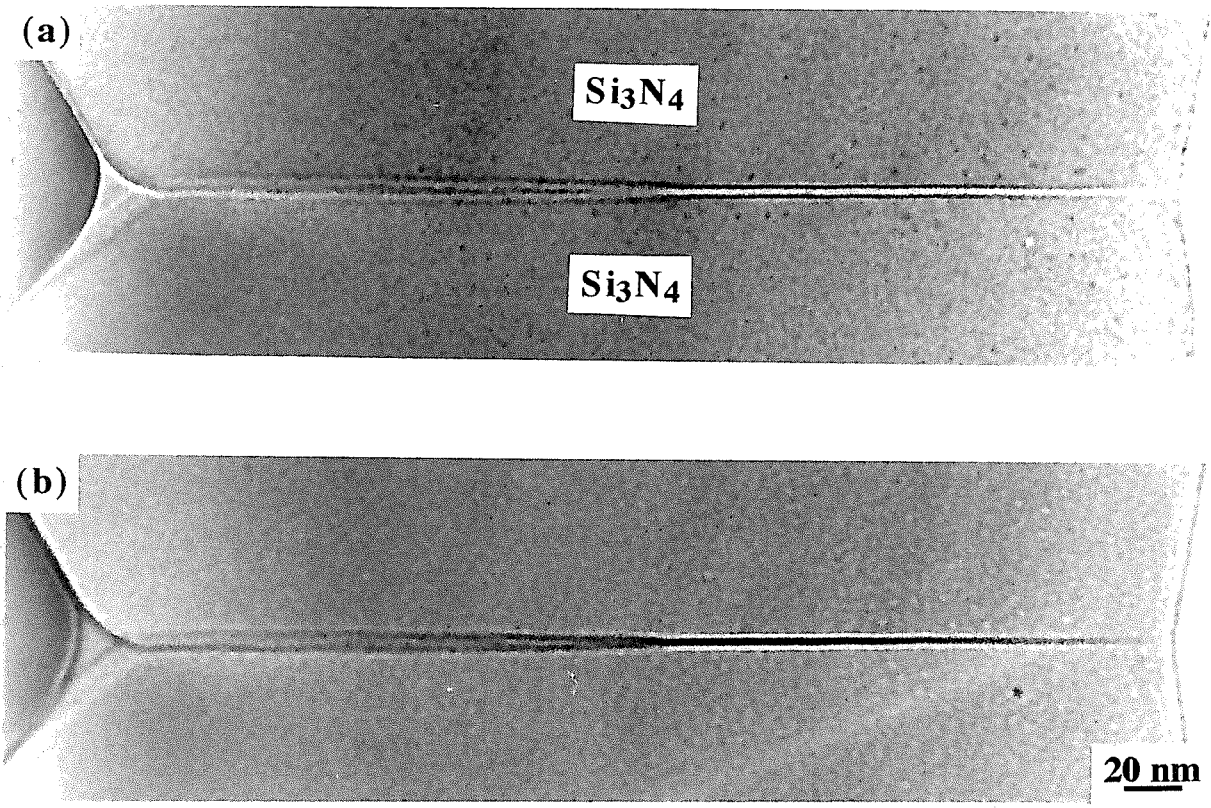

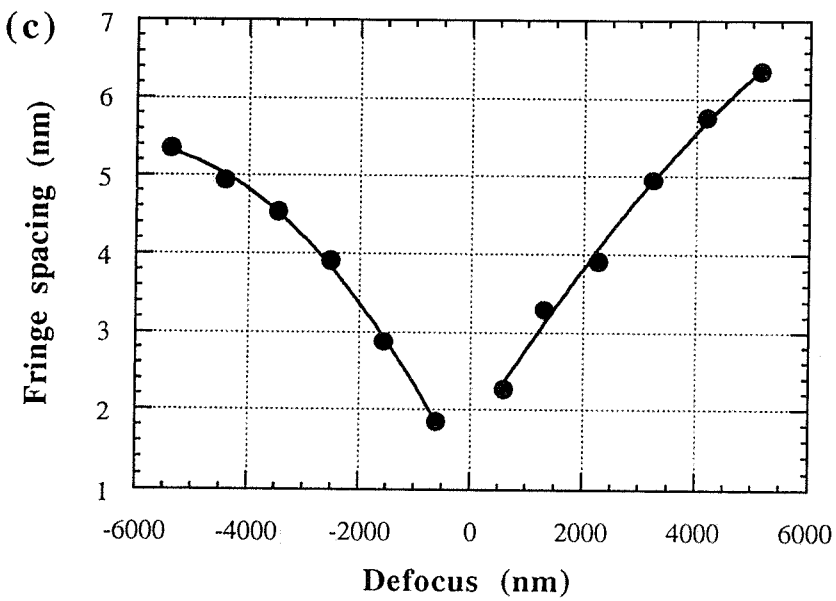

Fig. 6.9 A typical Fresnel fringe contrast at an edge-on Si_3N_4-Si_3N_4 grain boundary; (a) underfocus image ($\Delta F = -2510$ nm), (b) overfocus image ($\Delta F = +2270$ nm) and (c) plot of Fresnel fringe spacings as a function of defocus for the same grain boundary.

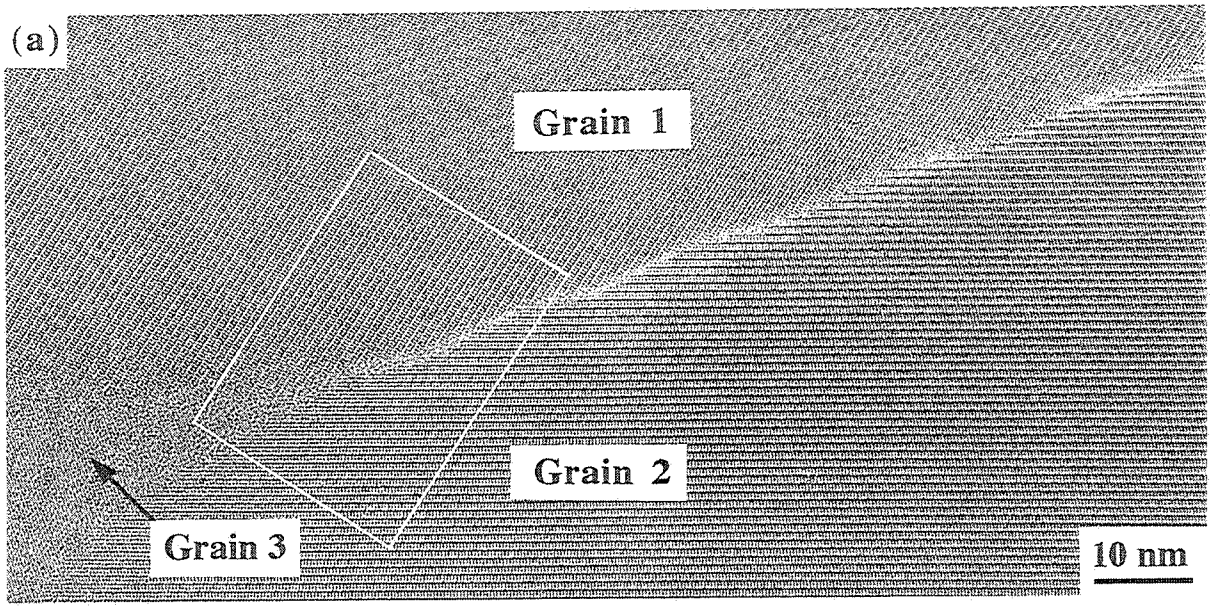

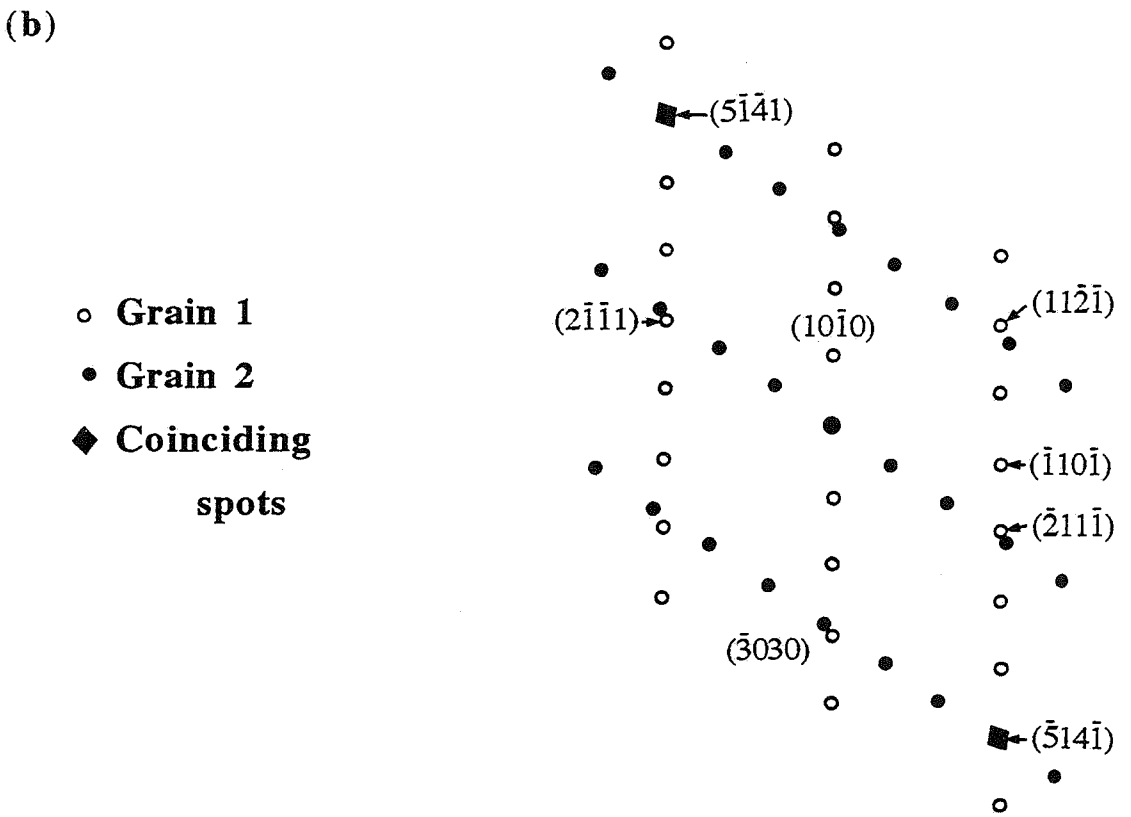

Fig. 6.10 (a) HREM image of a faceted grain boundary between two β-Si_3N_4 grains in the composites made from as received powders; (b) a superimposed schematic diffraction pattern from the interface showing that the electron beam direction is close to [011] in each grain.

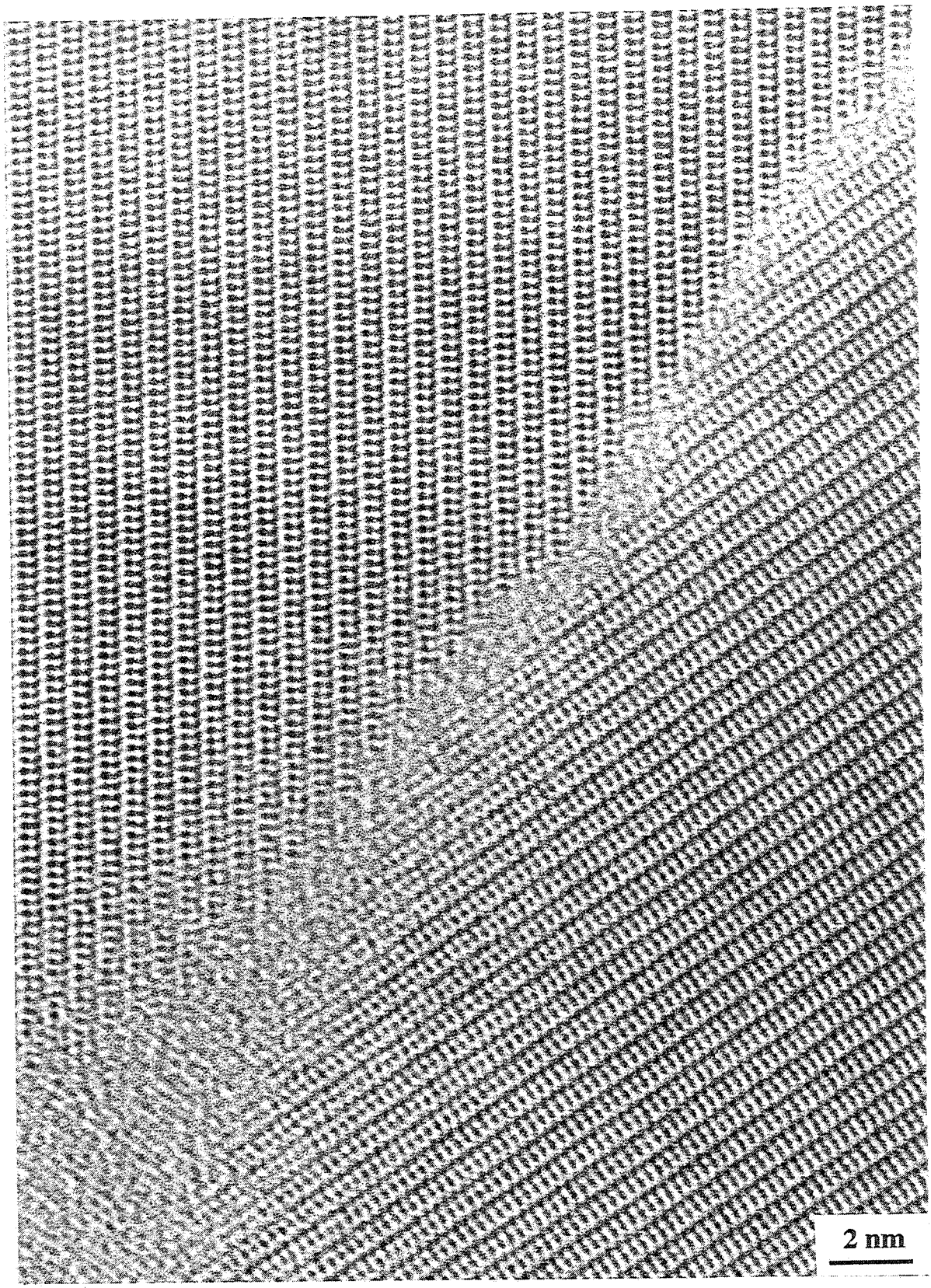

Fig. 6.11 The enlarged view from the boxed area in Fig. 6.10(a), showing that the interface can be described as an asymmetrical high angle tilt grain boundary.

overlapping in projection. That the HREM image from either side of the interface is different far away from the interface indicates that the grains are misoriented slightly with respect to the common [011] direction, making interpretation of the image complex, even if HREM image simulations were made. However, lattice fringes are evident at the triple junction from a third grain, rather than an amorphous phase, as observed in Fig. 6.8. Therefore, there are three different reasons for a film-free interface at this particular grain boundary. These are *(i)* the special crystallography of the interface, *(ii)* faceting and *(iii)* the absence of any clear amorphous triple junction phase. The first two could lower the energy of interface and energetically favour the existence of a solid-solid interface while the third one reinforces the idea that the interface is film-free.

A second, somewhat ambiguous, example of a grain boundary between Si_3N_4 grains is shown in Fig. 6.12(a), in which the specimen thickness increases rapidly from the right-hand side of the micrograph to the left-hand side. The orientation relationship between these grains are such that grain 1 is parallel to [001] and grain 2 is only few degrees away from this zone axis with the angle between corresponding (100) planes only 3°. Here, it is less clear whether there is a film at the interface. There is a discontinuity between the lattice planes of two grains which are separated with a 6-8 Å region.

A third example is shown in Fig. 6.12(b) from a low angle grain boundary in which both grains were oriented close to the [211] zone, and here it was more obvious that there was no intergranular film at the grain boundary.

Unfortunately, in neither case was it possible to confirm the presence or absence of an intergranular film by other techniques such as diffuse dark field or Fresnel fringe imaging, because both these techniques required the transfer of the sample from the JEOL 4000EX-II to another microscope with suitable objective apertures. In doing so, the areas shown in Figs. 6.10 and 12 were lost.

6.3.3 Interphase boundaries between SiC and Si_3N_4

Interphase boundaries between SiC and Si_3N_4 were of two types. The first type was formed between intragranular Si_3N_4 precipitates and surrounding 3C SiC grains, whereas the second type was between large 3C or α-SiC grains and abutting Si_3N_4 grains of a similar size. The interphase boundaries between SiC grains and the precipitates will be discussed first.

Interphase boundaries between SiC grains and Si_3N_4 precipitates

Some examples of fine Si_3N_4 precipitates distributed inside SiC grains have already been shown in Fig. 3.10 and 4.20. It is clear from these figures that the shapes of the precipitates were variable – in projection some were hexagonal in shape (Fig. 3.10) or elongated with round ends (Fig. 4.20), whereas others could be seen to be circular. Interestingly, in Fig. 4.20 a h-BN inclusion can be seen between the Si_3N_4 precipitate and the adjacent 3C SiC grain. This was a commonly observed feature.

Such nano-size intragranular particles, but SiC instead of Si_3N_4, have been observed in SiC-Si_3N_4 nanocomposites (Niihara *et al.*, 1990), where the strength increment of the Si_3N_4 matrix was correlated with the existence of the nano-size SiC particles.

In this work, as in the work of Niihara *et al.* (1990), most of these SiC-Si_3N_4 interphase boundaries were found to be curved, and consequently moiré fringes formed from the overlap between Si_3N_4 precipitates and SiC matrix were readily seen. Unfortunately for such interfaces, it is not possible to specify unambiguously whether or not there are any intergranular films at the interphase boundaries. An example between a circular Si_3N_4 precipitate and the surrounding 3C SiC grain is shown in Fig. 6.13(a) and (b). Both dark field images were obtained when the [110] SiC direction was set parallel to the electron beam and the composite diffraction pattern is shown in Fig. 6.13(c). It was found that the [0001] Si_3N_4 direction is 9° away from [110] SiC direction (Fig. 6.13(d)). It can be seen in both the diffraction patterns that the (002) 2.179 Å SiC spot overlaps with the $(30\bar{3}0)$ 2.195 Å Si_3N_4 spot. The dark field image shown in Fig. 6.13(a) was obtained using this coincident spot when [110] SiC direction was parallel to the electron beam, whereas the image in (b) was formed using the (111) SiC spot. At this resolution, the interphase boundary around the Si_3N_4 precipitate does not appear to contain any intergranular film.

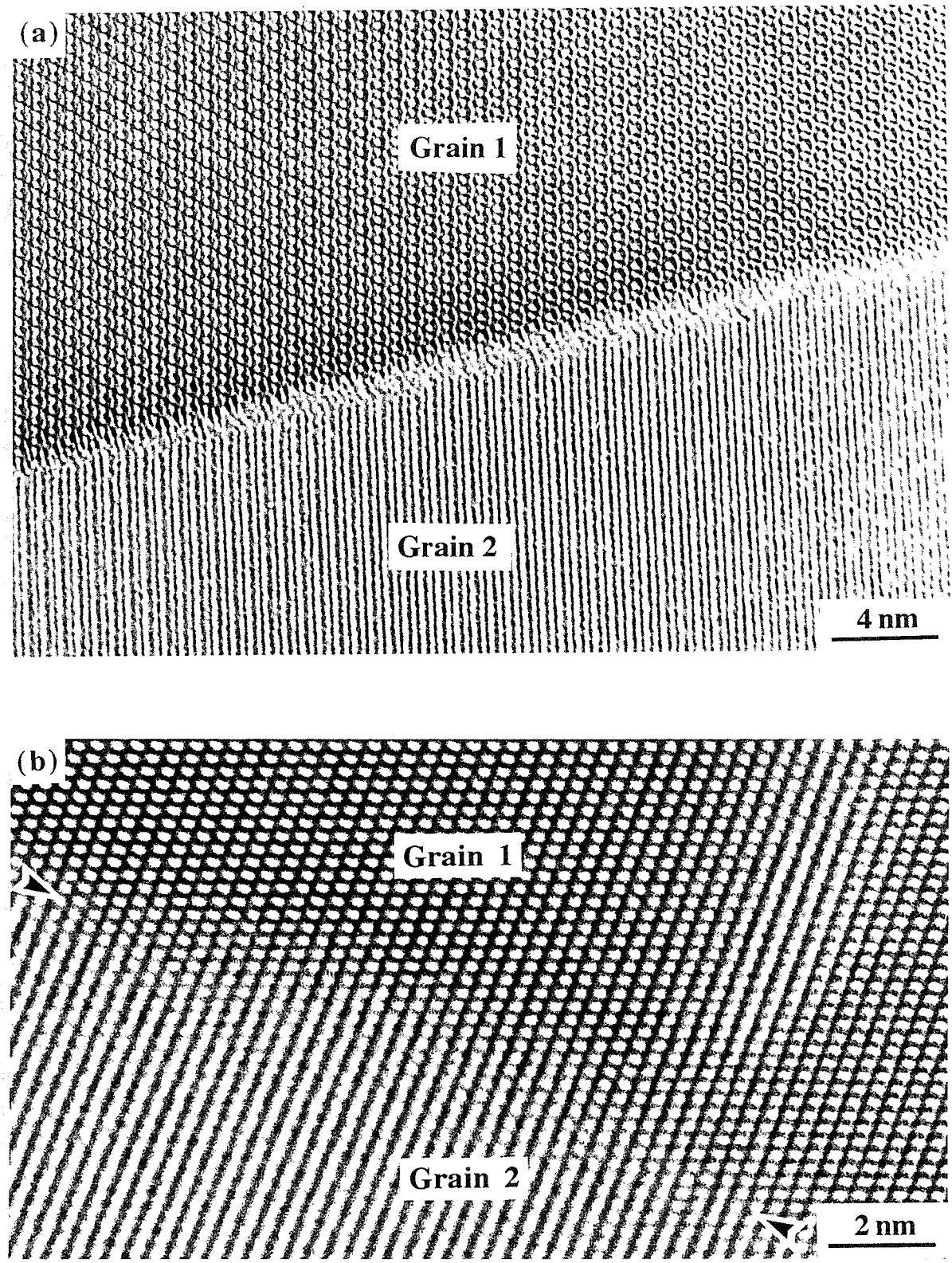

Fig. 6.12 Low angle grain boundaries between Si_3N_4 grains. In (a) the electron beam direction parallel to [001] in grain 1 and the specimen thickness increases from right to left. In (b) the beam direction parallel to [211] in grain 1 and here the grain boundary is clearly free of any thin intergranular amorphous film.

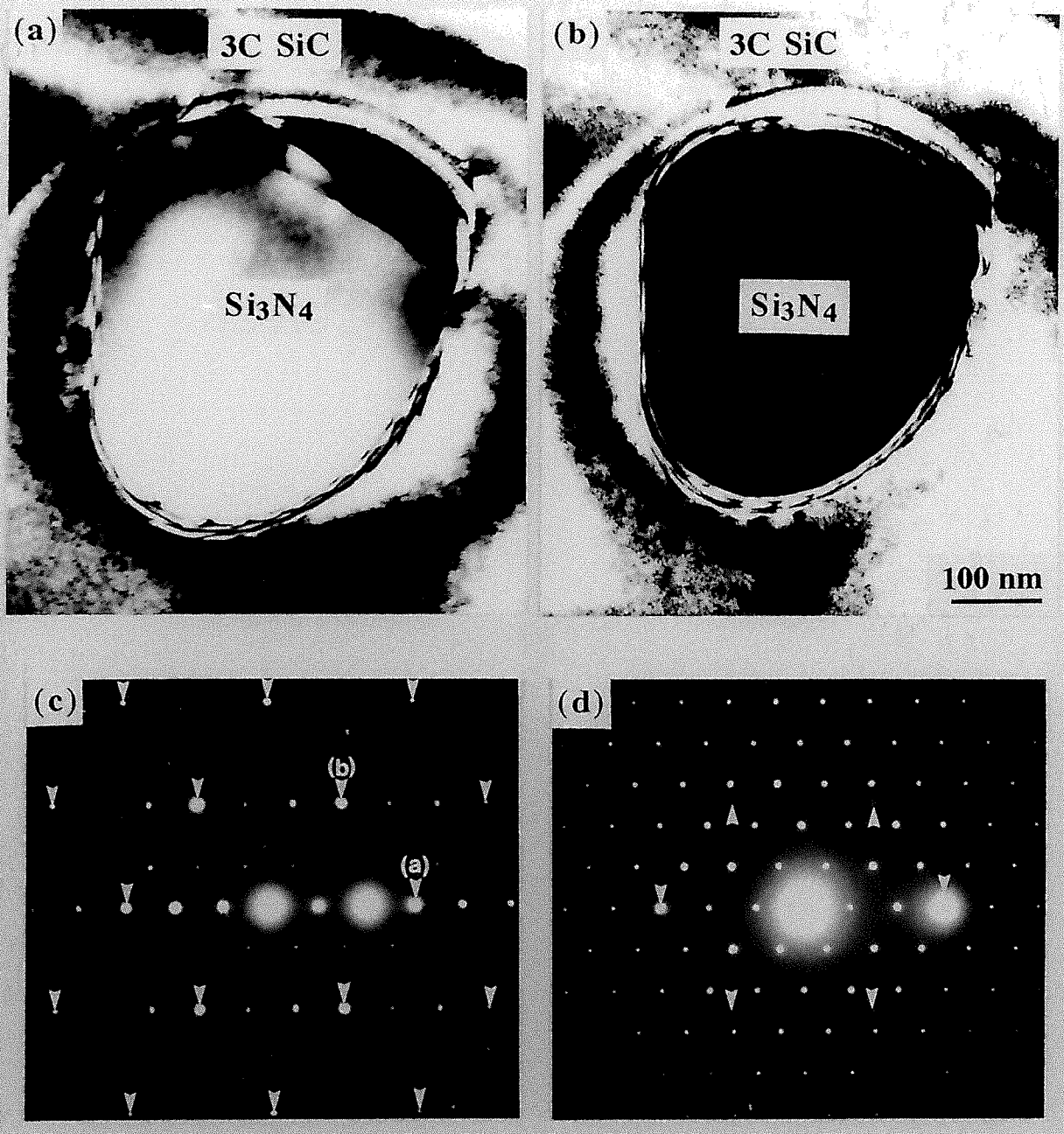

Fig. 6.13 (a) and (b) Dark field images of interphase boundaries between a Si_3N_4 precipitate and a surrounding 3C SiC grain when 3C SiC was aligned parallel to [110] direction. Composite diffraction patterns obtained when 3C SiC (c) and Si_3N_4 (d) were aligned parallel to [110] and [0001] directions, respectively. The SiC spots in both the diffraction patterns are indicated with arrows and the spots used to form the dark field images are labelled with *a* and *b* in (c). The indexed schematic diffraction pattern of (c) will be shown in Fig. 6.16.

Occasionally, however, flat interfaces between hexagonally shaped intragranular grains and matrix were observed, some of which were clearly wetted with an ≈ 10 Å thick intergranular film, as in the example shown in Fig. 6.14. In this particular case, the β-SiC grain was oriented parallel to a [110] while the β-Si_3N_4 grain was oriented parallel to a [02$\bar{2}$7] zone axis. The inset in Fig 6.14 shows the diffraction pattern in which the spots from β-Si_3N_4 precipitate are arrowed. The orientation relationship at this interface was such that:

$$[110]_{3C\ SiC} \parallel [02\bar{2}7]_{Si_3N_4} \text{ and } (110)_{3C\ SiC} \parallel (10\bar{1}0)_{Si_3N_4}$$

A ≈ 7 % mismatch between the (220) 1.54 Å SiC and (40$\bar{4}$0) 1.646 Å Si_3N_4 planes implies a non-special orientation relationship, consistent with the existence of an intergranular film.

In a further example, a smaller and a well faceted Si_3N_4 precipitate oriented parallel to [0001] direction is shown in Fig. 6.15(a). The surrounding SiC grain is ≈ 4° away from a <110> zone axis. Composite diffraction patterns obtained at two different conditions are presented in Fig. 6.15(b) and(c). In Fig. 6.15(a), the SiC grain does not show any lattice fringes since the interplanar-spacing of the 1.54 Å (220) SiC planes are smaller than the microscope resolution, but the white band of contrast evident along the SiC-Si_3N_4 interface indicates that the Si_3N_4 grain is probably surrounded with amorphous phase.

In order to establish the nature of these individual interphase boundaries, HREM images were obtained by tilting away from this condition. These showed that some of the interfaces on the SiC side are faceted and contain intergranular films.

It is interesting that interphase boundaries, formed between two opposite faces of the Si_3N_4 precipitate and surrounding SiC grain (interfaces *IB1* and *IB4*), are similar in character in that they are both faceted on SiC side and they both contain intergranular films. A HREM image of interface *IB1* when the SiC grain is parallel to [110] zone axis is shown in Fig. 6.16(a). Figs. 6.16(b) (*IB6*) and (c) (the curved interface between interfaces *IB1* and *IB6*) are HREM images obtained when the electron beam was tilted away from SiC [110] direction towards [0001] Si_3N_4 zone axis. The latter two appear to be free of intergranular films when observed edge-on, to a resolution defined by the (111) SiC spacing, *i.e.*, realistically, 5 Å. Unfortunately, the specimen thickness precluded the similar HREM observations on the other interphase boundaries.

The indexed diffraction patterns in Fig. 6.17 show the orientation relationships between the SiC grains and the Si_3N_4 precipitates shown in Figs. 6.13 and 6.15. In both cases, a [110] SiC direction is nearly parallel to the [0001] Si_3N_4 direction. In (a), (002) planes overlap with $(30\bar{3}0)$ planes of Si_3N_4 and $(1\bar{1}0)$ planes are parallel to $(1\bar{2}10)$ Si_3N_4 planes. The six fold symmetry of [0001] Si_3N_4 is reduced to two fold symmetry (close to, but not exactly) at most for the interphase boundary. The orientation relationship in Fig. 6.17(a) is close to:

$[110]_{3C\ SiC} \parallel [0001]_{Si_3N_4}$, $(001)_{3C\ SiC} \parallel (10\bar{1}0)_{Si_3N_4}$ and $(1\bar{1}0)_{3C\ SiC} \parallel (1\bar{2}10)_{Si_3N_4}$

In comparison, in Fig. 6.17(b) there is no such symmetry and the misorientation arising at the interface does not allow two low index planes to be parallel to each other.

It can be deduced from the above orientation relationships that when the (001) planes of SiC overlap with $(10\bar{1}0)$ planes of Si_3N_4 the interphase boundary is curved and does not contain an amorphous film (Fig. 6.13). In all other cases, as Fig. 3.10(b) and 6.15 demonstrate, the Si_3N_4 precipitates are distinctly faceted (which is a typical grain shape obtained in the presence of liquid phases) and the interphase boundaries are associated with intergranular films.

In contrast to these observations, Niihara *et al.* (1990) did not observe any intergranular films between intragranular SiC grains and Si_3N_4 matrix in a 34 vol% SiC-Si_3N_4 nanocomposite which was produced by hot pressing of amorphous chemically vapour deposited Si-C-N powder (also contains <2 wt% oxygen) mixed with 2 wt% alumina and 6 wt% yttria as sintering aids. They argued that the preferential formation of low energy interphase boundaries in the composite were responsible for the absence of intergranular films although they have not mentioned what happened to the liquid phase formed at hot pressing temperature (Izaki *et al.*, 1988). They found some interfaces of hexagonally shaped SiC grains developed parallel to the (0001) basal planes of the matrix. However, this was not the case in general, and most of the straight interfaces were oriented in different directions to the basal planes of the matrix. In a particular case, they found that the large misfit between $(20\bar{2}0)$ planes of Si_3N_4 and (111) planes of SiC is accommodated by fitting every third plane of silicon carbide to every (0001) plane of Si_3N_4 since the misfit was reduced from 34 % to about 1%. Unfortunately, they have not mentioned whether there was any intergranular films between matrix grains or it was also absent at other interfaces due to the powders fabrication process.

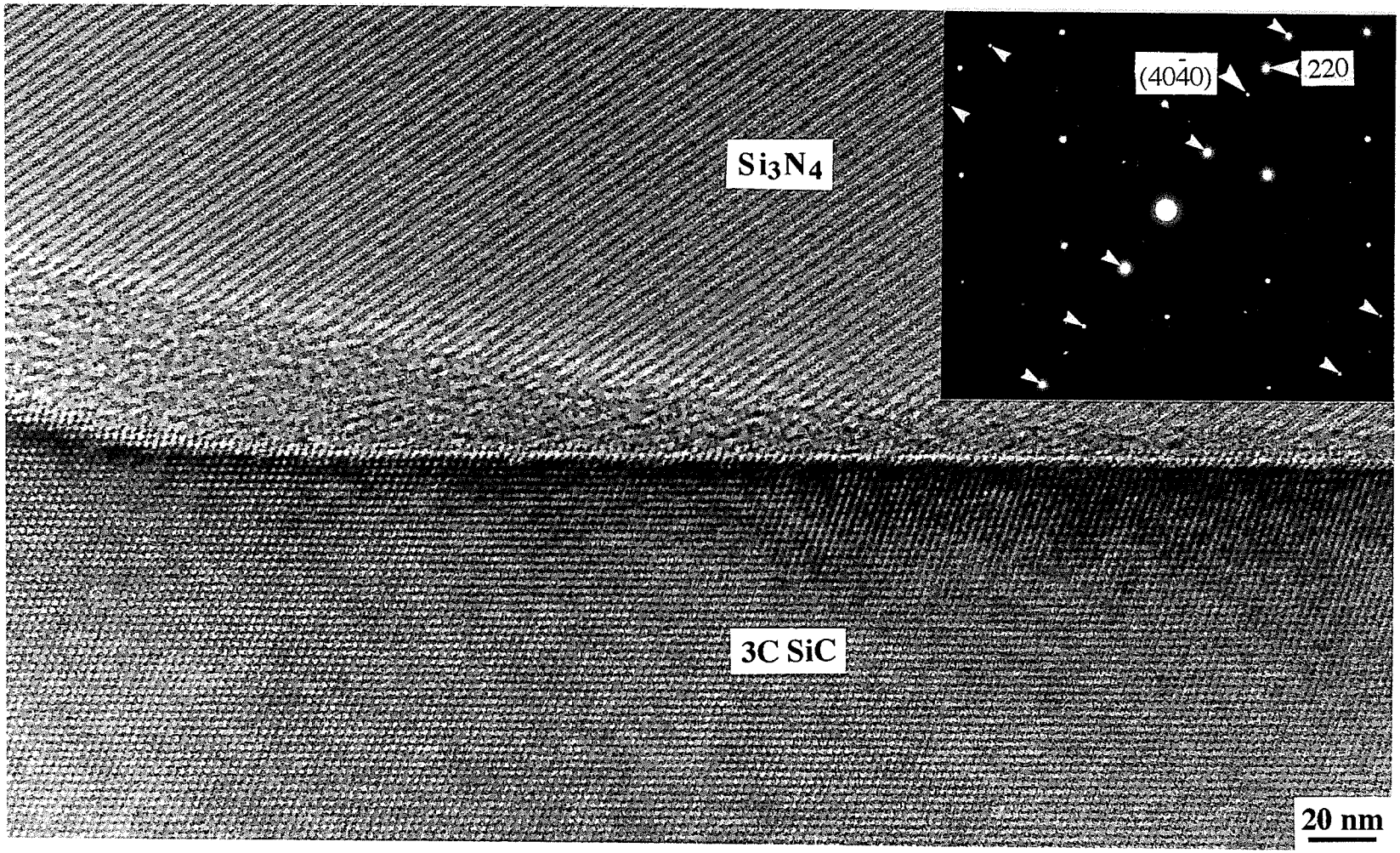

Fig. 6.14 An example of a thin intergranular film between a β-Si_3N_4 precipitate and a surrounding 3C SiC grain. The inset shows the diffraction pattern obtained from the interface when the 3C SiC grain was parallel to [110] zone axis. A triple junction is located to the left of the micrograph and the film thickness increases from right to left on the micrograph as a result.

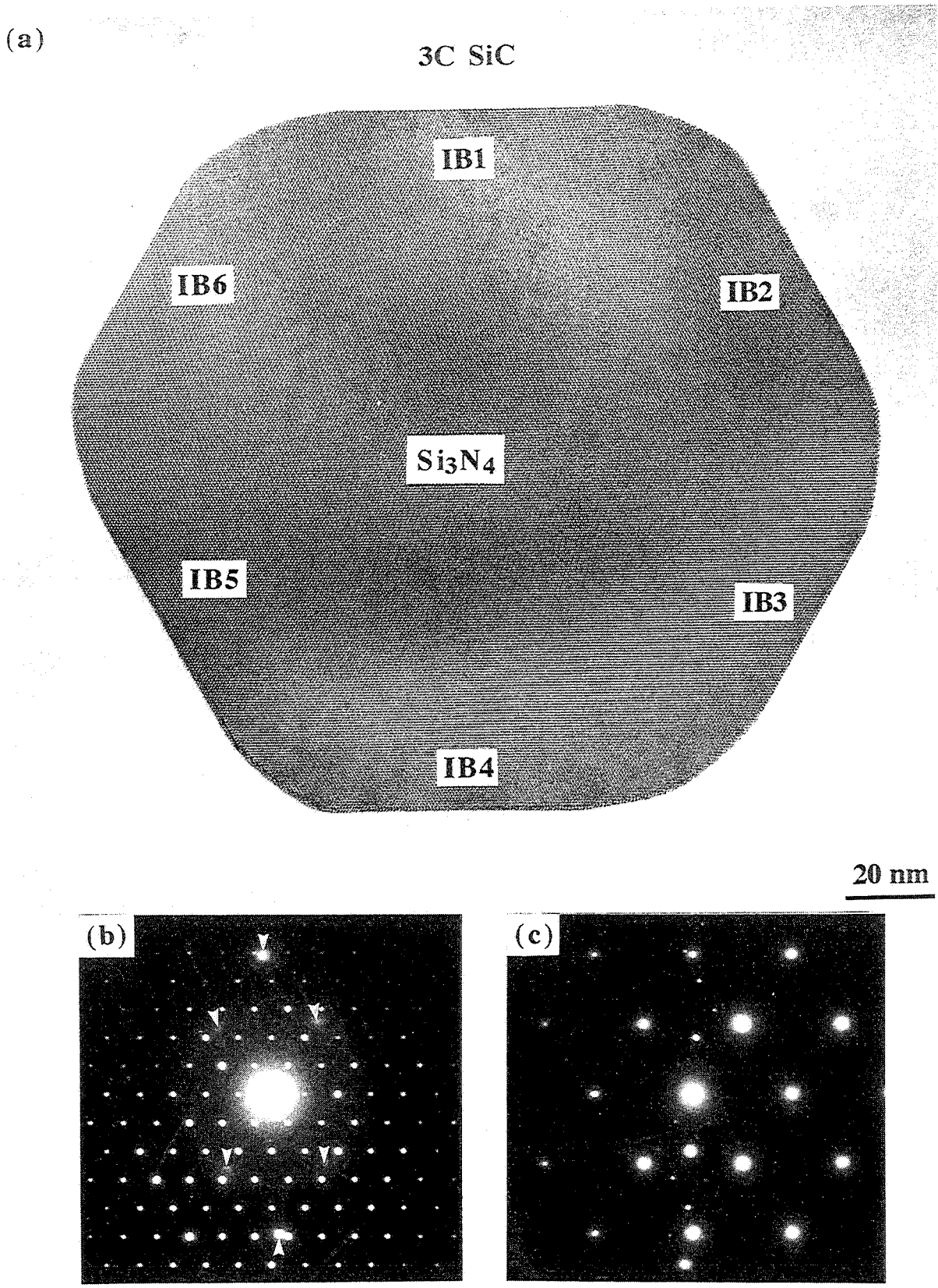

Fig. 6.15 (a) Low magnification high resolution image with [0001] incidence showing a cross section of an faceted Si_3N_4 precipitate embedded in 3C SiC grain. Diffraction patterns obtained (b) when the above conditions were set and (c) after tilting 4° away from this condition, *i.e.*, when SiC is parallel to [110] zone axis.

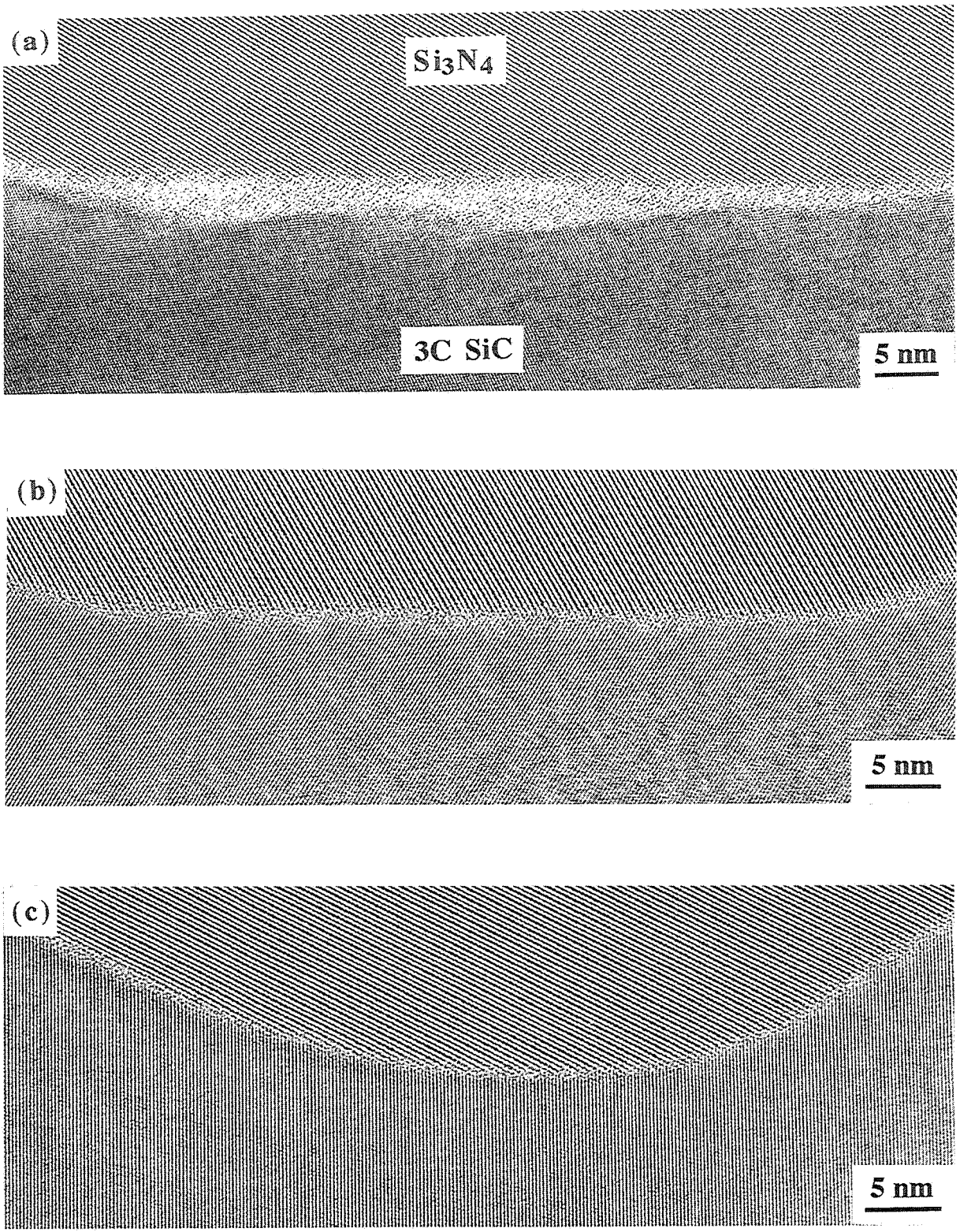

Fig. 6.16 (a) HREM image of the interfacial region denoted in Fig. 6.15(a) as IB1 when the SiC grain was parallel to [110]. (b) IB6 when the electron beam was 2° away from both the [110] SiC and [0001] Si_3N_4 directions. (c) The interface region between IB1 and IB6 imaged using the same conditions as in (b).

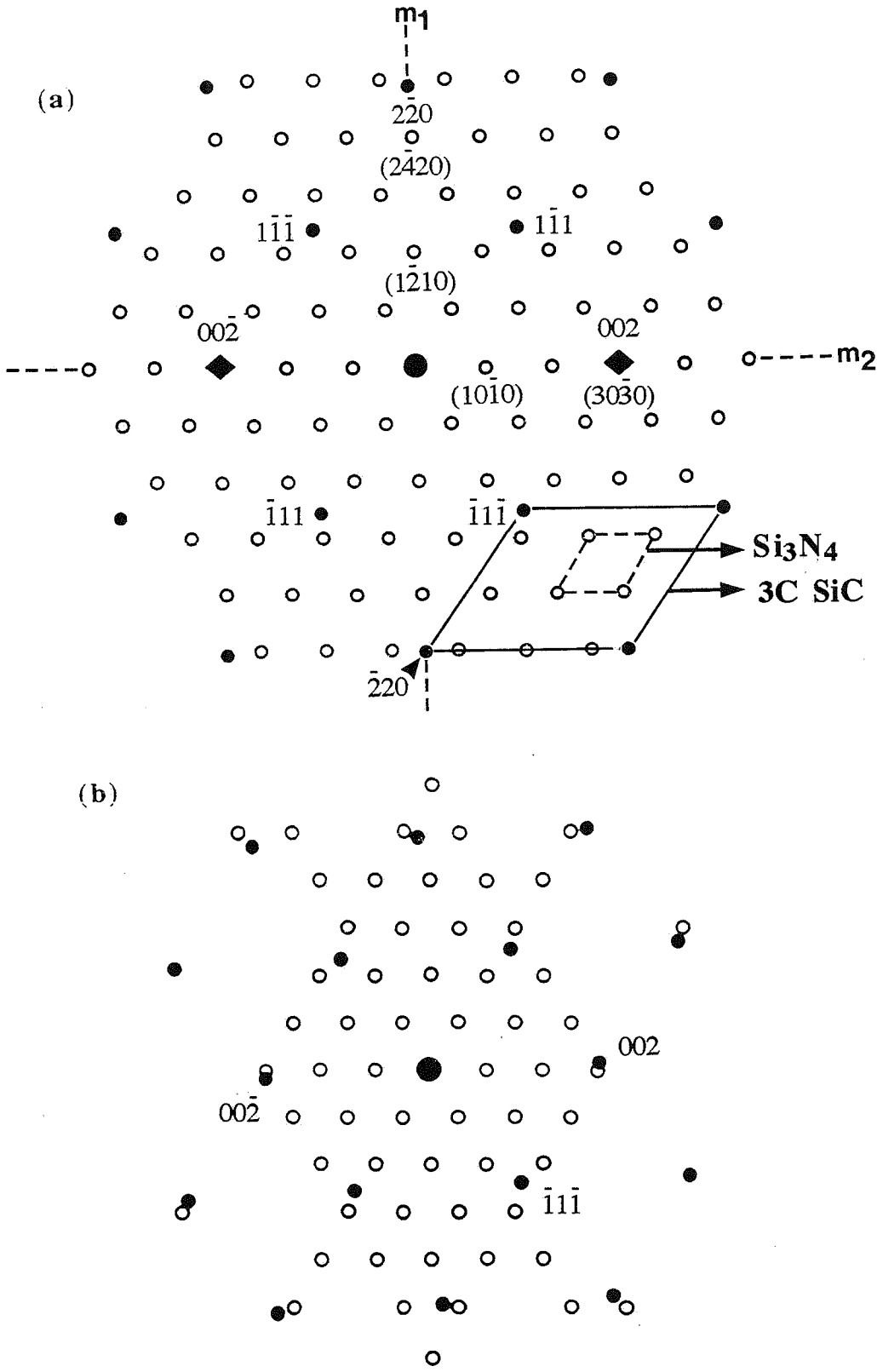

Fig. 6.17 The indexed schematic overlapping diffraction patterns corresponding to the images (a) in Fig. 6.13 and (b) in Fig. 6.15 showing the orientation relationships between SiC grains and intragranular Si_3N_4 precipitates.

Finally in relation to these Si_3N_4 precipitates, no intragranular Si_3N_4 precipitates were identified inside α-SiC grains and the size of the precipitates are much smaller than the mean particle size of the starting powder. Therefore, precipitates could have arisen from one of the following:

i) The precipitates found to be distributed inside 3C SiC grains could have been the small Si_3N_4 particles in the powder which went to the voids between large α-SiC grains in the starting powder during mixing and were trapped there and unable to grow any bigger during grain growth because of the insufficient supply of silicon and nitrogen atoms. These small particles obviously went through a solution reprecipitation mechanism and hence transformed to β-Si_3N_4. During the liquid phase sintering, 3C SiC grains next to small Si_3N_4 grains would grow faster and by surrounding small β-Si_3N_4 grains, they could cut off the silicon and nitrogen flux. This will prevent the grain growth of such trapped Si_3N_4 grains.

ii) They could have formed from the nitrogen gas phase (which is produced by the decomposition of Si_3N_4) reacting with SiC when the inside of the tantalum can is supersaturated with nitrogen gas. The drawback for this explanation is that no Si_3N_4 precipitate were found in the composites made from deoxidised compacts for which the grain growth was minimal.

Interphase boundaries between SiC and Si_3N_4 grains

The character of interphase boundaries between SiC and the Si_3N_4 grains of a similar size was different from that of interphase boundaries between SiC grains and Si_3N_4 precipitates. Most of the interphase boundaries observed either by HREM or Fresnel defocus imaging techniques were covered with thin intergranular films. The micrographs from a Fresnel through-focus series from Si_3N_4-α SiC and Si_3N_4-3C SiC grains shown in Fig. 6.18 demonstrate that both interphase boundaries are wetted with thin films. It can also be seen that the interphase boundary between Si_3N_4-α SiC is curved. This was a general observation – other Si_3N_4 α SiC interphase boundaries not shown here were also found to be curved.

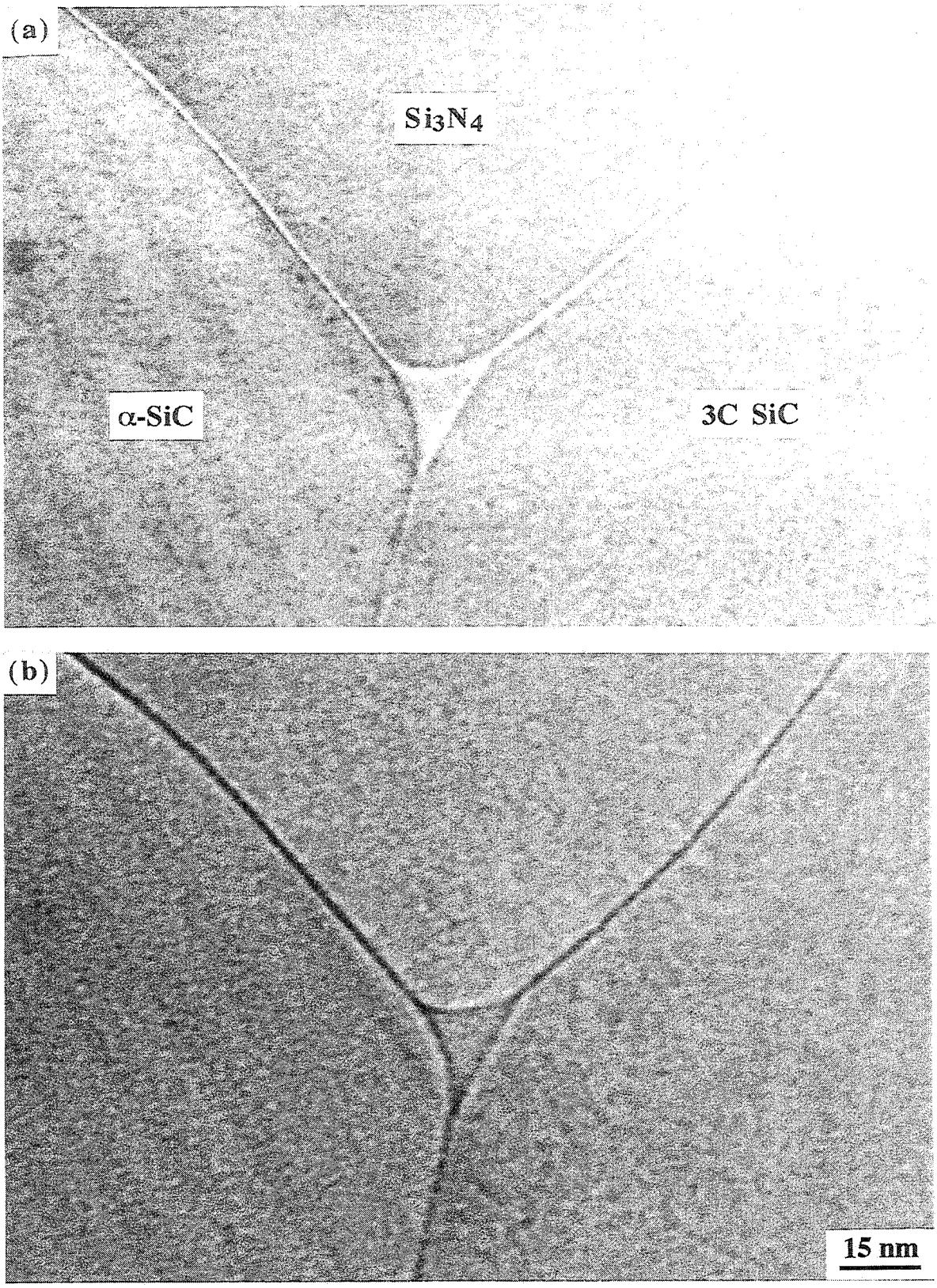

Fig. 6.18 (a) Underfocus and (b) overfocus Fresnel fringe profiles indicating the existence of intergranular films at three different interfaces connected to the same triple junction formed between a 3C SiC grain, a α-SiC grain and a Si_3N_4 grain.

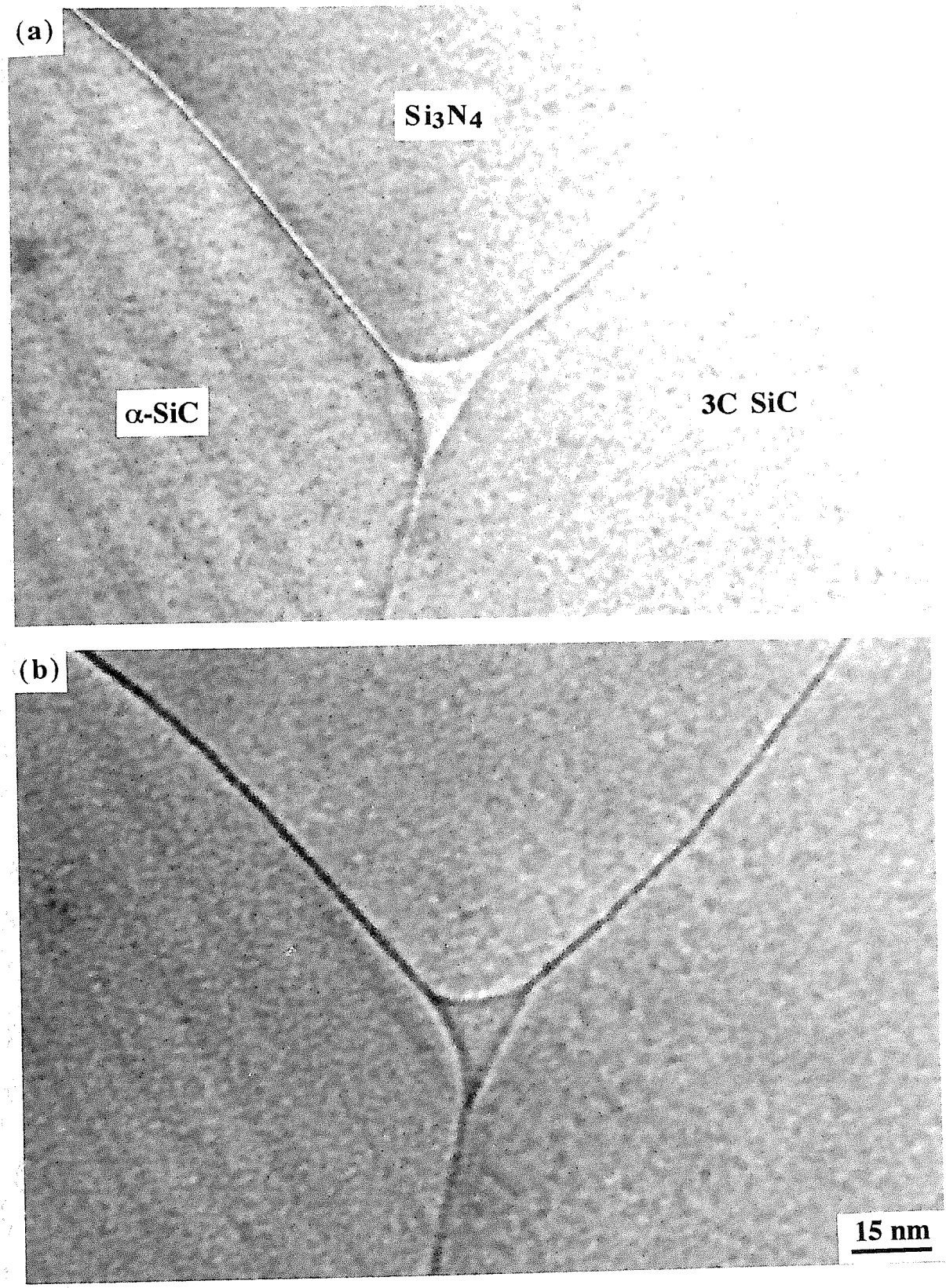

Fig. 6.18 (a) Underfocus and (b) overfocus Fresnel fringe profiles indicating the existence of intergranular films at three different interfaces connected to the same triple junction formed between a 3C SiC grain, a α-SiC grain and a Si_3N_4 grain.

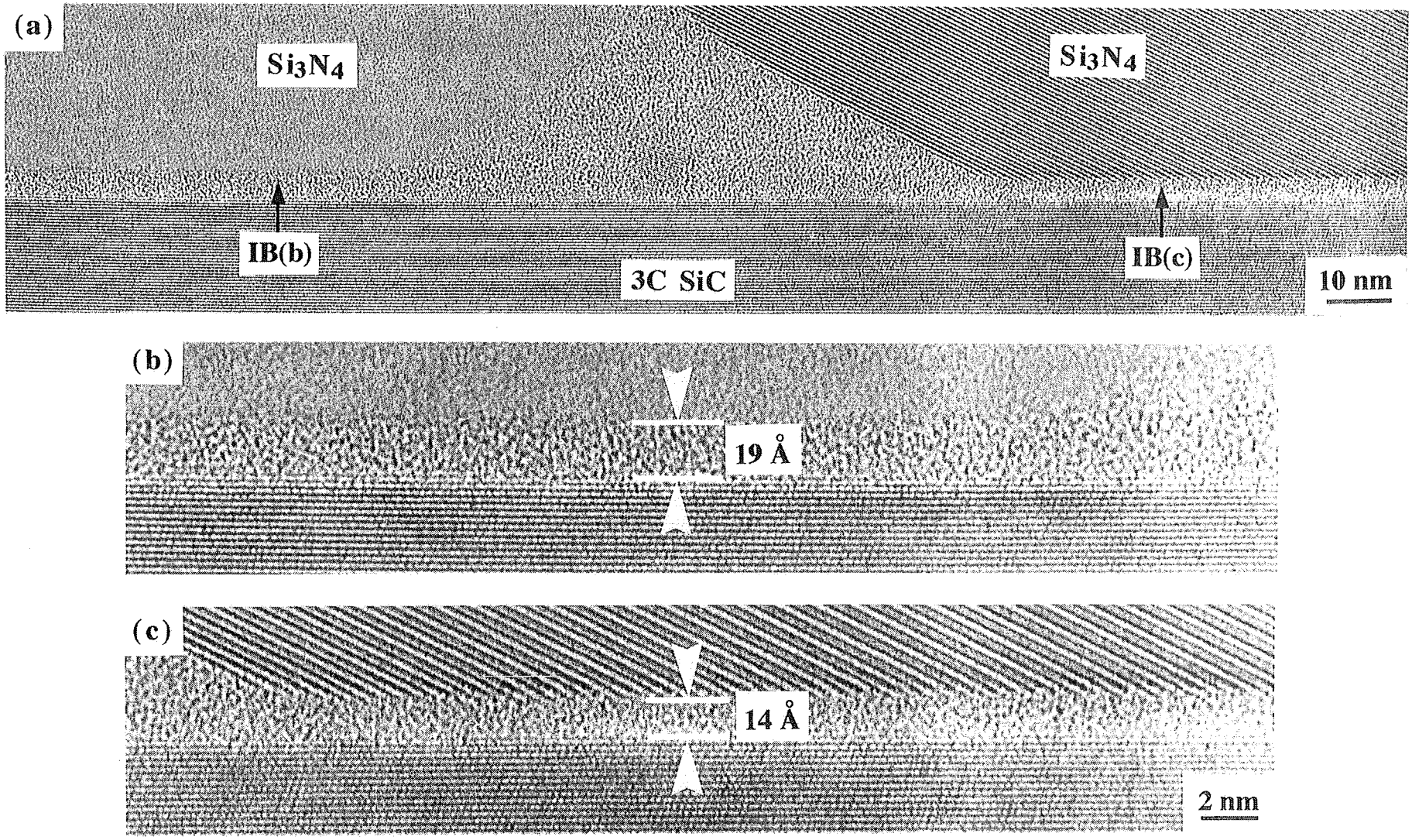

Fig. 6.19 (a) A HREM image of two interphase boundaries between a 3C SiC and a Si_3N_4 grains attached to the same triple junction; (b) and (c) are the enlarged views from the interfaces labelled as IB(b) and IB(c) in (a) showing the differences in the film thickness.

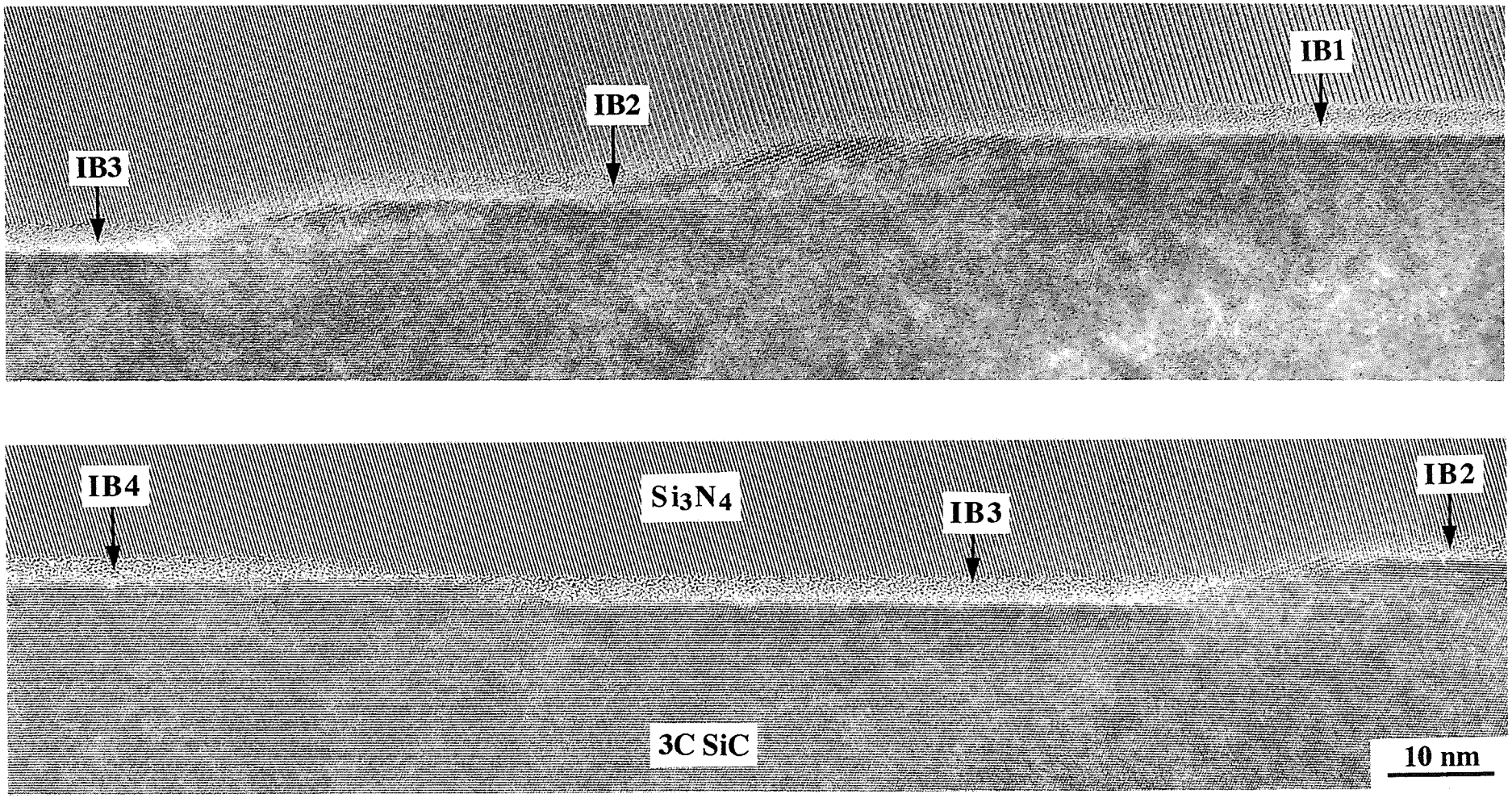

Fig. 6.20 High resolution image of an interphase boundary between a β-Si_3N_4 grain and a 3C SiC grain showing that the interface contains large steps and that some parts of the interface are not aligned parallel to the electron beam.

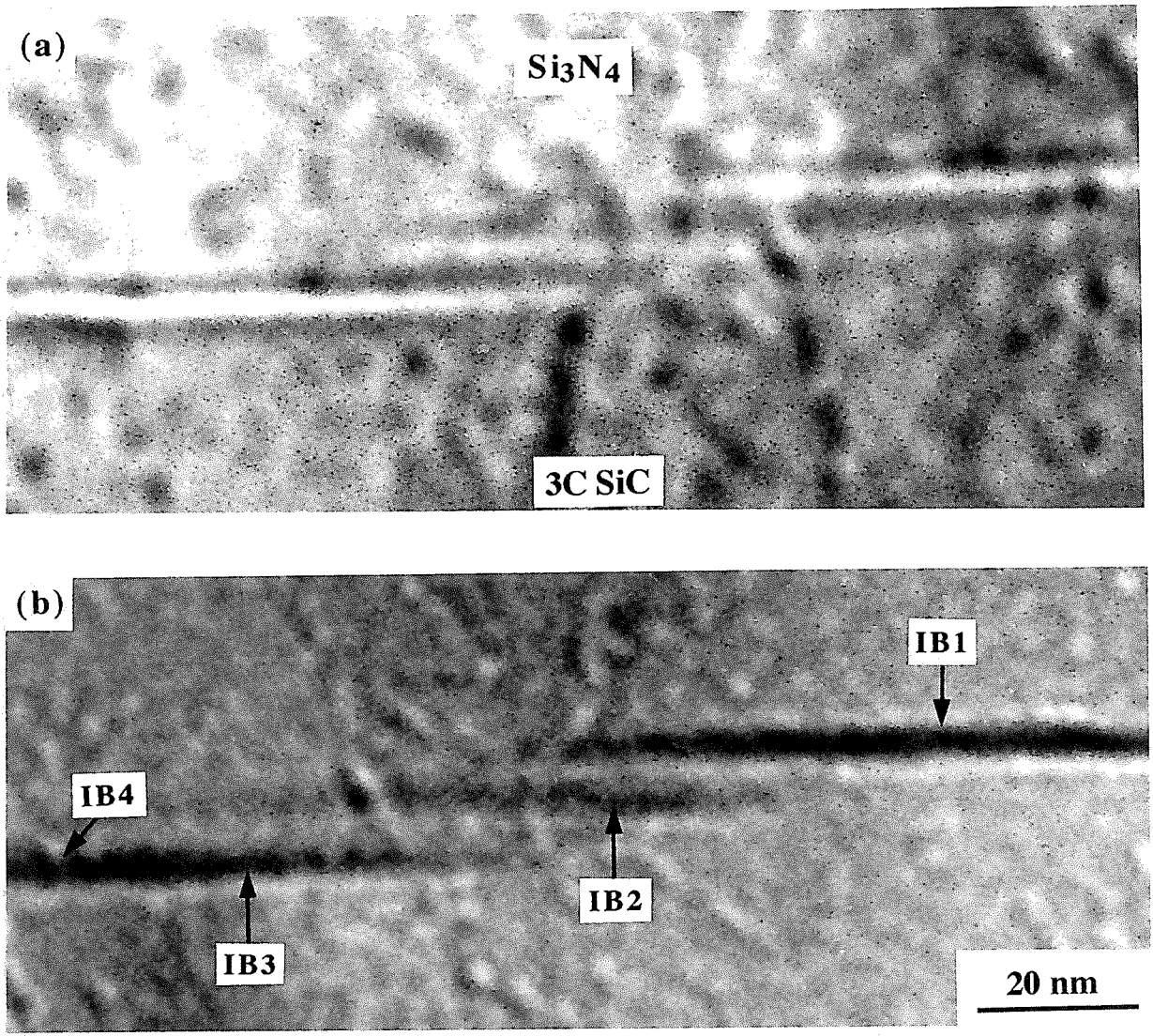

Fig. 6.21 (a) Underfocus and (b) overfocus Fresnel images of the same interphase boundary as Fig. 6.20. Analysis of the Fresnel fringes as a function of defocus shows that the interphase boundary contains a thin intergranular amorphous film throughout the area imaged in Fig. 6.20.

The interface in Fig. 6.20 contrasts with the observation of a discontinuous intergranular film between SiC whiskers and Si_3N_4 matrix grains reported by Das Chowdhury *et al.* (1992). However, an examination of the intergranular film-free region of the interface in their HREM image (Figure 1d from Das Chowdhury *et al.*) shows that firstly this region is noticeably thicker than where there is clear evidence of a thin film in a region of the interface located 20 nm away laterally along the interface and secondly there is a ribbon of bright contrast at the supposedly film free region. The bright contrast can of course arise from an intergranular film which is covered with crystalline phase if the interface is not edge-on at that particular region, as can be seen in the HREM image shown in Fig. 6.20.

Although Das Chowdhury *et al.* determined the oxygen concentration along the interphase by position resolved electron energy loss spectroscopy, they did not observe any sharp oxygen concentration peak for the intergranular film free region, while a sharp peak was observed for the region where intergranular film was observed. While they argued that this was consistent with a discontinuous layer of oxygen-rich material at the SiC-Si_3N_4 interphase boundary, their observations are more readily explicable in the same terms as Fig. 6.20.

Studies on the characterisation of SiC-Si_3N_4 interphase boundaries have been few, unlike those on Si_3N_4-Si_3N_4 grain boundaries. In addition to the studies by Das Chowdhury *et al.* (1992), Ünal *et al.* (1992) & Ünal and Mitchell (1992) identified the orientation relationships at SiC-Si_3N_4 interphase boundaries formed between chemical vapour deposited (CVD) α-Si_3N_4 on the (111) surface of 3C SiC single crystals. The most prominent orientation relationship was found to be:

$$[110]_{3C\ SiC} \parallel [0001]_{\alpha\text{-}Si_3N_4} \text{ and } (1\bar{1}1)_{3C\ SiC} \parallel (10\bar{1}0)_{\alpha\text{-}Si_3N_4}$$

They did not observe any intergranular film and concluded that some of the large lattice mismatch which occurred as a result of the above orientation relationship is relieved through rotations of the Si_3N_4 grains due to the absence of such films.

Further work by More *et al.* (1991) & Ünal *et al.* (1993) investigated the microstructure of hot pressed and hot isostatically pressed SiC whisker reinforced Si_3N_4 matrix composites. More *et al.* (1991) found a film thickness of 1 to 2 nm at SiC-Si_3N_4 interphase boundaries in 30 vol% SiC whisker reinforced and hot pressed material with the aid of 6 wt% Y_2O_3 and

1.5 wt% Al_2O_3 whereas Ünal *et al.* (1993) showed the existence of very large intergranular films (5-10 nm) at the interphase boundaries in 10 vol% SiC whisker reinforced and hot isostatically pressed material without the addition of densification aids. Although neither of the researchers reported any orientation relationship between SiC and Si_3N_4 crystals, the micrographs shown in both of those papers do not imply a special orientation relationship at the interphase boundaries.

In my work, the interphase boundaries between SiC and large β-Si_3N_4 grains did not have any special orientation relationships across the interfaces and support the observations of intergranular films of More *et al.* (1991) & Ünal *et al.* (1993). In contrast, when the interphase boundaries are formed between 3C SiC and β-Si_3N_4 precipitates, the grains were aligned so that the orientation relationships were close to;

$$[110]_{3C\ SiC} \parallel [0001]_{\beta\text{-}Si_3N_4} \text{ and } (200)_{3C\ SiC} \parallel (10\bar{1}0)_{\beta\text{-}Si_3N_4}$$

$$[110]_{3C\ SiC} \parallel [0001]_{\beta\text{-}Si_3N_4} \text{ and } (1\bar{1}1)_{3C\ SiC} \parallel (10\bar{1}0)_{\beta\text{-}Si_3N_4}$$

$$[110]_{3C\ SiC} \parallel [02\bar{2}7]_{\beta\text{-}Si_3N_4} \text{ and } (220)_{3C\ SiC} \parallel (40\bar{4}0)_{\beta\text{-}Si_3N_4}$$

When taken together with the results obtained by Ünal and co-workers, it suggests that the Si_3N_4 precipitates are formed either from a reaction between nitrogen gas and SiO_2 and/or SiC enabling epitaxial deposition of β-Si_3N_4 on 3C SiC and/or they are formed from Si_3N_4 supersaturated liquid epitaxially and then trapped inside 3C SiC grains during grain growth.

6.3.4 Interphase boundaries between h-BN inclusions and SiC grains

The interfaces between disc-like h-BN inclusions and SiC grains have been investigated by electron diffraction and TEM techniques. The most striking observation was that a large number of examples were found both within SiC grains and at interfaces where the {0001} h-BN planes were parallel to either {111} 3C SiC or {0001} α-SiC. If the inclusions are at interfaces they are generally associated with intergranular amorphous phases. Whenever they are embedded in the 3C SiC grains, the interface has structure which depends on its orientation.

Examples of h-BN-3C SiC interphase boundaries with the beam direction parallel to $[\bar{1}10]$ 3C SiC are shown in the dark field TEM image in Fig. 6.22(a) where {0001} planes of two BN inclusions are parallel to two sets of {111} planes, at 70.53° to one another, of the surrounding twinned 3C SiC grain. One of the inclusions appears dark because of the dark field conditions used: an objective aperture was placed on both the $(1\bar{1}1)$ SiC spot and the (0002) spot of h-BN_2. The position of the objective aperture is indicated in the diffraction pattern (Fig. 6.22(b)), which was obtained when the selected area aperture was covering both the inclusions and the twinned SiC grain. An indexed schematic representation of Fig. 6.22(b) is shown in Fig. 6.22(c). Note that neither of the h-BN inclusions were parallel to any low index zone axis.

HREM images such as the one from the boxed area in the Fig. 6.22(a) displayed in Fig. 5.10(a) show that in general there was a very thin residual intergranular film at the interphase boundaries between the h-BN inclusions and the surrounding SiC grains. In this case, the film was ≈ 12±1 Å thick. Interestingly, the end of h-BN inclusion starts to curve at the twin boundary separating the SiC grain and this curved interphase boundary is not wetted with an intergranular film. The orientation of two different sets of {111} SiC planes with respect to {0002} h-BN planes changes at the twin boundary. This must be effecting the wetting behaviour at these interphase boundaries since other observations at different interphase boundaries also showed the same behaviour. The grain boundary formed between the two inclusions will be discussed in Section 6.3.6.

A second example, shown in Fig. 6.23 demonstrates the existence of a half lens shaped intergranular film. It is interesting that the film does not extend to the interphase boundary beyond the point at (∗) where a SiC twin boundary is intersecting the interface. This is completely the reverse observation to that shown in Fig. 5.10(a), despite the fact that the orientation relationship across the interphase boundary is the same.

Although Clarke's theory (Clarke, 1987), as discussed in Chapter 5, explains the observation of this 12 Å thick amorphous film between h-BN and SiC when (0002) planes of h-BN are parallel to (111) planes of SiC (Fig. 5.10(a)), it does not explain the observation of a discontinuous amorphous phase as soon as the orientation changes between the inclusion and the SiC grain where the twin boundary intersects the inclusion.

There is no current theory to explain the situation shown in Fig. 5.10(a) other than a statement in opposition to the theory of Clarke (1987) and the analysis in Chapter 5, namely that the wetting behaviour is indeed effected by the changing misorientation across the interface when the orientation of a isotropic grain with respect to an anisotropic grain is different. It is worth noting that the film thickness at interface (labelled as *IB1*) in Fig. 6.23(b) goes up to ≈ 38 Å at the maximum which is more than three times higher than that of the film thickness (≈ 12 Å) established for these type of interphase boundaries. It is also interesting that the remaining part of the interface *(IB2)* which is not wetted with a film is three times longer than the wetted interface *(IB1)*[#]. Simple calculations by assuming that the interface *(IB1)* should not have been wet and hence distributing all the amorphous phase to the interface *(IB2)* can give a film thickness of ≈ 10-12 Å. This gives support to an argument that the reason for the existence of this film at a presumably energetically less favourable interface *(IB1)* in preference to a more favourable interface *(IB2)* is due to de-wetting which is encouraged by the existence of a lens shaped void at the less favourable interface *(IB1)* where the liquid which is squeezed out from interface *(IB2)* could collect.

In a further example, an h-BN inclusion is shown to exist between a 3C SiC grain and a α-SiC grain (Fig. 6.24(a)) where the orientation relationship can be deduced to be:

$$[110]_{\text{3C SiC}} \parallel [11\bar{2}0]_{\text{h-BN}} \text{ and } (1\bar{1}\bar{1})_{\text{3C SiC}} \parallel (0001)_{\text{h-BN}}$$

$$[11\bar{2}0]_{\alpha\text{-SiC}} \parallel [11\bar{2}0]_{\text{h-BN}} \text{ and } (0001)_{\alpha\text{-SiC}} \parallel (0001)_{\text{h-BN}}$$

These orientation relationships were by far the dominant observed types between SiC and h-BN grains in this study. Here, it can be seen that there is a large step between the h-BN inclusion and the 3C SiC grain, whereas the interface on the other side is flat. Although there is bright contrast at the interphase boundaries indicative of the existence of intergranular films, the thickness of the sample at this region prevented more detailed HREM observations at these interfaces to establish their nature. The above case is very interesting since it has been proposed that BN effects the stability of different SiC polytypes (*e.g.*, Ruh *et al.*, 1988). This will be discussed in detail in Chapter 7 in connection with the transformation behaviour of SiC polytypes.

[#] *Note that the entire interface is previously shown in Fig. 4.1(a).*

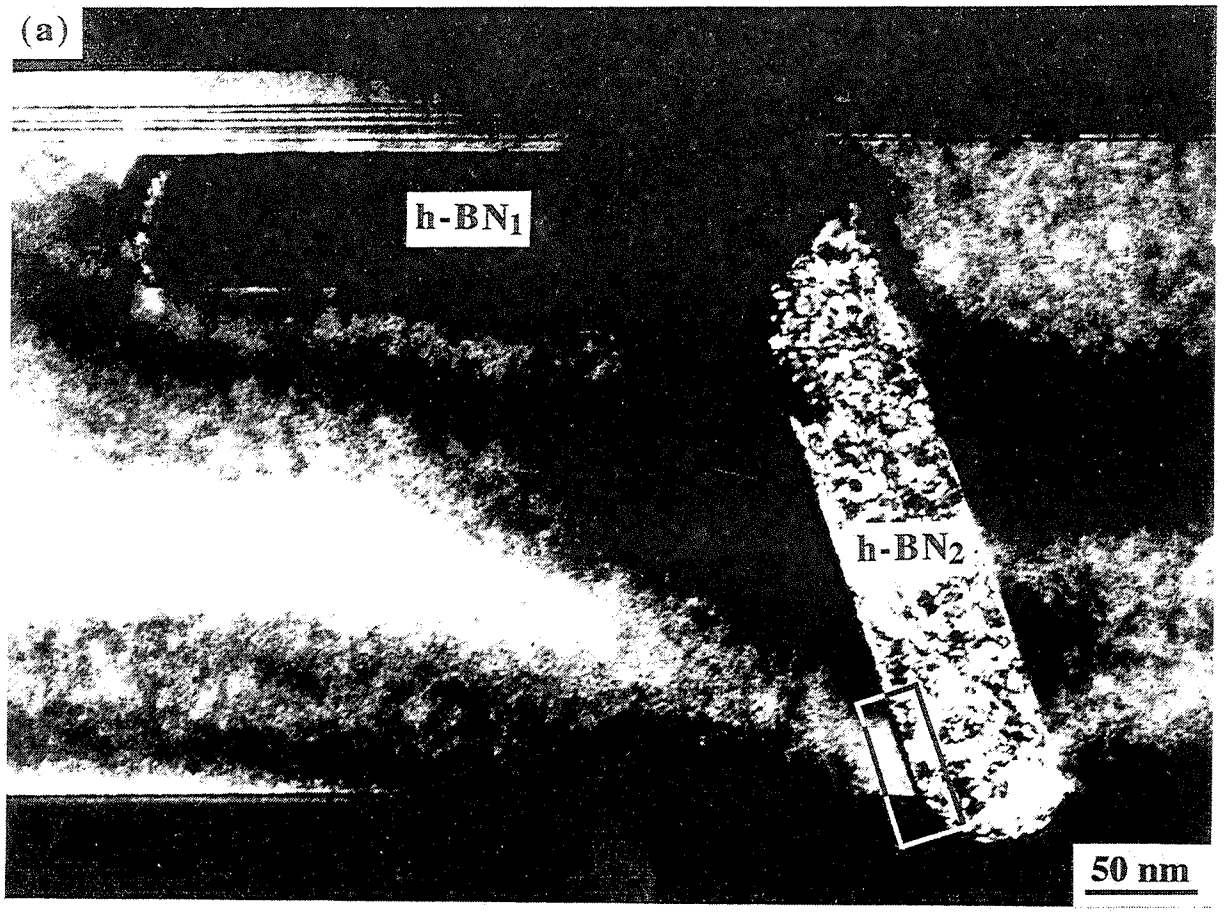

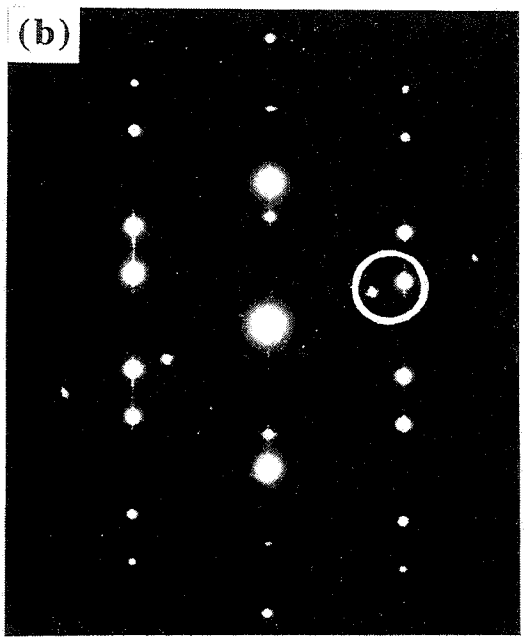

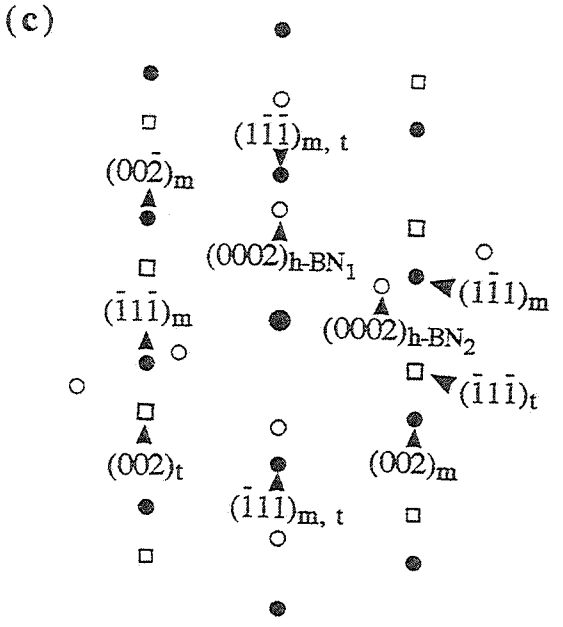

Fig. 6.22 (a) A dark field image of h-BN inclusions grown onto two sets of {111} 3C SiC planes; (b) the diffraction pattern obtained when the 3C SiC grain was parallel to [110] direction and (c) an indexed schematic diffraction pattern.

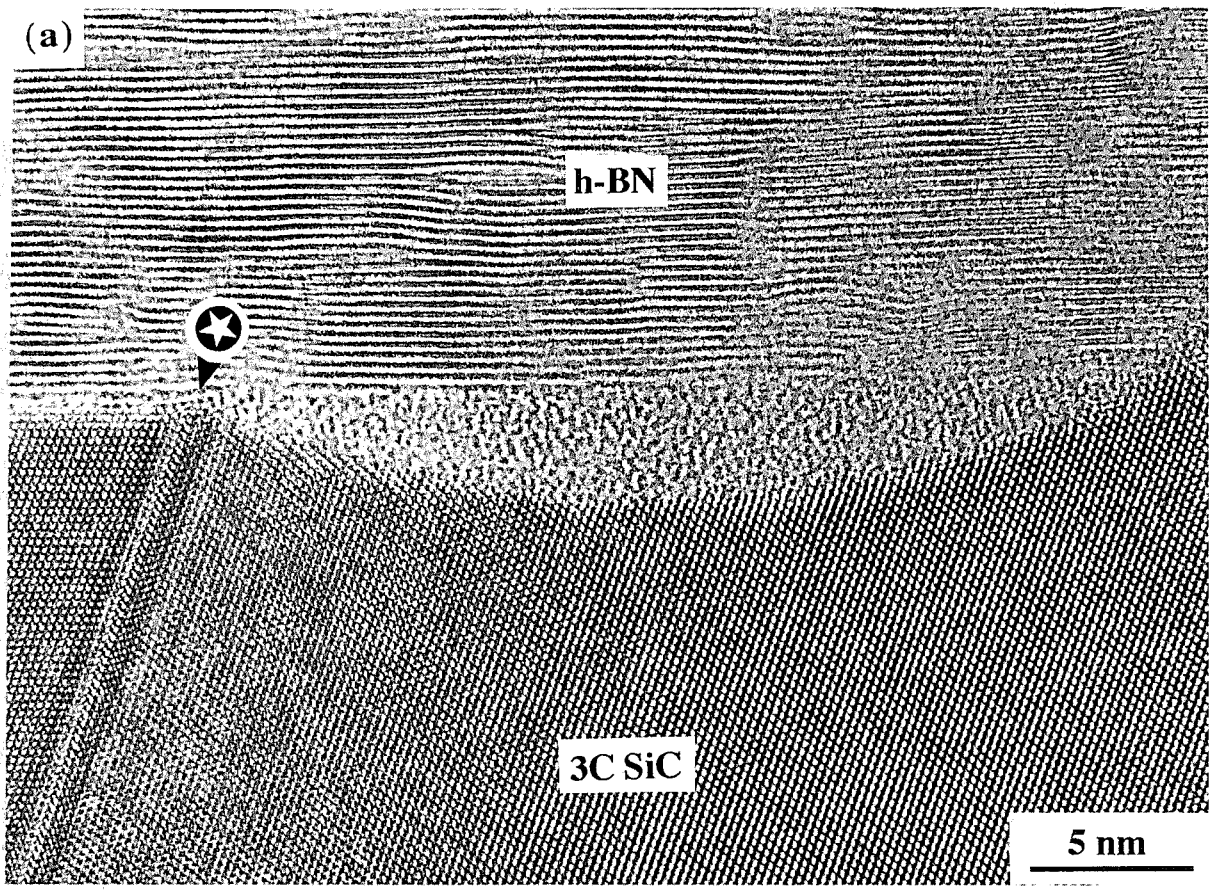

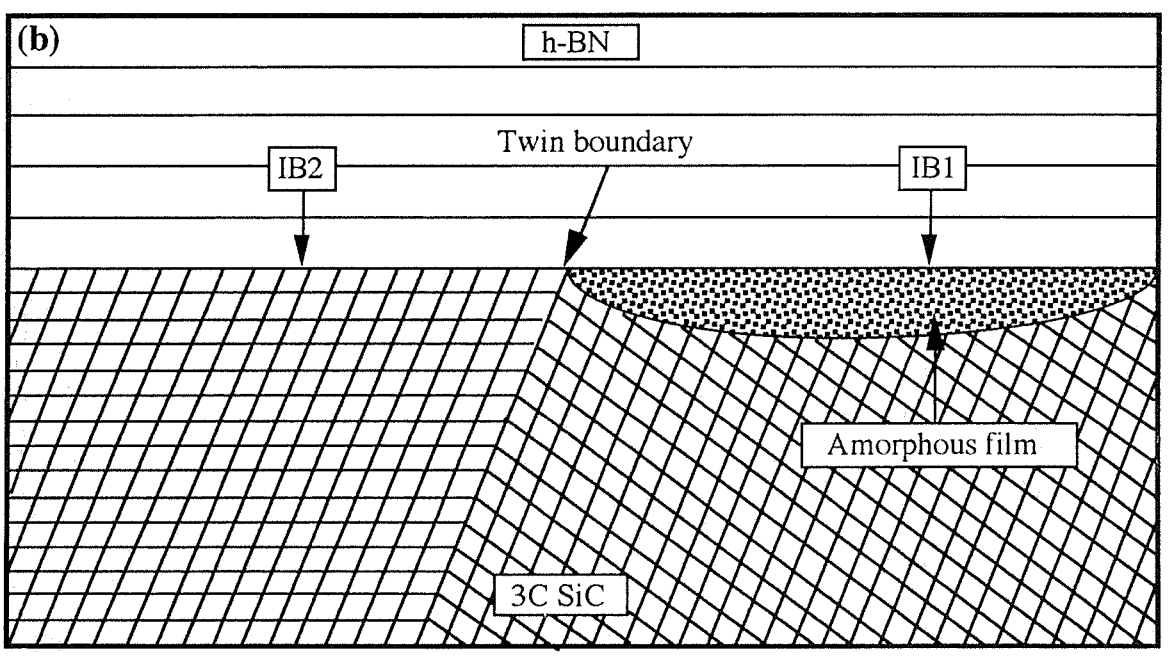

Fig. 6.23 (a) HREM image of an interphase boundary between h-BN and SiC grains shows that wetting behaviour is changed when a twin boundary intersects the interphase boundary and (b) its schematic representation. This figure is an enlarged view of Fig. 4.1(a).

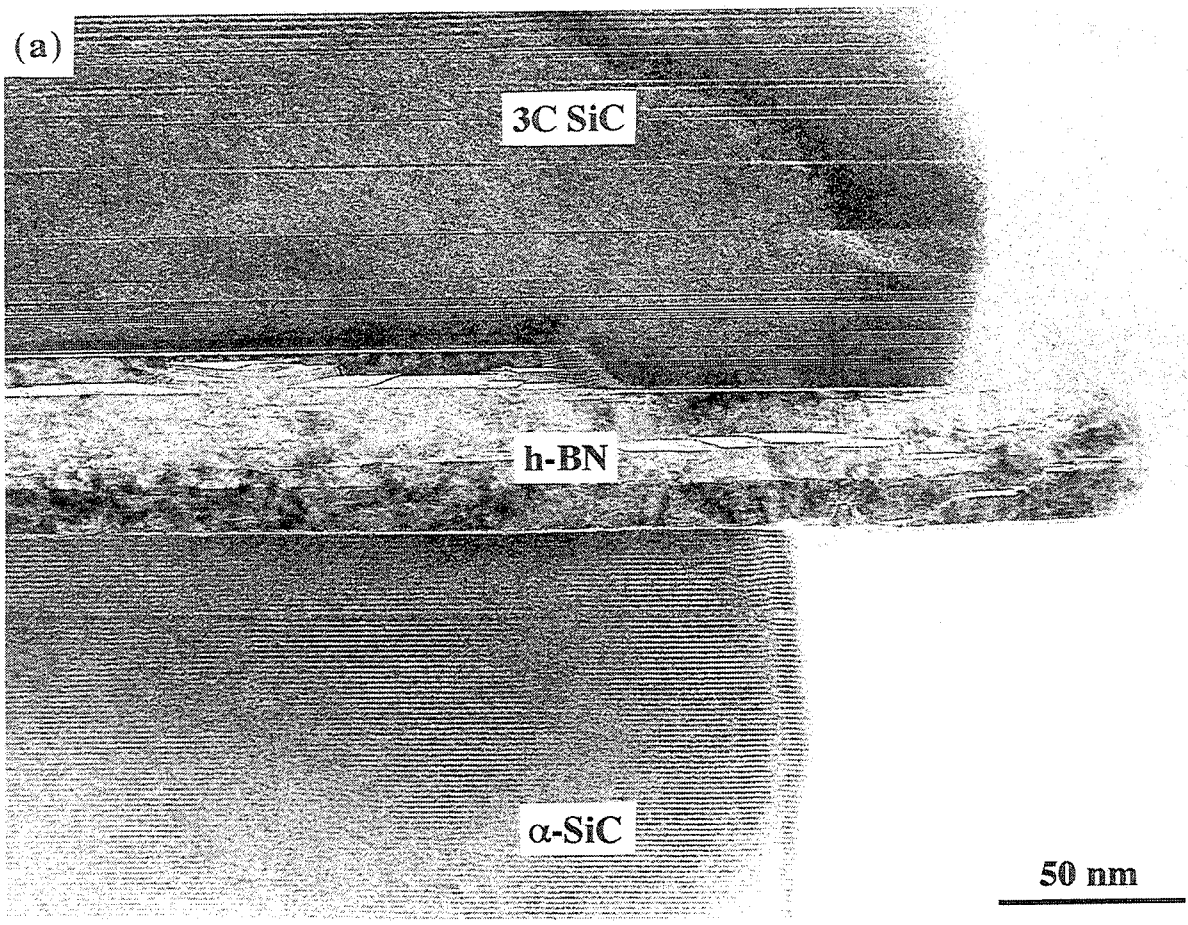

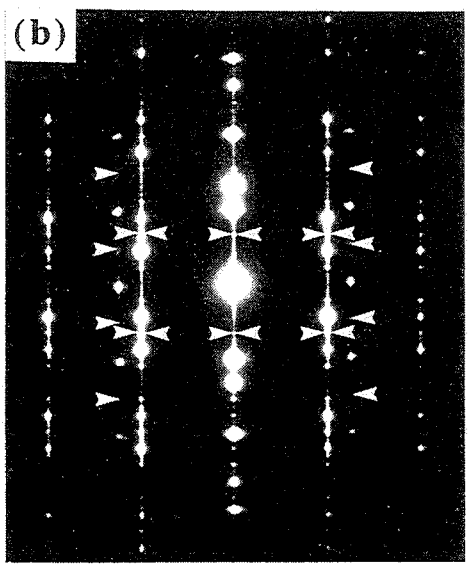

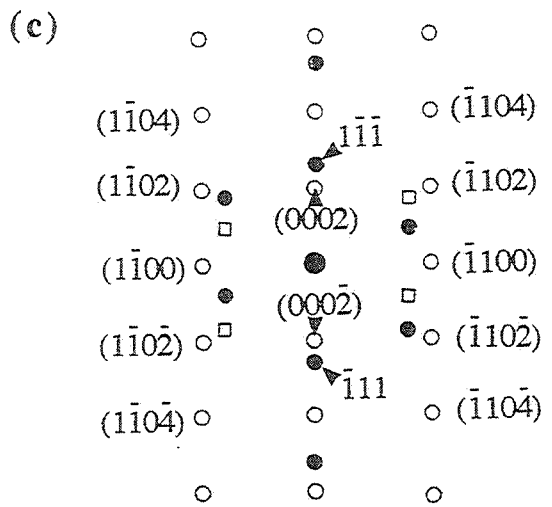

Fig. 6.24 (a) A bright field image of an h-BN inclusion sandwiched between a twinned 3C SiC and a α-SiC grain; (b) the diffraction pattern obtained when the aperture was covering both grains and the inclusion showing that in the h-BN inclusion and α-SiC grain the beam direction is parallel to [11$\bar{2}$0] and that in 3C SiC the beam direction is parallel to [110]; (c) indexed representation of (b).

The streaking which is evident in the diffraction pattern is due to one dimensional disorder in h-BN and SiC in the [0001] direction. In the $(0001)_{\alpha\text{-SiC}}$ or $(111)_{3C\ SiC}$ row, there is a strong spot corresponding to a ≈ 5 Å *d*-spacing (double arrowed) and there is also a second strong spot perpendicular to this and between twin spots at ≈ 2.66 Å spacing. These are respectively (0001) and $(1\bar{1}03)$ 2H SiC reflections which can be identified as being in the $[11\bar{2}0]$ 2H SiC zone. In addition, $(1\bar{1}01)$ type weak h-BN spots were also observed in the $[11\bar{2}0]$ h-BN diffraction pattern (arrowed in Fig. 6.24(b)) despite the fact that reflections with *(h + 2k = 3n and l)* is odd are all absent in h-BN (Pease, 1952) because of double diffraction.

In contrast to these observations, (0001) h-BN planes were not always parallel to (111) 3C SiC planes, and in these cases the interfaces contained thin intergranular films associated with small steps and ledges at interphase boundaries between h-BN and 3C-SiC.

A HREM image of such a h-BN-3C SiC interphase boundary when the beam direction was again parallel to [110] 3C-SiC is shown in Fig. 6.25 along with the diffraction pattern of the SiC and the inclusion. Here, the h-BN inclusion is parallel to a $[11\bar{2}0]$ zone axis and the angles between (0001) h-BN and the two sets of (111) 3C-SiC planes are 15 and 55°, respectively. These angles also correspond to the angles that facets make with the interface plane, which is parallel to (0001) h-BN planes. The orientation relationship is close to:

$$[110]_{3C\ SiC} \parallel [11\bar{2}0]_{h\text{-}BN} \text{ and } (111)_{3C\ SiC} \parallel (1\bar{1}02)_{h\text{-}BN}$$

The interphase boundary between the disc-like h-BN inclusion and the 3C SiC consists of different layers. It can be seen that the SiC grain is faceted and that the facets along the (111) planes extend for 15-20 nm in length and 4-6 nm in height. A thin graphite-like h-BN layer is found next to the facets and a small amount of what is most likely a silica-based amorphous phase (with unknown composition) is trapped between SiC facets and h-BN layer. This layer is followed by a 10 nm thick layer with disordered structure. The structure of these layers was established to be turbostratic carbon using the PEELS technique described in section 4.2.3. Next to this layer is again a h-BN layer. A thin film of the same contrast as the 10 nm thick layer is also observed between the main inclusions.

Ruh *et al.* (1992) observed similar films between h-BN bundles in B_4C-BN composites, but they did not comment on the nature of the film. The film they have observed at the interface is most probably a turbostratic carbon film since EDS analysis from delaminated regions of h-BN grains showed a carbon peak in addition to a nitrogen peak. They attributed the observation of carbon peak to the existence of a B(N,C) solid solution.

A second example where (0002) planes of h-BN are not parallel to (111) SiC planes has already been shown in Fig. 4.17(a), but has not been discussed. The diffraction pattern obtained from the interphase boundary is reproduced in Fig. 6.26 (without the spots arising from the twin band in the h-BN inclusion) where the 3C SiC grain and the h-BN inclusion was respectively parallel to [001] and $[10\bar{1}0]$ zone axis with an orientation relationship of:

$$[001]_{3C\ SiC} \parallel [10\bar{1}0]_{h\text{-}BN} \text{ and } (010)_{3C\ SiC} \parallel (0001)_{h\text{-}BN} \text{ and } (100)_{3C\ SiC} \parallel (1\bar{2}10)_{h\text{-}BN}$$

In this case, every three h-BN (0002) planes overlap with every two (200) SiC planes. The mismatch between these two planes is 53 %. By inserting a (200) 3C SiC plane, this mismatch is reduced to 2 %. However, it is observed that the interphase boundaries at either side of the inclusion which are perpendicular to *c*-axis of the inclusion are covered with intergranular films, whereas the interface perpendicular to the *a*-axis direction is curved and also forms moiré fringes.

The composite diffraction pattern (Fig. 6.26) shows that four fold symmetry of SiC (denoted as m_1, m_2, m_3, and m_4) is reduced to two fold (m_1 and m_3), whereas the two fold symmetry (m_1 and m_3) of the h-BN pattern is preserved in this orientation relationship.

Tilting away from this orientation relationship will not produce the same relationship as the one shown in Fig. 6.24 since the angle between [001] and [011] SiC directions is 45°, whereas the angle between $[10\bar{1}0]$ and $[11\bar{2}0]$ directions of h-BN is 30°.

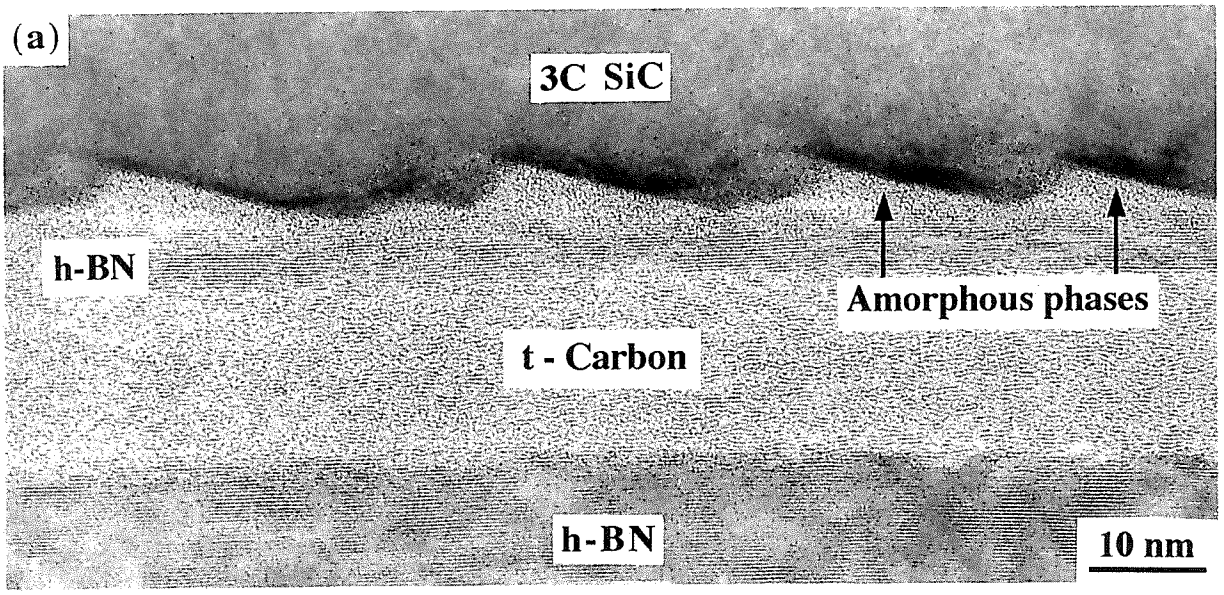

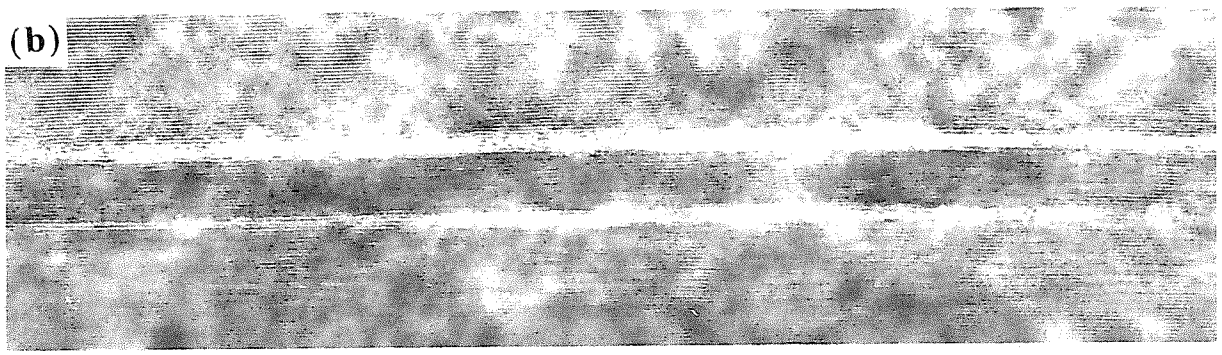

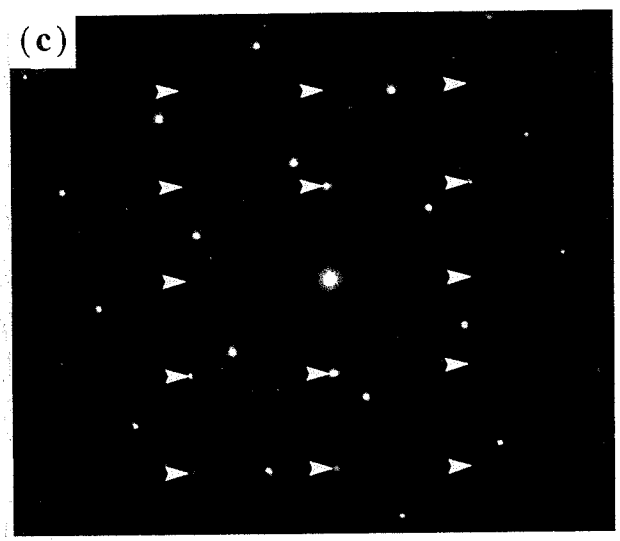

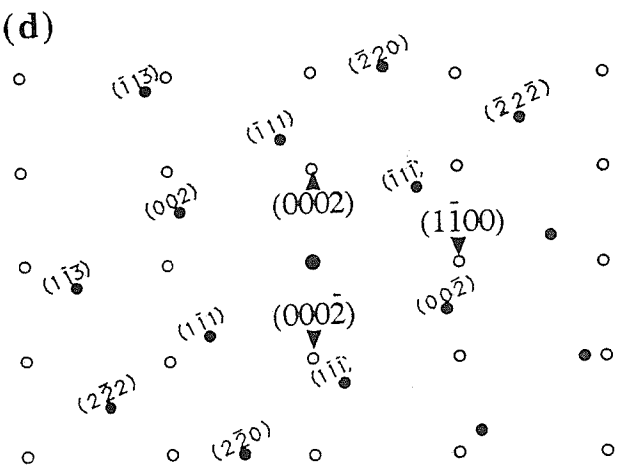

Fig. 6.25 (a) A HREM image of h-BN-3C SiC interphase boundary when (0002) h-BN planes are not parallel to (111) SiC planes. The main inclusion is separated from SiC grain with a thin h-BN layer and a turbostratic carbon layer. (b) A thin layer with a turbostratic structure dividing the BN inclusion in (a). (c) Diffraction pattern obtained when the SiC grain and h-BN inclusion were parallel to [$\bar{1}$10] and [11$\bar{2}$0] directions, respectively and (d) its schematic representation.

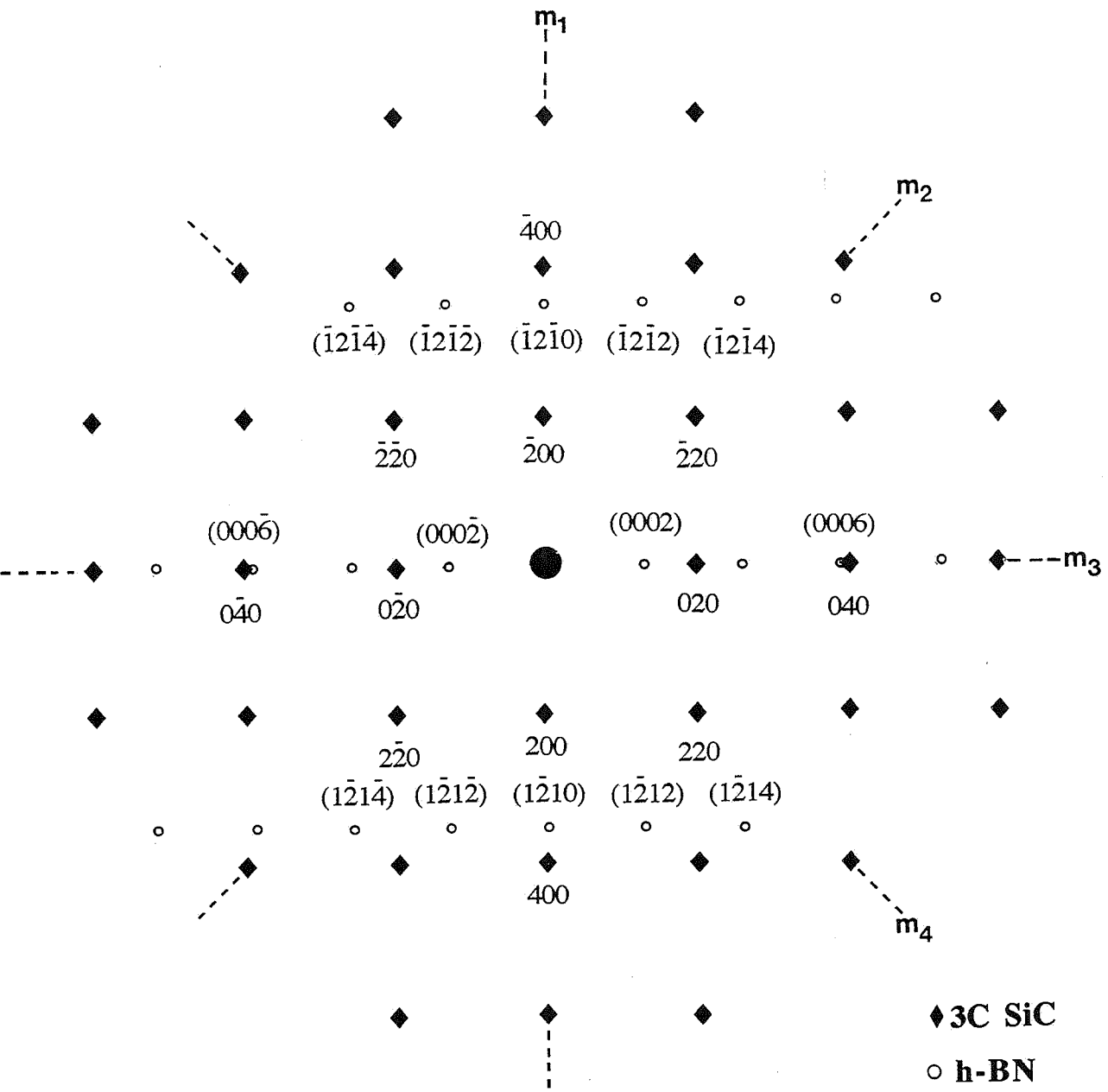

Fig. 6.26 Schematic of an indexed superimposed diffraction pattern obtained from an h-BN inclusion surrounded with a 3C SiC grain (reproduced from Fig. 4.17 without the twinned BN spots). The beam direction was parallel to [10$\bar{1}$0] h-BN and [001] 3C SiC direction and shows the small mismatch between (0006) h-BN and (040) SiC.

6.3.5 Interphase boundaries between h-BN inclusions and Si_3N_4 grains

Interphase boundaries have also been characterised between Si_3N_4 grains and h-BN inclusions in hot isostatically pressed Si_3N_4-SiC composites. These interphase boundaries have a different character from the h-BN-3C SiC interphase boundaries discussed in Section 6.2.4 and generally do not contain any intergranular films, particularly when (0001) h-BN planes were parallel to (100) Si_3N_4 planes, the most commonly observed case. Such interfaces are associated with a very small mismatch of ≈ 1.1 % from the difference between basis vectors in the corresponding planes of ($d_{(10\bar{1}0)} = 6.58$ Å) Si_3N_4 and ($d_{(0001)} = 6.66$ Å) h-BN.

The first kind of interphase boundaries observed are shown in Figs. 6.27 and 6.28. In both cases, (0001) h-BN planes are parallel to the $(10\bar{1}0)$ Si_3N_4 planes. These interfaces can be described as asymmetrical twist interfaces where the rotation angle about the interface plane normal is $\neq 0°$.

In Fig. 6.27, the Si_3N_4 grain is approximately oriented parallel to a $[4\bar{2}\bar{2}3]$ zone axis and the triple junction between three Si_3N_4 grains is filled with the inclusion and an amorphous intergranular phase, but this does not seem to be extending along the BN-Si_3N_4 interphase boundary. The low angle character of the interphase boundary could be the reason that the intergranular film does not extend to the interface from the triple junction. Note also that there is only one step along the interface (seen in (b)). The step height is ≈ 3.30 Å. The contrast and the single step along the interface could be arising due to the strain.

In the second example (Fig. 6.28), the Si_3N_4 grain is oriented parallel to a $[\bar{1}2\bar{1}3]$ and the h-BN inclusion parallel to $[11\bar{2}0]$ with the orientation relationship of:

$$[\bar{1}2\bar{1}3]\ \beta\text{-}Si_3N_4 \parallel [11\bar{2}0]\ \text{h-BN} \text{ and } (10\bar{1}0)\ \beta\text{-}Si_3N_4 \parallel (0002)\ \text{h-BN}$$

Here, the interface contained more than one step and step height is much bigger than the one in Fig. 6.27. However, the length and the height of the steps are not regular. The interface also seems to be free of an intergranular film but there is a similar dark contrast along the interface.

In contrast to the above observations, cases were also observed when the $(10\bar{1}0)$ Si_3N_4 planes were not parallel to (0002) BN planes. The first example of this kind is shown in Fig. 6.29 which is the enlarged view of Fig. 4.1(b). The Si_3N_4 grain is oriented parallel to a $[4\bar{2}\bar{2}3]$ zone axis and the BN inclusion approximately parallel to $[11\bar{2}0]$. However, the difference from the orientation relationship established for Fig. 6.27 is that the angle between the $(10\bar{1}0)$ Si_3N_4 planes and (0002) BN planes is $\approx 71^\circ$ and in this case (0004) (1.66 Å) planes are parallel to $(2\bar{1}\bar{1}2)$ (1.36Å) Si_3N_4 planes.

$$[4\bar{2}\bar{2}3]\ \beta\text{-}Si_3N_4 \parallel [11\bar{2}0]\ \text{h-BN} \text{ and } (2\bar{1}\bar{1}2)\ \beta\text{-}Si_3N_4 \parallel (0002)\ \text{h-BN}$$

In the second, more interesting example, there appears to be a series of ledges one atomic plane high and 7-10 nm long along the 100 nm length of interface (Fig. 6.30). The Si_3N_4 grain is oriented parallel to a [0001] zone axis and the h-BN inclusion is parallel to $[11\bar{2}0]$, *i.e.*, the *c*-axes of h-BN and Si_3N_4 are respectively perpendicular and parallel to the electron beam. Here, the $(10\bar{1}0)$ Si_3N_4 planes make an angle of 3.5-4° with the interface plane whereas the h-BN planes are parallel to the interface plane. Overlapping diffraction patterns showed that when the angle is 3.5°, this orientation relationship brings the other set of $\{10\bar{1}0\}$ planes parallel to $(\bar{1}10\bar{2})$ (1.795 Å) h-BN planes. Therefore, the orientation relationship here is:

$$[0001]\ \beta\text{-}Si_3N_4 \parallel [11\bar{2}0]\ \text{h-BN} \text{ and } (10\bar{1}0)\ \beta\text{-}Si_3N_4 \parallel (\bar{1}10\bar{2})\ \text{h-BN}$$

The expression for low angle grain boundaries can be used to calculate the distance between steps (Read and Shockley, 1950). The calculations for the angle of 3.5-4° between the corresponding planes and for a Burgers vector of 6.58 Å which is perpendicular to the interface plane agree well with the characteristics of the interface that the distance between the steps should be between 9.5-10.8 nm.

The section of the h-BN grain near the interface is in a different orientation to the rest of the grain. How and why this happens will be the subject of next section.

In summary, the interphase boundaries between h-BN and Si_3N_4 are associated with a very small mismatch when the (0001) h-BN planes are parallel to the (100) Si_3N_4 planes. It can be seen from the HREM images that these interphase boundaries are composed of steps and it is highly likely that there are not intergranular films at the interfaces.

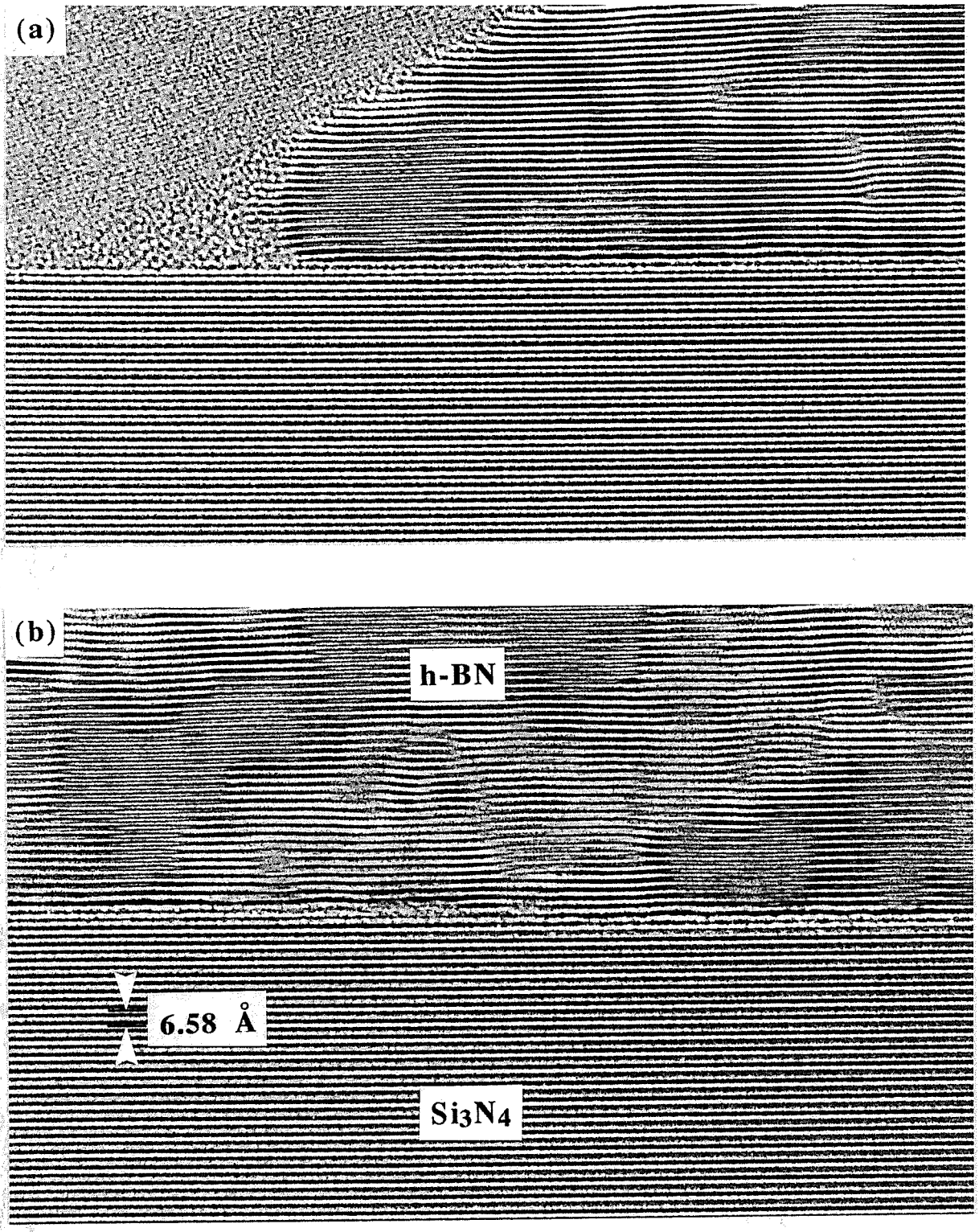

Fig. 6.27 (a) An interphase boundary between an h-BN and a Si_3N_4 grain showing that the amorphous phase from the triple junction does not seem to extend to the interface and (b) an extension of the same interface showing a single step at the interface.

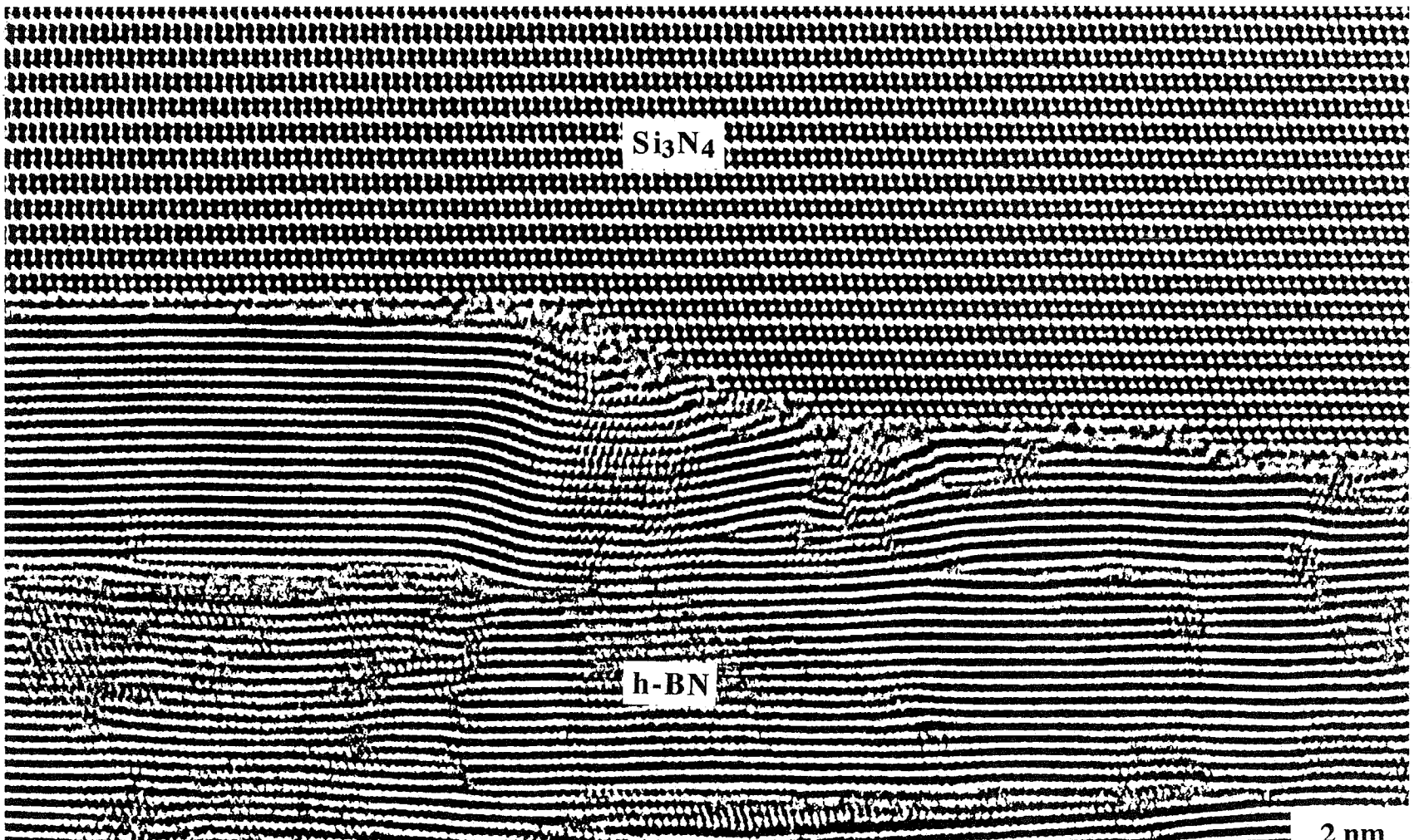

Fig. 6.28 A large step at an interphase boundary between an h-BN and a Si_3N_4 grain imaged when the h-BN and Si_3N_4 grains were approximately parallel to $[11\bar{2}0]$ and [011], respectively.

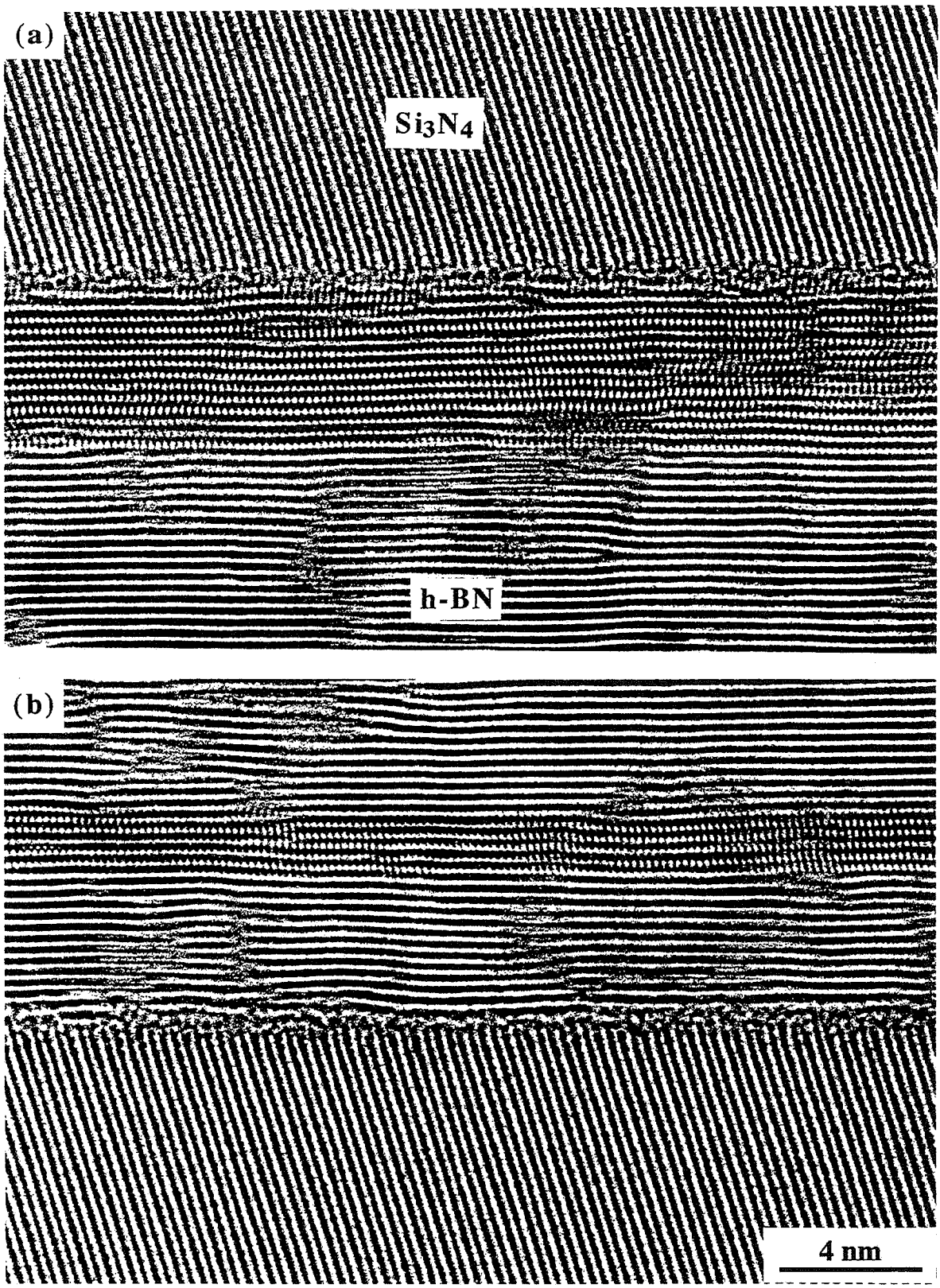

Fig. 6.29 HREM images of interphase boundaries from opposite sides of the BN inclusion surrounded by a β-Si_3N_4 grain showing that h-BN is oriented parallel to $[11\bar{2}0]$ near the interface in (a) whereas in (b) it is only in a $[11\bar{2}0]$ orientation slightly away from the interface.

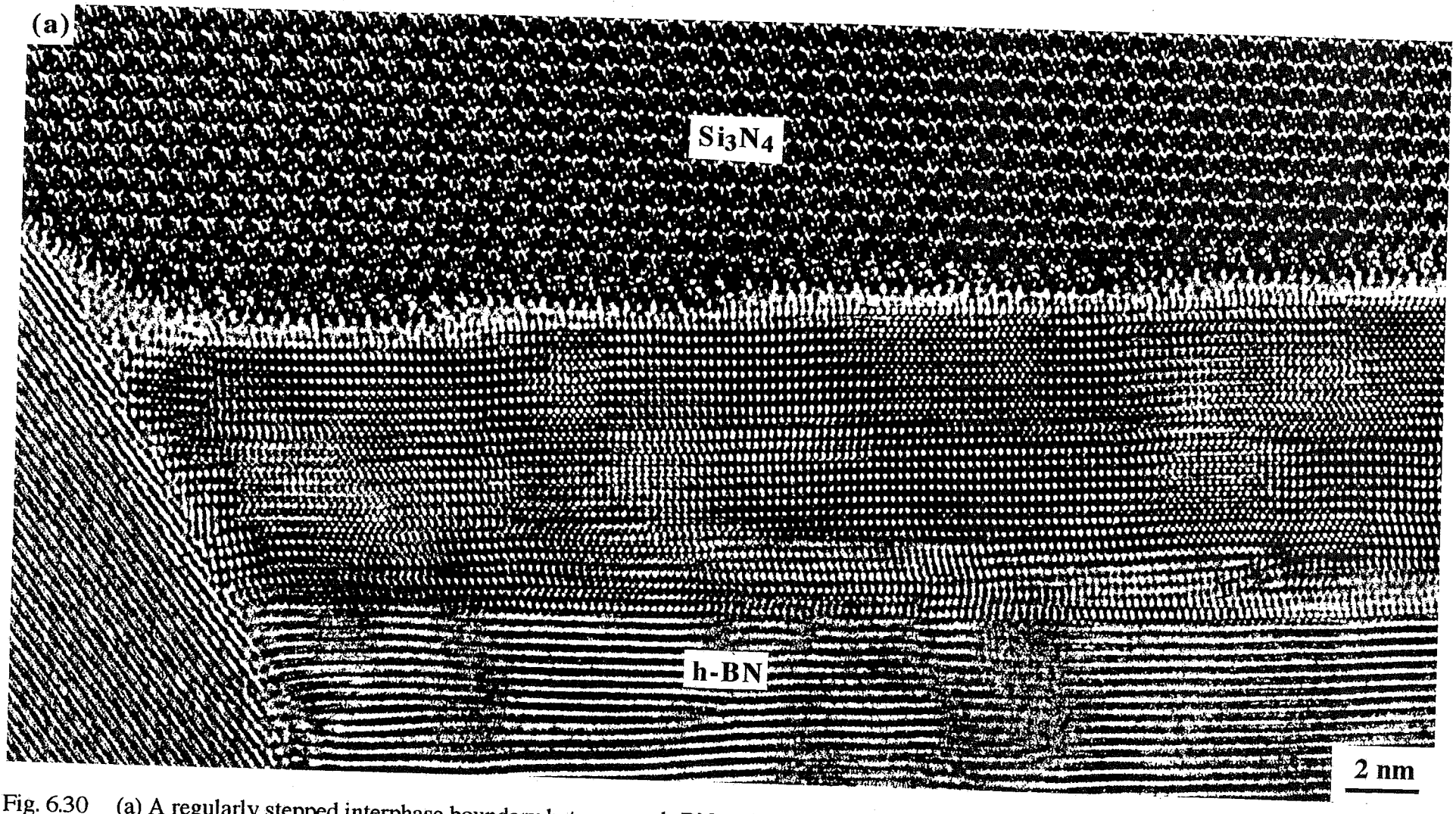

Fig. 6.30 (a) A regularly stepped interphase boundary between an h-BN and a Si_3N_4 grain where the beam directions of respective grains were parallel to $[11\bar{2}0]$ and [0001]; (b) and (c) are the continuation of the interface shown in (a).

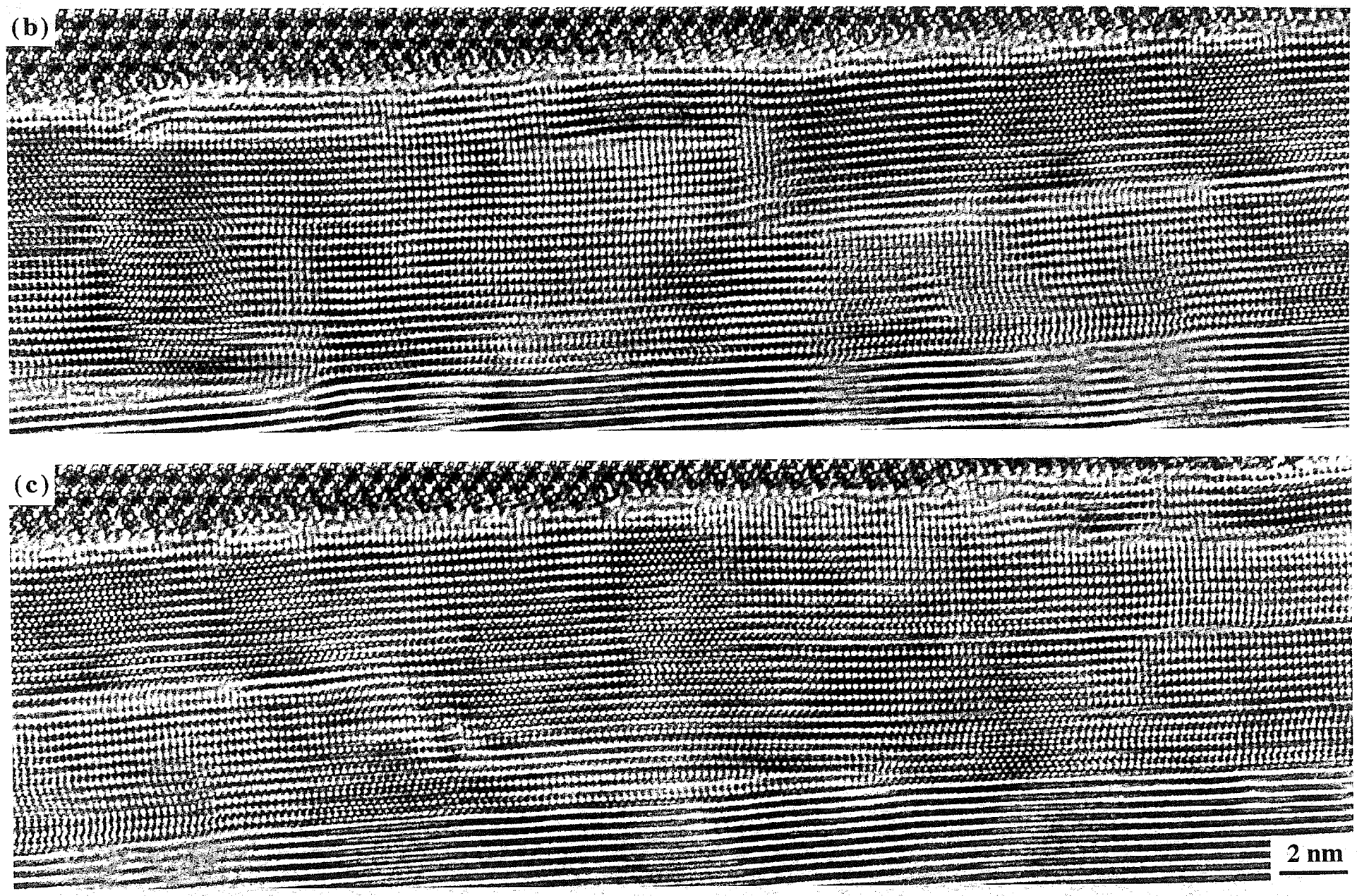
(b)
(c)
2 nm

6.3.6 Grain boundaries between h-BN inclusions

Four different kind of grain boundaries were observed between h-BN inclusions. The first three types of grain boundaries were formed when the *c*-axes of two h-BN inclusions were aligned *(i)* almost perpendicular to one another (Fig. 6.31 and 6.32), *(ii)* 110° to one another (Fig. 6.33) and *(iii)* 142-143° to each other (Fig. 6.34). Although according to the calculations carried out in Chapter 5, these interface combinations should all yield intergranular films containing either silica or boron oxide at the interfaces, none of the interfaces were found to contain any kind of intergranular film. This suggests that these interfaces could have special orientation relationships across them which favour the absence of such films.

The interfaces in Fig. 6.33 and 6.34 were sharp (flat), whereas the interface in Fig. 6.31 was faceted. The schematic diffraction pattern from the interface in Fig. 6.31 shown in Fig. 6.32 illustrates that both the grains are aligned nearly parallel to $[11\bar{2}0]$ h-BN zone axis and shows the following orientation relationship:

$$[11\bar{2}0]_{\text{grain 1}} \parallel [11\bar{2}0]_{\text{grain 2}} \text{ and } (0002)_{\text{grain 1}} \parallel (10\bar{1}0)_{\text{grain 2}}$$

The misfit between the (0002) and $(10\bar{1}0)$ planes is very large (≈ 54 %), but every two (0002) lattice points from grain 1 will nearly coincide with every three $(10\bar{1}0)$ lattice points from grain 2, *i.e.*, 2 × 3.33 Å ≈ 3 × 2.16 Å which reduces the mismatch to ≈ 3 % from 54 %. Interestingly, the composite diffraction pattern almost keeps the original 2mm symmetry of the $[11\bar{2}0]$ h-BN zone axis. A small deviation from the orientation relationship given above exists to achieve this since the grains are not exactly perpendicular and the angle between (0002) planes of grain 1 and 2 is ≈ 87°. This creates two mirror planes (labelled as t_1 and t_2) which are different from the original mirror planes (m_1 and m_2) in Fig. 6.32.

It can be seen that grain boundary consists of three large steps, each of which are followed by a smaller step. Unfortunately, at the interface neither of the grains are sufficiently well aligned parallel to $[11\bar{2}0]$ zone axis to reveal the 2.16 Å fringes and therefore nothing can be said about the plane matching (coherency) across the interface. However, at the steps the lattice fringes from one grain curved and connected to the lattice fringes from the other grain.

Miyazaki *et al.* (1992) also observed two vertically contacted h-BN grains in the pressureless sintered h-BN using a mechanochemically activated BN powder without the use of sintering aids (Hagio *et al.*, 1989). It is not clear whether they have observed a film at the grain boundary or not (despite the absence of sintering aids). The TEM pictures and the explanations are not sufficiently clear to be able to deduce the nature of the interface they have observed. Unfortunately, this is the only report available in the literature on the interface structure of h-BN materials.

The other point to note in Fig. 6.31 is that there is dark contrast inside h-BN inclusions and that there are areas where white fringes become black for a while and then white again (some of which are outlined in the Fig. 6.31). Although these features are not examined in detail, Gou and Ma (1991) proposed that contrast such as this could indicate the existence of stress in the inclusions as well as the presence of edge dislocations and antiphase domains.

The character of interphase boundaries between SiC and h-BN in Fig. 6.22 have already been reported in Section 6.3.4, but the grain boundary formed between the inclusions has been left deliberately to this section for completeness. The HREM image of the grain boundary in Fig. 6.33 showed that the angle between (0002) planes of inclusions shown in Fig. 6.22(a) is 110°, but that the interface plane makes an angle of 61° and 49° with the inclusion 1 and 2, respectively, instead of 55° with both inclusions. The lattice fringes from both grains at the grain boundary are connected to each other with curved lattice fringes similar to the curved fringes observed in Fig. 6.31 and the interface is faceted. The steps were much smaller than those observed in Fig. 6.31.

Twin boundaries formed inside h-BN inclusions have already been discussed in Section 4.2.7.4. These were formed mechanically to release the strains caused by a crack opening that is encouraged by the stresses created by the difference in the thermal expansion coefficients of the matrix and the precipitate. In addition, two h-BN inclusions were found connected to each other with their (0002) planes making an angle of 142-143°. A bright field TEM image along with the indexed diffraction pattern from both the inclusions are shown in Fig. 6.34 in which both the inclusions are aligned parallel to a $[10\bar{1}0]$ h-BN zone axis. The selected area diffraction pattern showed that $(1\bar{2}12)$ type reflections from both the grains are almost coincident. Only a 2° rotation of grain 2 is necessary to generate the twin orientation relationship discussed in Chapter 4. This will also make (0008) $_{\text{Grain 1}}$ and $(\bar{1}2\bar{1}6)$ $_{\text{Grain 2}}$ reflections almost coincident but slightly separated with 0.3 % misfit.

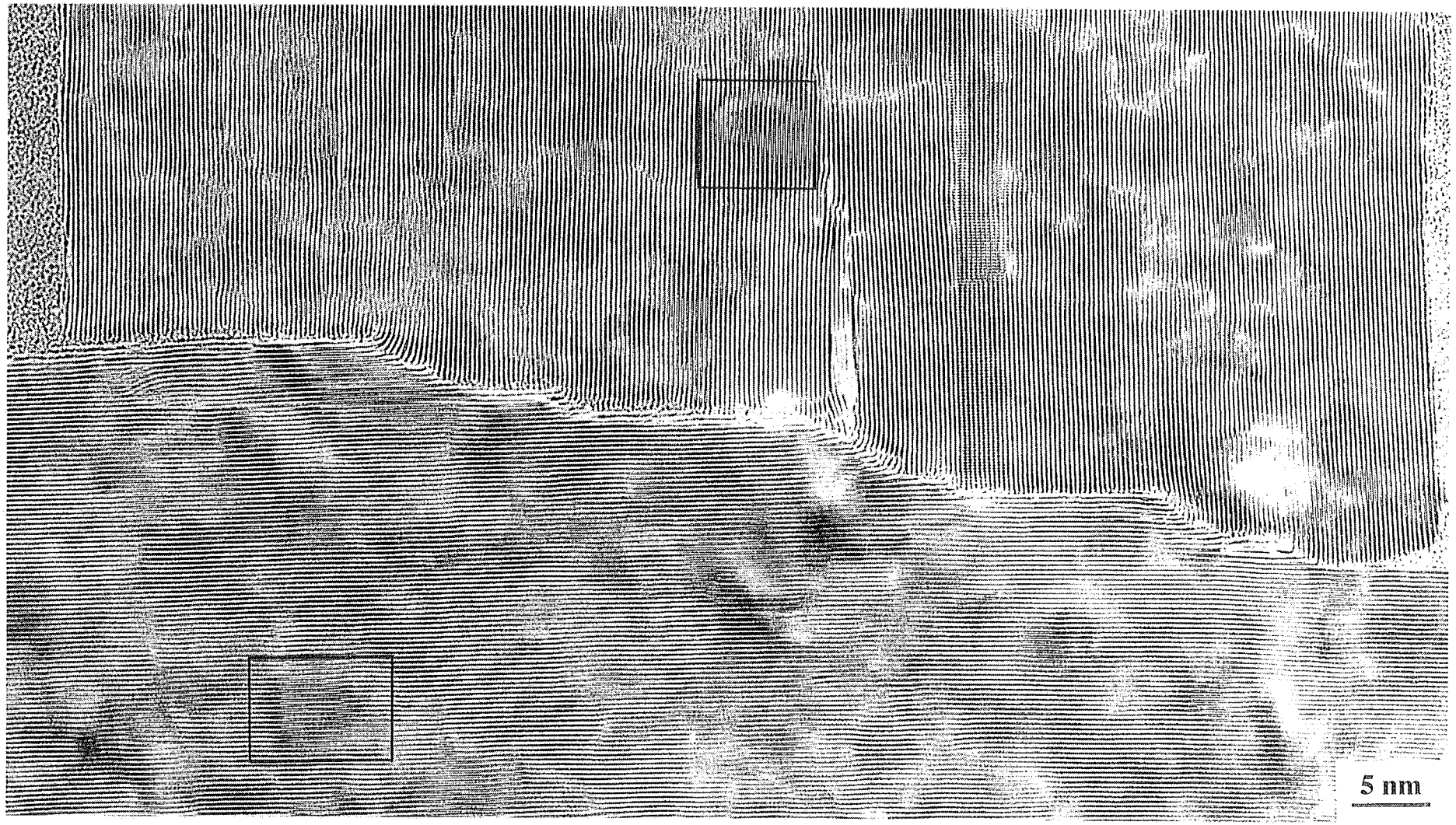

Fig. 6.31 A grain boundary between two h-BN grains is illustrating that the *c*-axes of the inclusions are almost perpendicular to each other and the beam directions in both grains are close to $[11\bar{2}0]$.

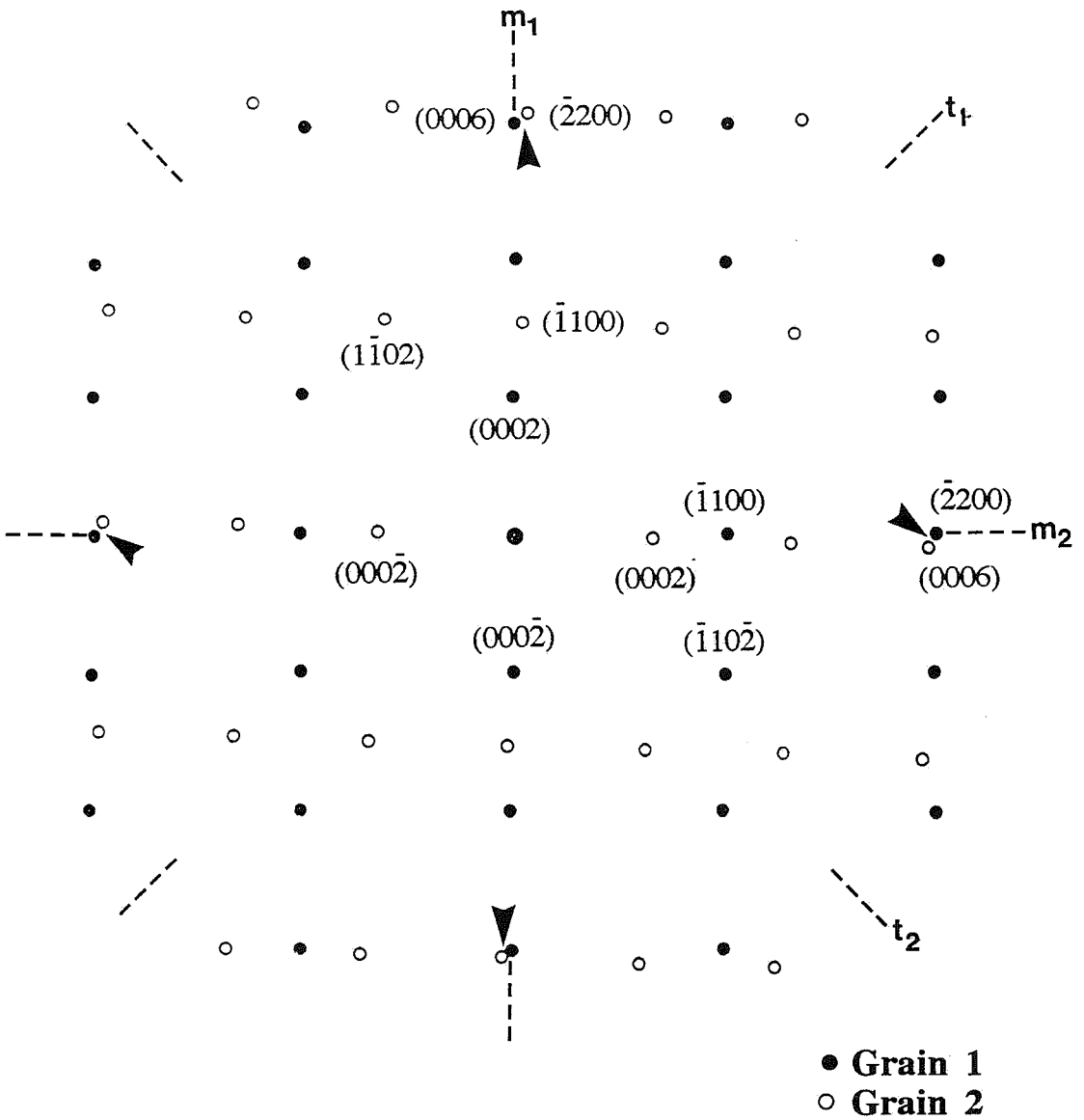

Fig. 6.32 Schematic of indexed superimposed diffraction pattern obtained from two almost vertically aligned h-BN inclusions (shown in Fig. 6.31) when the beam direction was approximately parallel to [11$\bar{2}$0] in both grains illustrating that there is a slight angle between them, so that the (0006) spot from grain 1 nearly overlaps with the ($\bar{2}$200) spot from grain 2.

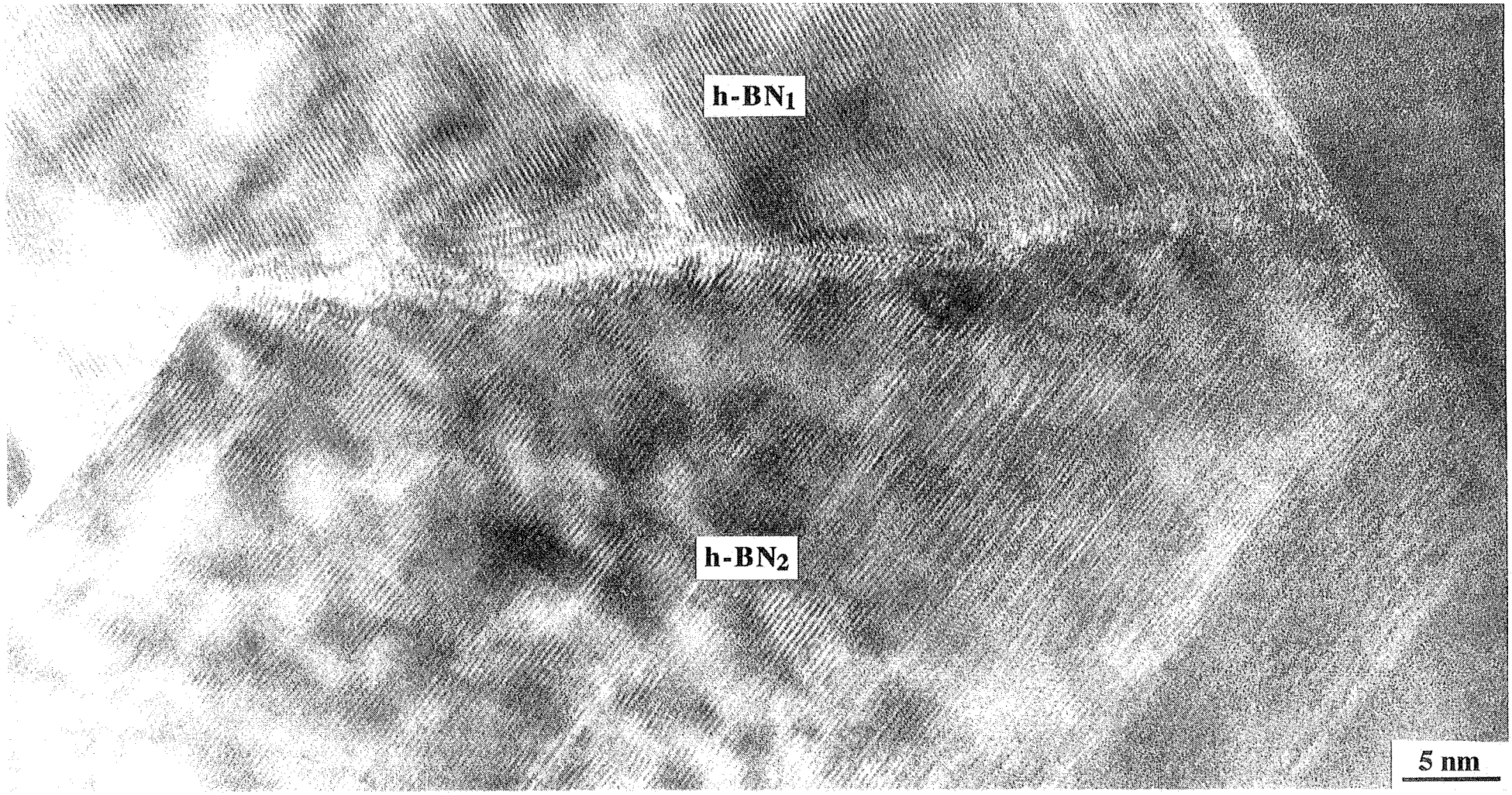

Fig. 6.33 High resolution image of a grain boundary between h-BN inclusions surrounded with a 3C SiC grain. For the diffraction information from the grain boundary, refer to Fig. 6.22.

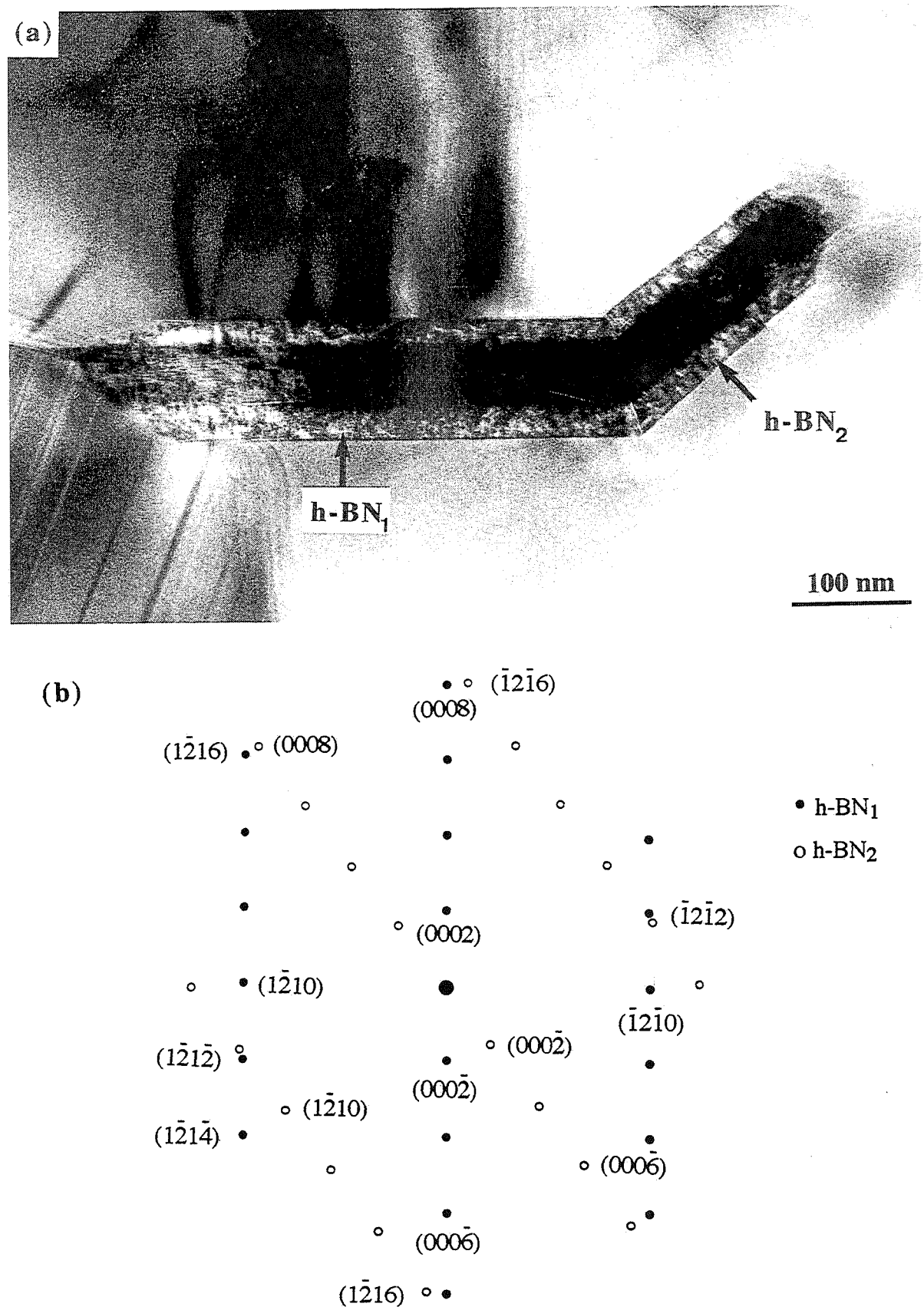

Fig. 6.34 (a) A bright field image of twinned h-BN grains. (b) The schematic diffraction pattern showing that both the grains are oriented parallel to a common [10$\bar{1}$0] direction.

In Figs. 6.24 and 6.34, it can be seen that some regions of h-BN inclusions diffract very strongly (and appear dark in the bright field micrographs) whereas other regions are not as strong. These less strong regions were sometimes in the middle of the inclusions (Fig. 6.24), but sometimes next to the interphase boundaries (Fig. 6.34). The interfaces between strongly diffracting regions and less strongly diffracting regions could be identified as low angle twist grain boundaries. Two enlarged HREM images from area in Figs. 6.30 and 6.31 shown in Fig. 6.35 demonstrate this. The interfaces form when there is a local lattice rotation in the inclusions so that one region is close to $[11\bar{2}0]$ zone axis, whereas the adjacent region is slightly twisted away from this zone axis.

These local lattice rotations are believed to arise to reduce the strains with the adjacent SiC or Si_3N_4 grains. As mentioned in Chapter 4, the thermal expansion coefficients of SiC and Si_3N_4 differ significantly from that of h-BN. Therefore, very high thermoelastic strains are expected at these interfaces. Such strains could cause the lattice rotations observed which would be consistent with a torque applied on the (0001) h-BN planes. Kraus-Lanteri *et al.* (1986) observed such an effect at a ZrO_2-Al_2O_3 interphase boundary - the ZrO_2 grain at the interface is parallel to [110] zone axis whereas away from the interface it is tilted 2° away from this zone.

HREM image simulations were carried to find out the degree of rotation required to explain images such as those in Fig. 6.35. The results indicated that a twist boundary of this kind can form inside a h-BN grain as a result of very small lattice rotations, which could be as small as 1° (Fig. 6.36).

In the micrographs shown in Fig. 6.35, it can be seen that there are three different regions. The first type (region 1 in (a) and region 2 in (b)) are oriented parallel to $[11\bar{2}0]$ zone axis, whereas region 3 in both micrographs are close to $[11\bar{2}0]$. Region 1 in (b) and region 2 in (a) are far away from this zone axis.

In summary, the grain boundaries between h-BN grains were free of intergranular films, but they were faceted. In two occasions, the special orientation relationships were destroyed by only a small rotation of one of the grain. The most commonly observed grain boundary type was the low angle twist grain boundary with the interface plane (0001).

6.4 Microstructural characterisation of composites made from deoxidised powder compacts

It was difficult to make reasonably thin samples of these composites because of the high porosity. The small amount of thin areas did not allow large scale observations. However, some interesting results obtained from limited, but rather time-consuming, observations will be presented here.

The general microstructure of the Si_3N_4-SiC composites prepared from deoxidised powder compacts have been discussed in Chapter 3. Although grain growth of α-SiC grains was evident in Fig. 3.11, the average grain size was smaller than that observed in the composites made from as-received starting powders.

The most striking observation was that in comparison with the composites prepared from as-received powders, most interfaces were found to be free of intergranular films. An example of a commonly observed interface type without an intergranular film is shown in Fig. 6.37 (see also Fig. 5.5). The diffraction pattern shown inset of the Fig. 6.37 shows that grain 2 is oriented parallel to the $[11\bar{2}0]$ α-SiC zone axis.

It was generally observed that the angle between (0006) 2.513 Å planes of one α-SiC grain and the (0006) or $(10\bar{1}2)$ 2.509 Å planes of a second α-SiC grain was very small and varied between 2° and 20°. For example, in Fig. 6.37, the angle between (0006) planes of both grains is ≈ 68°, but between the (0006) planes of grain 2 and the $(10\bar{1}2)$ planes of grain 1 the angle is ≈ 2-3°. Here, the grain boundary contains some small steps, but more obvious steps were observed at other low angle grain boundaries. In the case shown in Fig. 5.5, the angle between (0006) planes of grain 1 and $(10\bar{1}2)$ of grain 2 is ≈ 20°.

In all these cases, the grain boundaries were free of intergranular films. This is presumably due to the elimination of surface silica by the incorporation of carbon as a deoxidant prior to hot isostatic pressing. Other, HREM observations on pressureless sintered SiC laminates separated with graphite interlayers* has also shown that there are no amorphous films at the grain boundaries between α-SiC grains (S. Turan, unpublished work) due to the deoxidation effect of carbon.

---

* *Supplied by Dr W. J. Clegg at the University of Cambridge.*

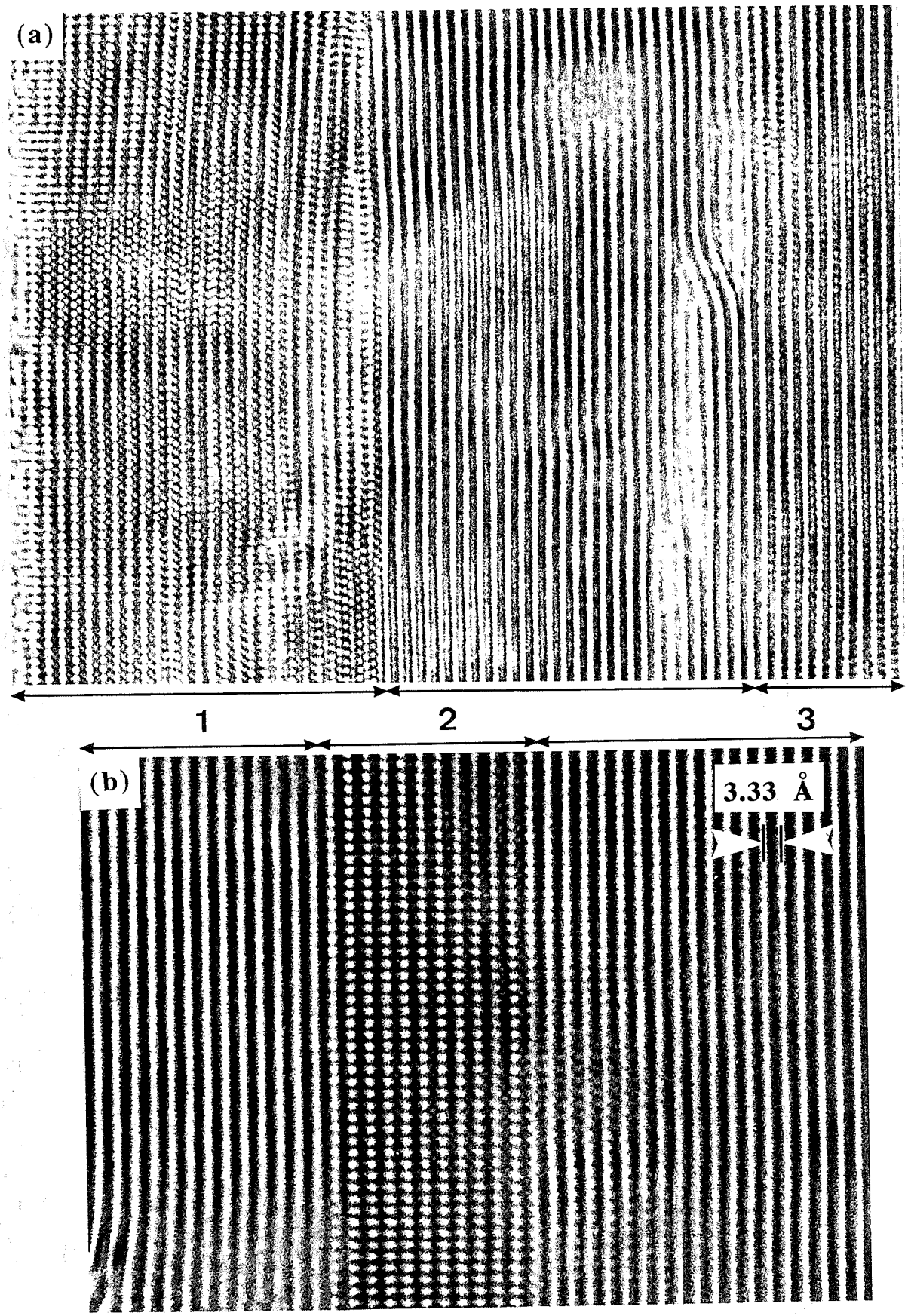

Fig. 6.35 The enlarged HREM images of twist boundaries in h-BN grains; (a) is from Fig. 6.30 and (b) is from Fig. 6.31.

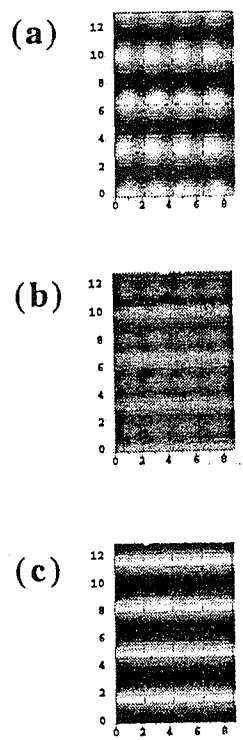

Fig. 6.36 HREM image simulations (a) for [11$\bar{2}$0] h-BN direction (b) for a beam tilt of 10 mrad and (c) for 20 mrad away from this zone axis. The specimen thickness and the defocus values used for the image simulations are 25 nm and 40 nm, respectively.

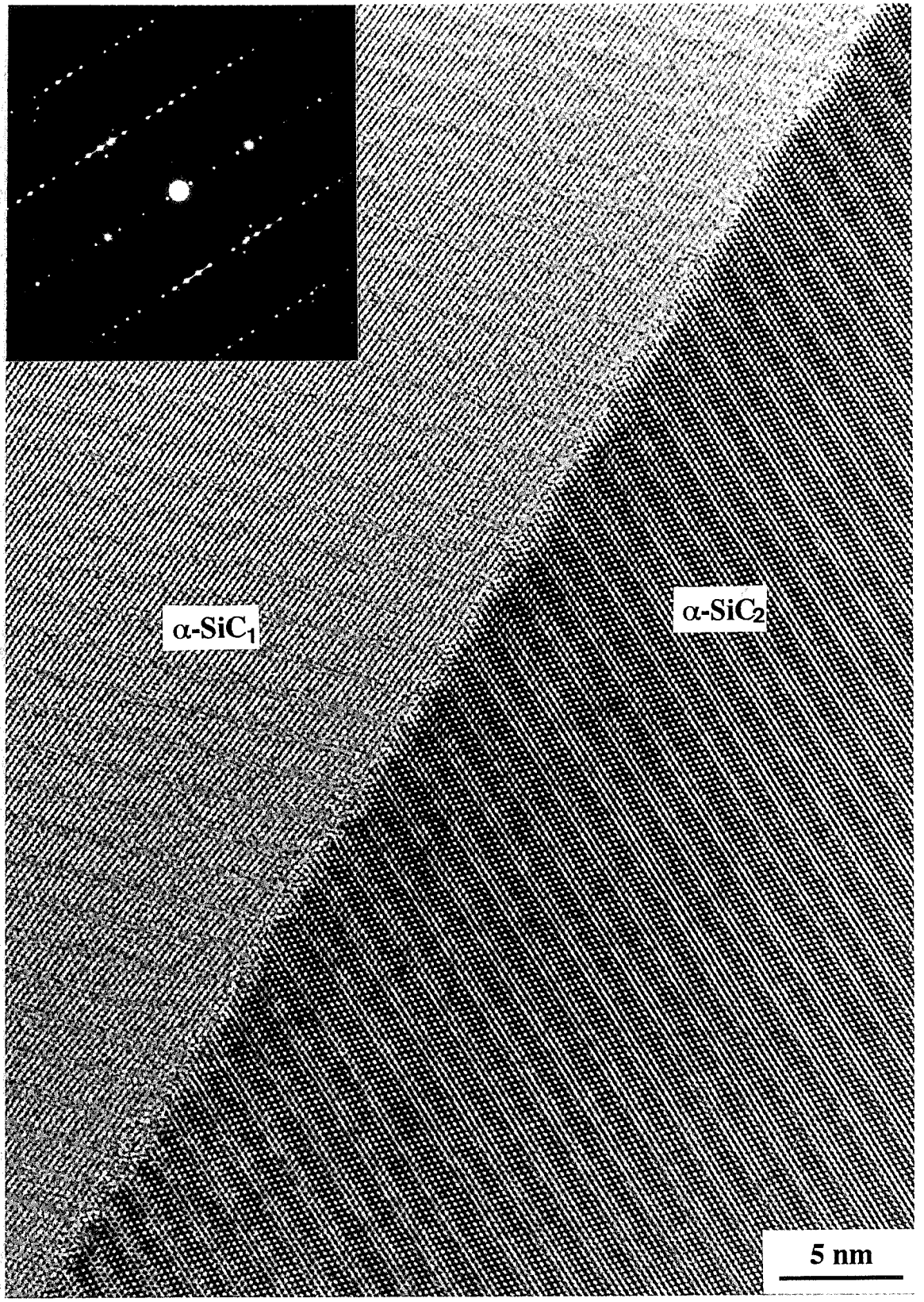

Fig. 6.37. HREM image of an intergranular-film-free grain boundary between two α-SiC grains in the 10 wt % Si_3N_4 reinforced SiC composite made from deoxidised green compacts.

However, intergranular films were occasionally observed between SiC grains such as in Fig. 6.38. In this case, the thickness of the film was ≈ 7.5 Å, less than the thickness of intergranular films seen in the composites made from the as-received powders without any deoxidation step. The top grain was oriented parallel to a [11$\bar{2}$1] type zone axis whereas the bottom grain was parallel to [11$\bar{2}$0] α-SiC or [110] 3C SiC (see inset of Fig. 6.38). Here, the angle between the $(0001)_{\alpha\text{-SiC}}$ lattice fringes is 82°.

The triple junction attached to this intergranular film and the other triple junctions observed throughout this study showed that their sizes were much smaller than the triple junctions observed in the composites made from the as-received powders. A similar observation was reported by Greil and Weiss (1982) who found that the size of the triple junctions were smaller when the liquid content of the material was lower.

Interestingly, although all the interfaces observed so far were between two α-SiC grains which were free of intergranular films, a small layer of 3C SiC was found next to the intergranular film in Fig. 6.38. This suggests that the liquid phase existing at the fabrication temperatures could have an effect on the stability of different polytypes of SiC. This will be the subject of Chapter 7.

The small amount of amorphous phase distributed at the grain boundaries and triple junctions could arise either as the remnants of surface silica after deoxidation or from the decomposition of the small amount of Si_2N_2O which can form unintentionally during the deoxidation process.

Graphite-like inclusions were also observed in the deoxidised composites, just as in the composites prepared from as-received powders (Fig. 6.39). The fact that the deoxidation was carried out in the presence of carbon would suggest these inclusions could be the remnants of carbon crystallised as graphite. However, this possibility is eliminated by PEELS analysis that the inclusions are indeed h-BN. A PEELS spectrum of B *K*-edge is shown in the inset of Fig. 6.39.

In comparison to the observations reported for the composites made from as-received powders, the inclusions were nearly dislocation-free and crack-free and the (0002) BN planes were straight. This is consistent with the idea that the porosity in the composites made from deoxidised green compacts has helped to relieve any thermal strains in the h-BN lattice and prevented the formation of dislocations and lattice rotations.

The other reason for the observation of defect free BN layers could be due to the absence of oxygen. Although this effect is unknown for BN, it is established for graphite that the ability for graphitization to occur increases with decreasing oxygen content (Rouzaud and Oberlin, 1989).

The inclusion was, perhaps not surprisingly, between two α-SiC grains. A thin slab of 3C SiC existed at one side of the inclusion. One of the α-SiC grains is parallel to [11$\bar{2}$0], but the h-BN is not parallel to any low index zone axis. The (0001) h-BN planes were parallel to (0001) α-SiC and (111) β-SiC planes, as was also observed in the composites made from as-received powders. By contrast, here the interphase boundary did not contain an intergranular film but had large steps associated with it.

As mentioned earlier, the inclusions were dislocation-free and the h-BN lattice planes were almost flat, but dislocations were observed where the large part of the inclusion is connected to the narrow region. Here, mostly three (0002) lattice planes connected to two fringes from the narrow region of the inclusion. On one occasion four fringes firstly joined to three for a short distance and then these three fringes become two in the narrow region.

The other interesting observation was that h-BN inclusions were not observed inside SiC or Si_3N_4 grains and that they were only at interfaces. As mentioned in Chapter 3, no Si_3N_4 precipitates in SiC grains were found either. This again supports the hypothesis that both the inclusions and Si_3N_4 precipitates found inside large matrix grains in the composites prepared from as-received powders are there as a consequence of β-SiC grain growth.

6.5 The composition of intergranular films

As has been discussed so far, intergranular amorphous phases have been observed as thin films at interfaces, but the major fraction of intergranular phase is found at the triple junctions. A compositional analysis was only carried out in the composites made from as-received powders since the amorphous phases were largely absent in the composites made from deoxidised green compacts.

The need to establish the composition of the intergranular films in all cases where they are seen has already been noted in Chapter 5. Any change in the chemical composition of an intergranular film will alter its refractive index in the visible and hence its value of the

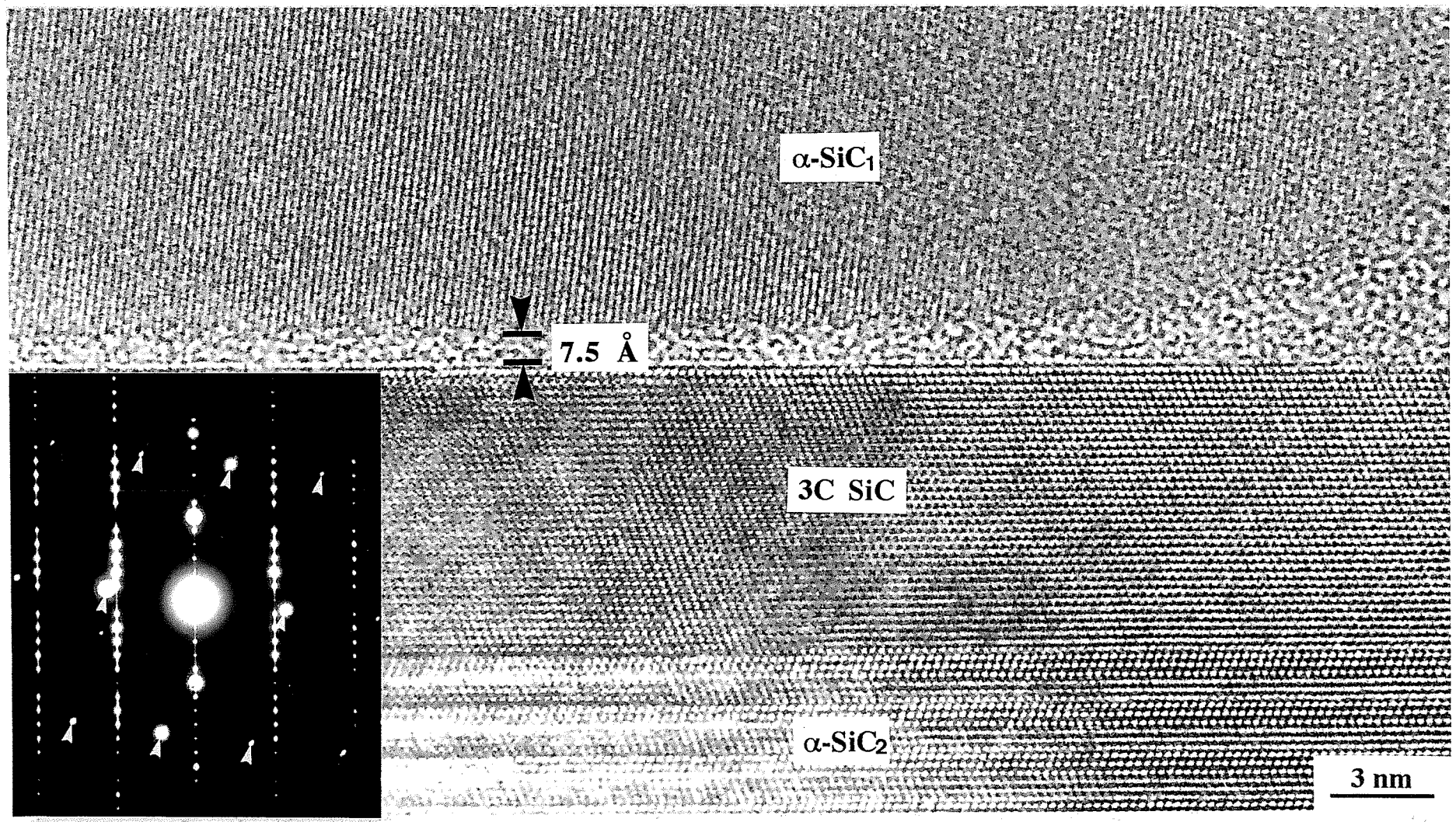

Fig. 6.38 High resolution image of a ≈ 7.5 Å thick amorphous intergranular film between a α-SiC and a 3C SiC grain. Note that apart from the thin band of 3C SiC in the middle of the image, the rest of the lower grain is α-SiC. The arrowed spots are from grain α-SiC_1.

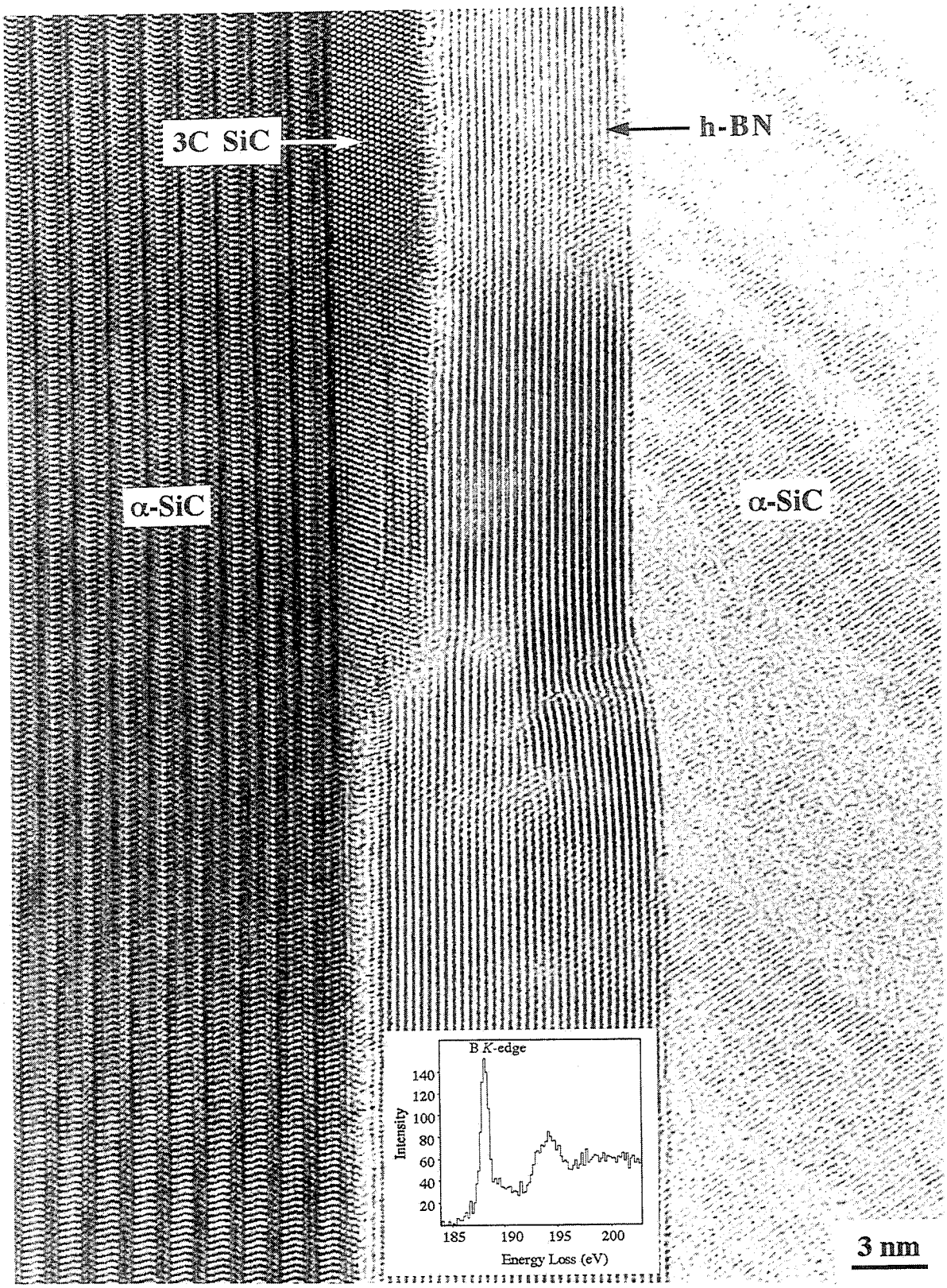

Fig. 6.39 A high resolution transmission electron microscope image at Scherzer defocus of a h-BN inclusion in the composites made from deoxidised compacts. The inset shows the B *K*-edge obtained from the inclusion.

Hamaker constant (Israelachvili, 1992). However, in general it is not possible to establish the chemistry of intergranular films accurately in the TEM because of a finite probe size, and thus a contribution to the overall chemical analysis from adjacent grains. A reasonable first approximation is that the composition at triple junctions derived from either PEELS or WEDX analysis is the same as at the interfaces nearby, although see the discussion about Fig. 6.19.

In this work, PEELS analysis on large triple junction phases showed they were clearly rich in amorphous silica (SiO_2), such as in the example shown in Fig. 6.40(a). The absence of carbon (C), calcium (Ca) and nitrogen (N) edges is very clear in the spectrum (Fig. 6.40(b)).

PEELS and WEDX analysis on a VG HB501 scanning transmission electron microscope (STEM) were also carried out at the interfaces and triple junctions shown in Fig. 6.1 and a second triple junction connected to the first one with an interphase boundary between upper 3C SiC grain and a Si_3N_4 grain. These results showed that the composition of the triple junction phases are again close to SiO_2 within the detection limit of the techniques. Elemental mapping was not very useful to show the existence of any remnants of either elemental silicon, carbon or nitrogen at the interfaces, due to the adjacent grains.

Other examples (Fig. 6.41) were found where there was evidence of a high level of C along with silicon (Si) *K*-edge of SiO_2 in the triple junction regions, but it is not clear whether the C *K*-edge arises from contamination, from an overlapping SiC grain or from a genuine amorphous carbon which is dissolved in silica during liquid phase sintering process. The C peak of SiC can be easily distinguished from an amorphous C peak (Kumar, 1994), but an amorphous C peak can still arise from two different sources. Therefore, it is very difficult to state the reason for the existence of C at the triple junctions and at interfaces although it is easy to state that carbon does not exist if the C signal is not obtained (*e.g.*, Fig. 6.40).

A calcium $L_{2,3}$-edge at 348 eV is also evident. Calcium is generally introduced to the system from starting powders.

PEELS analysis on the triple junction next to the h-BN inclusion shown in Fig. 6.41(a) revealed that the triple junction phase did not contain any boron or nitrogen, despite expectations, since the proposed mechanism of formation of h-BN inclusions (see Section 4.8) involves a reaction between liquid (or gaseous) boron oxide and nitrogen so that any left

over boron oxide would have been retained at the triple junctions nearby h-BN inclusions. However, it should not be forgotten that the boron oxide supply is limited and that therefore all the boron oxide could have been consumed before the cooling process was initiated. The other reason, of course could be that the boron concentration is below the detection limit of the PEELS analyser.

In the spectrum, the peak arrowed as 2 is special to the SiO_2 Si $L_{2,3}$-edge and does not occur if it is the SiC or elemental silicon Si $L_{2,3}$-edge (Carpenter, 1988). Stripped Si L-edges obtained from SiO_2 as a standard and from triple junctions shown in Fig. 6.40 (labelled as TJ1) and 6.41 (as TJ2) are shown in Fig. 6.42(a)[#]. Note the very good match between standard SiO_2 and TJ1 peaks at 108, 116 and 158 eV which agrees well with the results of Ponthieu *et al.* (1994). The peak at 116 eV arises from SiO_2, but in the case of TJ2 the first peak appears at a slightly lower energy (107 eV) and it is broadened. This might arise from an overlapping SiC grain and/or dissolved SiC in silica causing a peak broadening effect since the resolution of this particular PEELS analyser does not allow peaks at 106 eV and 108 eV to be resolved. In addition, a stripped Si L-edges is shown in Fig. 6.42(b) obtained from a small triple junction the micrograph of which is not shown here. Calibration of the spectrum in respect to Fig. 6.42(a) assuming that the triple junction contains amorphous SiO_2 showed that there is an additional peak at $\approx$ 100 eV which could be due to elemental Si in the triple junction. These results are also in good agreement to the results obtained by Skiff *et al.* (1985) & (1987) that the magnitude of the threshold onset peak increases continuously from Si to SiO_2 and that its onset energy increases from Si to SiO_2. This is because the energy difference between the final occupied orbital and first unoccupied orbital increases for the compounds of Si compared with elemental Si. The core energy levels in the compounds of Si also shift to lower energies compared with Si.

In all cases, it was necessary to orient the triple junctions accurately with respect to the electron beam to confirm their amorphous nature. As a result, some of the triple junctions which at first seemed to be amorphous, because of their weak diffraction contrast, were found instead to contain small crystallites within the amorphous phase. Furthermore, some of the triple junctions were completely crystalline, as in the example shown in (Turan and Knowles, 1995), where the crystalline phase was boron nitride.

[#] *It is worth noting that the peaks should be only compared if they are obtained at very similar spectrometer resolutions because the intensity of the peaks changes if the spectrometer resolutions are different although the peaks will appear at the same energy values (Kumar, 1994).*

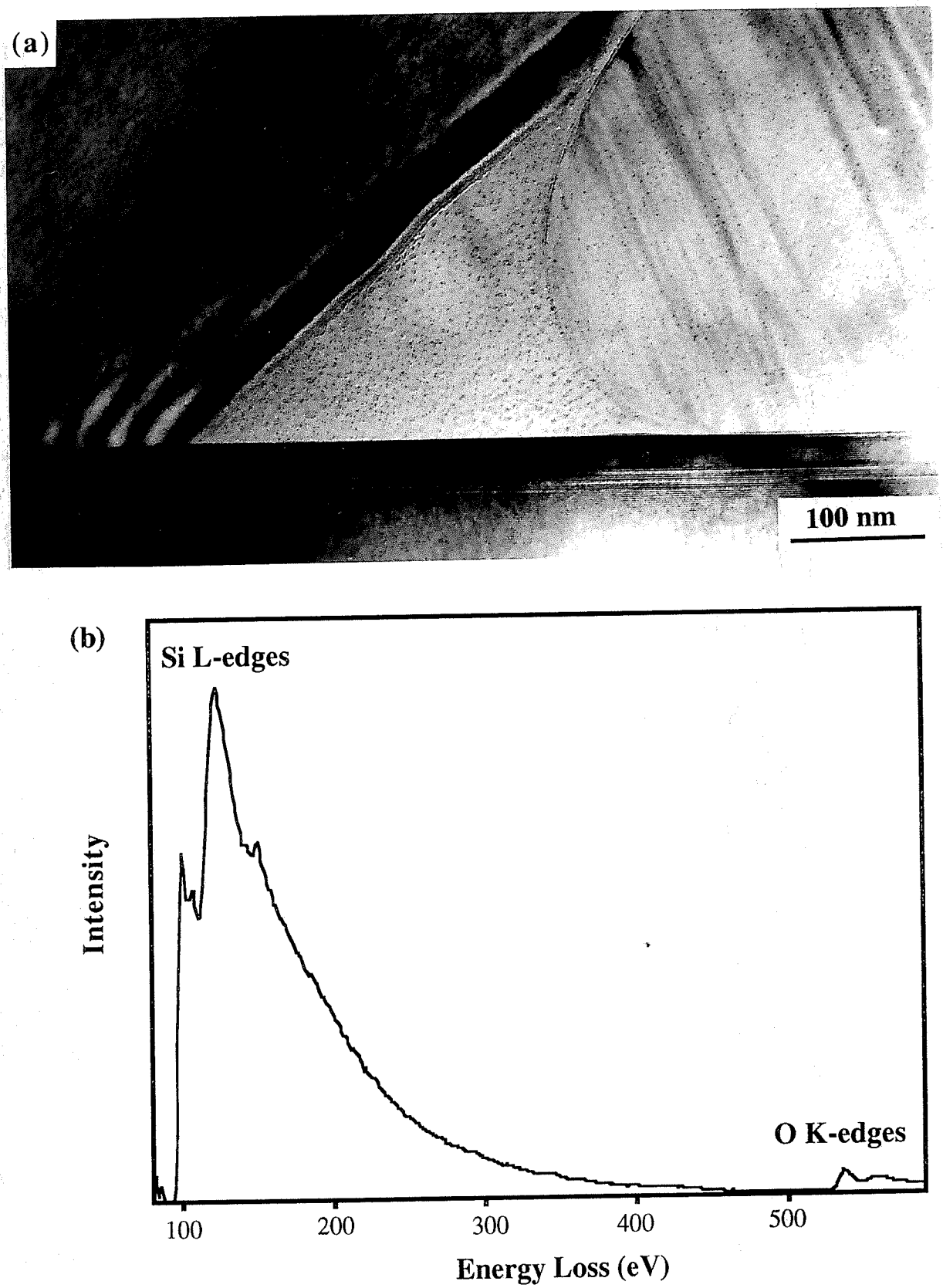

Fig. 6.40. (a) An example of a large triple junction phase between three SiC grains; (b) stripped silicon *L*-edges and unstripped oxygen *K*-edges of the triple junction phase showing that it is rich in amorphous silica.

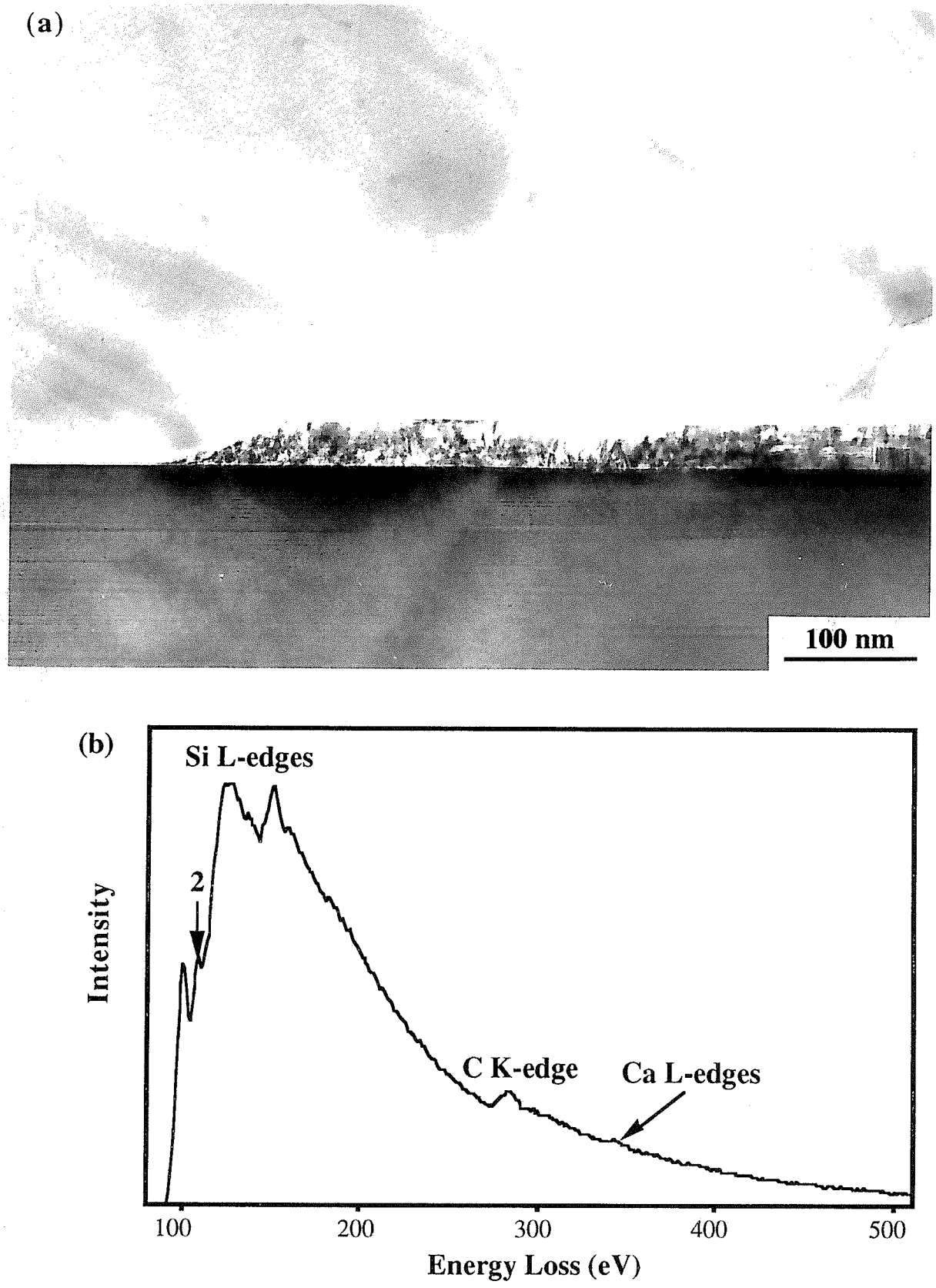

Fig. 6.41 An amorphous triple junction phase between three SiC grains and a h-BN inclusion next to the amorphous phase; (b) a PEELS spectra obtained from the amorphous phase is showing that it is rich in silica.

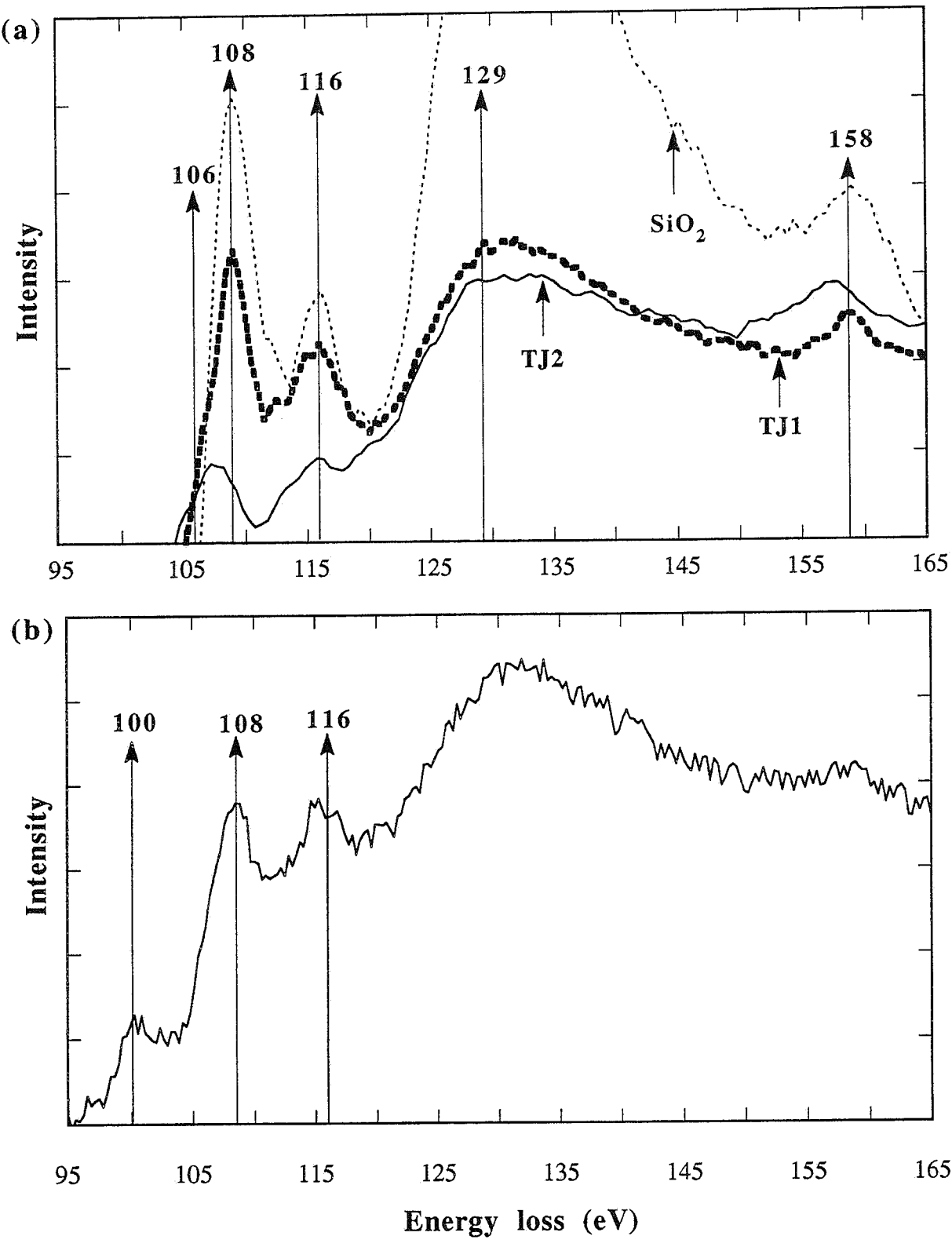

Fig. 6.42 (a) Comparison of Si *L*-edges obtained from a standard SiO_2, TJ1 and TJ2. (b) From a very small triple junction a micrograph of which is not shown here. This has an additional peak at ≈ 100 eV.

6.6 Discussion and conclusions

For the measurement of film thickness the HREM technique is the most reliable and accurate, whereas the diffuse dark field technique is the least reliable and was not used for the film thickness measurements. The use of underfocus Fresnel images extrapolated to Gaussian focus gives values close enough to the HREM results to enable them to be reliably used in the absence of very expensive HREM microscopes. Therefore, overfocus images can be ignored during experimentation. This could save time as well as money on negatives, unless the Fresnel data is also going to be used in conjunction with a PEELS analysis.

The drawbacks of the Fresnel technique to show the existence of an intergranular film have been highlighted by the example of a faceted interface showing typical Fresnel fringe contrast indicative of a film at the interface (Fig. 6.5).

Using these three techniques very carefully, it was found that most grain boundaries and interphase boundaries in the composites prepared from as-received powders were wetted with intergranular films. By contrast, most interfaces in the deoxidised material were free of such films. Occasionally, intergranular films were observed at interfaces in the composites made from the deoxidised powder compacts, but the thickness of the films were much lower than those in the composites prepared from as-received powders. This suggests that the volume of liquid phases present in the material during consolidation at high temperature has a noticeable effect on the relative magnitude of the equilibrium film thickness, in contrast to conclusions from previous observations (Weiss and Greil, 1982).

Qualitatively, the results obtained throughout this study from β-Si_3N_4 grain boundaries are in good agreement with published experimental results (Schmid and Rühle, 1984, Kleebe *et al.*, 1992 & 1993) and Clarke's predictions (Clarke, 1985, 1987 & Clarke *et al.*, 1993) that non-specific high angle grain boundaries in structural ceramics should contain intergranular films (*e.g.*, Fig. 6.8 and 6.9), while special grain boundaries (low angle, twin and some twist boundaries) should not contain any intergranular films (*e.g.*, Fig. 6.10), because their energies are lower than those of wetted grain boundaries as discussed in Chapter 5.

The intensive studies on the characterisation of grain boundaries in Si_3N_4-based materials in the literature has shown that high angle grain boundaries are covered with intergranular films of various thicknesses, whereas low angle boundaries are free of such intergranular films.

However, it is not stated whether the high angle grain boundaries have special or random orientation relationships. Since the diffraction patterns were not presented either, the crystallography of these interfaces cannot be deduced. The exception to this is that of Schmid and Rühle (1984) who documented that, besides low angle and twin boundaries, special (0001) twist grain boundaries ($\Sigma = 7$ ($\theta \approx 38.5°$) and $\Sigma = 13$ ($\theta \approx 27.5°$)) are stable without an intergranular film and that interfaces with low Σ misorientation possess relatively low energies and are formed favourably during the sintering of SiAlON ceramics.

According to Clarke's calculations (Clarke, 1987), intergranular SiO_2 films are not to be expected at SiC-SiC grain boundaries at equilibrium. This is believed to be a consequence of the relatively high refractive index of SiC (Clarke, 1987). To date, no such intergranular films have been reported in the literature for pressureless sintered SiC compacts with B and C additives, in agreement with this theoretical prediction. However, in this study clear thin intergranular films at SiC-SiC interfaces have been observed, such as in Fig. 6.1. In support of this, the recent experimental observations by Sigl and Kleebe (1993) have also provided evidence through HREM of thin 10 Å intergranular films at 6H SiC-6H SiC grain boundaries in pressureless sintered α-SiC powder mixed with yttrium aluminium garnet ($Y_3Al_5O_{12}$) to promote densification.

It is found that intergranular films at SiC - SiC interfaces are mostly absent in the composites made from deoxidised compacts, as discussed in Section 6.5, and are also absent in pressureless sintered SiC laminates separated with graphite interlayers. It is therefore clear from this discussion that intergranular films at SiC-SiC interfaces can only be detected if there are liquid making elements present during the consolidation process at a level sufficient to wet all interfaces that are able to accommodate such films and to leave behind an amorphous intergranular film on cooling. This qualitative explanation also accounts for the lack of intergranular films seen to date in pressureless-sintered SiC compacts if densification in such compacts takes place exclusively in the solid state, in line with theoretical expectations (Prochazka, 1975).

The twin boundaries and coherent interphase boundaries between 3C SiC and α-SiC grains (Fig. 5.1) were free of intergranular films, indicating that these interfaces have lower energies if they are not wetted. Some of the SiC-SiC interfaces were faceted when the (111) planes made an angle smaller than 20° with the interface and the facets were filled with an amorphous phase.

The film thickness at Si_3N_4-SiC interphase boundaries were higher than both the grain boundaries between SiC-SiC and Si_3N_4-Si_3N_4 supporting the hypothesis raised by Clarke (1987). However, most interestingly, the film thicknesses of two particular interphase boundaries formed between two different Si_3N_4 grain and a same SiC grain attached to the same triple junction were substantially different where most of the factors effecting the equilibrium film thickness are the same and a difference in the film thickness would not be expected. The only difference that could cause this observation is that the differently oriented Si_3N_4 grains may have different speed of re-precipitation which result in different film composition by accepting that differences in the misorientation should not effect the film thickness if the material is reasonably isotropic.

Most of these interphase boundaries were found to contain intergranular films. No special orientation relationship at these interphase boundaries was observed, in contrast to interphase boundaries between 3C SiC grains and Si_3N_4 precipitates which were dependent on the type of interface. It is found that when the interfaces are curved between Si_3N_4 precipitates and SiC grains, the interface was free of an intergranular film, but that when the interfaces were flat they were mostly associated with thin films. The most common feature was that (200) SiC spots overlapped with $(10\bar{1}0)$ Si_3N_4 spots and that the orientation relationship was close to:

$$[110]_{3C\ SiC} \parallel [0001]_{\beta\text{-}Si_3N_4} \text{ and } (002)_{3C\ SiC} \parallel (10\bar{1}0)_{\beta\text{-}Si_3N_4}$$

The precipitates were thought to form through a solution-reprecipitation process after the liquid is supersaturated with Si_3N_4 and then these small particles are retained inside 3C SiC grains during the grain growth at the final stage of densification.

Interphase boundaries have special orientation relationships between the h-BN and the SiC grains, but even so, most interfaces were covered with thin films when the (0001) h-BN and (111) 3C SiC planes were parallel. The most common orientation relationship was found to be:

$$[\bar{1}10]_{3C\ SiC} \parallel [11\bar{2}0]_{h\text{-}BN} \text{ and } (111)_{3C\ SiC} \parallel (0001)_{h\text{-}BN}$$

$$[11\bar{2}0]_{\alpha\text{-}SiC} \parallel [11\bar{2}0]_{h\text{-}BN} \text{ and } (0001)_{\alpha\text{-}SiC} \parallel (0001)_{h\text{-}BN}$$

When these two planes are not parallel to each other, the interface was faceted with amorphous phases filling the facets and the orientation relationship in this case was:

$$[\bar{1}10]_{3C\ SiC} \parallel [11\bar{2}0]_{h\text{-}BN} \text{ and } (111)_{3C\ SiC} \parallel (1\bar{1}02)_{h\text{-}BN}$$

Interphase boundaries between h-BN and Si_3N_4 grains were mostly free of intergranular films. This is consistent with the relatively low mismatch of corresponding planes between BN and Si_3N_4 when the (0001) h-BN and $(10\bar{1}0)$ Si_3N_4 planes were parallel.

To the best of my knowledge there are not any orientation relationship or detailed HREM observations on the interphase boundaries formed between h-BN and SiC or Si_3N_4 grains in the literature to compare with the results obtained throughout this study.

This is also the case for grain boundaries (with the exception of twin boundaries) between h-BN inclusions that have been characterised in this study. It was found that there are no films at the interfaces which were faceted. The most frequently observed grain boundary type between h-BN inclusions were so called low angle twist boundaries which formed as a result of the strains caused by the large thermal expansion mismatch between h-BN and SiC or Si_3N_4 grains. The twin boundaries have been identified in the literature firstly by Kurdymov *et al.* (1976) who found that the twin plane is $(1\bar{2}12)$ and then Hiraga *et al.* (1989) observed multiply-twinned h-BN precipitates inside turbostratic BN matrix with five (112) twin planes when the fivefold axis was parallel to [201] zone axis. In this study an interface was found to be very closely related to the twin relations found by Kurdymov *et al.* (1976), but there was a small, but significant, deviation from this orientation relationship.

The microanalysis on triple junctions in the composites prepared from as-received composites showed that the amorphous phases are rich in silica and they also contain some amount of carbon which could be the remnant of carbon dissolved during liquid phase sintering process or simply arising from a contamination or it is an overlapping SiC carbon peak. In other cases, elemental Si and Ca was also detected separately.

Chapter 7

$\alpha \rightarrow \beta$ Reverse Transformations of SiC

7.1 Introduction

SiC is a material currently being considered as a replacement for high temperature metal alloys in applications such as heat engines, turbochargers and jet nozzles possibly as SiC fibre SiC matrix composite. It is also a very important material in the semiconductor area. SiC is a wide band gap (2.3-3.3 eV (Jepps and Page, 1983)) semiconductor and since it does not fail mechanically at high temperatures, electronic devices made from SiC can be used at much higher temperatures than other wide band gap ($E_g > 2.3$ eV (Hench and West, 1990)) semiconductor competitors. For example, gallium arsenide cannot be used at temperatures above 150°C because of its loss of strength above this temperature (Pirouz and Yang, 1993). One factor limiting the application of SiC in this area is that SiC exhibits one dimensional disorder and many polytypes coexist. All the polytypes have different band gaps (the band gap of 3C SiC is 2.39 eV whereas it is 3.02 eV for 6H SiC (Schneer, 1955, Jepps and Page, 1983 & Hench and West, 1990)). Therefore, it is very important to know the mechanisms and factors affecting the phase transformations. Polytypism in general has been briefly discussed in Chapter 3 and will not form a part of this Chapter. Instead, the transformations and polytype stability will be introduced followed by experimental results and discussions.

7.2 Background to polytype stability and SiC phase transformations

7.2.1 Polytype stability

The stability of certain polytypes in SiC powder depends largely on the production route. In general, β-SiC appears to form preferentially when SiC made via the reaction of molten Si with carbon or by pyrolysis of certain silanes (Knieppenberg, 1963). The carbothermic reduction of silica at high temperatures in excess of 2600°C (which is known as Acheson

process (Acheson, 1882)) leads to the generation of α-SiC crystals (Srinivasan, 1989). If the Acheson process is carried out at somewhat lower temperatures (1500-1600°C), the resulting material is in the form of cubic β-SiC (Wei, 1983). Knieppenberg (1963) and Inomata *et al.* (1968) produced stability diagrams for the occurrence of SiC polytypes as a function of temperature (Fig. 7.1).

Impurities have an important influence on polytype stability particularly impurities from groups 3 and 5 in the periodic table (*i.e.*, p and n-type in SiC). The p-type impurities (Al and B) stabilise the hexagonal polytypes whereas n-type impurities (P and N) tend to stabilise the cubic polytype (Knieppenberg, 1963). For example, Jepps (1979) annealed REFEL β-SiC under nitrogen atmosphere at different pressures (1 to 3 MPa) and at different temperatures (1800 to 2250°C) and found that nitrogen inhibits the β → α transformation and stabilises β-SiC, whereas under same temperatures and pressures, but in argon atmosphere, the β → α transformation had occurred.

In addition, B favours the 6H polytype preferentially in the sintered product (Bocker *et al.*, 1979) while addition of aluminium enhances the occurrence of the 4H polytype. The effect of impurities on the occurrence of SiC polytypes are shown in Fig. 7.2.

In order to address the effect of impurities on the β → α transformation, Heuer *et al.* (1978) annealed two samples cut from a single pressureless sintered material at identical conditions, 1950°C for 2 h in vacuum, one of which was in a BN crucible and the other one in a graphite crucible. They found that the transformed composite grains were 5 to 10 times larger in the BN experiment and concluded that the result is affected by impurities arising from the decomposition of BN.

7.2.2 The β → α SiC transformation

The α-form is more stable at very high temperatures and therefore partial transformation to this form will occur when the β-form is heated to very high temperatures. The β → α transformation has been of interest for some time (Verma and Krishna, 1966), partly because the α-form that develops in a fine-grained polycrystalline β matrix usually occurs as large plates and reduces the strength of SiC material. From packing considerations, the growth of

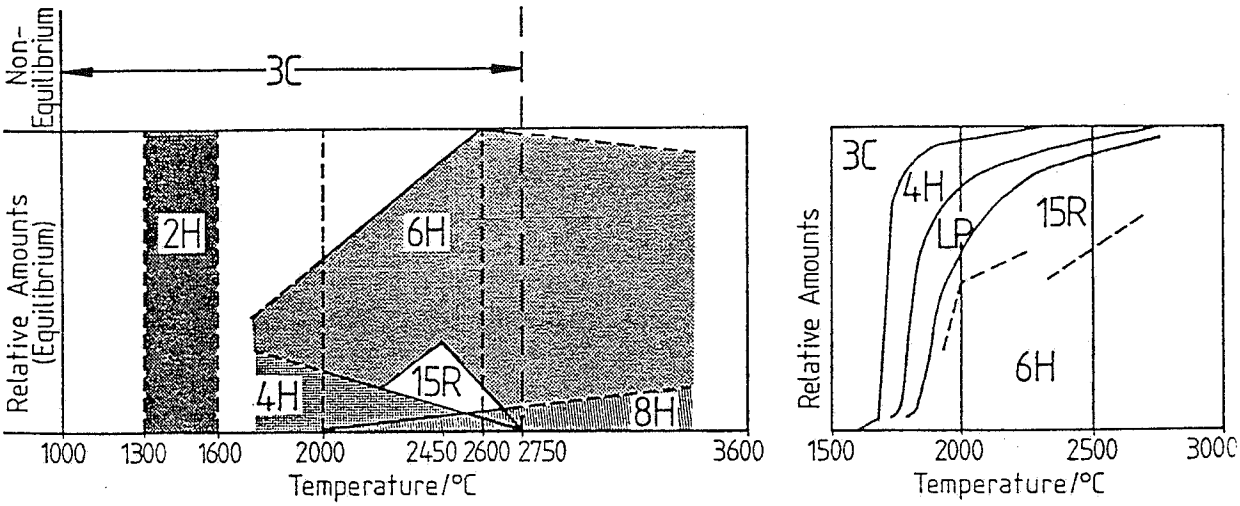

Fig. 7.1 Suggested stability diagrams for silicon carbide polytypes (a) after Knippenberg (1963) and (b) after Inomata *et al.* (1968). LP represents long period polytypes.

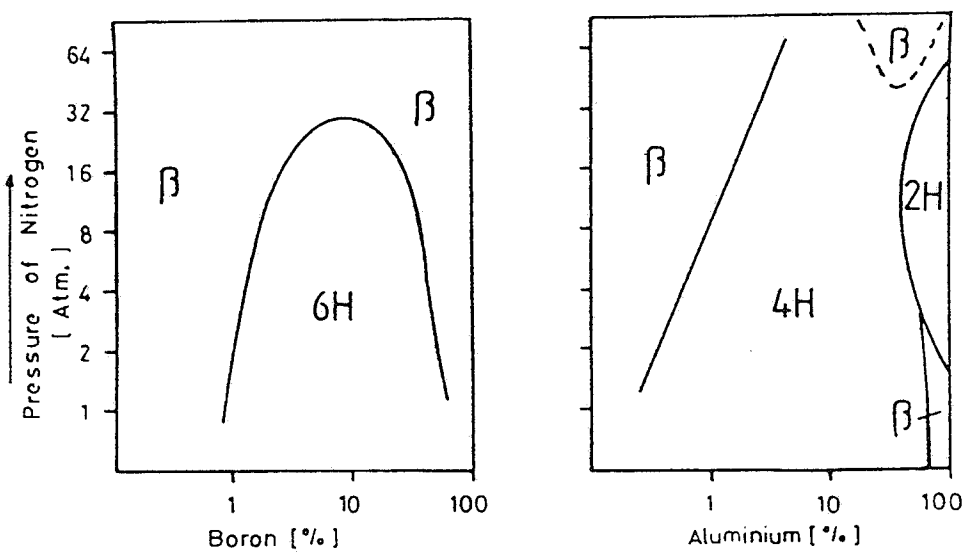

Fig. 7.2 Suggested variations of SiC polytypic structure with impurity content (after Inomata *et al.*, 1969). In both cases the presence of nitrogen alone appears to stabilise the 3C SiC structure though increasing amounts of either aluminium or boron together with nitrogen are seen to stabilise other polytypes which may also reflect the presence of BN and AlN.

large tabular grains also reduces the maximum density that can be reached. Therefore, as pointed out by Jepps and Page (1983) polytype transformations are in general not desirable and the understanding of transformations between the polytypes are important since they may help us to understand the ill-defined conditions under which one polytype becomes unstable with respect to another. Furthermore, the control of microstructural or property changes, occurring as a result of either deliberately-induced or unwanted phase transformations, is important in using SiC for either engineering or electronic applications.

It is now well established (Heuer *et al.*, 1978, Mitchell *et al.*, 1978, Ogbuji *et al.*, 1981 & 1981a) that the β phase transforms to α phase during annealing at temperatures greater than 2000°C by a process of solid-state transformation followed by recrystallization (Shinozaki *et al.*, 1978) with columnar growth of large α-SiC grains. The anisotropic grain growth is governed by a general ledge mechanism of interface advance. Heuer *et al.* (1978) investigated the microstructure of pressureless sintered and hot pressed materials fabricated with the same starting powder (β-SiC) and the same amount of additives (0.5 wt% B and 1% C). Pressureless sintering was carried out at 2050°C in Ar for 1 h while hot pressing was done at 1900°C and 40 MPa pressure. The volume fraction of α-SiC formed by transformation during hot pressing was 10% higher than the pressureless sintered materials.

A key observation was made by Shinozaki and Kinsman (1975) who discovered that α plates resulting from this transformation were "sandwiched" between "envelopes" of β in a well-defined orientation relation with the α phase; $\{111\}_\beta$ // $(0001)_\alpha$. The transformation in ultrafine grain β-SiC involves the initial formation of α-plates preferentially on one of the (111) β-SiC variants and therefore the product α phase is coherent with the parent β phase.

7.2.3 The α → β SiC 'reverse' transformation

Although the β → α-SiC phase transformation occurring by high temperature annealing is frequently observed and well established (Heuer *et al.*, 1978), the reverse α → β transformation is less frequently observed since at the temperature where β-SiC is stable (thought to be 1400-1600°C (Inomata *et al.*, 1969a & Jepps, 1979)) the activation energy for the transformation is too high for it to proceed at any detectable rate. The reverse transformation in SiC powders was first observed at 2500°C under 0.2 MPa of nitrogen pressure (Kieffer *et al.*, 1969). A small amount of α → β transformation in association with

morphological changes from equiaxed to slightly elongated shape was discovered (Kinsman and Shinozaki, 1981) in ultrafine grained α-SiC throughout the temperature range in which large tabular grains of β-SiC develop.

A complete reverse transformation of α to β in reaction bonded SiC was achieved at 2500°C under 3 MPa nitrogen pressure by Jepps and Page (1981) who found that for a given temperature and time, the greater the nitrogen pressure the faster the α → β transformation rate. For a given pressure, the greater the temperature, the higher the transformation rate. As previously mentioned in 7.2.1, the α-phase was stabilised under the same experimental conditions in an inert atmosphere of argon instead of nitrogen. Using dark field TEM, Jepps and Page detected a relatively thick intergranular film between adjacent β-SiC grains and suggested that this was a remnant of a high temperature liquid phase, indicating that the α → β transformation may have proceeded via a liquid phase route.

The earlier experiments also indicated the importance of nitrogen and argon gases. Lilov *et al.* (1976) observed that relative amounts of 3C, 6H and 15R is dictated by the nitrogen partial pressure and concluded that at 2300°C the amount of 3C increased with increasing nitrogen pressure.

The reverse transformation also occurs at extremely high pressures existing under hardness indenters and in wear tracks (Trefilov *et al.*, 1978 & Page *et al.*, 1978) and in controlled high pressure experiments (Sokhor *et al.*, 1968). Sokhor *et al.* (1968) obtained the complete transformation at pressures of (3-7 GPa) and at relatively low temperatures (1200-1400°C). However, under same conditions using purer starting powders than Sokhor *et al.* (1968), Whitney and Shaffer (1969) found no transformation. They only observed the transformation in the presence of BN impurities. Shaffer and Whitney (1971) claimed that a cubic SiC-based solid solution is the major phase in materials formed by reacting silicon, carbon and boron (or BN) under a nitrogen atmosphere at a temperature between 1300 and 2600°C and a pressure between 1 and 700 MPa.

Recently, Yang *et al.* (1992) carried out compression tests on single crystals of 6H SiC grown by the Acheson technique. As a result of the compression, an orientation where there were equal resolved shear stresses on the primary glide plane (0001) and the cross-slip plane $(10\bar{1}0)$, it was found that 6H crystals partially transformed to the 3C phase in

the temperature range 1100-1400°C under moderate shear stresses (≈ 50 MPa). Yang and Pirouz (1993) also carried out high temperature microindentations on a high quality single polytype single crystal 6H SiC grown by the Tairov-Tsvetkov technique and the reverse transformations were conclusively observed in the vicinity of the indentations by TEM.

7.2.4 Transformation Mechanisms

The results obtained to date indicate that more than one transformation mechanism is possible. Solid state transformations suggested from results on single crystal experiments were initially considered to occur by three possible mechanisms (Pandey and Krishna, 1974). Firstly, the periodic slip mechanism envisages that changes in the layer sequence take place by the movement of partial dislocations round a screw dislocation (Powell and Will, 1972). Secondly, in a variation on mechanism first proposed by Jagodzinski (1954), changes in the stacking sequence could occur by randomly introduced stacking faults which eventually order and result in the new structure (a layer displacement mechanism). Thirdly, for powder compacts, a vapour or surface flow mechanism based on observations of changes in crystal morphologies and transformation rates has been proposed by Bootsma *et al.* (1971). This mechanism involves first of all the detachment of atoms from the crystal surface followed by the redeposition as a crystal of different polytype structure onto a nucleus provided either by a disordered region or by solid state transformation. To account for the transformations occurring in polycrystalline compacts, Jepps (1979) suggested a combination of solid-state and fast materials transportation mechanisms.

Recently, Pirouz and Yang (1993) suggested a dislocation model for SiC polytypic transformations. The model is based on the asymmetry in the mobility of partial dislocations $1/6\langle 2\bar{1}\bar{1}\rangle$ and $1/6\langle 1\bar{2}1\rangle$ (which are obtained from the dissociation of a perfect $1/2\langle 1\bar{1}0\rangle$ dislocation) in SiC. The asymmetry in dislocation velocity is attributed to the different core structure of the two partial dislocations since the atoms along one partial are all silicon whereas the atoms along the other partial are all carbon.

7.2.5 Transformation Kinetics

The kinetics of the $\beta \rightarrow \alpha$ transformation was discussed by Jepps (1979). Whitney (1963) & Bootsma *et al.* (1971) calculated the activation energies for $\beta \rightarrow \alpha$ transformations. Within the limits of accuracy their results were nearly the same (661 ± 126 kJmol^{-1} and

573±84 kJ mol^{-1}, respectively). An Arrhenius plot of transformation rate data obtained by X-ray polytype analysis by various researchers is shown in Fig. 7.3.

Both Whitney and Bootsma *et al.* concluded from their data that the transformations were reconstructive ones, proceeding either through a vapour transport mechanism (Whitney, 1963) or by a near surface transport mechanism (Bootsma *et al.*, 1971). This conclusion was reached after a comparison of the activation energies for the transformation with the activation energy for vaporisation which is calculated by Whitney (1963) as 502 $kJmol^{-1}$. Inomata *et al.* (1969) also proposed a similar mechanism of transformation, but they observed that single cubic crystals with no stacking faults (from X-ray) did not transform at 2300°C after a long heating time. They concluded that a nucleus of 6H material was necessary and that this would have to be formed by a solid state mechanism. Jepps (1979) also calculated the activation energy for the $\alpha \rightarrow \beta$ transformation (336 kJ mol^{-1}). It is noticeable in Fig. 7.3 that the activation energy for the $\alpha \rightarrow \beta$ transformation is lower than for the $\beta \rightarrow \alpha$.

7.3 Materials

In addition to the Si_3N_4-SiC composites described in section 3.3, a monolithic SiC* and a 16 wt% TiB_2 particulate reinforced SiC composite@ both supplied by BP Chemicals and a layered SiC composite♠ in which the SiC laminates were separated with a graphite layer were investigated.

The monolithic SiC had been produced at above 2000°C and 0.1 MPa Ar pressure by pressureless sintering of the ultra-pure submicron powder derived from original Acheson process mixed with non-oxide sintering aids. The structure of the starting powder is not known, but the Acheson process generally produces α polytypes. The TiB_2 reinforced composite was produced under similar processing conditions and again the structure of starting powder is unknown, whereas the starting powder was in the form of β-SiC in the layered SiC composite.

---

* *Trade name is HEXOLOY SA.*

@ *Trade name is HEXOLOY ST.*

♠ *See Clegg et al. (1990) for the details of material preparation and properties.*

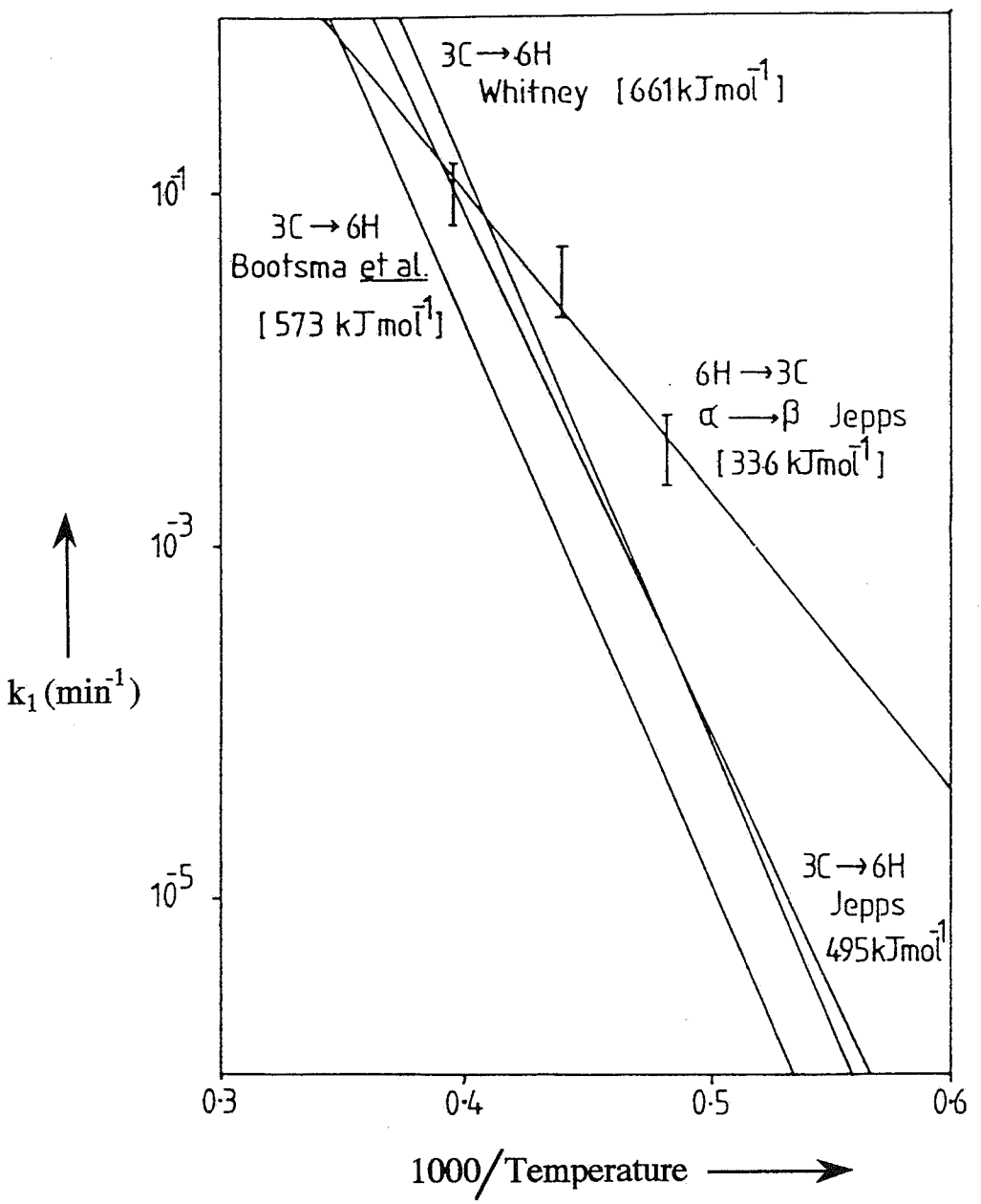

Fig. 7.3 An Arrhenius plot together with the calculated activation energy for the $\alpha \rightarrow \beta$ transformation. Plots for the 3C → 6H transformation are also included. It is apparent that the activation energy for the $\alpha \rightarrow \beta$ transformation is significantly less than that for $\beta \rightarrow \alpha$ (after Jepps and Page, 1983).

7.4 Results

7.4.1 XRD results

In order to follow structural changes during the fabrication process, it is necessary to know the exact structure of the starting powders. Therefore, XRD analysis carried out on UF15 SiC starting powder used for the production of Si_3N_4-SiC composites and its indexed XRD pattern has been given in Fig. 3.5(a) in Chapter 3 and the part of the XRD pattern relevant to the work described in this Chapter is reproduced in Fig. 7.4.

Qualitative XRD analysis revealed that UF15 SiC powder is in the form of α-SiC, the predominant polytype being 6H. There could be a certain amount of 3C, 4H and 15R polytypes. However, 3C cannot be detected because there is no special peak for 3C polytype - all the 3C peaks overlap 6H SiC peaks. All the other polytypes have separate peaks. For example, the 4H polytype has separate peaks at 45.34°, 49.83° and 57.41° but the highest peak appears at 34.77°. 15R has peaks at 46.07° and 55.8° and the strongest peak overlaps with 6H+3C peak at 35.77°, but the second strongest peak appears at 34.77° which overlaps with a 4H peak. The other peak special to both the 4H and 15R polytypes appears at 33.56°. These 4H and 15R peaks are definitely absent in the XRD pattern of the starting powder and therefore it can be concluded that the powder is free of 4H and 15R polytypes within the limit of detection. Most peaks of 21R and 33R polytypes overlap with other polytypes, but the peak at 45.34° is special to 21R and 33R. This peak is present in the XRD pattern, indicating that UF15 SiC starting powder consists of a mixture of mainly 6H, 21R and 33R polytypes with a small quantities of other polytypes.

XRD analysis on composites made from as-received powders showed that 3C is the major SiC phase. A small amount of α-SiC phase mainly as 6H SiC was also identified. 21R and 33R polytypes retained their structure in the 20 wt% Si_3N_4 composite prepared from as-received powders, but completely transformed, presumably to 3C, in the 10 wt% Si_3N_4 composite. On the other hand, α-SiC remained the major phase for the composites made from deoxidised compacts. This result is obtained by comparison of the intensities of the peaks appearing at 34.22° and 38.30° (arrowed peaks in Fig. 7.4(c)) which are special to α-SiC polytypes. Their absence is the only way of deducing that the structure is

predominantly 3C polytype, particularly in the presence of Si_3N_4 which makes the quantification of individual polytypes even more difficult. Comparative XRD patterns within $2\theta = 30 - 50^\circ$ are shown in Fig. 7.4 for 10 wt% Si_3N_4 reinforced composites made from as-received powders and deoxidised compacts. Relevant data for the peaks shown in Fig. 7.4 are tabulated in Table 7.1.

As explained in section 7.3, the structure of starting SiC powder for monolithic SiC and TiB_2-SiC composite was not given by the producer, but they are most probably α-SiC powders. X-ray diffraction showed that both Hexoloy SA and ST have a α-SiC structure indicating that α-SiC remained as α after the consolidation process if the starting powder was α-SiC. In the case of the layered SiC composite, the β-form of SiC transformed to α-form during densification.

7.4.2 Diffraction pattern analysis in TEM

Electron diffraction patterns can be used to identify and confirm the presence of certain polytypes of silicon carbide, but the method is inappropriate where fine scale phase mixtures exist since the overlapping diffraction patterns are complicated and difficult to interpret. In any case statistics are poor on phase distribution from electron microscopy.

Nevertheless, during TEM investigations, electron diffraction patterns were used to identify the structure of SiC grains in Hexoloy SA, Hexoloy ST and layered SiC composite. The results, although statistically poor, confirmed the X-ray diffraction analysis. Electron diffraction patterns showed mostly 6H polytype structure, although the 4H polytype was observed few times. One possible reason for the rare occurrence of 4H is that it is found experimentally that boron (which is one of the trace elements used as a sintering aid for Hexoloy SA, Hexoloy ST and layered SiC composite) stabilises the 6H polytype (Bocker *et al.*, 1979) in SiC.

The diffraction pattern analysis in the composites made from as-received powders and from deoxidised compacts have been discussed in Section 3.4.

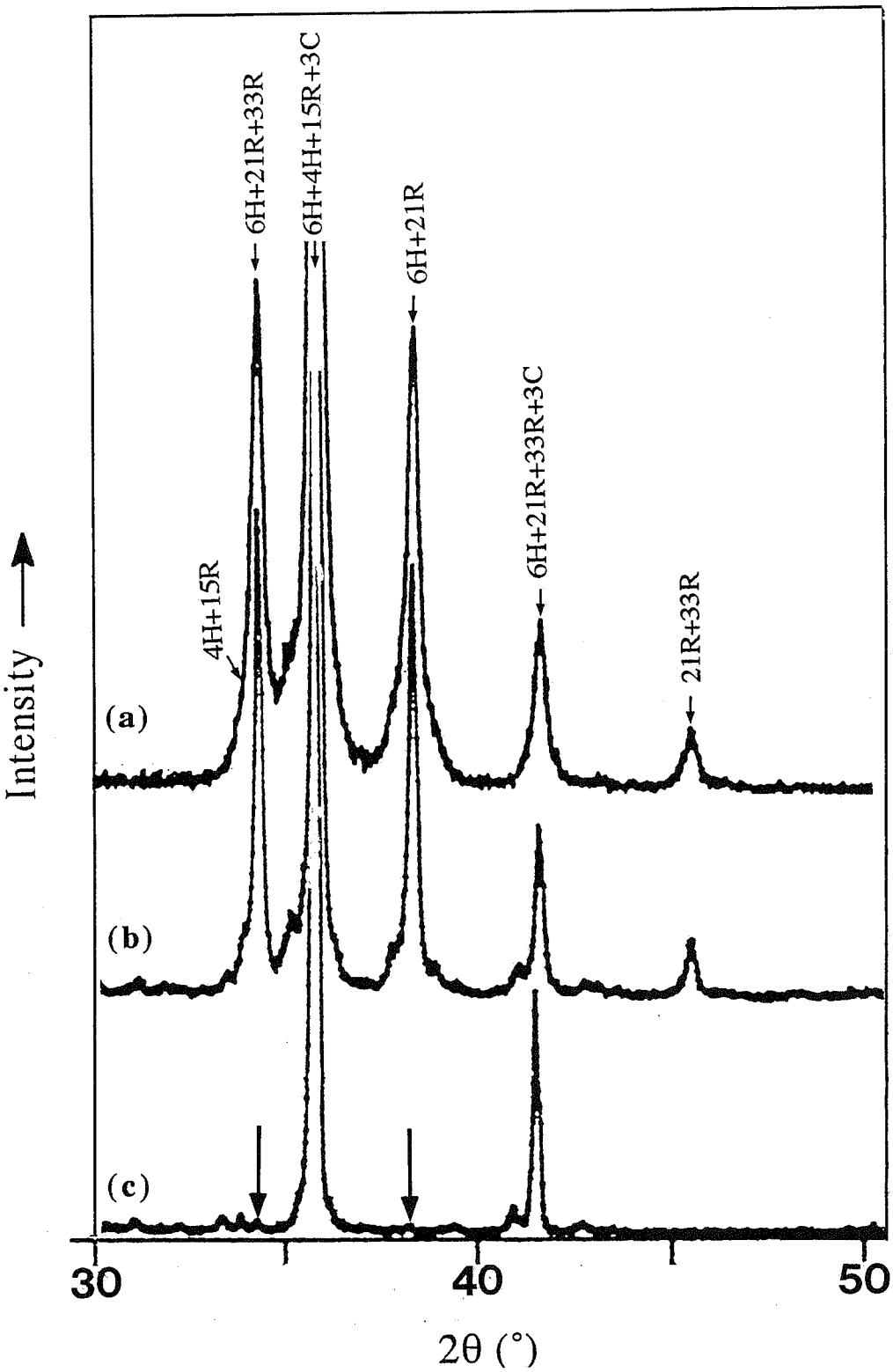

Fig. 7.4 Comparison of X-ray diffraction patterns from (a) UF15 SiC starting powder and ((b) and (c)) 10 wt% Si_3N_4 reinforced SiC composites prepared from (b) deoxidised powders and (c) as-received powders. Here, only the SiC peaks are indexed (fully indexed patterns have been displayed in Figs. 3.5 and 3.6).

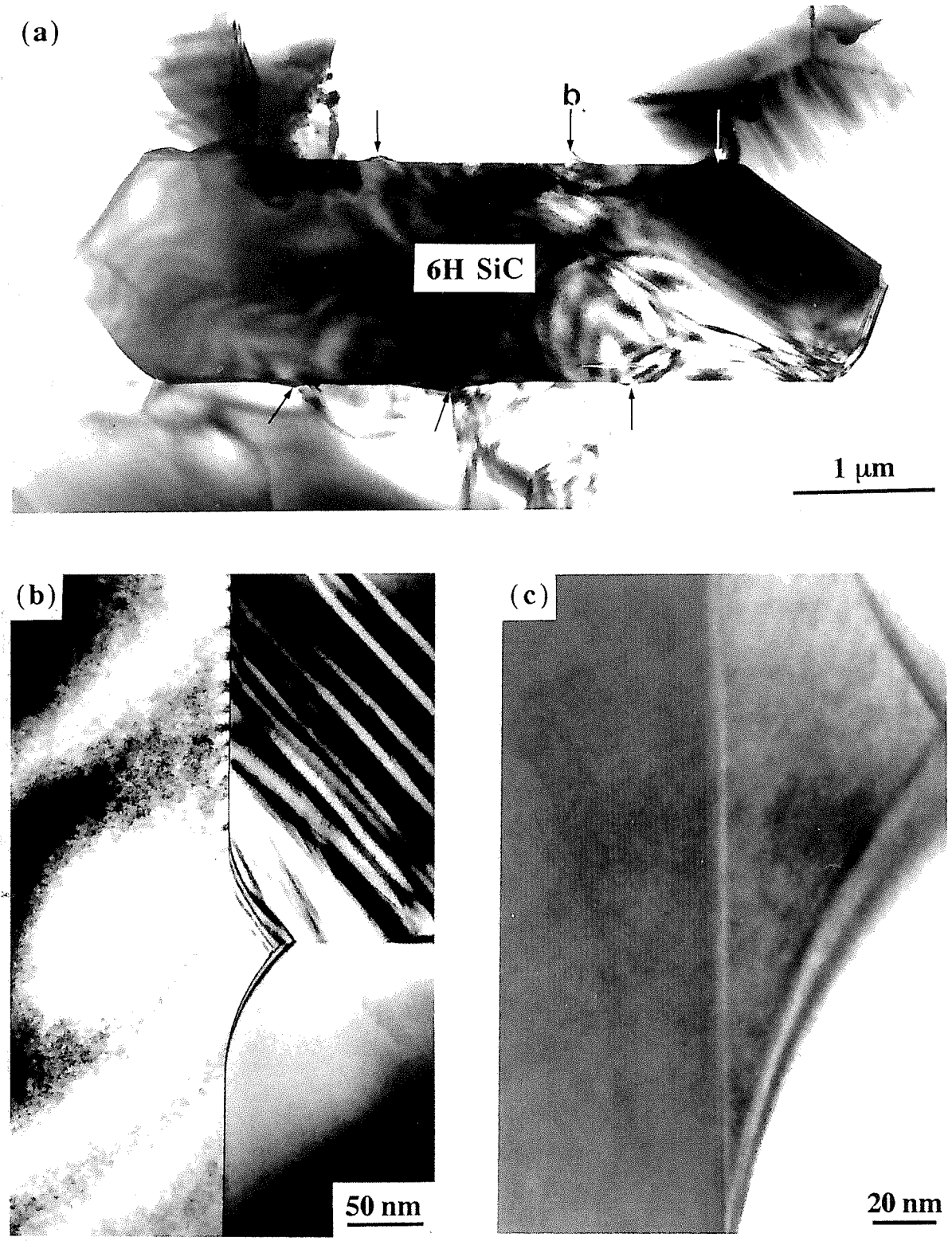

Fig. 7.5 (a) Crystalline triple junctions attached to a 6H SiC grain in Hexoloy SA sample; (b) an enlarged view of junction marked "b" in (a) and (c) lattice fringe image after tilting away from the condition used in (b) revealing that the structure of triple junction is 3C cubic polytype.

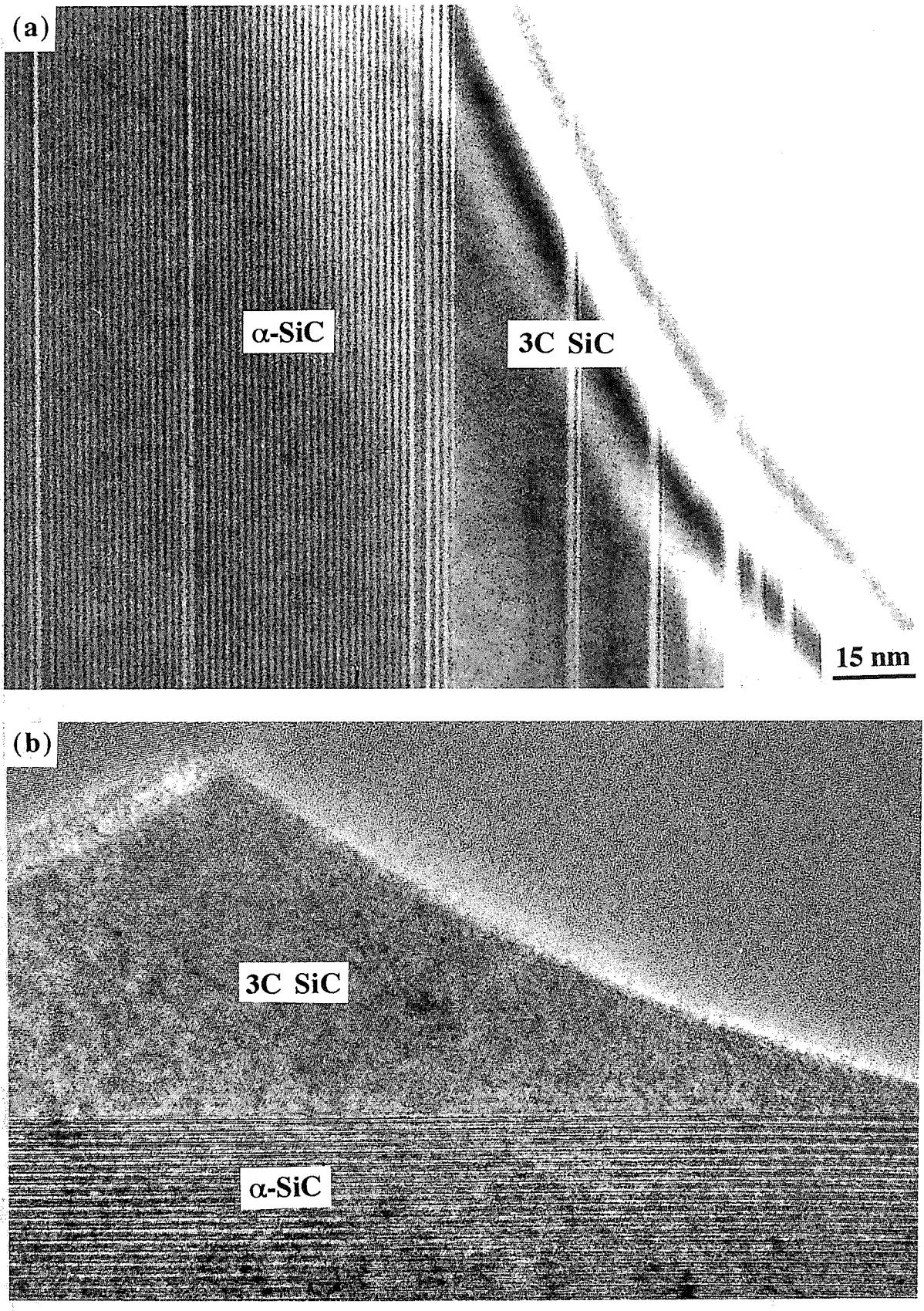

Fig. 7.6 3C SiC crystalline triple junction regions attached to α-SiC grains; (a) in 16 wt% TiB_2-SiC composite and (b) in layered SiC composite with graphite interlayer.

$2\theta_B$	*d*-spacing (Å)	**3C** (29-1129)	**6H** (29-1131)	4H (29-1127)	**15R** (22-1301)	**21R** (22-1319)	**33R** (22-1316)
33.56°	2.67			100 (25)	101 (40)		
34.22°	2.62		101 (40)			104 (70)	104 (50)
34.77°	2.58			101 (100)	104 (80)		
35.48	2.53					0,0,21 (100)	0,0,33 (100)
35.77°	2.51	111 (100)	006 (100)	004 (65)	0,0,15 (80)		
36.37°	2.47					018 (20)	
37.47°	2.40				107 (70)	1,0,10 (20)	
37.80°	2.38						1,0,16 (60)
38.30°	2.35		103 (20)	102 (94)		1,0,11 (10)	
38.81°	2.32				018 (60)		
40.45°	2.23					1,0,13 (10)	
41.42°	2.18	200 (20)	104 (10)		1,0,10 (10)	1,0,14 (10)	1,0,22 (30)
42.86°	2.11				1,0,11 (30)		
43.29°	2.09			103 (16)			1,0,26 (20)
45.34°	2.00					1,0,16 (30)	1,0,28 (20)
46.07°	1.97				1,0,13 (10)		
49.83°	1.83			104 (7)			

Table 7.1 Selected crystallographic data for the crystalline SiC polytypes detected in the composites and SiC starting powders giving the JCPDS file numbers, $2\theta_B$ for CuK_α radiation (λ = 1.5418), *d*-spacings and *hkl* values for the peaks identified. The relative intensities of each peak within a column is shown inside () next to *hkl* values.

7.4.3 Transmission electron microscopy observations

7.4.3.1 Hexoloy SA material

During the TEM observations of Hexoloy SA material on a JEOL 2000-FX, the phases seen at triple junctions could all be identified as crystalline phases. An example is shown in Fig. 7.5(a) where six individual grain boundaries form triple junctions with a 10 μm long main grain. Although in Fig. 7.5(b) the triple junction shown appears to be part of an elongated grain, the discontinuity of lattice fringes in Fig. 7.5(c) (which is obtained by tilting away 15° from the conditions of image obtained in Fig. 7.5(b) to one where the electron beam is parallel to the $[11\bar{2}0]$ zone axis) indicate that this triple junction phase is not part of the main grain and is in fact epitaxed to the main SiC grain. Lattice fringes revealed that the main grain is 6H polytype with fringe spacings of ≈ 15 Å in the elongated grain. The triple junction phase could of course be one of the other polytypes of SiC epitaxed to the 6H grain whose interplanar spacing is less than 15 Å, but the thickness of this particular area precluded more detailed HREM imaging to confirm this.

7.4.3.2 Hexoloy ST material

Similar triple junctions were observed in a JEOL 2000-FX on a TiB_2 particulate reinforced SiC composite in that large 6H SiC grains were capped with 3C SiC forming a triangle* at the triple points (Fig. 7.6(a)). In this case, the triple junction phase contains stacking faults.

7.4.3.3 Layered SiC composite with graphite interlayer

The TEM observations in a JEOL 2000-FX and a 4000-EX were very similar to those obtained from Hexoloy SA material and shown in Fig. 7.5(a), in that elongated α-SiC grains were epitaxially capped with several 3C SiC triple junction grains. Fig. 7.6(b) shows a HREM observation of one of those 3C grain at the triple junction. The other observation was that β-SiC starting powder transformed into α-SiC polytypes, mainly to 6H polytype, although some 4H polytype was also seen.

---

* *Of course, this is a pyramid shape in three dimension, but since only two dimensional images are shown these phases will be called triangles.*

7.4.3.4 As-received Si_3N_4-SiC composites

TEM observations of Si_3N_4-SiC composites on a JEOL 4000-EX revealed some interesting results. Although similar caps were observed, the main grains were identified as 3C SiC, whereas the triangle shaped cap was a mixture of α-SiC polytypes. Two examples at relatively low magnifications are shown in Fig. 7.7. In this material, the triangle shape of the crystalline cap was completed with amorphous triple junction phases, whereas it was completely crystalline in both the Hexoloy materials.

The key observation here is that the interfaces in this sample are associated with intergranular films and that the intergranular film is observed at grain boundaries between two 3C SiC grains. As soon as an interphase boundary starts between a 3C SiC grain and a α-SiC cap, the intergranular film is absent and spreads instead to another high angle interphase boundary. This is clearly shown in Fig. 7.8(a). The high resolution image of one of the triple junction is shown in Fig. 7.8(b) where the triple junction phase can be identified as 6H SiC from the stacking sequence. The 3C-6H interface is free of intergranular film.

In summary, when the starting powder is in β or α-form, the triple junction phase is in the form of β-SiC, but when the starting powder is in the form of α and transforms to β due to the reasons which will be discussed in the next section, the triple junction phase is a α-SiC mixture. The 3C caps attached to 4H SiC (Allard *et al.*, 1989 & Duval-Riviere and Vicens, 1994) and 6H SiC (Kinsman and Shinozaki, 1981) have been largely observed in SiC monolithic ceramics independent of the structure of starting powder, but not in TiB_2-SiC and layered SiC composites. This is believed to be the first time that a α-SiC triple junction phase attached to a main 3C SiC grain has been observed in SiC based materials.

7.5 Discussion

7.5.1 XRD and diffraction pattern analysis

XRD and TEM diffraction analysis showed that α-SiC transformed into 3C SiC in the composites made from as-received composites, whereas the starting powder of α-SiC remained untransformed for the composites made from deoxidised compacts. The transformations cannot be assigned in the case of monolithic SiC and TiB_2-SiC composite since their initial powder structures are unknown.

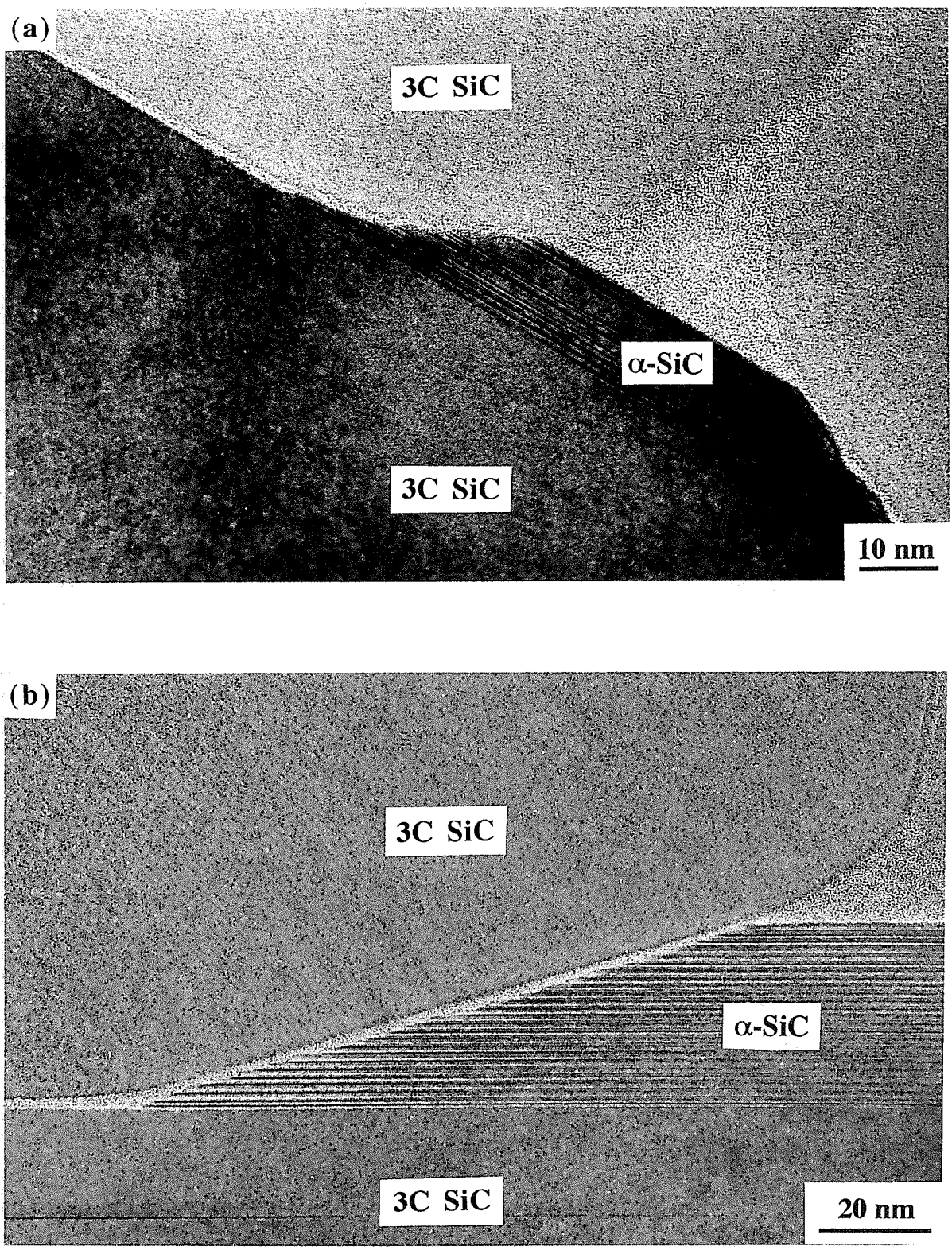

Fig. 7.7 Examples of crystalline triple junctions attached to 3C SiC grains in the Si_3N_4-SiC composites made from as-received powders. The images clearly show that the triangle shape of the triple junctions are completed with amorphous phases and that the structure of the crystalline phases are α-SiC in both occasions.

7.5.2 The effect of existence and content of Si_3N_4 (or nitrogen atmosphere) on the reverse transformation

The amount of SiC phases stable for both kind of composites are not significantly effected by changing the amount of Si_3N_4 content although less α-SiC was identified for 10 wt% reinforced Si_3N_4 composite than for 20 wt% reinforced composite prepared from as-received powders. Therefore, it can be concluded that Si_3N_4 content does not have a rate controlling effect on the α → β reverse transformation of SiC, but the effect of Si_3N_4 on the reverse transformation is less clear.

In order to clarify the effect of Si_3N_4 on α → β SiC reverse phase transformations, SiC powder without the addition of Si_3N_4 should be hot isostatically pressed at the same conditions used for hot isostatic pressing of the composites. Although this experiment has not been carried out during this study, Dutta (1988) hot isostatically pressed α-SiC compacts wrapped with graphite foil and coated with BN in a tantalum can without any sintering aids at 2100°C[$] but did not report any transformation from α to β. In addition, the absence of reverse transformation in the presence of Ar atmosphere in reaction bonded SiC demonstrates that the reverse transformation requires a nitrogen atmosphere (Jepps and Page, 1981).

7.5.4 The effect of a liquid medium on the reverse transformations

Both the observations by Jepps and Page (1981) & Dutta (1988) indicate that the presence of Si_3N_4 in the composite prepared from as-received powders investigated in this study is necessary along with high temperature and high pressures for the reverse transformation to occur. However, meeting these conditions is not sufficient since the transformation did not take place when deoxidised powders were hot isostatically pressed at a high temperature and pressure in the presence of Si_3N_4 (or more properly in a nitrogen atmosphere because of the decomposition of Si_3N_4).

[$] *These conditions are almost identical to the fabrication route adopted during the hot isostatic pressing of Si_3N_4-SiC composites as discussed in section 3.3.*

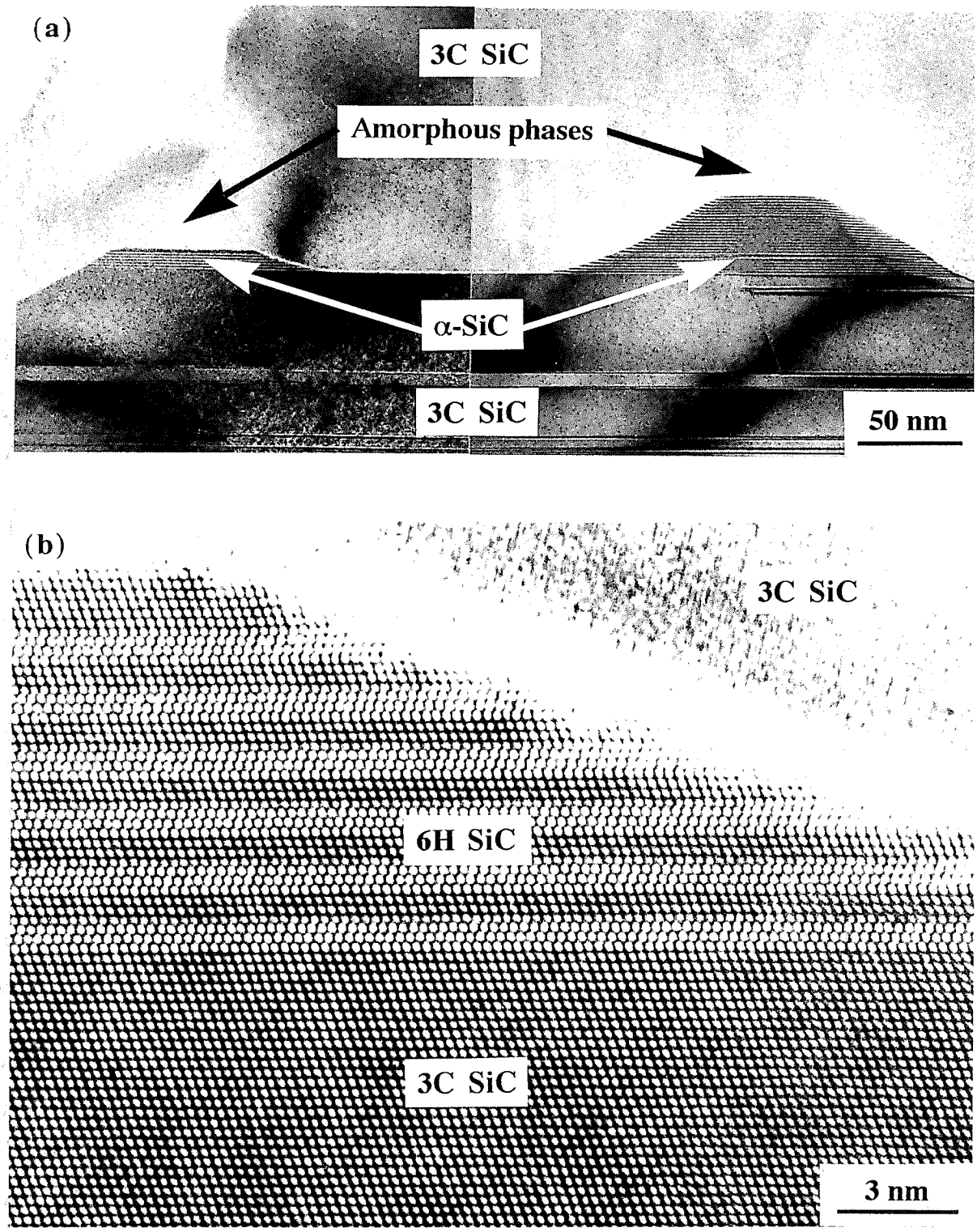

Fig. 7.8 (a) An elongated and twinned 3C SiC grain capped with α-SiC polytypes at either end of the grain (note that the middle portion of the grain boundary does not have any α-SiC) and (b) HREM image of the triple junction shown at left side of the Fig. (a) showing that the structure of the cap is 6H SiC.

In order to understand why the reverse transformation did not take place in the composites made from deoxidised compacts, it is necessary to highlight the microstructural differences between the composites. The most striking difference was that intergranular phases were largely observed in the composites made from as-received powders whereas such phases were largely absent in the composites made from deoxidised compacts as discussed in Chapter 6 and reported in Turan and Knowles (1995).

In addition to the observations reported in Chapter 6, the following observations are relevant. For example, some of these films were quite thick in the composites made from as-received powders, as shown in Fig. 7.9. The film thickness revealed by HREM is 3.3 nm in comparison to the usual observations that the thickness of intergranular films were around 10 Å. The micrograph also shows the typical microstructure observed throughout the composites where a α-SiC grain is sandwiched between two 3C SiC grains and has large triple junctions. The smooth semi-circular shape of the α-SiC grain in the middle suggests that solution-reprecipitation took place in this sample.

In contrast to this, HREM observations showed that intergranular films are largely absent at the interfaces in the composites made from deoxidised compacts. In one occasion a 7.5 Å thick film was observed between a α-SiC and a small slab of 3C SiC which is sandwiched between α-SiC and the film (Fig. 6.36). Whenever the liquid films were absent, 3C SiC was absent as well. These observations strongly suggest that the liquid phase, available during the hot isostatic pressing temperatures of the composites made from as-received powders which contains surface silica, plays an important role on the reverse transformation of α-SiC to β-SiC.

A simple conclusion which can be drawn from these results is that the reverse transformation is affected by liquid phases. The importance of the existence of liquid phases were realised in earlier observations. Jepps and Page (1981) detected a relatively thick intergranular film between adjacent β-SiC grains, but they did not carry out a control experiment without liquid phases (*e.g.*, on monolithic SiC with B and C sintering aids) to determine whether or not the presence of liquid phase is a necessary condition to enable the $\alpha \rightarrow \beta$ reverse transformation to occur. However, it is usual practice to observe intergranular films in reaction bonded silicon carbides (Jepps, 1979 & Ness, 1985) and neither Jepps nor Ness observed the

reverse transformation when the nitrogen atmosphere was replaced with Ar atmosphere although the sample contained liquid phases. Thus, it cannot be concluded that the reverse transformations was encouraged by liquid phases alone.

Interestingly, Jepps (1979) also annealed hot pressed SiC (B-doped) whose structure was primarily 4H (the details of production is in Martin, 1980). The results indicated that, under 10 atm. nitrogen pressure, 4H transforms completely to 6H at 2250°C while 100% 4H is stabilised under Ar atmosphere with no observable trace of cubic polytype. However, Jepps did not comment on why 6H did not transform to 3C, although this was the case in REFEL SiC under nitrogen pressure. This is a further indication for the necessity of liquid phases to be present in the $\alpha \rightarrow \beta$ reverse transformation.

The starting SiC powder presumably contains some surface silica which is a typical contamination in such non-oxide powders and the silica would supply the necessary liquid phase for the reverse transformations.

All this suggests strongly that a combination of liquid phase and nitrogen atmosphere is necessary to produce the $\alpha \rightarrow \beta$ reverse transformation.

7.5.5 Does the existence of BN effect the rate of reverse transformation?

The other parameter that could effect the rate of reverse transformations is the presence of boron nitride. h-BN inclusions were detected in composites made from both as-received powders and deoxidised compacts (the details have been discussed in Chapter 4, Turan and Knowles (1993) & (1995a)). However, from the XRD patterns alone, it can be deduced that the presence of h-BN does not have a pronounced effect on the rate of reverse transformation.

Murata and Smoak (1978) investigated the densification behaviour and the solid solubilities of α-SiC with varying amount of BN additions at 2200°C in a graphite furnace under Ar atmosphere. They did not report any kind of transformation after densification and it seems that α phase stayed as α.

Ruh *et al.* (1984) has hot pressed β-SiC powders with different BN content at 2100°C for 1 hr under 35 MPa pressure. Although XRD revealed the presence of several SiC polytypes

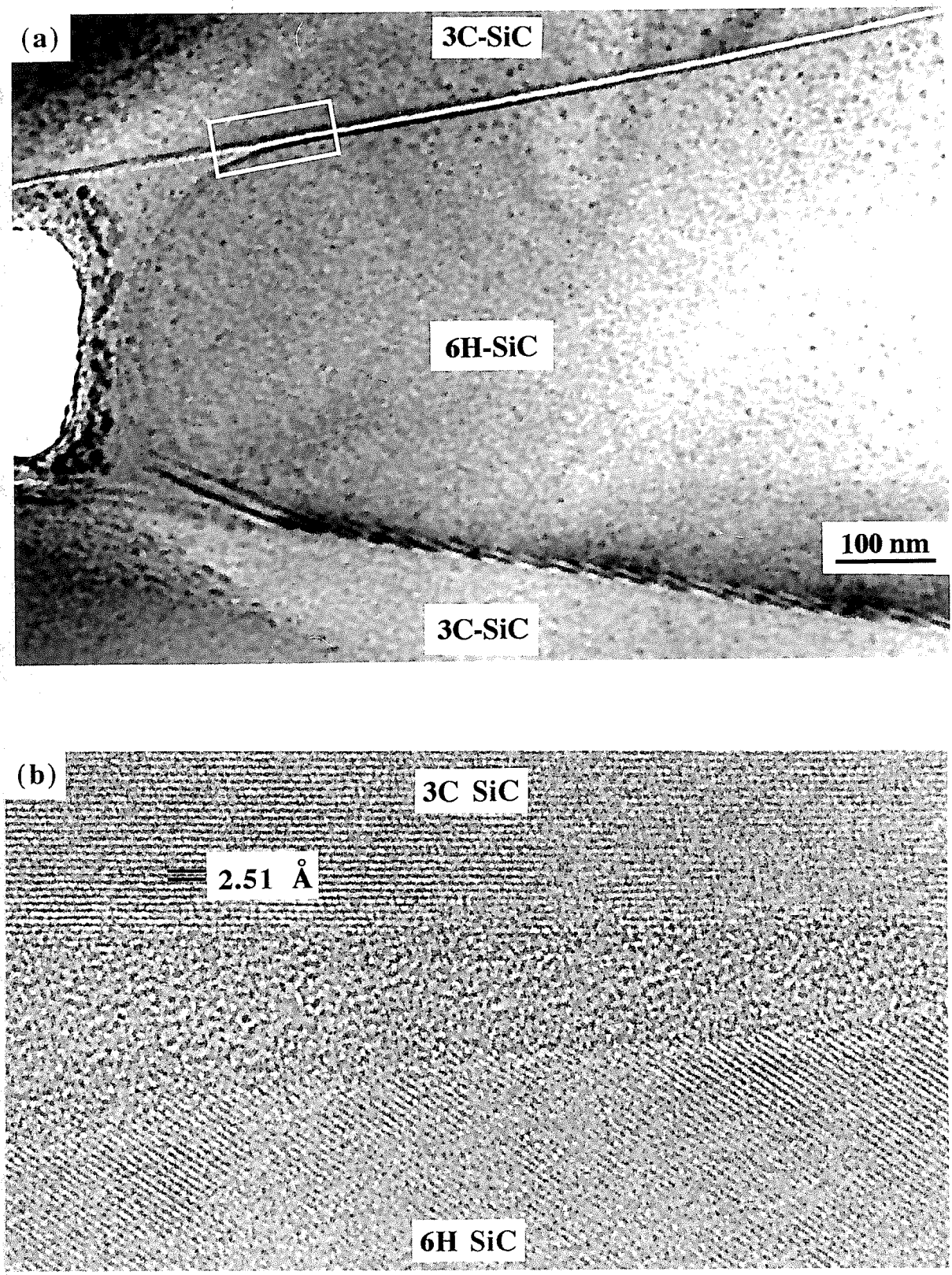

Fig. 7.9 (a) An underfocus bright field image of a 6H SiC grain sandwiched between two 3C SiC grains; (b) HREM image of the interface from the boxed area in (a) shows that the thickness of the film is ≈ 3.3 nm.

including 21R, 15R, 6H, 4H and 3C, the SiC patterns were similar regardless of the BN content (they stated that the amount of each polytype present was impossible to quantify). It can, therefore, be assumed from their work that the BN content does not effect polytype transformations of SiC.

Zangvil and Ruh (1985) has also hot pressed 50 wt% BN-3C SiC mixture at 2100-2300°C for 1 to 8 hr. Using their TEM micrographs as evidence, which showed that the main hexagonal grains are capped with 3C SiC when they are found adjacent to the BN grains, they concluded that BN stabilises 3C SiC.

Ruh *et al.* (1988) demonstrated that the amount of stabilised 3C increased with the increasing amount of BN additions above 30 %* in hot pressed β-SiC powder at 2100°C for 1 h, 35 MPa pressure under vacuum in contrast to earlier observations by Ruh *et al.* (1984). They again observed 3C cubic polytype next to BN grains. Away from the interphase boundary they observed hexagonal polytypes and concluded that BN stabilises 3C SiC.

Ruh *et al.* (1988) also reported that 3C is the major polytype along with small amount of α polytypes for SiC phase while graphitic BN is the major BN phase for hot isostatically pressed SiC-BN composites at 2000°C for 2 h using β-SiC and cubic BN powders. It is relevant to note that prior to hot isostatic pressing, the samples were sealed in quartz containers in the presence of nitrogen. Under same hot isostatic pressing conditions but using Si, C and cubic BN, they obtained two different composites with a composition of 80% 3C+20% h-BN and 40% 3C+60% h-BN. In this case, no trace of 6H SiC was identified. They occasionally observed a similar microstructure in hot isostatically pressed SiC-BN composites at 2000°C and 190 MPa nitrogen atmosphere for 1 h, in that the stabilised phase next to BN was again 3C and away from the interface it was hexagonal polytypes. However, XRD results mainly identified the 3C with small amounts of rhombohedral and hexagonal polytypes. The results obtained from the studies on the stability of certain SiC polytypes and SiC phase transformations is summarised in Table 7.2.

Ruh and coworkers concluded from TEM observations and XRD analysis that BN stabilises 3C polytype, but they did not explain why 3C was obtained in hot isostatically pressed BN-SiC composites whereas the amount of stabilised 3C polytype increased with an

---

* *It is not stated in the reference whether it is vol% or wt%.*

Study	Conditions	Stable polytype / Polytype transf.
Kieffer *et al.* (1969)	0.2 MPa N_2, 2500°C	α→β
Whitney & Shaffer (1969)	α-SiC, in the presence of BN impurities	α→β
Murata & Smoak (1978)	α-SiC with BN addition as a sintering aid, in graphite furnace under Ar	No transformation reported
Heuer *et al.* (1978)	β-SiC, B and C, 2050°C in Ar	β→α
Jepps (1979), Jepps and Page (1981) & Jepps and Page (1983)	α-SiC, Si, 1-3 MPa N_2, 1800-2500°C β-SiC, Si, 1-3 MPa N_2, 1800-2500°C α-SiC, Si, 1-3 MPa Ar, 1800-2250°C β-SiC, Si, 1-3 MPa Ar, 1800-2250°C	α→β β-SiC α-SiC β→α
Bocker *et al.* (1979)	α-SiC with B addition α-SiC with Al addition	6H 4H
Dutta (1988)	α-SiC, wrapped in graphite foil and coated with BN, hipped at 2100°C	No transformation reported
Ruh *et al.* (1988)	β-SiC and BN, hot pressed under vacuum at 2100°C for 1 hr at 35 MPa in graphite dies lined with graphite foil	β-SiC (main phase) & β-SiC regions next to BN grains
Ruh *et al.* (1988)	β-SiC and BN sealed in quartz (in the presence of N_2) and hipped at 2000°C, for 1 hr under 186-200 MPa.	β-SiC (main phase) & β-SiC regions next to BN grains
Composites from as-received powders	α-SiC, α-Si_3N_4 and surface silica	α→β
Composites from deoxidised compacts	α-SiC, α-Si_3N_4, no surface silica	No transformation

Table 7.2 Summary of SiC phase transformations reported in the literature with the experimental conditions used.

increasing amount of BN added in the hot pressed BN-SiC composites. This raises the question whether the amount of 3C SiC stabilised was a function of nitrogen content or BN content as proposed by Ruh and coworkers. I believe it to be the former for the following reasons. Hot isostatic pressing of the composites in the work of Ruh and coworkers were carried out when a nitrogen atmosphere was present in the quartz containers. Since the starting powders were not treated to eliminate surface silica, these experimental conditions supplied the necessary ingredients (*i.e.*, nitrogen and liquid phase) for 3C SiC to be stabilised. Although nitrogen was not present during hot pressing, the nitrogen atmosphere could have been created from the dissociation of BN, and, together with liquid silica the 3C SiC structure is again stabilised. This is consistent with the thermodynamical analysis presented in Section 4.2.8 that BN could dissociate when nitrogen atmosphere is not available at the hot pressing and hot isostatic pressing temperatures (> 2000°C) used during the studies of Ruh and coworkers. It is also relevant to note that in my work 6H SiC was stabilised in the composites made from deoxidised green compacts in which nitrogen (through the dissociation of Si_3N_4) and BN was present but liquid phase was absent. It therefore remains to be able to explain the TEM observations of Ruh *et al.* that whenever they observed a BN grain next to a SiC grain, a portion of SiC grain at the interface was 3C SiC.

The TEM observations by Ruh and coworkers are very similar to the observations in the monolithic SiC, TiB_2-SiC and layered SiC composites shown in Figs. 7.5 and 7.6. Shinozaki and Kinsman (1978), Kinsman and Shinozaki (1978) & (1982) observed similar triple junction phases in pressureless sintered α-SiC in the temperature range of 1900-2200°C. Duval-Riviere and Vicens (1994) observed 3C caps on 4H main grains in hot pressed α-SiC powder (doped with 0.3 wt% Al) at 1950°C and attributed this to a phase transformation from 4H to 3C, but they did not explain why transformation did not take place in the main grains and occurred exclusively at the triple junctions.

The most complete mechanism was proposed by Shinozaki *et al.* (1988) for the observations of 3C SiC at triple junctions capping α-SiC grains. The schematic of proposed mechanism for the observation of remnants of 3C SiC grains at triple junctions is shown in Fig. 7.10. They stated that, in association with morphological changes from equiaxed to elongated shape in ultrafine grained α-SiC, a thin layer (100-200 Å thick) of β phase forms coherently along $\{0001\}_\alpha$ throughout the temperature range in which large tabular grains developed. In β-SiC starting powder, as the α plate morphology becomes confined in the β grain

(Fig. 7.10(a)) and a cooperative reaction front develops. The plate edge advances as a disordered interface and the β grain boundary remains contiguous with the plate edge and extends with it. Thus a sheet of β phase forms within a grain (Fig. 7.10(c)) where the α plate habit plane remains intact and planar. Because the β envelope is often thin, the overall plate shape on a macro scale appears almost perfectly planar. In the case of α SiC starting powder, the usual apparently transient formation of small amounts of β phase at α grain boundaries (Fig. 7.10(d)) affords the same mechanism of coupled growth to account for the formation of large tabular grains (Fig. 7.10(e) and (f)). The distinctive and relatively small amount of β phase sheaths formed in the α-SiC grains enhances the growth of tabular grains. Thus the microstructural development at or above the normal sintering temperatures is controlled in the same manner, regardless of the starting powder phases. When the tabular grains mature, all the β phase disappears except for some remnants in the pockets of grain junctions. However, this mechanism does not explain the shapes of the remnants of triple junction phases.

It is likely that the 3C SiC polytype observed next to h-BN grains in the papers presented by Ruh and coworkers are remnants of transformation from the β-SiC starting powder. The observations of Duval-Riviere and Vicens (1994) can also be explained by this mechanism rather than by products of transformation. Therefore, the proposal by Ruh and coworkers that the BN stabilises the 3C SiC merits re-examination.

In this study, h-BN inclusions were found to exist mostly next to 3C SiC but this is expected since α-SiC transformed into 3C SiC. As shown in Chapter 6, the inclusions were also observed next to 6H SiC grains. In particular in Fig. 6.22, it can be seen that the grains at either side of h-BN inclusion have a different structure, one being 3C SiC whereas the other one is clearly a 6H SiC grain. Some of the interphase boundaries observed at low magnifications to be between 3C SiC and h-BN were found at higher magnifications to have a narrow band of 6H SiC sandwiched between 3C SiC and h-BN grains, as shown in Fig. 7.11. It is not clear whether the band of 6H crystal is the remnant of a reverse transformation or whether it is stabilised by the existence of the h-BN grain nearby.

Therefore, these observations are at variance with the proposal by Ruh and coworkers made to explain their TEM observations, although it is of course possible that BN affects the stability of 3C indirectly by dissociation at high temperatures.

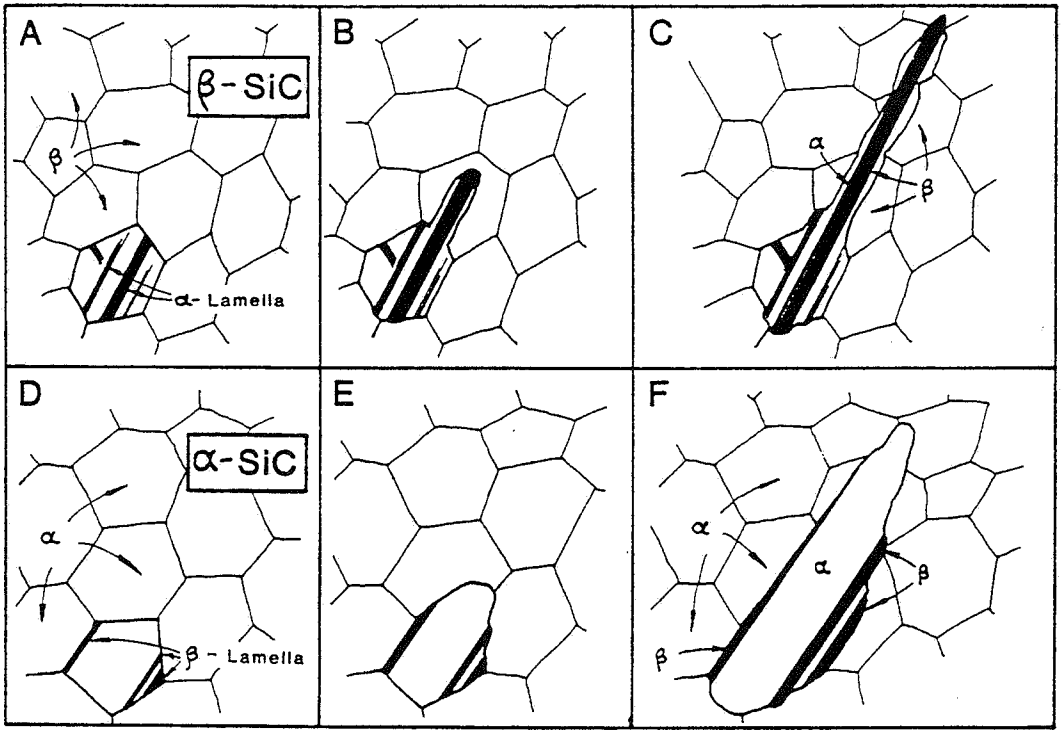

Fig. 7.10 Schematic growth sequence for β and α-SiC starting powders (after Kinsman and Shinozaki, 1988). In both cases, elongated α-SiC grains form associated with remnants of β-SiC near interfaces.

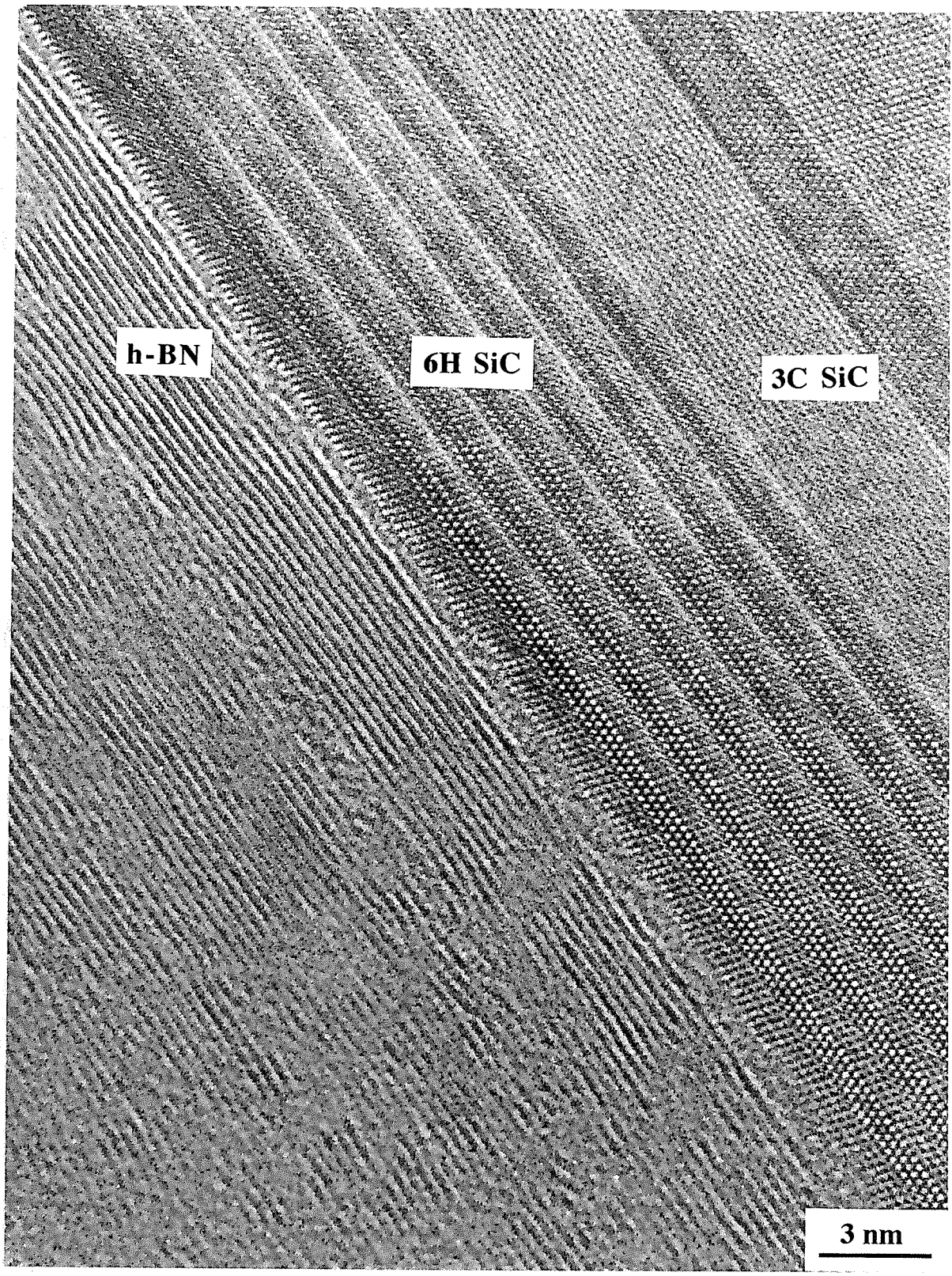

Fig. 7.11 An HREM image of an interphase boundary between a SiC and a h-BN shows that, although the main SiC grain has a twinned cubic 3C structure, ≈ 9 nm thick slab of 6H SiC exists between a h-BN inclusion and a 3C SiC grain.

7.5.5 What is the mechanism of the reverse transformation?

Thus far, it is established that liquid phases and a nitrogen atmosphere are necessary for the occurrence of the α → β SiC reverse transformation. However, two questions still remain. First of all, *how does the reverse transformation take place*? and secondly, *how can the observations of α-SiC at triple junctions be explained*?

The mechanism responsible for the reverse transformation in this study is not consistent with the solid state transformation mechanism discussed in section 7.2.4. For example, if the most recent dislocation model proposed by Pirouz and Yang (1993) for the α → β reverse transformation in SiC is used to explain the experimental results, an obvious problem arises. If this was the transformation mechanism observed in this study, it would have also taken place in the composites made from deoxidised compacts. That this was not so implies that this is not the mechanism responsible for the transformations observed in the composites made from as-received powder unless dislocation movement is activated by liquid phases (to the best of my knowledge there is no report to suggest this). In the model of Pirouz and Yang, it is also necessary to have 3C nuclei sites for the transformations. One might consider that these transformation nuclei sites could have been diminished during the deoxidation of green compacts which was carried out at 1900°C where the 3C SiC, existing in the mainly α starting powder, is not stable and transforms to 6H SiC. However, 6H SiC can be described as twinned 3C SiC and this could act as an nuclei site for the transformations. Furthermore, 3C SiC regions were detected in main 6H SiC grains in the composites made from deoxidised compacts. Therefore, a liquid phase transformation mechanism is required to account the experimental observations.

The observations suggest that there are similarities to liquid phase activated densification associated with α → β phase transformations in Si_3N_4 ceramics. As is well known (Ziegler *et al.*, 1986), the α → β-Si_3N_4 phase transformation is greatly assisted by the presence of surface silica layer which can form a liquid phase at high temperatures. There are three requirements for the complete liquid phase densification and hence the α → β phase transformation of Si_3N_4:

(i) an appreciable amount of liquid,
(ii) an appreciable solubility of solid and
(iii) complete wetting of the solid by the liquid (Hampshire and Jack, 1981).

These conditions are satisfied for silicon nitride by the formation of an oxynitride liquid.

The newly proposed liquid phase transformation mechanism to explain the observations of the $\alpha \rightarrow \beta$ reverse transformations in SiC-Si_3N_4 composites is as follows:

The composition of liquid phases in these composites has been established to be almost pure silica at room temperature (see Section 6.6), but this does not mean that the liquid composition at the fabrication temperature is the same. The first assumption made here that the composition of high temperature liquid was a mixture of silicon, oxygen and nitrogen created from the decomposition of Si_3N_4 or from the dissolved Si_3N_4. This is a valid assumption since the reverse transformation does not take place in the absence of nitrogen atmosphere and/or a liquid phase. But, *what actually is the role of nitrogen on the transformations? Does it reduce the melting temperature of silica glass and hence increase the solubility limit of SiC? Does it reduce the activation energy necessary for the reverse transformations as suggested by Jepps and Page (1983)?*

The role of Si_3N_4 or nitrogen can be assigned from the SiO_2-SiC (Fig. 7.12(a)) and SiO_2-Si_3N_4 (Fig. 7.12(b)) phase diagrams. In the SiO_2-SiC system, it can be seen that the first liquid forms at 1723°C, whereas in the SiO_2-Si_3N_4 system, silicon oxynitride-rich silica liquid forms at a much lower temperature of $\approx$ 1500°C. Assuming that the transformation mechanisms are the same for all the polytype transformations, *i.e.*, diffusional re-arrangement, followed by growth of transformed nuclei, the addition of nitrogen appears either to reduce the activation energy for lattice diffusion, or if the subsequent grain growth becomes the rate determining step, it reduces the activation energy for the growth of β grains (Jepps, 1979). As shown in Fig. 7.3, the activation energy for the $\alpha \rightarrow \beta$ transformation under 30 atm nitrogen pressure is lower than for the $\beta \rightarrow \alpha$ transformation. It would, therefore, appear that as well as stabilising the cubic polytype, the nitrogen either;

(i) reduces the activation energy necessary for the transformation or

(ii) the transformation mechanism is different from that of the $\beta \rightarrow \alpha$ transformation in SiC.

Nitrogen from the decomposed Si_3N_4 can combine with silica and form a low melting point liquid. α-SiC particles dissolve in this liquid as can be deduced from the TEM observations which show that the remaining α-SiC grains have very smooth semi-circular faces and that

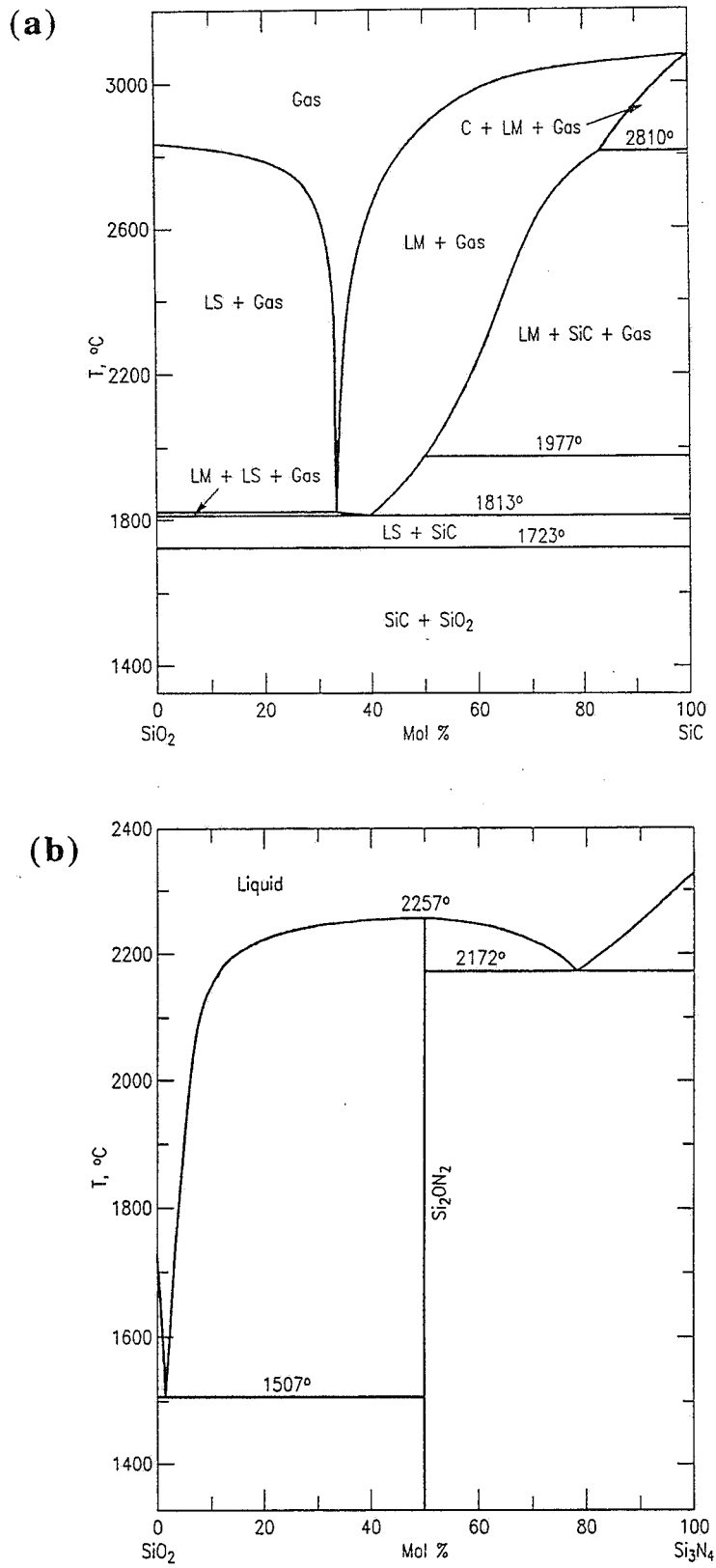

Fig. 7.12 Calculated binary phase diagrams (a) between silica and SiC (after Weiss *et al.*, 1981) and (b) between silica and Si_3N_4 (after Richter *et al.*, 1991).

when the liquid is exceedingly supersaturated, SiC reprecipitates as the 3C SiC polytype. For polycrystals, once sufficient nuclei exist, the transformation will be dominated by fast transport mechanisms and accompanied by grain growth and recrystallisation. This is indeed the case for the composites prepared from as-received powders where very large twinned SiC grains grow very quickly, while the remaining finer grained material is still in the form of α-SiC polytypes. It is also important to note that the thickness of intergranular films at these interphase boundaries are much higher than expected theoretical values as established in Chapter 5 and as reported in Chapter 6. This indicates that the films might contain some remnants of dissolved SiC and nitrogen which would have the effect of increasing the film thickness since they would increase the refractive index of the silica-rich film.

There are two possible explanation for the existence of α-SiC triple junctions. The first mechanism could explain whether or not the α-SiC triangle grains at the triple junctions are remnants from the starting powder. The observations of α-SiC regions at the triple junctions can be explained in a similar way to the mechanism proposed by Shinozaki *et al.* (1988) and shown in Fig. 7.10, but it requires a different interface advance mechanism. If a similar mechanism is proposed for α → β reverse transformation to explain the remnants of α-SiC at triple junctions, it must, first of all, be assumed that liquid phase wets the coherent interphase boundaries between 6H SiC and 3C SiC at high temperatures. This is a difficult criterion to satisfy since the energy of such interphase boundaries found to be very small (Mitchell *et al.*, 1978) even though Clarke (1985) proposed that some of the special interfaces such as this can be wet at high temperatures and dewet at room temperatures (see Fig. 5.3). This might be the reason that the interphase boundary shown in Fig. 7.8(b) is free of an intergranular film at the observation temperature. Once transformation starts, α-SiC dissolves in nitrogen rich silica liquid and reprecipitates as 3C SiC which grows faster in the direction parallel to the interface and slower on the direction perpendicular to the interface. When the growth stops, the undisolved α-SiC remains at triple junctions. This mechanism will only be possible if the energy of "SiC-liquid-SiC" grain boundary is smaller than half the energy of the coherent interphase boundary between α-SiC and 3C SiC. However, there are no calculations to confirm or deny this possibility at the time.

The second possibility is that at the fabrication temperatures, liquid phase wets the randomly oriented α-SiC grain boundaries, and starts dissolving SiC which increases the liquid volume available for the liquid phase sintering. Then, SiC recrystallises on the α-SiC grains and grows as 3C SiC – Heine *et al.* (1991) showed that adding a Si-C bilayer in the cubic stacking sequence is energetically more favourable for growth than adding twinned bilayers (as would be the case in growing 6H SiC). There is some experimental evidence for this because some of the 3C grains contained α-SiC regions in the middle of the grains. They could, of course, be the remnants of a slower solid state transformation.

Towards the end of liquid phase densification, when two 3C SiC grains meet each other to preserve the equilibrium thickness at the fabrication temperature which is established to be higher than the equilibrium film thickness at lower temperatures (Clarke, 1989 & Cinibulk *et al.*, 1993a), the growth of 3C SiC stops. When cooling starts more 3C SiC forms and the film thickness will progressively become smaller. During further cooling, nitrogen will reform Si_3N_4 at temperatures below 2100K[#] according to thermodynamical data. It is suggested that the new conditions favour the formation of α-SiC, and that therefore the excess SiC existing in the liquid precipitates out as α-SiC. It is hardly surprising to see that remaining SiC in the liquid recrystallises as α-SiC epitaxial to 3C grain since the energy of these interphase boundaries are several magnitude smaller than a random interface (Mitchell *et al.*, 1978). The schematic of the reverse transformation is shown in Fig. 7.13 and is consistent with the results shown in Figs. 7.7 and 7.8.

Jha (1993) has attempted to recalculate the phase equilibria in the Si-C-N-O system. The phase equilibria[¶] as a result of this study is shown in Fig. 7.14. He concluded that β-SiC is a low oxygen potential polytype which can transform to α-polytypes in the presence of oxygen impurities. This is also consistent with the above proposed mechanism that at the pressure and temperature where Si_3N_4 starts to reform and as a result nitrogen leaves the liquid phase, the stable SiC polytype is α-SiC.

[#] *The dissociation temperature of Si_3N_4 is 2160 K according to the thermodynamical data presented by Pehlke and Elliot (1959) whereas it is 2050 K according to Hendry (1977).*

[¶] *Note that this phase equilibria does not consider a nitrogen rich SiO_2 liquid phase which will reduce the boundary temperature between solid and liquid SiO_2 from around 2000 K to 1750 K (see the phase equilibria in Fig. 7.12(b).*

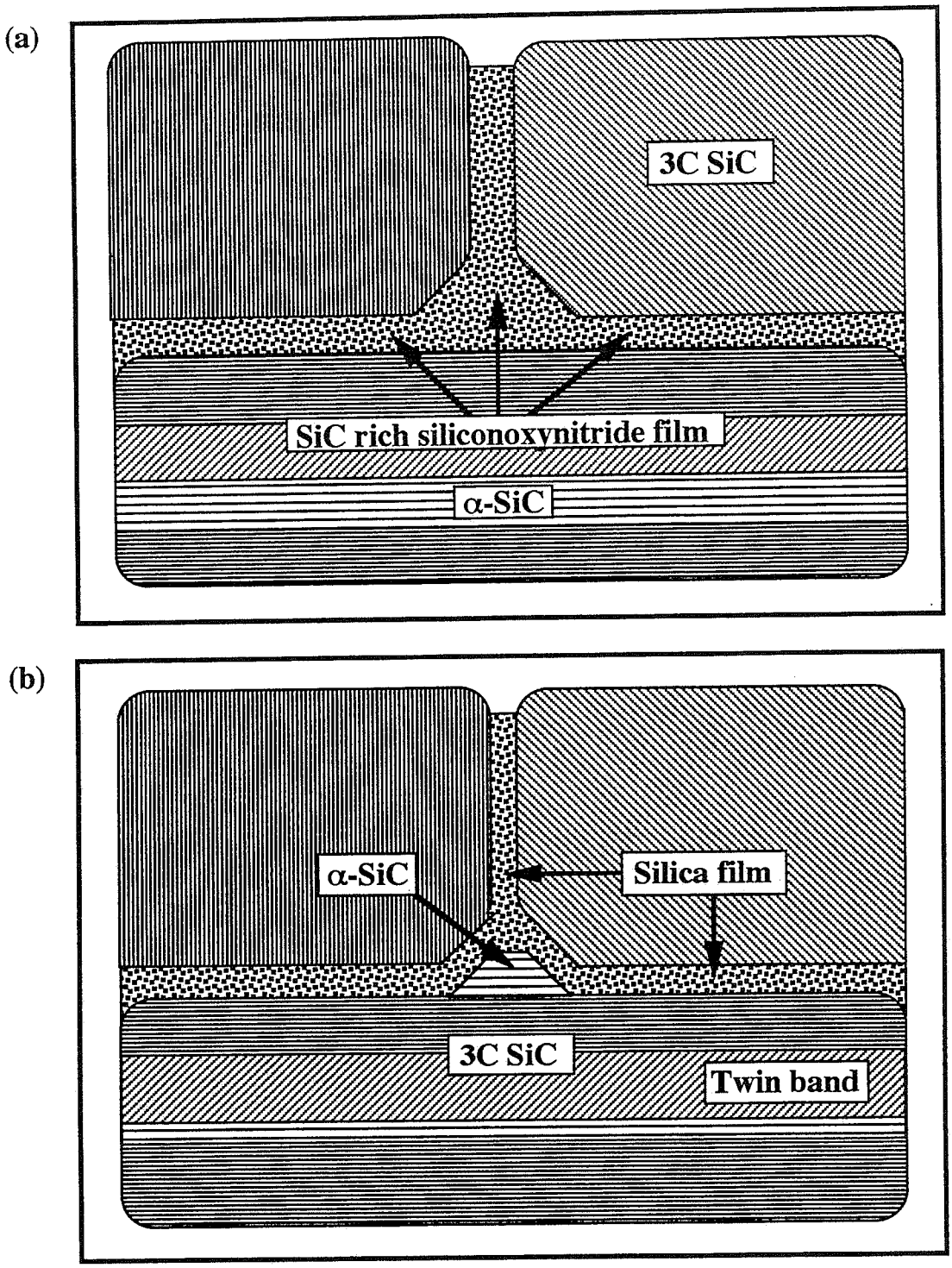

Fig. 7.13 Schematic view of liquid phase transformation mechanism for $\alpha \rightarrow \beta$ SiC reverse transformation; (a) at fabrication temperature of 2100°C just before cooling started and (b) at room temperature or after a temperature where last liquid become solid.

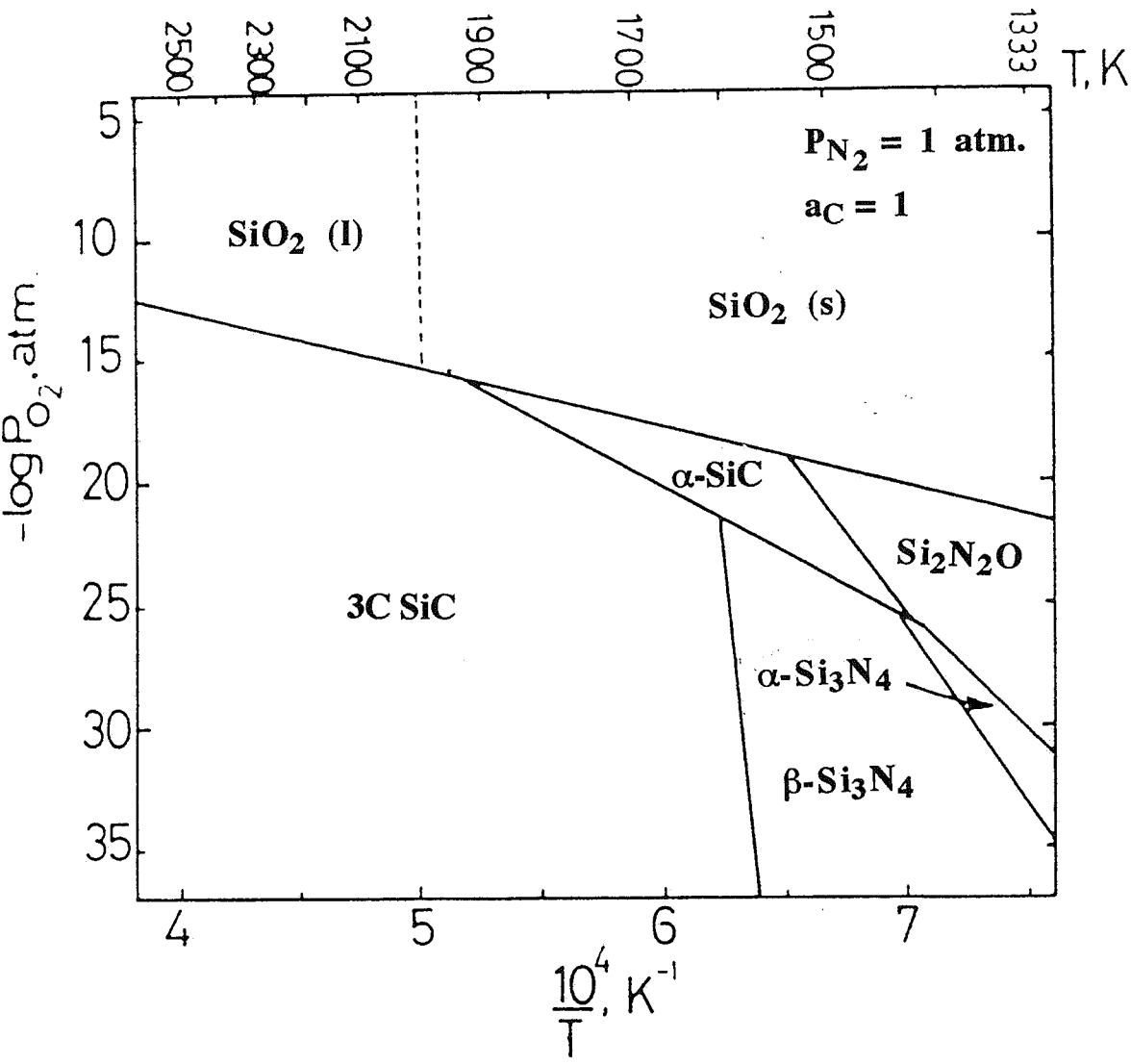

Fig. 7.14 Recalculated Si-C-O-N phase equilibria (after Jha, 1993).

7.6 Conclusions

X-ray diffraction and transmission electron microscope techniques have been used to investigate the stable phases in a monolithic SiC, a 16 wt% TiB_2 reinforced SiC composite, a layered SiC composite and a range of SiC-Si_3N_4 composites fabricated from as-received powders and from deoxidised compacts.

X-ray diffraction and transmission electron microscope analysis enabled the identification of an unexpected near-complete phase transformation of α-SiC into β-SiC in composites prepared from as-received powders, while α-SiC remained untransformed in the composites prepared from deoxidised material.

The existence of intergranular phases in composites prepared from as-received powders and the relative absence of such films in composites prepared from deoxidised powder compacts indicates that the α → β reverse SiC transformation is encouraged by the presence of a liquid phase during consolidation.

Si_3N_4 is also necessary to encourage the α → β reverse transformation since Dutta (1988) did not report any transformation when he hot isostatically pressed α-SiC powder alone at the same conditions as Si_3N_4-SiC composites. It is suggested that the role of Si_3N_4 is to dissociate to nitrogen and liquid silicon during the process of heating up to hot isostatic pressing conditions, and thereby lowering the temperature of liquid formation and increasing the amount of liquid. The existence of nitrogen in the liquid may also decrease the activation energy necessary for the reverse transformation.

The observation of h-BN inclusions next to 6H SiC grains is not consistent with the proposal by Ruh and coworkers that BN stabilises 3C SiC. Their experimental observations can be explained in terms of the mechanism proposed by Shinozaki *et al.* (1988) that the 3C regions near interfaces are remnants of starting powder. The observations in monolithic SiC, TiB_2 reinforced SiC composite and layered SiC composite in this study show that 3C regions will exist whether BN is present or not. Similar comments apply to the observations by Duval-Riviere and Vicens (1994) that 3C triple junctions were a remnant of starting powder rather than a transformation product from 4H to 3C SiC as they proposed.

The triple junction phase was a mixture of α-SiC in the composites made from as-received powders rather than the usual observation in SiC based materials that it is always 3C SiC. It is believed that the triple junction phase forms during cooling period which favours the formation of α-polytype, possibly because of the depletion of nitrogen from the liquid phase at a lower temperature.

In summary, when taken together with the observations by Jepps and Page (1981), Dutta (1988) and the observations reported throughout this study the α → β reverse transformation in the composites made from the as-received powders, but not from the deoxidised material, indicate that the factors favouring the α → β reverse transformation are:

(i) high temperature,

(ii) high externally applied pressure,

(iii) a nitrogen atmosphere (supplied in this work by the decomposition of Si_3N_4),

(iv) a liquid medium present in sufficient quantity.

Chapter 8

Conclusions and Suggestions for Future Work

8.1 Summary and conclusions

Microstructural characterisation of hot isostatically pressed SiC matrix composites with either 10 or 20 wt% Si_3N_4 reinforcement has been undertaken in this study. The composites were hot isostatically pressed in tantalum cans at 2100°C for one hour under a pressure of 200 MPa. The aim of the research was to obtain an understanding of how the composite microstructure evolved during processing where one batch was processed from as-received powders and the other had been processed from powder compacts which had been deoxidised to eliminate surface silica on the powder particles.

First of all, the densities of the composites were measured using the Archimedes method. The density measurements showed that full theoretical density was achieved for the composites prepared from the as-received powders, while much lower densities were obtained for the composites prepared from the deoxidised material.

X-ray diffraction (XRD) and mainly transmission electron microscope (TEM) techniques have been used to investigate the microstructure of these Si_3N_4-SiC composites.

The first, and most striking, finding revealed by XRD and TEM analysis was that the α-SiC starting powder had almost completely, but unexpectedly, transformed to 3C SiC cubic polytype in the composites made from as-received powders, while α-SiC remained untransformed in the composites made from deoxidised green compacts. Although it has been suspected by several researchers (Jepps and Page, 1983, Coppi and Richarz, 1986 & Pezzotti *et al.*, 1994) that surface silica and/or liquid phases could effect the existence and rate of reverse transformations, this is believed to be the first time that it has shown experimentally that the α → β SiC reverse transformation has taken place because of the existence of a liquid phase. It can be further concluded that the reverse transformation actually proceeds through a silicon oxynitride liquid since the reverse transformation does not take place when either liquid phase or nitrogen is absent or when nitrogen is replaced by an argon atmosphere.

Crystalline triple junction phases were found and identified as α-SiC polytypes which were epitaxially attached to 3C SiC main grains with an orientation relationship of:

$$[110]_{3C\ SiC} \parallel [11\bar{2}0]_{\alpha\text{-}SiC} \text{ and } (1\bar{1}\bar{1})_{3C\ SiC} \parallel (0001)_{\alpha\text{-}SiC}$$

These observations are in contrast to all the observations reported in the literature where 3C triple junction phases are found to be attached to α-SiC main grains with this same orientation relationship. Although in the literature these 3C triple junction phases were the remnants of the α → β-SiC transformation (Shinozaki and coworkers), the α-SiC triple junction phases identified in this work are proposed to arise from the change in sintering conditions towards the end of the densification process favouring the formation of α-SiC instead of 3C.

An incomplete transformation of α-Si_3N_4 into β-Si_3N_4 was found in the deoxidised compacts, but this transformation went to near completion in the composites made from as-received powders.

Conventional and high resolution transmission electron microscopy observations showed the existence of submicron size graphite-like inclusions at interfaces, and inside SiC and Si_3N_4 grains. Similar inclusions in SiC and Si_3N_4 ceramics in the literature have been observed and identified as graphite. However, in this study the graphite-like inclusions present in hot isostatically pressed Si_3N_4–SiC composites were found by PEELS analysis to be h-BN instead. It is possible that some of the inclusions identified as graphite in the literature could be h-BN. This ambiguity in the identification arises because of the close structural relationship between h-BN and graphite. Therefore, a reliable identification cannot be made unless the diffraction and HREM observations are confirmed with PEELS analysis.

PEELS analysis on these inclusions showed that the intensity of π^* and σ^* peaks were largely dependent on how the *c*-axis of h-BN was aligned with respect to the electron beam. Their intensities can also be altered using different experimental parameters, such as a different scattering angle.

Considerations of the possible ways in which these inclusions can form in the composites suggested that they are formed from B_2O_3 present as a thin surface film on the BN particles sprayed onto the surface of the tantalum cans prior to hot isostatic pressing. B_2O_3 is able to evaporate and penetrate the powder compacts during hot isostatic pressing and then react with Si_3N_4 and SiC to form the observed inclusions.

HREM observations on these inclusions have also shown that very small conjugate kink and twin bands are formed to accommodate large thermal stresses created by the difference in the thermal expansion coefficients of h-BN and matrix grains. Since the thermal expansion coefficient of h-BN in the direction perpendicular to *c*-axis is smaller than SiC and Si_3N_4, surrounding SiC or Si_3N_4 grains will contract more than h-BN when the system is cooled down from high temperature and put the disc-like BN inclusions under compressive stress from both ends. This together with weak binding forces in the *c*-axis direction resulted in microcracks and kinking and/or twinning inside h-BN inclusions. The observations of crack and dislocation-free inclusions in porous samples (deoxidised samples) support the above argument. In the latter case, the stresses set up during cooling are released through porosity. The large strain also resulted in lattice rotations of a few degrees in BN inclusions.

Transmission electron microscopy techniques namely HREM, diffuse dark field and Fresnel defocus imaging have been tested on a single grain boundary to asses their capability at showing the presence of intergranular films at interfaces and the accuracy of measuring their thickness. It is shown that HREM is the most accurate for showing the existence of intergranular films and the determination of film thickness. Diffuse dark field coupled Fresnel imaging technique can be used reliably to show the presence or absence of the films and to measure their thickness when the HREM technique is not available.

The TEM techniques mentioned above were used to identify the grain boundary and interphase boundary structure. Most interfaces in the composites prepared from as-received powders were found to be wetted by ≈ 10 Å wide intergranular films, with the exception of twin boundaries and what could be inferred to be special low energy interfaces. By contrast, most interfaces in the deoxidised material were free of such intergranular films.

Occasionally, intergranular films were observed at interfaces in the composites made from the deoxidised powder compacts, but the thickness of the films were much lower than those in the composites prepared from as-received powders. This suggests that the volume of liquid phases present in the material during consolidation at high temperature has a noticeable effect on the relative magnitude of the equilibrium film thickness, in contrast to a previous study by Greil and Weiss (1983) who concluded that volume of liquid phase does not effect the equilibrium film thickness using an unreliable technique (*i.e.*, diffuse dark field).

Clarke's theory on the equilibrium film thickness at interfaces has been discussed and used to explain the experimental results obtained throughout this study and others in the literature. Clarke (1987) has proposed (in his well accepted and largely used theory) that:

(i) the amorphous intergranular films at the interfaces have an equilibrium thickness arising as a result of competition between attractive van der Waals forces and repulsive steric forces.

(ii) the thickness does not depend on the misorientation across the interface, but depends on the dielectric properties of adjacent grains and the film.

In this study by accepting that the first proposition is valid, it is theoretically and experimentally shown that misorientation will effect the film thickness and, unlike in Clarke's work, it is also established that the refractive indices are more effective than dielectric constants whose effects can be ignored on the theoretical film thickness calculations.

Clarke also proposed that SiC grain boundaries should not contain any intergranular films, on the basis that SiC has very high refractive index. His theory is supported by the published data in the literature (*e.g.*, Carpenter *et al.*, 1991) that indeed these interfaces are free of such films. My experiments have shown otherwise: intergranular films do exist at SiC-SiC interfaces. An obvious explanation to support the observation for the presence or absence of these films at these interfaces is that a possible liquid phase in pressureless sintered SiC ceramics (on which most literature work has been based) had been removed from the system prior to TEM analysis of interfaces.

Some interfaces between SiC grains were free of intergranular films. These were either low angle boundaries and twin boundaries or coherent interphase boundaries between α-SiC and β-SiC grains. The other interesting observation at such interfaces was that when the angle between (111) planes of adjacent SiC grains at the interface was smaller than 20°, the interface was faceted despite the existence of an intergranular film.

A similar trend was observed between Si_3N_4 grains, in that special interfaces (low angle and twin (Σ=9) boundaries) were free of such films, while non-special high angle boundaries were wetted with intergranular films.

Interphase boundaries between SiC and Si_3N_4 grains were two kinds, because Si_3N_4 was found to be in two different forms: *(i)* grains of a similar size to SiC matrix grains and *(ii)* precipitates of a smaller size inside 3C SiC grains.

Most of the SiC-Si_3N_4 interphase boundaries between the 3C SiC grains and intragranular Si_3N_4 precipitates were found to be curved, with readily observable moiré fringes. It is of course very difficult to specify unambiguously whether or not there are any intergranular films at such interphase boundaries. Occasionally, however, flat interfaces between hexagonally shaped Si_3N_4 intragranular grains and SiC matrix were observed, some of which were wetted with a $\approx$ 10 Å thick intergranular film. In addition, some of the interfaces on the SiC side of these interphase boundaries were faceted.

HREM and Fresnel defocus imaging showed that the vast majority of interphase boundaries between the large SiC and Si_3N_4 grains were clearly covered with thin intergranular films, ambiguity arising where the interfaces were curved. Interestingly, the film thicknesses at these interphase boundaries were not constant, in contrast to expectations based on recent experimental and theoretical work of others in this area.

The orientation relationships found across the interphase boundaries between these Si_3N_4 precipitates and the 3C SiC grains were non-random, in the sense that there were planes in the two phases parallel or nearly parallel to one another. This was in contrast to the orientation relationships seen across interphase boundaries between large 3C or α-SiC grains

and adjacent Si_3N_4 grains of a similar size which appeared to be random. The most common orientation relationship between Si_3N_4 precipitates and SiC grains was:

$$[110]_{3C\ SiC} \parallel [0001]_{\beta\text{-}Si_3N_4} \text{ and } (002)_{3C\ SiC} \parallel (10\bar{1}0)_{\beta\text{-}Si_3N_4}$$

Most of the interphase boundaries between the grains of SiC and BN were covered with intergranular films despite the fact that (111) 3C SiC or (0001) α-SiC planes were generally parallel to (0001) h-BN planes. The most prominent orientation relationship observed was:

$$[110]_{3C\ SiC} \parallel [11\bar{2}0]_{h\text{-}BN} \text{ and } (1\bar{1}\bar{1})_{3C\ SiC} \parallel (0001)_{h\text{-}BN}$$

$$[11\bar{2}0]_{\alpha\text{-}SiC} \parallel [11\bar{2}0]_{h\text{-}BN} \text{ and } (0001)_{\alpha\text{-}SiC} \parallel (0001)_{h\text{-}BN}$$

It is believed (Ruh and coworkers) that h-BN stabilises 3C SiC. This conclusion has been reached through TEM observations that whenever h-BN grains are found next to SiC grains, the immediate region of SiC is in 3C form and the rest of the grain consists of other polytypes. In my work, h-BN grains were mostly found next to 3C grains, apparently supporting the belief of Ruh and coworkers, but in my work 3C arises due to the reverse transformation assisted by silicon oxynitride liquid. Interestingly, on quite a few occasions h-BN grains were found next to a few layers of α-SiC, with the remaining part of adjacent grains 3C. Therefore, it cannot be concluded from my work that h-BN stabilises one polytype in preference to another polytype.

It has also been shown that interphase boundaries between h-BN and Si_3N_4 were free of intergranular films, in contrast to interphase boundaries between h-BN and SiC. (100) Si_3N_4 planes were mostly parallel to (0001) h-BN planes across these interfaces.

Finally, the existence of intergranular phases in composites prepared from as-received powders and the relative absence of such films in composites prepared from deoxidised powder compacts, coupled with the much lower densification rates for composites prepared from deoxidised powders, both suggest strongly that densification took place efficiently in the composites made from as-received powders because of liquid phase sintering.

8.2 Future work

In this dissertation, it has been shown from both a theoretical and an experimental analysis that the thickness of an intergranular film is effected by the relative misorientation of the crystalline phases either side of the film if at least one of the crystals adjacent to the film is anisotropic. In this context, the determination of thickness of intergranular films as a function of misorientation across the interface is important to confirm further the results obtained in Chapter 5. For example, the thicknesses of films can be measured between h-BN grains in liquid phase sintered h-BN ceramics. Further studies about the effect of liquid volume content on the equilibrium film thickness using HREM technique are also necessary.

The dielectric properties of Y_2O_3, Yb_2O_3, $Y_2Si_2O_7$ and $Yb_2Si_2O_7$ should be determined accurately for Hamaker constant calculations in the context of the general statement that interphase boundaries contain thicker intergranular films than grain boundaries.

Although most of the results in the literature (*e.g.*, Dutta, 1988) indicate that α-SiC does not transform to β-SiC when a liquid silica phase is present, but nitrogen is absent, it would be a final confirmation that surface silica alone does not effect the α → β SiC reverse transformation if as-received α-SiC powder is hot isostatically pressed under the same conditions used in this study.

One of the problems that could not be tackled due to the experimental limitations was the characterisation of $\Sigma = 8$ twin boundaries in h-BN by HREM, such as the one shown in Fig. 4.17. The structure imaging of such interfaces is now feasible after the advent of 1 Å point-to-point resolution microscopes (Phillipp *et al.*, 1994) and so it would obviously be of interest to do this.

BN particulate composites with either an oxide or a non-oxide matrix are potentially attractive materials because of the increased thermal shock resistance that arises relative to the unreinforced matrix. In addition, because of the crack deflection ability and disc-like shape of h-BN grains, the fracture toughness of a matrix material should be increased. Such composites have been produced by other workers with the addition of h-BN powders,

but the resulting composite microstructures have been associated with high porosity. An alternative method for producing such composites would be to nitride B_2O_3 in-situ through a vapour reduction process.

The other recent development in ceramics that has attracted a large interest is that of "nanocomposite materials" developed originally by Prof. K. Niihara in Japan. Becasue they are easy and cheap to produce and are said to have higher fracture toughness and higher yield strenght than monolithic ceramics, it would be worthwhile exploring the possibilities of producing nanocomposites containing disc-like h-BN with SiC and/or Si_3N_4.

In the light of this study, it is proposed that the following processing procedure could be usefully examined with the aim of obtaining dense SiC or Si_3N_4 materials with a desired microstructure:

(i) eliminate large grains prior to fabrication by sedimentation – to increase densification rate (Hermansson *et al.*, 1986)

(ii) use sintering aids of B_2O_3, Y_2O_3 and Al_2O_3 – to lower the sintering temperature significantly (Mulla and Krstic, 1991). In a nitrogen atmosphere, B_2O_3 can be converted to BN and will not effect the high temperature properties of the liquid film.

(iii) use a nitrogen or an argon atmosphere to assist SiC phase transformations ($\alpha \rightarrow \beta$ or $\beta \rightarrow \alpha$, respectively) for the desired end structure.

(iv) if a nitrogen atmosphere is used it should result in the formation of nano-size β-Si_3N_4 precipitates which could be beneficial to strength (Niihara *et al.*, 1991).

The conditions in *(ii)* and *(iii)* would help producing plate-like grains and increase the fracture toughness.

REFERENCES

Acheson, A.G. (1892) G.B Patent 17911.

Ahn, C.C. and Krivanek, O.L. (1983)*A Reference Guide of Electron Energy Loss Spectra Covering All Stable Elements* EELS Atlas, A joint project of the ASU HREM facility and Gatan, USA.

Alexander, K.B., Angelini, P. and Becher, P.F. (1990) Electron microscopy of interfaces in SiC whisker reinforced alumina composites. *Mat. Res. Soc. Symp. Proc.*, **183**, 273-79.

Allard, L.F., Nolan, T.A. and Rawlins, M.H. (1989) Structure of a grain boundary phase in a monolithic silicon carbide ceramic. *Am. Cer. Soc. Bull.*, **68**, 1450.

Alliegro, R., Coffin, L.B. and Tinkepaugh, J.R. (1956) Pressure-sintered silicon carbide. *J. Amer. Cer. Soc.*, **39**, 386-89.

Babcock, C.L. (1977) *Silicate Glass Technology Methods*. John Wiley.

Bansal, N.P. and Doremus, R.H. (1986) *Handbook of Glass Properties*. Academic Press, London.

Baronnet, A. (1981) Some aspects of polytypism in crystals. *Prog. Crystal Growth Charact.*, **178**, 151-211.

Baronnet, A. and Olives, J. (1983) The geometry of micas around kink band boundaries: I. A crystallographic model. *Tectonophysics*, **91**, 359-73.

Billington, S.R., Chown, J. and White, A.E.S. (1963) The sintering of silicon carbide. *In Special Ceramics 2*, Ed: P. Popper. p19-34.

Birnie, D.P. III. (1986) A model for silicon self diffusion in silicon carbide: anti-site defect motion. *J. Amer. Cer. Soc.*, **69**, C33.

Bloss, F. D. (1971) *Crystallography and Crystal Chemistry*. Holt, Rinehart and Winston, Inc., New York.

Blumenthal, W. and Evans, A.G. (1984) High-temperature failure of polycrystalline alumina: II. Creep crack growth and blunting. *J. Am. Cer. Soc.*, **67**, 751-59.

Bocker, W., Landfermann, R.H. and Hausner, H. (1979) Sintering of alpha SiC with additions of aluminium. *Powd. Met. Intl.*, **11**, 83-85.

Bollmann, W. (1967) On the geometry of grain and phase boundaries: I. General Theory. *Phil. Mag.*, **16**, 363-81.

Bollmann, W. (1967a) On the geometry of grain and phase boundaries: II. Applications of general theory. *Phil. Mag.*, **16**, 383-99.

Bollmann, W. (1970) *Crystal Defects and Crystalline Interfaces*. Springer, Berlin.

Bonnet, R., Cousineau, E. and Warrington, D.H. (1981) Determination of near-coincident cells for hexagonal crystals, related DSC lattices. *Acta Crystallogr.*, **A37**, 184-89.

Boothroyd, C. B. and Stobbs, W. M. (1984) Fresnel effects at grain boundary dislocations. *Phil. Mag.*, **A49** (1), L5-L8.

Bootsma, G.A., Knippenberg, W.F. and Verspui, G. (1971) Phase transformations, habit changes and crystal growth in SiC. *J. Cryst. Growth*, **8**, 341-53.

Braue, W., Göring, J. and Ziegler, G. (1989) Correlation of subcritical crack growth and microstructure in HIP-SiC. *In Proceedings of the 3rd International Symposium on Ceramic Materials for Components and Engines*. Ed: V.J. Tennery. American Ceramic Society, Westerville, OH. p817-30.

Braue, W. (1992) Interfacial boundaries in Si_3N_4-based ceramic composites: Constraints from matrix effects and stability of microstructure. *J. Euro. Cer. Soc.*, **10**, 175-93.

Braue, W. and Carpenter, R.W. (1990) Analytical electron microscopy of graphite-rich inclusions in sintered α-SiC. *J. Mat. Sci.*, **25**, 2943-48.

Bruggeman, G.A., Bishop, G.H. and Hartt, W.H. (1972) *The Nature and Behaviour of Grain Boundaries*, Ed: H. Hu. Plenum Press, New York. p83-122.

Budd, P.M. and Goodhew, P.J. (1988) *Light-Element Analysis in the Transmission Electron Microscopy: WEDX and EELS*. Oxford Science Publications.

Buljan, S.T., Baldoni, J.G. and Huckabee, M.L. (1987) Si_3N_4-SiC composites. *Am. Cer. Soc. Bull.*, **66**, 347-52.

Bundy, F.P. and Wentorf, R.H. (1963) Direct transformation of hexagonal boron nitride to denser forms. *J. Chem. Phys.*, **38**, 1144-49.

Buseck, P.R., Cowley, J.M. and Eyring, L. (1992) *High-Resolution Transmission Electron Microscopy and Associated Techniques*. Oxford University Press, Oxford.

Cahn, J.W. and Kalonji G. (1982) Symmetry in solid state transformation morphologies. *Proceedings of International Conference on Solid → Solid Phase Transformations*, Eds: H.I. Arranson, D.E. Laughlin, R.F. Sekerka and C.M. Wayman. p3-14.

Carpenter, R.W. (1988) High resolution interface analysis. *Mat. Sci. and Eng.*, **A107**, 207-16.

Carpenter, R.W., Braue, W. and Cutler, R.A. (1991) Transmission electron microscopy of liquid phase densified SiC. *J. Mat. Res.*, **6**, 1937-44.

Carter, N.L., Christie, J.M. and Griggs, D.T. (1964) *J. Geol.*, **72**, 687-733.

Carter, C.B., Elgat, Z. and Shaw, T.M. (1987) Lateral twin boundaries. *Phil. Mag.*, **A55**, 21-38.

Carter, W.D. Holloway, P.H., White, C. and Clausing, R. (1988) Boron distribution in sintered silicon carbide. *Adv. Cer. Mat.*, **3**, 62-65.

Christian, J.W. (1975) *The Theory of Transformations in Metals and Alloys*, 2nd Edition. Pergamon Press, Oxford.

Cinibulk, M.K., Kleebe, H.-J. and Rühle, M. (1993) Quantitative comparison of TEM techniques for determining amorphous intergranular film thickness. *J. Am. Cer. Soc.*, **76**, 426-32.

Cinibulk, M.K., Kleebe, H.-J., Schneider, G.A. and Rühle, M. (1993a) Amorphous intergranular films in silicon nitride ceramics quenched from high temperatures. *J. Am. Cer. Soc.*, **76**, 2801-08.

Cinibulk, M.K. and Kleebe, H.-J. (1993) Effects of oxidation on intergranular phases in silicon nitride ceramics. *J. Mat. Sci.*, **28**, 5775-82.

Clarke, D.R. (1979) On the detection of thin intergranular films by electron microscopy. *Ultramicroscopy*, **4**, 33-44.

Clarke, D.R. (1979a) High resolution techniques and application to nonoxide ceramics. *J. Am. Cer. Soc.*, **62**, 236-46.

Clarke, D.R. (1982) Characterization of grain boundaries in electronic ceramics by TEM. *Grain Boundaries in Semiconductors*, Eds: H.J Leamy, G.E. Pike, C.H. Seager. Elsevier Science Publishing. p3-12.

Clarke, D.R. (1985) Grain boundaries in polyphase ceramics. *J. de Phys. Colloque C4*, **46**, 51-59.

Clarke, D.R. (1987) On the equilibrium thickness of intergranular glass phases in ceramic materials. *J. Am. Cer. Soc.* **70**, 15-22.

Clarke, D.R. (1987a) Grain boundaries in polycrystalline ceramics. *Ann. Rev. Mat. Sci.*, **17**, 57-74.

Clarke, D.R. (1989) High-temperature microstructure of a hot-pressed silicon nitride. *J. Am. Cer. Soc.*, **72**, 1604-09.

Clarke, D.R. (1990) Perspectives concerning grain boundaries in ceramics. *Am. Cer. Soc. Bull.*, **69**, 682-85.

Clarke, D.R. (1991) Glassy phases in ceramics. *Concise Encyclopedia of Advanced Ceramic Materials*, Ed: R.J. Brook. Pergamon Press, Oxford. p183-87.

Clarke, D.R. and Thomas, G. (1977) Grain boundary phases in a hot-pressed MgO fluxed silicon nitride. *J. Am. Cer. Soc.*, **60**, 491-95.

Clarke, D.R. and Thomas, G. (1978) Microstructure of Y_2O_3 fluxed hot-pressed silicon nitride. *J. Am. Cer. Soc.*, **61**, 114-19.

Clarke, D.R., Zaluzec, N.J. and Carpenter, R.W. (1981) The intergranular phase in hot-pressed silicon nitride: I. Elemental Composition. *J. Am. Cer. Soc.* **64**, 601-07.

Clarke, D.R. and Gee, M.L. (1992) Wetting of surfaces and grain boundaries. *In Materials Interfaces*, Eds: D. Wolf and S. Yip. Chapman and Hall, London. p255-72.

Clarke, D.R., Shaw, T.M., Philipse, A.P. and Horn, R.G. (1993) Possible electrical double-layer contribution to the equilibrium thickness of intergranular glass films in polycrystalline ceramics. *J. Am. Cer. Soc.* **76**, 1201-04.

Clegg, W.J., Kendall, K., Alford, N.McN., Button, T.W. and Birchall, J.D. (1990) A simple way to make tough ceramics. *Nature*, **347**, 455-57.

Cobbold, P.R., Cosgrove, J.W. and Summers, J.M. (1971) Development of internal structures in deformed anisotropic rocks. *Tectonophysics*, **12**, 223-53.

Coblenz, W.S. and Lewis, D. (1988) In situ reaction of B_2O_3 with AlN and/or Si_3N_4 to form BN-toughened composites. *J. Am. Cer. Soc.*, **71**, 1080-85.

Colliex, C., Manoubi, T., Gasnier, M. and Brown, L.M. (1985) Near edge fine structures on electron energy loss spectroscopy core loss edges. *Scan. Elec. Mic. II*, 489-512.

Coppi, P.A.K. and Richarz, W. (1986) Phase transformation and grain growth in silicon carbide powders. *Int. J. High Tech. Cer.*, **2**, 99-103.

Crocker, A.G. and Abell, J.S. (1976) The crystallography of deformation kinking. *Phil. Mag.*, **33**, 305-10.

Cullen, S.L., Botton , G., Kirkland, A.I., Brown, P.D. and Humphreys, C.J. (1993) *Inst. Phys. Conf. Ser.* **138**, 79-82.

Cutler, R.A. and Jackson, T.B. (1989) Liquid phase sintered SiC. *Ceramic Materials and Components for Engines*. Proc. of the Third Intl. Sym. Ed: V.J. Tennery. Am. Cer. Soc, Westerwille, OH. p309-18.

Das Chowdhury, K.D., Carpenter, R.W. and Kim, M.J. (1992) Analysis of interfaces by the Fresnel fringe technique. *EMSA Bulletin* , **22**, 61-66.

Davidge R.W., Sleurs, J. and Buekenhout, L. (1988) Hipping of technical ceramics: A synopsis. *Proc. Int. Conf. on Hot Isostatic Pressing of Materials: Applications and Developments*. Organised by The Royal Flemish Society of Engineers. Antwerp, Belgium. p 5.1-5.13.

Davis, R.F., Carter, Jr., C.H., Nutt, S.R., More, K.L. and Chevacharoenkul, S. (1987) Structure and chemistry of interfaces in SiC-containing materials. p897-909. *Proceedings of the 22nd University Conference on Ceramics at the University of California*, Berkeley.

Davis, R.F., Lane, J.E., Carter, Jr., C.H., Bentley, J., Wadlin, W. H., Griffis, D.P., Linton, R.W. and More, K.L. (1984) Microanalytical and microstructural analyses of B and Al regions in sintered α-SiC. *Scanning Electron Microscopy III*, 1161-67.

Derjaguin, B.V. and Churaev, N.V. (1974) Structural component of disjoining pressure. *J. Colloid Interface Sci.*, **49**, 249-55.

Derjaguin, B.V., Rabinovich, Y.I. and Churaev, N.V. (1978) *Nature*, **272**, 313-18.

Dieter, G.E. (1986) *Mechanical Metallurgy*, 3rd edition. McGraw Hill.

Disko, M.M., Krivanek, O.L. and Rez, P. (1982) Orientation-dependent extended fine structure in electron-energy-loss spectra. *Phys. Rev.*, **B25**, 4252-55.

Doyle, P.A. and Turner, P.S. (1968) Relativistic Hartree-Fock X-ray and electron scattering factors. *Acta. Cryst.*, **A24**, 390-97.

Duffy, D.M. and Tasker, P.W. (1986) A dislocation model for the structure of [001] twist boundaries in ionic oxides. *Phil. Mag.*, **A53**, 113-22.

Dutta, S. (1988) High strength silicon carbides by hot isostatic pressing. *3rd International Symposium on Ceramic Materials and Components for Engines*, Las Vegas. p683-95.

Dutta, S. (1988a) Improved processing of α-SiC. *Adv. Cer. Mat.*, **3**, 257-62.

Duval-Riviere, M.L. and Vicens, J. (1994) Polytypic transformation and gliding behaviour in polycrystalline α-SiC deformed by compression at high temperatures. *Phil. Mag.*, **A69**, 451-70.

Dzyaloshinskii, I.E., Lifshitz, E.M. and Pitaevskii, L.P. (1961) The general theory of van der Waals forces. *Adv. Phys.*, **10**, 165-209.

Egerton, R.F., (1986) *Electron Energy-Loss Spectroscopy in the Electron Microscope*. Plenum Press, New York, USA

Ergun, S. (1968) Optical studies of carbon. *Chemistry and Physics of Carbon*, Ed: P. L. Walker, Vol:3, p45-119, Edward Arnold LTD, London.

Evans, A.G. and Adler, W.F. (1978) Kinking as a mode of structural degredation in carbon fiber composites. *Acta Metallurgica*, **26**, 725-38.

Finnis, M.W. and Rühle, M. (1993) Structures of interfaces in crystalline solids. *In Materials Science and Technology: A comprehensive treatment*, Eds: R.W. Cahn, P. Haasen, E.J. Kramer. Volume 1: *Structure of Solids*, p533-605. Vol. Ed: V. Gerold. VCH Publishers Inc., New York.

Forwood, C.T. and Clarebrough, L.M. (1991) *Electron Microscopy of Interfaces in Metals and Alloys*. Institute of Physics Publishing, Bristol and Philadelphia.

Frank, F.C. and Stroh, A.N. (1952) On the theory of kinking. *Proc. Phys. Soc.*, **B65**, 811-21.

Franklin, R.E. (1951) The structure of graphitic carbons. *Acta Cryst.* **4**, 253-61.

Freise, E.J. and Kelly, A. (1963) The deformation of graphite crystals and the production of the rhombohedral form. *Phil. Mag.*, **8**, 1519-33.

Freise, E.J. and Kelly, A. (1963) Twinning in graphite. *Proc. Roy. Soc.*, **A264**, 269-76.

Frevel, L.K., Peterson, D.R. and Saha, C.K. (1992). Polytype distribution in SiC. *J. Mat. Sci.*, **27**, 1913-25.

Gazzara, C.P. and Messier, D.R. (1977) Determination of phase content of Si_3N_4 by X-ray diffraction analysis. *Am. Cer. Soc. Bull.*, **56**, 777-80.

German, R.L. (1985) *Liquid phase sintering*. Plenum press, New York and London.

Goeuriot-Launay, D., Brayet, G. and Thevenot, F. (1986) Boron nitride effect on the thermal shock resistance of an alumina-based ceramic composite. *J. Mat. Sci. Let.*, **5**, 940-42.

Gourbilleau, F. and Nouet, G. (1993) Analysis of SiC-SiO_2 interfaces by TEM. *Mat. Sci. For.*, **126-128**, 599-602.

Goux, C. (1961) Bull. cercle etudes Metaux, **8**, 185. in Randle, V. and Ralph, B. (1986) A practical approach to the determination of th ecrystallography of grain boundaries. *J. Mat. Sci.*, **21**, 3823-28.

Greenwood, N.N. (1973) *The Chemistry of Boron*; pp. 916-919. Pergamon Press, Oxford, U.K.

Greil, P. and Weiss, J. (1982) Evaluation of the microstructure of β-SiAlON solid solution materials containing different amounts of amorphous grain boundary phase. *J. Mat. Sci.*, **17**, 1571-78.

Greskovich, C. and Prochazka, S. (1987) Selected sintering conditions for SiC and Si_3N_4. *In Ceramic Microstuctures '86: Role of Interfaces*, Eds: J.A. Pask and A.G.Evans. Plenum Press, Newyork. p601-10.

Greskovich, C. and Rosolowski, J.H. (1976) Sintering of covalent solids. *J. Am. Cer. Soc.*, **59**, 336-43.

Guo, J.K. and Ma, L.T. (1991) ZrO_2 transformation and interface characteristics in ZrO_2 matrix composites. *In Advanced Structural Materials*, Ed: Y. Han. Elsevier Science Publishers, Amsterdam. p343-51

Hagio, T., Kobayashi, K., Yoshida, H., Yasunaga, H. and Nishikawa, H (1989) Sintering of the mechanochemically activated powders of hexagonal boron nitride microstructure of pressureless sintered h-BN. *J. Am. Cer. Soc.*, **72**, 1482-84.

Hall, E.L. (1992) Analytical electron microscopy. *In Materials Science and Technology: A comprehensive treatment*, Eds: R.W. Cahn, P. Haasen, E.J. Kramer. Volume 2A: *Characterisation of materials: Part I.* Vol. Ed: E. Lifshin. VCH Publishers Inc., New York. p147-219.

Hamaker, H.C. (1937) The London-van der Waals attraction between spherical particles, *Physica*, **4**, 1058-72.

Hamminger, R., Grathwohl, G. and Thummler, F. (1983) Microanalytical investigation of sintered SiC (Part 2). Study of the grain boundaries of sintered SiC by HRAES. *J. Mat. Sci.*, **18**, 3154-60.

Hamminger, R. (1989) Carbon inclusions in sintered silicon carbide. *J. Am. Cer. Soc.*, **72**, 1741-44.

Hampshire, S.(1994) Nitride ceramics. *In Materials Science and Technology: A comprehensive treatment*, Eds: R.W. Cahn, P. Haasen and E.J. Kramer. Vol 11: *Structure and properties of ceramics*. Vol. Ed. M.V. Swain. VCH Publishers Inc., New York. p119-73.

Hampshire, S. and Jack, K.H. (1981) In Special Ceramics **7**, Ed: P. Popper. British Ceramic Research Association. p37-49.

Hansen, S.C. and Philips, D.S. (1983) Grain boundary microstructure in a liquid phase sintered alumina. *Phil. Mag.*, **A47**, 209-34.

Hardie, D and Jack, K.H. (1957) Crystal structure of silicon nitride. *Nature*, **180**, 332-33.

Heine, V., Cheng, C. and Needs, R.J. (1991) The preference of silicon carbide for growth in the metastable cubic form. *J. Am. Cer. Soc.*, **74**, 2630-33.

Hench, L.L. and West, J.K. (1990) *Principles of Electronic Ceramics*. John Wiley.

Henderson, C.M.B. and Taylor, D. (1975) Thermal expansion of nitrides and oxynitride of silicon in relation to their structures. *Trans. J. Brit. Cer. Soc.*, **74**, 49-53.

Hendry, A. (1977) Thermodynamics of silicon nitride and oxynitride. In Nitrogen Ceramics, Ed: F.L. Riley. Noordhoff International, Leyden, Netherlands.

Hermansson, L., Nystrom, L. and Adlerborn, J. (1986) Hot isostatic pressing of silicon carbide with no sintering agents. *In Ceramic Materials and Components for Engines*, Eds: W. Bunk and H. Hausner. p353-60.

Hess, J.B. and Barrett, C.S. (1949) Structure and nature of kink bands in zinc. *Trans. A.I.M.E.*, **185**, 599-606.

Heuer, A.H., Fryburg, G.A., Ogbuji, L.U. and Mitchell, T.E. (1978) β → α transformation in polycrystalline SiC: I. Microstructural aspects. *J. Am. Cer. Soc.*, **61**, 406-12.

Hillig, W.B. (1985) Prospects for ultra high temperature ceramic composites. *In Tailoring Multiphase and Composite Ceramics*, Eds: R.E Tressler, G.L. Messing, C.G. Pantano, R.E. Newnham. Plenum, New York, USA. p609-712.

Hiraga, K., Tsuno, K., Shindo, D., Hirobayashi, M., Hayashi, S. and Hirai, T. (1983) Structure of α- and β-Si_3N_4 observed by 1MV electron microscopy. *Phil. Mag.*, **A47**, 483-96.

Hiraga, K., Oku, T., Hirabayashi, M., Matsuda, T. and Hirai, T. (1989) Fivefold multiply-twinned precipitates in chemically vapour-deposited boron nitride studied by transmission electron microscopy. *J. Mat. Sci. Let.*, **8**, 130-34.

Hoffman, U. and Wilm, D. (1936) *Z. Electrochem.*, **42**, 504.

Hosoi, J., Oikawa, T., Inoue, M., Matsui., Y. and Endo, T. (1982) Study of boron nitride by electron energy-loss spectroscopy. *J. Electron Spectrosc. Relat. Phenom.*, **27**, 243-54.

Hough, D.B. and White, L.R. (1980) The calculation of Hamaker constants from Lifshitz theory with applications to wetting phenomena. *Adv. in Colloid and Interface Sci.*, **14**, 3-41.

Hull, D. and Bacon, D.J. (1984) *Introduction to Dislocations*, 3rd edition. Pergamon Press, Oxford.

Inomata, Y., Inoue, A., Mitomo, M. and Suzuki, H. (1968) Relation between growth temperature and the structure of SiC crystals grown by the sublimation method. *Yogyo-Kyokai-Shi.*, **76**, 313-19.

Inomata, Y., Inoue, Z. and Kijima, K. (1969) On the formation of the 15R type in the β → α transformation of SiC. *Yogyo-Kyokai-Shi.*, **77**, 313-18.

Inomata, Y., Inoue, Z., Mitomo, M. and Tanaka, H. (1969a) Polytypes of SiC crystals grown from molten silicon. *Yogyo-Kyokai-Shi.*, **77**, 83-88.

Ishii, T. and Sato, T. (1983) Growth of single crystals of hexagonal boron nitride. *J. Crys. Growth*, **61**, 689-90.

Israelachvili, J.N. (1992) *Intermolecular and Surface Forces*, 2nd. edition. Academic Press, London.

Jack, K.H. (1983) The characterisation of α'-SiAlONs and the α-β relationships in SiAlONs and silicon nitrides. *Progress in Nitrogen Ceramics*, Ed: F.L. Riley. (Nato ASI Series. Series E, Applied Sciences – no. 65) Martinus Nijhoff Publishers, The Hague, The Netherlands, p45-60.

Jaffe, H.W. (1988) *Introduction to Crystal Chemistry*. Cambridge University Press.

Jagodzinski, H. (1954) Poytypism in SiC crystals. *Acta Crystallog.*, **7**, 300-05.

Janney, M.A. (1987) Mechanical properties and oxidation behaviour of a hot pressed SiC-15 vol% TiB_2 composite. *Am. Cer. Soc. Bull.*, **66**, 322-24.

Jepps, N.W. (1979) *Polytypism and Polytype Transformation in Silicon Carbide*. Ph.D. Thesis. University of Cambridge.

Jepps, N.W. and Page, T.F. (1981) The 6H → 3C 'reverse' transformation in silicon carbide compacts. *J. Am. Cer. Soc.*, **64**, C177-C178.

Jepps, N.W. and Page, T.F. (1983) Polytypic transformations in silicon carbide. *Prog. in Cryst. Growth and Charact.* **7**, 259-307.

Jha, A. (1993) Phase equilibria in the Si-C-N-O system and the kinetic analysis of silicon carbide whisker growth. *J. Mat. Sci.*, **28**, 3069-79.

Kara, F. (1994) *Processing and characterisation of mullite based ceramics*, Ph.D. Thesis, University of Cambridge, UK.

Kargol, J.A. and Albright, D.L. (1977) The effect of relative crystal orientation on the liquid metal induced grain boundary fracture of aluminum bicrystals. *Met. Trans.*, **A8**, 27-34.

Kato, K., Inoue, Z., Kijima, K., Kawada, I., Tamaka, H. and Yamane, T. (1975) *J. Am. Cer. Soc.*, **58**, 90-

Kieffer, A. R., Ettmayer, P., Angel, E. and Schmidt, A. (1969) Phase stability of SiC in the ternary system Si-C-N. *Mat. Res. Bull.*, **4**, S153-S166.

Kim, D-Y., Wiedorhorn, S.M., Hockey, B.J., Handwerker, C.A. and Blendell, J.E. (1994) Stability and surface energies of wetted grain boundaries in aluminum oxide. *J. Am. Cer. Soc.*, **77**, 444-53.

Kingery, W. D. (1974) Plausible concepts necessary and sufficient for interpretation of ceramic grain boundary phenomena: I. Grain boundary characteristics, structure, and electrostatic potential. *J. Am. Cer. Soc.*, **57**, 1-8.

Kingery, W. D., Bowen, H.K. and Uhlmann, D.R. (1976) *Introduction to Ceramics*, 2nd Edition. Wiley.

Kinsman, K.R. and Shinozaki, S.S. (1978) An uncommon mode of morphological development among coherent phases (SiC). *ScriptaMetallurgica*, **12**, 517-23.

Kinsman, K.R. and Shinozaki, S.S. (1982) Influence of interfacial structure on the morphology of the α to β and β to α transformation in polycrystalline SiC. *Proceedings of International Conference on Solid → Solid Phase Transformations*, Eds: H.I. Arranson, D.E. Laughlin, R.F. Sekerka and C.M. Wayman. p605-09.

Kleebe, H.-J. and Cinibulk, M.K. (1993) Transmission electron microscopy characterisation of a ceria-fluxed silicon nitride. *J. Mat. Sci. Lett.*, **12**, 70-72.

Kleebe, H.-J., Corbin, N., Willkens, C. and Rühle, M. (1990) Transmission electron microscopy studies of silicon nitride/silicon carbide interfaces. *Mat. Res. Soc. Symp. Proc.*, **170**, 79-84.

Kleebe, H.-J., Hoffmann, M.J. and Rühle, M. (1992) Influence of secondary phase chemistry on grain boundary film thickness in silicon nitride. *Z. Metallkd.*, **83**, 610-17.

Kleebe, H.-J., Cinibulk, M.K., Cannon R.M. and Rühle, M. (1993) Statistical analysis of the intergranular film thickness in silicon nitride ceramics. *J. Am. Cer. Soc.*, **76**, 1969-77.

Knieppenberg, W.F. (1963) Growth phenomena in silicon carbide whiskers. *Philips Res. Rep.*, **18**, 161-274.

Kraus-Lanteri, S.P., Mitchell, T.E. and Heuer, AH. (1986) Structure of incoherent ZrO_2/Al_2O_3 interfaces. *J. Am. Cer. Soc.*, **69**, 256-58.

Krivanek, O.L., Shaw, T.M. and Thomas, G. (1979) Imaging of thin intergranular phases by high-resolution electron microscopy. *J. Appl. Phys.*, **50**, 4223-27.

Kronberg, M.L. and Wilson, F.H. (1949) *Trans. AIME*, **185**, 501-14.

Kumar, A. (1994) *Microstructure-property relationships of SiC fibre-reinforced magnesium aluminosilicates*, Ph.D. Thesis, University of Cambridge, UK.

Kurdymov, A.V., Ostrovskaya, N.F. and Pilyankevich, A.N. (1976) Twinning in graphite-like boron nitride. *Sov. Phys. Crystall.*, **21**, 229-31.

Kurishita, H. and Yoshinaga, H. (1989) Grain boundary fracture in molybdenum. *Materials Forum*, **13**, 161-73.

Kwon, O-H. and Messing, G.L. (1991) A theoretical analysis of solution-precipitation controlled densification during liquid phase sintering. *Acta Metall. Mat.*, **39**, 2059-68 .

Lange, F. F. (1973) Effect of microstructure on strength of Si_3N_4-SiC composite system. *J. Am. Cer. Soc.*, **56**, 445-50.

Lange, F. F. (1975) Hot-pressing behaviour of silicon carbide powders with addition of Al_2O_3. *J. Mat. Sci.*, **10**, 314-20.

Lange, F. F. (1982) Volatilization associated with the sintering of polyphase Si_3N_4 materials. *J. Am. Cer. Soc.*, **65**, C120-21.

Lange, F. F. (1982a) Liquid phase sintering: Are liquids squeezed out from between compressed particles? *J. Am. Cer. Soc.*, **65**, C23.

Lange, F.F. and Gupta, T.K. (1976) Sintering of SiC with boron compounds. *J. Am. Cer. Soc.*, **59**, 537-38.

Leapman, R. D. and Silcox, J. (1979) Orientation dependence of core edges in electron energy-loss spectra from anisotropic materials. *Phys. Rev. Lett.*, **42**, 1361-64.

Leapman, R. D., Fejes, P.L. and Silcox, J. (1983) Orientation dependence of core edges from anisotropic materials determined by inelastic scattering of fast electrons. *Phys. Rev.*, **B28**, 2361-73.

Lee, B-T., Pezzotti, G. and Hiraga, K. (1994) Microstructure and fracture behaviour of SiC-platelet-reinforced Si_3N_4 matrix composites. *Mat. Sci. and Eng.*, **A177**, 151-60.

Lee, W.E. and Rainforth, W.M. (1994) *Ceramic Microstructures: Property control by processing*. Chapman and Hall, London.

Lewis, D. and Rice, R.W. (1981) Thermal shock fatigue of monolithic ceramics and ceramic-ceramic particulate composites. *Cer. Eng. and Sci. Proc.*, **2**, 712-18.

Lewis, D., Ingel, R.P., McDonoughs, W.J. and Rice, R.W. (1981) Microstructure and thermomechanical properties in alumina- and mullite-boron nitride particulate ceramic-ceramic composites. *Cer. Eng. and Sci. Proc.*, **2**, 719-27.

Lewis, M.H. (1989) *Glasses and Glass-Ceramics*. Chapman and Hall, New York.

Lifshitz, E.M. (1956) *Soviet Phys. JETP (English Transl.)*, **2**, 73-83.

Lilov, S.K., Tairov, Y.M., Tsvetkov, V.F. and Chernov, M.A. (1976) Structural and morphological peculiarities of the epitaxial layers and monocrystals of silicon carbide highly doped by nitrogen. *Phys. Stat. Sol.*, **37**, 143-50.

Lou, L.K.V, Mitchell, T.E. and Heuer, A.H. (1978) Impurity phases in hot pressed Si_3N_4. *J. Am. Cer. Soc.*, **61**, 392-96.

Lowden, R.A. and More, K.L. (1990) The effect of fiber coating on interfacial shear strength and the mechanical behaviour of ceramic composites. *Mat. Res. Soc. Symp. Proc.*, 170, 205-14.

Lu, P., Danforth, S.C. and Symons, W.T. (1993) Microstructure and grain boundary characterization of HIP'ed high purity silicon nitride. *J. Mat. Sci.*, **28**, 4217-22.

Lutz, E.H. and Swain, M.V. (1992) Fracture toughness and thermal shock behaviour of silicon nitride-boron nitride ceramics. *J. Am. Cer. Soc.*, **75**, 67-70

Mahanty, J. and Ninham, B.W. (1976) *Dispersion Forces*. Academic press, London.

Marion, J.E., Hsueh, C.H. and Evans, A.G. (1987) Liquid phase sintering of ceramics. *J. Am. Cer. Soc.*, **70**, 708-13.

Martin, J.M., Belin, M., Mansot, J.L., Hssein, K., Zanehi, G. and Sevely, J. (1988) EELS graphitic boron nitride fine structure studies. *Ins. Phys. Conf.*, No: 93, Vol: 2, Chapter 4, Presented in EUREM 88, 175-76.

Martin, S. (1980) Aspects of the hot-pressing of silicon carbide. Ph.D. Thesis, University of Cambridge.

Matthews, J.W. (Ed.) (1975) *Epitaxial Growth A and B.* Academic Press, New York.

McColm, I.J. (1983) *Ceramic Science for Materials Technologists.* Blackie and Son Ltd, Glasgow.

McCrone, W. C., McCrone L.B. and Delly J.G. (1978) *In Polarised Light Microscopy.* Ann Arbor Science Publishers, Michigan.

McMurtry, C.H., Boecker, W.D.G., Seshadri, S.G., Zanghi, J.S. and Garnier, J.E. (1987) Microstructure and material properties of SiC-TiB_2 particulate composites. *Am. Cer. Soc. Bull.*, **66**, 325-29.

Mieskowski, D., Mitchell, T.E. and Heuer, A.H. (1984) Bubble formation in oxide scales on SiC. *J. Am. Cer. Soc.*, **67**(1), C17-C18.

Mitchell, T.E., Ogbuji, L.U. and Heuer, A.H. (1978) $\beta \rightarrow \alpha$ transformation in polycrystalline SiC: II. Interfacial energetics. *J. Am. Cer. Soc.*, **61**, 412-13.

Miyazaki, Y., Harada, H., Sakamaki, S. and Hagio, T. (1992) Microstructure of pressureless sintered h-BN. *J. of the Cer. Soc. of Jap. Int. Edition,* **99**, 566-69.

More, K.L., Carter, C.H., Bentley, J., Wadlin, W.H., LaVanier, L. and Davis, R.F. (1986) Occurrence and distribution of boron-containing phases in sintered α-SiC. *J. Am. Cer. Soc.*, **69**, 695-98.

More, K.L., Koester, D.A. and Davis, R.F. (1991) Microstructural characterisartion of a creep-deformed SiC whisker-reinforced Si_3N_4. *Ultramicroscopy,* **37**, 263-78.

Morrisey, K.J. and Carter, C.B. (1984) Faceted grain boundaries in Al_2O_3. *J. Am. Cer. Soc.*, **67**, 292-301.

Moulson, A.J. and Herbert, J.M. (1990) *Electroceramics: Materials, properties, applications.* Chapman and Hall, London.

Mulla, M.A. and Krstic, V.D. (1991) Low temperature pressureless sintering of β-SiC with aluminium oxide and yttrium oxide additions. *Am. Cer. Soc. Bull.*, **70**, 439-43.

Murata, Y. and Smoak, R.H. (1978) Densification of silicon carbide by the addition of BN, BP, and B_4C, and correlation to their solid solubilities. *Proc. of Int. Sym. of Factors in Densification and Sintering of Oxide and Nonoxide Ceramics,* Ed: S. Somiya and S. Saito, Gakujutsu Bunken Fukyu-Kai Ookayama, Tokyo, p382-99

Ness, J.N. (1985) *The microstructure of reaction-bonded silicon carbide.* Ph.D. Thesis, University of Cambridge.

Ness, J.N., Stobbs, W.M. and Page, T.F. (1986) A TEM Fresnel diffraction-based method for characterizing thin grain boundary and interfacial films. *Phil. Mag.*, **A54**, 679-702.

Nezuka, K., Miyamoto, Y. and Koizumi, M. (1988) Mechanical and thermal properties of dense Si_3N_4 without additives sintered by HIP. *In Proceedings of the International Conference on Hot Isostatic Pressing*, Ed: T. Garvare. Centek Publishers, Luleå, Sweden. p359-65.

Nicolas, A. and Poirier, J.P. (1976) *Crystalline Plasticity and Solid State Flow in Metamorphic Rocks.* Wiley, New York.

Niihara, K., Suganuma, K., Nakahira, A. and Izaki, K. (1990) Interfaces in Si_3N_4-SiC nano-composite. *J. Mat. Sci. Lett.*, **9**, 598-99.

Norton, M.G. and Carter, C.B. (1990) Interfaces in structural ceramics. *MRS Bulletin*, **10**, 51-59.

Oda, K. and Yoshio, T. (1993) Oxidation kinetics of hexagonal boron nitride powder. *J. Mat. Sci.*, **28**, 6562-66.

Ogbuji, L.U., Mitchell, T.E. and Heuer, A.H. (1981) The $\beta \rightarrow \alpha$ transformation in polycrstalline SiC; III. The thickening of a plates. *J. Am. Cer. Soc.*, **64**, 91-99.

Ogbuji, L.U., Mitchell, T.E., Heuer, A.H. and Shinozaki, S. (1981a) The $\beta \rightarrow \alpha$ transformation in polycrstalline SiC: IV. A comparison of conventionally sintered, and chemically vapour deposited samples. *J. Am. Cer. Soc.*, **64**, 100-05.

Ohring, M. (1992) *The Materials Science of Thin Films.* Academic Press.

Omori, M. and Takei, H. (1982) Pressureless sintering of SiC. *J. Am. Cer. Soc.*, **65**, C92.

Orowan, E. (1942) A type of plastic deformation new in metals. *Nature* , **149**, 643-45.

Pacault, A. (1971) The kinetics of graphitization. In *Chemistry and Physics of Carbon*, Ed: P.L. Walker. Vol. **7**, 107-54. Marcel Dekker Inc., New York.

Page, T.F., Sawyer, G.R., Adewoye, O.O. and Wert, J.J. (1978) Hardness and wear behaviour of SiC and Si_3N_4 ceramics. *Proc. Br. Cer. Soc.*, **26**, 193-208.

Palache, C. (1941) *Am. Mineralogist*, **26**, 709.

Pandey, D. and Krishna, P. (1974) Mechanisms of solid-state transformations in silicon carbide. *In Silicon Carbide-1973*, Eds: R.C. Marshall, J.W. Faust, Jr. and C.E. Ryan. Proc. III Int. Conf. on SiC., Florida. p198-205.

Parsegian, V.A. and Weiss, G.H. (1972) Dielectric anisotropy and the van der Waals interaction between bulk media. *J. Adhesion*, **3**, 259-67.

Pease, R.S. (1952) An X-ray study of BN. *Acta Cryst.*, **5**, 356-61.

Pehlke, R.D. and Elliott, J.F. (1959) High-temperature thermodynamics of the silicon, nitrogen, silicon nitride system. *Trans. Metall. Soc. AIME*, **215**, 781-85.

Pezzotti, G. (1993) Si_3N_4/SiC-platelet composite without sintering aids: A candidate for gas turbine engines. *J. Am. Cer. Soc.*, **76**, 1313-20.

Pezzotti, G., Ueda, S., Niihara, K. and Nishida, T. (1994) Estimate of polytype fractions and dislocation density in SiC before and after sintering in Si_3N_4 matrix. *J. Mat. Sci.*, **29**, 6311-19.

Phillipp, F., Hoschen, R., Osaki, M., Mobus, G. and Rühle M. (1994) New high-voltage atomic resolution microscope approaching 1 Å point resolution installed in Stuttgart. *Ultramicroscopy*, **56**, 1-10.

Pirouz, P. and Yang, J.W. (1993) Polytypic transformations in SiC: the role of TEM. *Ultramicroscopy*, **51**, 189-214.

Ponthieu, C., Marhic, C., Lancin, M. and Herbots, N. (1994) SIMS, EDX, EELS, AES, XPS study of interphases in nicalon fibre-LAS glass matrix composites: Part II. Chemistry of the interphases. *J. Mat. Sci.*, **29**, 4535-44.

Popper, P. and Davies, D.G.S. (1961) The preparation and properties of self-bonded SiC. *Powder Met.*, **8**, 113.

Porter, D.A. and Easterling, K.E. (1992) *Phase Transformations in Metals and Alloys*, 2nd edition. Chapman and Hall, London.

Powell, J.A. and Will, H.A. (1972) Low-temperature solid-state phase transformations in 2H silicon carbide. *J. Appl. Phys.*, **43**, 1400-08.

Prewo, K.M. (1986) The development of fiber reinforced glasses and glass ceramics. *Tailoring Multiphase and Composite Ceramics*, Ed: R. E. Tressler, G. L. Messing, C.G. Pantano and R.E. Newnham. Plenum Press, New York. p529-47.

Price, N.J. and Cosgrove, J.W. (1990) *Analysis of Geological Structures*. Cambridge University Press, Cambridge.

Prochazka, S. (1973) Sintering of silicon carbide. General Electric Report 73CRD325.

Prochazka, S. (1974) Sintering of silicon carbide. *In Ceramics for High-Performance Applications*, Eds: J.J. Burke, A.E. Gorum and R.N. Katz. p239.

Prochazka, S. (1975) The role of boron and carbon in the sintering of silicon carbide. *In Special Ceramics*, **6**, 171-81.

Qing, L., Xiaoxu, H. and Mei, Y. (1989) Calculation of tilt angles for crystal specimen orientation adjustment using double-tilt and tilt rotate holders. *Micron and Microsc. Acta*, **20**, 255-59.

Qing, L., Qing-Chang, M. and Bande, H. (1992) New method for determining grain boundary parameters. *Ultramicroscopy*, **41**, 317-21.

Rahaman, M.N., Boiteux, Y. and De Jonghe, L.C. (1986) Surface characterisation of silicon nitride and silicon carbide powders. *Am. Cer. Soc. Bull.*, **65**, 1171-76.

Raj, R. (1981) Morphology and stability of the glass phase in glass-ceramic systems. *J. Am. Cer. Soc.*, **64**, 245-48.

Ramsdell, R.S. (1947) Studies in silicon carbide. *Am. Mineralogist*, **32**, 64-82.

Randle, V. (1993) *The Measurement of Grain Boundary Geometry*. Institute of Physics Publishing, Bristol and Philadelphia.

Read, W.T. and Shockley, W. (1950) Dislocation models of crystal grain boundaries. *Phys. Rev.*, **78**, 275-89.

Reed-Hill, R.E. and Abbaschian, R. (1992) *Physical Metallurgy Principles*, 3rd edition. PWS-Kent publishing Company, Boston.

Reimer, L. (1989) *Transmission Electron Microscopy – Physics of Image Formation and Microanalysis*. Springer Series in Optical Sciences 36, Springer and Verlag.

Reimer, L., Zepke, U., Moesch, J., Schulze-Hillert, S., Ross-Messemer, M., Probst, W. and Weimer, E. (1992) *EELSpectroscopy*. Carl Zeiss, Oberkochen, Germany.

Renlund, G.M., Prochazka, S. and Doremus, R.H. (1991) Silicon oxycarbide glasses: Part II. structure and properties. *J. Mat. Res.*, **6**, 2723-34.

Rice, R.W., Becher, P.F., Freiman, S.W. and Mcdonough, W.J. (1980) Thermal structural ceramic composites. *Cer. Eng. and Sci. Proc.*, **1**, 424-43.

Richter, H.J., Herrmann, M. and Hermel, W. (1991) Calculation of heterogeneous phase equilibria in the system Si-Mg-N-O. *J. Eur. Cer. Soc.*, **7**, 3-9.

Riley, F.L. (Ed.) (1983) *Progress in Nitrogen Ceramics* (Nato ASI Series. Series E, Applied Sciences – no. 65) Martinus Nijhoff Publishers, The Hague, The Netherlands.

Rochow, E.G. (1973) *The Chemistry of Silicon*. Pergamon Press, Oxford.

Ross, F.M. (1989) *The application of Fresnel fringe contrast analysis to the oxidation of silicon*, Ph.D. Thesis, University of Cambridge.

Rouzaud, J.N. and Oberlin, A. (1989) Structure, Microtexture, and Optical Properties of Anthracene and Saccharose-Based Carbons. *Carbon*, **27**, 517-29.

Ruh, R., Bentsen, L.D. and Hasselman, D.P.H. (1984) Thermal diffusivity anisotropy of SiC/BN composites. *J. Am. Cer. Soc.*, **67**, C83-4.

Ruh, R., Kearns, M., Zangvil, A. and Xu, Y. (1992) Phase and property studies of boron carbide-boron nitride composites. *J. Am. Cer. Soc.*, **75**, 864-72.

Ruh, R., Zangvil, A. and Wills, R.R. (1988). Phase and property studies of SiC-BN composites. *Adv. Cer. Mat.*, **3**, 411-15.

Rühle, M. and Petzow, G. (1981) Microstructure and chemical composition of grain boundaries in ceramics. *In surfaces and interfaces in ceramic and ceramic-metal systems*. Eds: J. Pask and A. Evans. Plenum Press, New York. Mat. Sci. Res. Vol: 14, 167-75.

Rühle, M. (1984) TEM observations of grain boundaries in ceramics. *Mat. Res. Soc. Symp. Proc.*, **31**, 317-323.

Rühle, M. and Sass, S.L. (1984) The detection of the change in mean inner potential at dislocations in grain boundaries in NiO. *Phil. Mag.*, **A49**, 759-82.

Rühle, M. Bischoff, E. and David, O. (1984) Structure of grain boundaries in ceramics. *Ultramicroscopy*, **14**, 37-46.

Ruska, J., Gauckler, L.J., Lorenz, J. and Rexer, H.U. (1979) The quantitative calculation of SiC polytypes from measurements of XRD peak intensities. *J. Mat. Sci.* **14**, 2013-17.

Sakka, S., Kamiya, K. and Yoko, T. (1983) Preparation and properties of Ca-Al-Si-O-N oxynitride glasses. *J. of Non Crystalline Solids*, **56**, 147-52.

Scaife, B. K. P. (1989) *Principles of Dielectrics*. Clarendon Press, Oxford.

Schmid, H. and Rühle, M. (1984) Structure of special grain boundaries in SiAlON ceramics. *J. Mat. Sci.*, **19**, 615-28.

Schneer, C.J. (1955) Polymorphism in one direction. *Acta Crystallog.*, **8**, 279-85.

Shaffer, P.T.B. (1969) Review of the structure of silicon carbide. *Acta Crystallogr.*, **B25**, 477-88.

Shaffer, P.T.B. (1974) *In Silicon Carbide-1973*, Eds: R.C. Marshall, J.W. Faust, Jr. and C.E. Ryan. Proc. III Int. Conf. on SiC., Floridal. p343.

Shaffer, P.T.B. and Whitney, E.D. (1971) Silicon carbide containing boron and nitrogen in solid solution. U.S. Pat. No. 3554717.

Shinozaki, S.S. and Kinsman, K.R. (1975) Structural considerations relating to the $\beta \rightarrow \alpha$ transformation in silicon carbide. *Am. Cer. Soc. Bull.*, **54**, 739-.

Shinozaki, S.S. and Kinsman, K.R. (1978) Evolution of microstructure in polycrystalline silicon carbide. *Processing of Prystalline Ceramics*. Plenum Press, New York. p641-52.

Shinozaki, S.S., Hangas, J., Donlon, W.T., Williams, R.M. and Juterbock, B.N. (1988) Analytical electron microscopy on the effects of sintering aids in pressureless sintered

SiC materials. *Advanced Ceramics II*, Ed: S. Somiya. Elsevier Science Publishers LTD, New York. p7-28.

Shinozaki, S.S. and Sato, H. (1978) Microstructure of SiC prepared by chemical vapor deposition. *J. Am. Cer. Soc.*, **61**, 425-29.

Shinozaki, S.S., Noakes, J. E. and Sato, H. (1978) Recrystallisation and phase transformation in reaction sintered SiC. *J. Am. Cer. Soc.*, **61**, 237-42.

Sigl, L.S. and Kleebe, H-J. (1993) Core/rim structure of liquid-phase-sintered silicon carbide. *J. Am. Cer. Soc.*, **76**, 773-76.

Simpson, Y.K., Carter, C.B., Morrissey, K.J., Angelini, P. and Bentley, J. (1986) The identification of thin amorphous films at grain boundaries in Al_2O_3. *J. Mat. Sci.*, **21**, 2689-96.

Sinclair, W. and Simmons, H. (1987) Microstructure and thermal shock behaviour of boron nitride composites. *J. Mat. Sci. Let.*, **6**, 627-29.

Singh, M. and Wiedemeier, H. (1991) High temperature thermal and environmental stabilities of boron nitride, aluminium nitride and silicon nitride ceramics. *Materials at High Temperatures*, **9**, 139-44.

Skiff, W.M., Carpenter, R.W. and Lin, S.H. (1985) Si_L core edge fine-structure in an oxidation series of silicon compounds: A comparison of microelectron energy loss spectra with theory. *J. Appl. Phys.*, **58**, 3463-69.

Skiff, W.M., Carpenter, R.W. and Lin, S.H. (1987) Near-edge fine-structure analysis of core-shell electronic absorption edges in silicon and its refractory compounds with the use of electron-energy-loss microspectroscopy. *J. Appl. Phys.*, **62**, 2439-49.

Smith, D.J. (1989) *Instrumentation and Operation for High-Resolution Electron Microscopy.* Advances in Optical and Electron microscopy, Vol. 11, Ed: T. Mulvey and C.J.R. Sheppard. Academic Press, London. p1-55.

Sokhor, M.I., Kondakov, V.G. and Fel'dgun, L.I. (1968) Transition of silicon carbide from the hexagonal to the cubic phase under the influence of high pressures and high temperature. *Sov. Phys. Dokl.*, **12**, 749-51.

Soule, D.E. and Nezbeda, C.W. (1968) Direct basal-plane shear in single-crystal graphite. *J. Appl. Phys.* **39**, 5122-39.

Spence, J.C.H. (1988) *Experimental High Resolution Electron Microscopy*, 2nd Edition. Oxford University Press, Oxford.

Srinivasan, M. (1989) The silicon carbide family of structural ceramics. *In Treatise On Materials Science and Technology.* Vol: **29**, 99-159.

Starkey, J. (1968) The geometry of kink bands in crystals: A simple model. *Contrib. Mineral. Petrol.*, **19**, 133-41.

Stenton, N. and Harmer, M.P. (1983) *Adv. Cer.*, **7**, 156.

Stephen, A.P. and Brown, L.M. (1981) EXELFS in graphitic boron nitride. *In Quantitative Microanalysis with High Spatial Resolution.* The Metals Society, London. p152-58.

Stobbs, W.M. (1990) New TEM techniques for the characterisation of a boundary. *In EUROMAT '89.* 1007-18.

Stobbs, W.M. and Ross, F.M. (1989) The Fresnel method for the characterisation of interfaces. NATO ASI series B, Physics, **203**. Ed: D. Cherns. Plenum Press, London. p183-202.

Stroh, A.N. (1958) The cleavage of metal single crystals. *Phil. Mag.*, **3**, 597-606.

Stull, D.R. and Prophet, H. (1971) *JANAF Thermomechanical Tables*, 2nd edition. National Bureau of Standards, Washington, DC.

Stutz, D.H., Prochazka, S. and Lorenz, J. (1985) Sintering and microstructure formation of β-SiC. *J. Am. Cer. Soc.*, **68**, 479-82.

Suematsu, H., Suzuki, T., Iseki, T. and Mori, T. (1991) Kinking and cracking caused by slip in single crystals of silicon carbide. *J. Am. Cer. Soc.*, **74**, 173-78.

Sun, C.P. and Balluffi, R.W. (1982) Secondary grain boundary dislocations in [001] twist boundaries in MgO: I. Intrinsic structures. *Phil. Mag.*, **A46**, 49-63.

Susnitzky, D.W. and Carter, C.B. (1990) Structure of alumina grain boundaries prepared with and without a thin amorphous intergranular film. *J. Am. Cer. Soc.*, **73**, 2485-93.

Sutton, A.P. and Balluffi, R.W. (1987) On geometric criteria for low interfacial energy. *Acta Metall.*, **35**, 2177-201.

Suzuki, H. and Hase, T. (1979) Some experimental consideration on the mechanism of pressureless sintering of silicon carbide. *Proc. of Int. Sym. of Factors in Densification and Sintering of Oxide and Nonoxide Ceramics,* Ed: S. Somiya and S. Saito. Gakujutsu Bunken Fukyu-Kai Ookayama, Tokyo, p345.

Suzuki, H. and Hase, T. (1980) Boron transport and change of lattice parameter during sintering of β-SiC. *J. Am. Cer. Soc.*, **63**, 349-50.

Suzuki, K., Ono, T. and Shinohara, N. (1982) Dense sintered silicon carbide ceramic. U.S. Patent 4, 354, 991.

Tabor, D. and Winterton, R. H. S. (1969) The direct measurement of normal and retarded van der Waals forces. *Proc. Roy. Soc.*, **A312**, 435-50.

Tabor, D. (1991) *Gases, Liquids and Solids*; 2nd Edition. Cambridge University Press, Cambridge, U.K. p247-49.

Takemura, H., Y. Miyamoto and M. Koizumi, (1988) Fabrication of dense Si_3N_4–SiC whisker composite without additives by HIP. *In Proceedings of the International Conference on Hot Isostatic Pressing*, Ed: T. Garvare. Centek Publishers, Luleå, Sweden. p329-35.

Tanaka, I., Pezzotti, G. Okamoto, T., Miyamoto, Y. and Koizumi, M. (1989) Hot isostatic press sintering and properties of silicon nitride without additives. *J. Am. Cer. Soc.*, **72**, 1656-60.

Tanaka, I., Kleebe, J.-H., Cinibulk, M.K., Bruley, J., Clarke, D.R. and Rühle, M. (1994) Calcium concentration dependence of the intergranular film thickness in silicon nitride. *J. Am. Cer. Soc.*, **77**, 911-14.

Thomas, G. and Goringe, M.J. (1979) *Transmission Electron Microscopy of Materials*. Wiley Interscience, New York.

Thomas, J., Weston, N. E. and O'Connor, T. E. (1963). Turbostratic BN, thermal transformation to ordered-layer-lattice BN. *J. Am. Chem. Soc.*, **84**, 4619-22.

Tighe, N.J., Sun, J. and Hu, R.-M. (1986) Microstructures of SiC and Si_3N_4 with fibrous inclusions. *Proc. of the 44th Annual Meeting of the Electron Microscopy Society of America, Ed: G.W. Bailey*. San Francisco Press, p492-93.

Trefilov, V.I., Borisenko, V.A., Gnesin, G.G., Gridneva, I.V., Mil'man, Y.V. and Chugunova, S.I. (1978) On phase transition under pressure in silicon carbide. *Sov. Phys. Dokl.*, **23**, 207-08.

Turan, S. and Knowles, K.M. (1993) Transmission electron microscopy of BN inclusions in Si_3N_4-SiC composites *Inst. Phys. Conf. Ser.* **138**, 387-90.

Turan, S. and Knowles, K.M. (1995) A comparison of the microstructure of silicon nitride–silicon carbide composites made with and without deoxidised starting powders. *J. of Mic.*, **177**, 287-304.

Turan, S. and Knowles, K.M. (1995a) Formation of boron nitride inclusions in hot isostatically pressed silicon nitride-silicon carbide composites. *J. Am. Cer. Soc.*, **78**, 680-684.

Ünal, O. and Mitchell, T.E. (1992) CVD Si_3N_4 on single crystal SiC: Part II. High resolution electron microscopy and atomic models of the interface. *J. Mat. Res.*, **7**, 1445-54.

Ünal, O., Petrovic, J.J. and Mitchell T.E. (1992) CVD Si_3N_4 on single crystal SiC: Part I. Characterisation and orientation relationship at the interface. *J. Mat. Res.*, **7**, 136-147.

Ünal, O., Petrovic, J.J. and Mitchell T.E. (1993) Mechanical properties of hot isostatically pressed Si_3N_4/SiC composites. *J. Mat. Res.*, **8**, 626-34.

Verma, A. R. and Krishna, P. (1966) Polymorphism and polytypism in crystals. John Wiley and Sons, New York.

Vetrano, J.S., Kleebe, H.-J., Hampp, E., Hoffmann, M.J., Rühle, M. and Cannon, R.M. (1993) Yb_2O_3-fluxed sintered silicon nitride: Part I. Microstructure characterisation *J. Mat. Sci.*, **28**, 3529-38

Wakai, F., Kodama, Y., Sakaguchi, S., Murayama, N., Izaki, K. and Niihara, K. (1990) A superplastic covalent crystal composite. *Nature* **344**, 421-23.

Wakino, K.T., Okada, Yoshida, N. and Tomono, K.(1993) A new equation for predicting the dielectric constant of a mixture. *J. Am. Cer. Soc.*, **76** [10] 2588-94.

Watson, G.K, Moore, T.J, Millard, M.L. (1985) Effect of hot isostatic pressing on the properties of sintered alpha silicon carbide. *Am. Cer. Soc. Bull.*, **64**, 550-54.

Wei, G.C. and Becher, P.F. (1984) Improvements in mechanical properties in SiC by addition of TiC particles. *J. Am. Cer. Soc.*, **67**, 571-74.

Wei, G.C. (1983) β-SiC powders produced by carbothermic reduction of silica in a high temperature rotary furnace. *J. Am. Cer. Soc.*, **66**, C111-C113.

Weiss, J., Lukas, H.L., Lorenz, J., Petzow, G. and Krieg, H. (1981) Calculation of heterogeneous phase equilibria in oxide-nitride systems. *CALPHAD: Comput. Coupling Phase diagrams Thermochem.*, **5**, 125-140.

Whitney, E.D. (1963) Polymorphism in silicon carbide. *Nature*, **199**, 278-80.

Whitney, E.D. and Shaffer, P.T.B. (1969) Investigation of the phase transformation between α and β silicon carbide at high pressures. *High Temp.-High Press.* **1**, 107-10.

Wickersheim, K.A. and LaFever, R.A. (1961) Infrared transmittance of crystalline yttrium oxide and related compounds. *J. Opt. Soc. Am.*, **51**, 1147.

Wolf, D. (1982) On the stability of (001) CSL twist boundaries in MgO: A theoretical study. *J. De Phys. Colloque C6*, **43**, 45-63.

Wolf, D. (1992) Atomic-level geometry of crystalline interfaces. *In Materials Interfaces*, Eds: D. Wolf and S. Yip. Chapman and Hall, London. p1-57.

Wood, G.J., Stobbs, W.M. and Smith, D.J. (1984) Methods for the measurement of rigid-body displacements at edge-on boundaries using HREM. *Phil. Mag.*, **A50**, 375-91.

Wood, R.M. (1993) *OpticalMaterials*. Institute of Materials.

Wrobleska, G.H. and Hamminger, R. (1991) Microanalytical investigations of the intermediate sintering state of silicon carbide.*Ceramics International*, **17**, 199-203.

Wrobleska, G.H., Nold, E. and Thümmler, F. (1990) The role of boron and carbon additions on the microstructural development of pressureless sintered silicon carbide. *Ceramics International*, **16**, 201-09.

Xu, Y., Zangvil, A., Landon, M. and Thevenot, F. (1992) Microstructure and mechanical properties of hot-pressed silicon carbide-aluminum nitride compositions.

Xu, Y.-N. and Ching, W. Y. (1991) The calculation of ground-state and optical properties of boron nitrides in the hexagonal, cubic and wurtzite structures. *Phys. Rev.*, **B44**, 7787-98.

Yang, J.W. and Pirouz, P. (1993) The $\alpha \rightarrow \beta$ polytypic transformation in high-temperature indented SiC. *J. Mat. Res.*, **8**, 2902-07.

Yang, J.W., Suzuki, T., Pirouz, P., Powell, J.A. and Iseki, T. (1992). *Mat. Res. Soc. Symp. Proc.*, **242**, 531-36.

Young, C.T., Steele, J.H. and Lytton, J.L. (1973) Characterisation of bicrystals using Kikuchi patterns. *Met. Trans.*, **4**, 2081-89.

Zangvil, A. and Ruh, R. (1985) Solid solutions and composites in the SiC-AlN and SiC-BN systems. *Mat. Sci. and Eng.*, **71**, 159-64.

Ziegler, G., Heinrich, J. and Wotting, G. (1987) Review: Relationships between processing, microstructure and properties of dense and reaction-bonded silicon nitride. *J. Mat. Sci.*, **22**, 3041-86.